UNIVERSIDADE ESTADUAL PAULISTA
CAMPUS DE ARARAQUARA
PROGRAMA DE PÓS-GRADUAÇÃO EM QUÍMICA

Bacterial cellulose and silk fibroin biopolymers: Biotemplates to design nanostructured materials for optical applications.

MOLÍRIA VIEIRA DOS SANTOS

Ph.D thesis
2016

MOLÍRIA VIEIRA DOS SANTOS

Biopolímeros de celulose bacteriana e fibroína da seda: biotemplates para a preparação de materiais nanoestruturados para aplicações ópticas

Tese apresentada ao Instituto de Química,
Universidade Estadual Paulista,
como parte dos requisitos para obtenção
do título de Doutor em Química.

Orientador: Prof. Dr. Sidney José Lima Ribeiro.

Araraquara
2016

FICHA CATALOGRÁFICA

Santos, Molíria Vieira dos
S237b Bacterial cellulose and silk fibroin biopolymers: biotemplates to design nanostructured materials for optical applications = Biopolímeros de celulose bacteriana e fibroína da seda: biotemplates para a preparação de materiais nanoestruturados para aplicações ópticas / Molíria Vieira dos Santos. – Araraquara: [s.n.], 2016
163 p.: il.

Tese (doutorado) – Universidade Estadual Paulista, Instituto de Química
Orientador: Sidney José Lima Ribeiro

1. Biopolímeros. 2. Cristais líquidos. 3. Sílica. 4. Luminescência. 5. Laser em física. I. Título.

Elaboração: Seção Técnica de Aquisição e Tratamento da Informação
Biblioteca do Instituto de Química, Unesp, câmpus de Araraquara

MOLÍRIA VIEIRA DOS SANTOS

Bacterial cellulose and silk fibroin biopolymers: Biotemplates to design nanostructured materials for optical applications.

Thesis presented to the Institute of Chemistry,
São Paulo State University "Júlio de Mesquita Filho",
to obtain the Ph.D in Chemistry.

Advisor: Prof. Dr. Sidney José Lima Ribeiro.

Araraquara
2016

MOLÍRIA VIEIRA DOS SANTOS

Tese apresentada ao Instituto de Química, Universidade Estadual Paulista, como parte dos requisitos para obtenção do título de Doutora em Química.

Araraquara, 04 de outubro de 2016.

BANCA EXAMINADORA

Prof. Dr. Sidney José Lima Ribeiro (Orientador)
Instituto de Química – UNESP, Araraquara - SP

Profª Drª Rogéria Rocha Gonçalves
Faculdade de Filosofia Ciências e Letras – USP, Ribeirão Preto - SP

Prof. Dr. Cleber Renato Mendonça
Instituto de Física – USP, São Carlos - SP

Prof. Dr. Ubirajara Pereira Rodrigues Filho
Instituto de Química – USP, São Carlos -SP

Prof. Dr. Masahide Takahashi
Faculdade Osaka Prefecture University – Osaka, Japão

1. DATA

MOLÍRIA VIEIRA DOS SANTOS

1.1. Date of birth: 04/29/1986
1.2. Nationality: Brazilian
1.3. Citizenship: Poços de Caldas
1.6. Profession: Chemist
1.7. E-mail: moliria.santos@gmail.com

2. ACADEMIC EDUCATION

2.1. Bachelor in chemistry – State of São Paulo University "Júlio de Mesquita Filho" (UNESP/Araraquara) – 2010.
2.2. Master in chemistry – State of São Paulo University "Júlio de Mesquita Filho" (UNESP/Araraquara) – 2012.

3. BIBLIOGRAPHIC PRODUCTION

3.1. Presentations in conferences: 13 international and 9 national.

3.2. Extended abstracts published in conference proceedings:

1) SANTOS, M. V.; TOLENTINO, C.; RIBEIRO, S.; BARUD, H.; DE ARAUJO, C. B.; GOMES, A.; DE MELO, L. **Biopolymer Random Laser Consisting of Rhodamine 6G and Silica Nanoparticles Incorporated to Bacterial Cellulose**. In: Conference on Lasers and Electro-Optics 2012. Washington: OSA, 2012. p. JW4A.51.

2) SILVA, R. R.; TOLENTINO, C.; SANTOS, M. V.; MELO, L.; RIBEIRO, S. J. L.; ARAUJO, C. B.; GOMES, A.; BARBOSA-SILVA, R. **Efficient Distributed Feedback Dye Laser in Silk Fibroin Films**. In: Conference on Lasers and Electro-Optics 2012. Washington: OSA, 2012. p. JW4A.53.

3.3. Publications in journals:

1) CAIUT, J. M. A.; BARUD, H.; SANTOS, M.; Oliveira U. L.; MENEZES, J. F. S; MESSADDEQ, Y.; RIBEIRO, S. J. L. Luminescent multifunctional biocellulose membranes. **Proceeding SPIE**, v. 8104, p. 81040Z-1-81040Z-9, 2011.

2) MARQUES, L. F.; DOS SANTOS, M. V., RIBEIRO, S. J. L., CASTELLANO, E. E.; MACHADO, F. C. Terbium (III) and dysprosium (III) 8-connected 3D networks containing 2,5-thiophenedicarboxylate anion: Crystal structures and photoluminescence studies. **Polyhedron**, v. 38, p. 149 - 156, 2012.

3) SANTOS, M. V., DOMINGUEZ, C. T., SCHIAVON, J. V.; BARUD, H. S.; MELO, L. A., RIBEIRO, S. J. L.; GOMES, A. S. L.; ARAÚJO, C. B. Random laser action from flexi biocellulose-based device. **Journal of Applied Physics**, v. 115, p. 083108, 2014.

4) SILVA, R. R.; DOMINGUEZ, C. T.; SANTOS, M. V.; BARBOSA-SILVA, R.; CAVICCHIOLI, M.; CHRISTOVAN, L. M., DE MELO, L. S. A., GOMES, ANDERSON S. L., DE ARAÚJO, CID B., RIBEIRO, SIDNEY J. L. Silk fibroin biopolymer films as efficient hosts for DFB laser operation. **Journal of Materials Chemistry C**, v. 1, p. 7181, 2013.

5) MARQUES, L. F.; CORRÊA, C. C.; DA SILVA, R. R., DOS SANTOS, M. V.; RIBEIRO, S. J. L.; MACHADO, F. C. Structure, characterization and near-infrared emission of a novel 6-connected uninodal 3D network of Nd(III) containing 2,5-thiophenedicarboxylate anion. Inorganic Chemistry Communications, v. 37, p. 66 - 70, 2013.

6) RIBEIRO, S. J.L.; DOS SANTOS, M. V.; SILVA, R. R.; PECORARO, É.; GONÇALVES, R. R.; CAIUT, J. M. A. (2015) Optical Properties of Luminescent Materials, in T**he Sol-Gel Handbook - Synthesis, Characterization, and Applications: Synthesis, Characterization and Applications**, 3-Volume Set (eds D. Levy and M. Zayat), Wiley-VCH Verlag GmbH & Co. KGaA, Weinheim, Germany. doi: 10.1002/9783527670819.ch30

7) LIMA, L. R.; SANTOS, D. B.; SANTOS, M. V.; BARUD, H. S.; HENRIQUE, M. A.; PASQUINI, D.; PECORARO, E.; RIBEIRO, S. J. L.; Cellulose nanocrystals from bacterial cellulose. **Química Nova**, v. 38, n. 9, p. 1140 - 1147, 2015.

8) MARQUES, L. F., CUIN, A. C.; GUSTAVO S.G., SANTOS, M. V., RIBEIRO, S.J.L.; MACHADO, F. C. Energy Transfer process in highly photoluminescent binuclear hydrocinnamate of europium, terbium and gadolinium containing 1,10-phenanthroline as ancillary ligand. **Inorganica Chimica Acta**, v. 441, p. 67 - 77, 2015.

9) GONÇALVES, L. P.; FERREIRA-NETO, E. P.; ULLAH, S.; SOUZA, L. V. Y.; ORLANDO A. E.; SANTOS, M. V.; RIBEIRO, S. J. L.; R-F, U. PEREIRA Enhanced photochromic response of ormosil-phosphotungstate nanocomposite coatings doped with TiO2 nanoparticles. **Journal of Sol-Gel Science and Technology**, v. 76, p. 386 - 394, 2015.

10) NIGOGHOSSIAN, K.; SANTOS, M. V.; BARUD, H.S.; SILVA, R. R., ROCHA, L.A.; CAIUT, J. M. A.; ASSUNÇÃO, R. M. N., SPANHEL, L. P. M.; MESSADDEQ, Y. RIBEIRO, S.J.L. Orange pectin mediated growth and stability of aqueous gold and silver nanocolloids. **Applied Surface Science**, v. 341, p. 28 - 36, 2015.

11) MARQUES, L. F.; CORREA, C. C.; RIBEIRO, S. J.L.; SANTOS, M. V.; DUTRA, JOSÉ D. L.; FREIRE, R. O.; MACHADO, F. C. Synthesis, structural characterization, luminescent properties and theoretical study of three novel lanthanide metal-organic frameworks of Ho(III), Gd(III) and Eu(III) with 2,5-thiophenedicarboxylate anion. **Journal of Solid State Chemistry**, v. 227, p. 68 - 78, 2015.

12) RIBEIRO, S. J. L.; SILVA, R. R.; SALVI, D. T. B.; SANTOS, M. V.; BARUD, H. S; MARQUES, L. F.; SANTAGNELI, S. H.; TERCJAK, A. Multifunctional organic-inorganic hybrids based on cellulose acetate and 3-glycidoxypropyltrimethoxysilane. **Journal of Sol-Gel Science and Technology**. doi:10.1007/s10971-016-4089-x.

13) SILVA, D. L. C.; KASSAB, L. R. P.; MARTINELLI, J. R.; SANTOS, A. D., RIBEIRO, S. J. L.; SANTOS, M. V. Characterization of thin carbon films produced by the magnetron sputtering technique for optoelectronics and photonics applications. **Material Research**. doi: 10.1590/1980-5373-MR-2015-0058.

I dedicate this thesis to my best friend and husband Igor,
who I admire and love for his kindness and honor.

“The mind that opens up to a new idea never returns to its original size.”

Albert Einstein

ACKNOWLEDGEMENTS

My advisor likes to spread during our work in the lab “You should enjoy your work and everything gonna be all right”. Surely, the development of this PhD research yielded me many good results, which were only achieved thanks to the living together and collaboration of a number of people and institutions. However, sometimes I had hard times and all my love for chemistry helped me to overcome and reach the end.

I am glad of had been advised by Prof. Dr. Sidney José Lima Ribeiro, who I admire for his expertise, enthusiasm and promptitude. I am deeply grateful for all support, guidance and opportunities, which were essentials to my progress.

Prof. Dr. Edison Pecoraro has also been an important person during all my graduation. Thank you for teaching me each step in the optical lab, for the valuable discussions and for helping me with my questions about the experiments.

I have many reasons to acknowledge my dear friend Prof. Dr. Hernane da Silva Barud, but the one I am must thankful is for his guidance during my undergrad, for teaching me since the start, points of experimental science and for encourage my career. Thanks also to Prof. Dr. Agnieszka Terjak and Dr. Juncal Guitierrez for help me with part of my work in this thesis.

My gratitude to the whole Photonics Materials Group: Professor Dr. Marcelo Nalin, Dr. Silvia Helena Stangnelli, Dr. Mauricio Cavichioli, Dr. Danilo Manzani and Ferminio Cesar Polachini; and especially to my labmates, including the former generation, Robson and Rafael; my contemporaneous, Lippy, Denise and Leandro; and also to the youngers Camila, Lais, Karina, Gustavo, Lais Galvão, Andréia, Mariana, Thais, Lívia and Tárcio. Thank you all for the help in several points, for the pleasurable working hours and for the quality interaction.

I would like to thanks Prof. Dr. Anderson S. L. Gomes and Prof. Dr. Cid B. de Araújo and their students Dr. André L. Moura and Dr. Vlademir Jerez, from Universidade Federal de Pernambuco - Recife, for had been my collaborators, providing investigation of random laser action of the silica monoliths synthesized in this thesis.

I really appreciate the opportunity of had worked in Aveiro University, through the partnership with Prof. Dr. Luis Dias Carlos and Prof. Dr. Maria Rute Sá Amorin Ferreira André, by which I could expand my knowledge to the luminescence and optical materials get in touch with many interesting people. Thank you to the whole Luis’s Group for the help and hospitality. Concerning my stay in Aveiro, I never thought I would meet some of my dear friends at Aveiro

University. Thanks Sangeetha, Cyntia, Denis, Vânia and Sandra for the friendship and protection abroad.

I would like to express my appreciation to my family, my husband Igor and his family, especially to my mom Inez and my sisters Flávia and Patrícia, even with all its simplicity they provided me the chance to get here. Also, my appreciation to the new family members Crystian, Ícaro and Pedro, who I love with all heart.

Finally, my acknowledgments to São Paulo State University - Araraquara – through Institute of Chemistry – that has held all my studies since the beginning of my undergrad in 2006. I am finishing a 10-year process, which definitely changed my perspectives. And to São Paulo Research Foundation (FAPESP) for the financial support in all those steps, manly for the grants of my scholarship: 2014/12424-2.

ABSTRACT

Among all natural polymers, bacterial cellulose and silk fibroin offer unlimited opportunities for processing, functionalization, and biological integration. This thesis presents the preparation and characterization of nanostructured materials based on bacterial cellulose produced by *Gluconacetobacter xylinus* bacteria, as well as regenerated silk fibroin stemmed from the cocoons of silkworms (*Bombyx mori*) for optical applications.

Firstly, dried bacterial cellulose membranes were utilized to prepare cellulose nanocrystals (CNC). CNC were casted in the form of thick iridescent films whose color originates in the periodic patterning of layers in a chiral nematic texture created by self-assembly of rod crystallites. Once the CNC films were obtained, self-sustainable films were coated with a low molecular weight nematic liquid crystal (LC), 4′-(hexyloxy)-4-biphenylcarbonitrile (HOBC). The materials were obtained as free-standing iridescent films, with chiral nematic structure that exhibited modulated optical properties, in response to external stimulus, such as thermal gradient or relatively small electrical voltage. The scanning electron microscopy (SEM) confirmed that the composite film structure comprises the multi-domain Bragg reflectors. The relationship between the surface structure and thermo-responsive properties of investigated HOBC coated with CNC film was examined using transmission optical microscopy (TOM). Additionally, electrostatic force microscopy (EFM) measurement was employed to prove the effect of external stimuli, in this case applied voltage, on the HOBC liquid crystal coated with CNC film.

The second part of this thesis involves the design of luminescent iridescent films through the combination of CNC suspension with tetraethoxysilane (TEOS) and ethanolic solutions of Rhodamine 6G (Rh6G). These materials were obtained as freestanding composite films with chiral nematic organization. The optical properties of such films can be tuned through changes in the silica/CNC proportion during the preparations. Photoluminescence measurements, as function of the detection angle, were realized in order to investigate the influence of photonic structure in the light emission of composite films. Our findings demonstrated that the photonic structure of the film acts as an inner- filter, causing selective suppression of the light emitted with a variation of the detection angle. This behavior was found to be dependent of the bandgap position on the photonic structure of these materials.

Lastly, we designed structured organic-inorganic hybrids (OIH) based on silica and silk fibroin. The materials were obtained as robust monoliths possessing different fibroin fractions. The SEM images demonstrated in-situ self-assembly of fibroin nanofibers dispersed into the

IOH monoliths. Structural characterization of OIH monoliths was performed by Raman and solid state NMR spectroscopies. Our findings demonstrated that precipitated fibroin presented prevailing β-sheet conformation. Furthermore, we demonstrated that the fibroin nanofibers can be used as biotemplates, acting as a sacrificial material to development porous silica monoliths. The porous silica monoliths doped with rhodamine 6g (Rh6G) exhibited efficient RL action with low threshold power excitation and narrowing linewidth. From the spectral behavior, it is inferred that the RL operates in the diffusive regime in hierarchical macro–mesoporous network. In addition, analysis of the emission spectra showed two gain mechanisms coupled, specifically the random lasing and the stimulated Raman scattering, which suggest that designed materials can also be promising for random Raman laser applications.

Keywords: bacterial cellulose, silk fibroin, cellulose nanocrystals, nematic liquid crystal, silica, organic-inorganic hybrids, photonic devices and random lasers.

RESUMO

Entre os polímeros naturais, celulose bacteriana e fibroína da seda oferecem inúmeras oportunidades para funcionalização, processamento e integração biológica. Esta tese apresenta a preparação e caracterização de novos materiais nanoestruturados para aplicações ópticas utilizando celulose bacteriana produzida pela bactéria *Gluconacetobacter xylinus*, como também em fibroína regenerada extraída de casulos do bicho da seda (*Bombyx mori).*

Primeiramente, membranas de celulose bacteriana secas foram utilizadas para a preparação de nanocristais de celulose (NCC). Os nanocristais de celulose foram processados na forma de filmes espessos e iridescentes nos quais a cor tem origem de padrões periódicos de camadas em uma estrutura nemática quiral criada pelo alto montagem dos bastões cristalinos. Uma vez obtido o filme de NCC, o mesmo foi revestido com um cristal líquido nemático de baixo peso molecular, 4'- (hexiloxi) - 4 - bifenilcarbonitrila (HOBC). O material foi obtido como um filme auto-suportado, iridescente, formado por uma estrutura nematic quiral e que exibe moduladas propriedades em resposta a estímulos externos, tais como, gradiente de temperatura e relativa pequena voltagem elétrica. Imagens de microscopia eletrônica de varredura (MEV) confirmaram a estrutura do filme formada por múltiplos domínios refletores de Bragg. A relação entre a estrutura da superfície e as propriedades de resposta térmica do revestimento de HOBC no filme foram investigadas utilizando microscopia óptica de transmissão (TOM). Além disso, medidas de microscopia de força eletrostática foram empregadas para provas o efeito do estímulo externo, neste caso da voltagem aplicada, no revestimento de cristal líquido HOBC no filme.

A segunda parte desta tese envolve a preparação de filmes iridescente luminescentes através da combinação da suspensão de NCC com tetraetoxisilano (TEOS) e uma solução etanólica de rodamina 6G (Rh6G). Estes materiais foram obtidos como filmes compósitos auto suportados com ordenação nemática quiral. As propriedades ópticas dos filmes foram sintonizadas através de mudanças na proporção de sílica/NCC na preparação. Medidas de fotoluminescência em função do ângulo foram realizadas a fim de investigar a influência da estrutura fotônica com ordenação nemática quiral na emissão de luz pelos filmes compósitos. Os resultados demonstraram que a estrutura fotônica dos filmes atuam como um filtro interno causando supressão seletiva da luz emitida com a variação do ângulo de detecção. Este comportamento mostrou-se dependente da posição da banda proibida destes materiais.

Por fim, nós preparamos híbridos orgânico - inorgânicos (HOI) baseados em sílica e fibroína da seda. Os materiais foram obtidos em forma de monolitos robustos conte

diferentes concentrações de fibroína. As imagens de MEV apresentam a precipitação de nanofibras de fibroína dispersas dentro dos HOIs. A caracterização estrutural das amostras foi realizada por espectroscopia Raman e ressonância magnética nuclear (RMN) do estado sólido. Os resultados demonstraram que a fibroína precipitada apresenta preferencial conformação folha- β. Nós demonstramos ainda que as nanofibras de fibroína podem ser utilizadas como moldes, atuando com um material de sacrifício para a produção de monolitos de sílica porosos. Os monolitos de sílica porosa dopados com rodamina 6G (Rh6G) exibiram eficiente ação laser aleatório (LA), com baixo limiar laser e estreita largura de banda. A partir do comportamento espectral, infere-se que o LA opera no regime difusivo na rede hierarquia formada por macro e mesoporos. Além deste comportamento, através de análise do espectro de emissão foi observado o acoplamento de dois mecanismos, laser aleatório e espalhamento Raman estimulado, o que sugere que o material obtido também pode ser promissor para aplicações em laser aleatório Raman.

Palavras-chaves: Celulose bacteriana, fibroína da seda, nanocristais de celulose, sílica, híbridos orgânicos-inorgânicos, dispositivos fotônicos e lasers aleatórios.

LIST OF FIGURES

Figure 1. Chemical structure of cellulose. Inter and intramolecular hydrogen-bonding network (adapted from (LIN; DUFRESNE, 2014a)). 20
Figure 2. a) Schematic of the unit cells for cellulose Iα (triclinic, dashed line) and Iβ (monoclinic, solid line); b) Relative configuration of Iα with respect to Iβ unit cell. (Adapted from (MOON et al., 2011)) 21
Figure 3. a) Transmission electron micrographs (TEM) of sugar beet CMF (adapted from ((DUFRESNE; CAVAILLE; VIGNON, 1997))); b) TEM hardwood CNF (adapted from ((SAITO et al., 2007))); c) Scanning electron micrographs (SEM) of wood CNC (adapted from ((HANLEY et al., 1997))); and BC ribbons (adapted from ((IFUKU et al., 2007))). 22
Figure 4. Hierarchical structure of cellulose; top image (from large unit to small unit): cellulose nanocrystals (CNC), micro/nanofibrillated cellulose (MFC and NFC); bottom image (from tiny unit to small unit), biosynthesis of bacterial cellulose (BC) (adapted from (LIN; DUFRESNE, 2014b)). 23
Figure 5. Schematics of idealized cellulose fibers showing one of the suggested configurations of the crystalline and amorphous regions, and cellulose nanocrystals after sulfuric acid hydrolysis of the disordered regions, exhibiting the characteristic sulfate half ester surface groups formed as a side reaction (adapted from (DOMINGUES; GOMES; REIS, 2014). 25
Figure 6. a) Shows the formation of a chiral nematic liquid crystal phase and its coexistence with an isotropic phase in a CNC suspension of 5wt% (upper image) (GRAY, 2012). The helical arrangement of CNC is illustrated schematically next to a scanning electron electron microscopy image of an actual CNC helix (adapted from (GRAY, 2012)). b) Optical microscope image (crossed polars) of the bulk CNC film (scale bar 40 μm (GRAY, 2012)). c) Characteristic regularly spaced lines in an aqueous suspension with 5 wt% CNC, observed in transmission (adapted from (LAGERWALL et al., 2014)). 27
Figure 7. Selective reflection of circularly polarized light by a chiral nematic structure. The rods represent the average orientation of the director, which lies perpendicular to the films and rotates through the film (Adapted from (GIESE et al., 2015)).....29
Figure 8. a) Dry chiral nematic CNC films in a polystyrene Petri dish. Polarization optical micrograph at the center of the film. Correlation of optical and electron microscopy of the different domains; b-d) Cross-sectional SEMs images correlated with the white circles show areas b, c and d. (Adapted from (STEINER; VIGNOLINI, 2014)) 30
Figure 9. a) Evaporating and self-assembly of CNCs with silica sol-gel precursor to yield an iridescent composite, whose structural color depends on the silica loading. b) After removal of the CNCs through calcination or acid hydrolysis mesoporous sol-gel derived films are obtained that retain their intense structural colors. c) Transmittance spectra of the iridescent composite. d) Transmittance spectra of mesoporous silica films. (Adapted from (SHOPSOWITZ et al., 2010)). 33
Figure 10. Synthetic route to new nanostructured materials with chiral nematic order. In the presence of a suitable precursor, CNCs form a composite material. Removal of the template leaves a mesoporous material which can be functionalized by infiltration of the pores or used as a hard template. Alternatively, carbonization followed by removal of silica yields chiral nematic mesoporous carbon (Adapted from (GIESE et al., 2015)) 34

Figure 11. a) *Bombyx mori* (*B. mori*) silkworms together with two silk cocoons; b) Silk cocoons (Images from http://inhabitat.com/the-silk-pavilion-mit-researchers-to-3d-print-a-silkworm-inspired-structure/). 36
Figure 12. a) SEM images of the morphologies of silkworm cocoons from *Bombyx mori*;(Adapted from (ZHANG et al., 2013a)) b) Structure of Bombyx mori silk thread (Adapted from ((PEREIRA; SILVA; DE ZEA BERMUDEZ, 2015))). 37
Figure 13. Illustration of antiparallel β-sheets, with the surface of one sheet projecting entirely methyl groups of alanine residues and the other surface of the same sheet projecting only hydrogen atoms of glycine residues. The intersheet distances alternate at5.5Å and 3.7Å respectively (Adapted from (KOH et al., 2015)). 39
Figure 14. Generating new materials from silks. Native silkworm silk on the right illustration (Image from http://inhabitat.com/the-silk-pavilion-mit-researchers-to-3d-print-a-silkworm-inspired-structure/). Regenerated silk fibroin on the left illustration (Adapt from (PREDA et al., 2013) . The illustration above shows a range of materials can be generated from silks through processing into hydrogels, films fibers, sponges, microspheres, particles and tubes. The properties of these systems can be modified depending on the processing modes used and then generated into functional devices and technology platforms. 42
Figure 15. Differential Scanning Calorimetry (DSC) obtained for HOBC. 50
Figure 16. HOBC Structure, crystal-nematic transition (TC-N) and nematic-isotropic transition (TN-I) obtained by DSC. 50
Figure 17. Schematic diagram of the preparation method of the CNC/HOBC. 52
Figure 18. a and b) POM images of iridescent film of CNC showing a fingerprint texture characteristic of chiral nematic ordering; c and d) POM image of CNC/HOBC displays formation of spherulites of HOBC covering a larger area of the CNC surface. 55
Figure 19. SEM images of CNC film: a) SEM image of film surface formed by aligned nanocrystals cellulose; b) Side view of a cracked film showing the layered structure of the nanocrystals and the rod-like morphology with the rods twisted in a left-handed orientation; c) Image of fracture surface across the CNC film; d) Higher magnification side view of fracture surface across the CNC film shows the stacked layers that result from the helical pitch of the chiral nematic phase. 56
Figure 20. SEM images of CNC/ HOBC composite: a) Image of film surface of CNC covered by the liquid crystal HOBC; b) Side view of a cracked film shows the layered structure of the nanocrystals and the rod-like morphology with the rods twisting in a left-handed orientation; c) Image of cross section of fracture film (thickness 60.2 μm); d) The magnification of the side view of the fractured surface across film, shows the layered structure of the nanocrystals. 57
Figure 21. ATR-FTIR spectra: a) HOBC, b) CNC and c) CNC/HOBC. 58
Figure 22. Emission spectra of neat HOBC and CNC/HOBC composite recorded at 298K, under excitation at 280nm. 59
Figure 23. Transmission spectra of the films CNC and CNC/ HOBC 60
Figure 24. a) Specular reflectance of CNC/HOBC composite between 20 and 70 degree; b) Variation of the peak position of the reflectance spectra as function of the cos θ for CNC/HOBC. 61
Figure 25. Transmission spectra as function of the temperature: a) HOBC; b) CNC/HOCB. 62
Figure 26. TOM micrographs of CNC/HOBC during heating taken at: (a) 30 ºC (b) 47 °C, (c) 56 °C, (d) 60 °C and during cooling at: (e) 60°C (f) 55°C (g) 45°C (h) 30°C. (scale bar, 200 μm). 63

Figure 27. TM-AFM (3μm x 3μm) height (a) and phase (b) images of CNC and TM-AFM height (a) and phase (b) images of CNC/HOBC film. 64
Figure 28. a) AFM phase image (3μm x 3μm) and EFM phase images (3μm x 3μm) of CNC/HOBC film obtained applying b) 0 V, c) 6 V and d) -6 V. 65
Figure 29. Photograph of CNC/silica composites films with different amount of silica. Viewing is normal to the film surface. 70
Figure 30. Photograph of CNC/silica doped with Rh6G composites films with different amount of silica. Viewing is normal to the film surface. 71
Figure 31. Specular reflectance scheme. 72
Figure 32. The modular experimental setup to measurements of photoluminescence spectra as function of the angle ($-90° < \theta < 90°$). 73
Figure 33. TG curves of composite films) CNC-Rh; b) CS1-Rh; c) CS2-Rh; d) CS3-CS4-Rh. 74
Figure 34. Polarized optical microscopy (POM) images with crossed polarizers: a) CS1-Rh and b) CS4-Rh. 75
Figure 35. a) Photograph of composite CS4-Rh; b) oblique sectional view of a fracture surface across of composite CS4-Rh; c) and d) SEM images of its cross –section of CS4-Rh. 76
Figure 36. a) Transmission spectra of CNC, CS1, CS2, CS3 and CS4; b) Variation of the peak position of the reflectance spectra as function of the cos θ for CNC/silica composites. . 77
Figure 37. a) Transmission spectra of CNC, CS1-Rh, CS2-Rh, CS3-Rh and CS4-Rh; b) Variation of the peak position of the reflectance spectra as function of the cos θ for CNC/silica composites doped with Rh6G. 77
Figure 38. Figure S3. a) Specular reflectance of CS4 between 20 and 60 degree, b) Specular reflectance of CS4-Rh between 15 and 60 degree. 78
Figure 39. Variation of the P of chiral nematic structure of composites with different silica proportion. 80
Figure 40. Emission spectra of composite CNC/silica doped with Rh6G in front face acquisition mode excited at 348nm. 81
Figure 41. Emission spectra of CNC film in front face acquisition mode excited at 345nm. . 82
Figure 42. a) Emission spectra of CS4-Rh composite as function of the detection angle (0 ° to -90°), excited at 348nm; b) Emission spectra of CS4-Rh composite as function of the detection angle (0° to 90°), excited at 348nm; c) Variation of the λ_0 and linewidth of emission bands of composite CS4-Rh as function of the detection angle ($-90° < \theta < 90°$); d) Variation of the maximum wavelength (λ_0) of emission bands of composite BC-Rh as function of the detection angle ($-90° < \theta < 90°$). 84
Figure 43. a) Color diagram of reflection of CS4-Rh composite film as function of the detection angle ($0◦ < \theta < 60°$); b) Color diagram of emission color of CS4-Rh composite film as function of the detection angle ($0◦ < \theta < 90◦$), excited at 348nm 85
Figure 44. Emission spectra of CS4-Rh excited at 348 nm acquired at 20° and 90°. Reflectance spectra acquired at 20° and 50°. 85
Figure 45. Variation of the maximum emission wavelength for composite films CNC/silica doped with Rh6G as function of the detection angle ($-90^{\circ} < \theta < 90°$) a) CNC-Rh; b) CS1-Rh; c) CS2-Rh; d) CS3-Rh. 85
Figure 46. a) Photograph of silica/fibroin hybrids monoliths. b) SEM image of the surface of monolith SF3; c) SEM image of agglomerate of fibroin nanofibers on the surface of monolith SF3; d) Image of the fracture of the monolith SF3. 87

Figure 47. Thermogravimetric curves of silica/fibroin hybrid monoliths: a) SF0; b) SF1; c) SF2; d) SF3 and e) SF4. 98
Figure 48. Raman spectra of silica/fibroin hybrid monoliths: a) SF1; b) SF2; c) SF3 and d) SF4. 100
Figure 49. $^{29}Si\{^{1}H\}$ CP MAS spectra of silica/fibroin hybrid monoliths contained differents fibroin concentrations: a) SF1; b SF3 and d) SF4. 101
Figure 50. 13C{1H} CP-MAS spectra of silica/fibroin hybrid monoliths containing differents fibroin concentrations: a) SF1; b) SF3 and c) SF4. 102
Figure 51. ^{1}H spin echo MAS spectrum of SF4 silica/fibroin hybrid monoliths. 103
Figure 52. FSLG $^{13}C\{^{1}H\}$ CP HETCOR spectra of SF4 sample obtained with two contact times 0.5 e 2.5ms. (υr=14kHz, $\upsilon 0$=188.6MHz, t1=5s). 105
Figure 53. A schematic illustration of the self-assembly of fibroin nanofibers inside the bulk of silica composites materials and posterior calcination of fibroin nanofibers to form porous ceramic. 106
Figure 54. a) Photograph of silica monoliths; b) SEM image of the porous surface of monolith S3; c and d) Images of fracture of S3, showing porous with diameter of hundreds of nanometers inside the bulk of silica. 107
Figure 55. a) Nitrogen adsorption/desorption isotherms; b) Pore size distribution; c) plot of $\log(\ln(\rho))$ versus $\log(\theta)$; d) Evolution of the specific surface area, pore diameter and surface fractal dimension of the samples. 108
Figure 56. a) Peak intensity vs. pumping energy per pulse showing the nonlinear behavior of porous silica monoliths containing Rh6G; b) Full width half maximum (FWHM) linewidth vs. pumping energy per pulse. The minimum linewidth was ≈ 4 nm for pumping above the threshold. 111
Figure 57. Spectral behavior of the S4 containing Rh6G as of pumping energy per pulse. Minimum linewitdh observed is about 0.5 nm. The inset shows the yellow emission colour of the sample S4 doped with Rh6G excited with irradiated with a laser ate 532nm. 112

LIST OF TABLES

Table 1. Examples of CNCs isolated from different sources.....26
Table 2. Variation of the helicoidal pitch of composites films.....79
Table 3. Decay time values (λ_{EXC}= 330nm): CNC (λ_{EM}= 480nm) (τ_1); Dye-doped CNC/silica composites, λ_{EM}= 400nm (τ_1) and λ_{EM}= 560 nm (τ_2). Quantum yield values: CNC-Rh, λ_{EXC}= 528nm and λ_{EM}= 567nm; Dye-doped CNC/silica composites, λ_{EXC}= 528nm and λ_{EM}= 556nm. 83
Table 4. Heat ramp used to calcinate the fibroin fraction in the silica/fibroin hybrids monoliths. Heat temperature, heating rate and the time that the samples were kept in the matching temperature are presented. 94
Table 5. Samples composition and degradation temperature of fibroína (Tonset) determined by thermogravimetric curves. 99
Table 6. Physico-chemical properties of calcinated samples.....109
Tabela 7. Values of energy thresholds and slope efficiency of silica monoliths.....111

LIST OF ABBREVIATIONS

AFM- Atomic Force Microscopy

8CB - 4-Cyano-4′octylbiphenyl

BC - Bacterial cellulose

BET- Brunauer, Emmett, Teller

CNC - Cellulose nanocrystal

DP- Degree of polymerization

DSC- Differential scanning calorimetry

EFM - Electrostatic force microscopy

EPE- Excitation pulse energy

HOBC- 4'-(hexyloxy)-4-biphenyl carbonitrile

IOH- Inorganic organic hybrids

LCs - Liquid crystals

MFC - Microfibrillated cellulose

NFC - Nanofibrillated cellulose

M_W - Molecular weight

NMR - Nuclear magnetic resonance spectroscopy

PLA - Poly(l-lactic acid)

PL- Photoluminescence

POM- Polarized optical microscopy

RL- Random laser

Rh6G- Rhodamine 6G

SF- Silk Fibroin

SEM - Scanning electron microscopy

TOM - Transmission optical microscopy

TEOS - Tetraethylorthosilicate

TEM - Transmission electron microscopy

TG- Thermogravimetric

UV - Ultraviolet

CONTENTS

1. INTRODUCTION 19
1.1. Cellulose. 19
1.1.1. Nanocelluloses. 21
1.1.2. Cellulose nanocrystals. 24
1.1.3 Self-assembly and organization of cellulose nanocrystals. 26
1.1.4. Cellulose nanocrystals as templates for the chemical synthesis of inorganic materials. 32
1.2. Silk fibroin. 35
1.2.1 Primary Structure of silk fibroin. 37
1.2.2. Secondary structure of silk fibroin. 38
1.2.3. Extraction and processing of silk fibroin. 40
2. OBJECTIVES 45
PART I. MULTIFUNCTIONAL MATERIALS BASED ON CELLULOSE NANOCRYSTALS. 46
3. Optical platform based on cellulose nanocrystals (CNC) – 4-(hexyloxy)-4-biphenylcarbonitrile (HOBC) bi-phase nematic liquid crystal films. 47
3.1. Introduction. 47
3.2. Materials and methods. 49
3.2.1. Materials. 49
3.2.2. Preparation of cellulose nanocrystals (CNC). 51
3.2.3. Preparation of the composite film. 52
3.2.4. Characterization of CNC and CNC/HOBC films. 52
3.3 Results and discussions 54
3.3.1- Morphological Characterization. 54
3.3.2- Structural Characterization. 57
3.3.3- Optical Characterization. 59
3.4. Conclusions 66
4. Cellulose based photonic materials displaying modulated photoluminescence. 67
4.1. Introduction 67
4.2. Materials and methods. 69
4.2.1-Preparation of bacterial cellulose membranes: 69
4.2.2-Preparation of cellulose nanocrystals (CNC): 69
4.2.3-Preparation of nanocrystalline CNC-silica composite films. 70
4.2.4- Preparation of nanocrystalline CNC-silica composite doped with broad band emitters (Rhodamine 6G (Rh6G)): 71

4.2.5. Characterization of CNC and composite films. 71
4.2- Results and discussions 73
4.4 Conclusions 87
PART II. MULTIFUNCTIONAL MATERIALS USING SILK FIBROIN AS A BIOTEMPLATE. 89
5. Silk fibroin as a biotemplate for hierarchical porous silica monoliths for random laser applications 90
5.1. Introduction 90
5.2. Materials and methods. 92
5.2.1- Extraction of silk fibroin 92
5.2.2-Preparation of organic-inorganic hybrids monoliths based on silica and fibroin. 93
5.2.2-Preparation of porous silica monoliths 93
5.2.3-Preparation of porous monoliths of silica containing Rh6G. 94
5.2.4-Characterization of materials. 94
5.3. Results and discussions 95
5.3.1. Characterization of organic-inorganic hybrid monoliths based on silica and fibroin. 96
5.3.2. Characterization of porous silica monoliths 107
5.3.3. Characterization of the random laser action in the silica monoliths containing Rh6g. 110
5.3. Conclusions 113
6. GENERAL CONCLUSION. 114
REFERENCES 148

Organization of the thesis

In light of recent studies, cellulose nanocrystals extracted from bacterial cellulose and regenerated silk fibroin from silkworm cocoons are attractive alternatives to design multifunctional materials, reason why this is the focus of such thesis.

Therefore, this study is divided into four chapters. The first chapter is devoted to introduce cellulose nanocrystals and silk fibroins, their preparation, properties and recent applications. Subsequently to the introductory section, the preparation of multifunctional materials based on cellulose nanocrystal is presented on second and third chapter.

Further, the second chapter presents the preparation of free-standing CNC films coated with low molecular weight nematic liquid crystal (LC), 4′-(hexyloxy)-4-biphenylcarbonitrile (HOBC), which integrate iridescence, conductive and thermal response. Such composite films were morphologically characterized by the SEM and POM, and optically by electron spectroscopy. Emphasis is given to the characterization of morphological and optical properties of the composite in function of the temperature. Additionally, the conductive response brush surface was evaluated using electrostatic force microscopy (EFM) measurements.

Afterwards, the third chapter encompasses the preparation and characterization of iridescent luminescent films based on dye-doped CNC/silica composites. Such composite films were morphologically characterized through SEM and POM, and optically by electron spectroscopy. In this section, the focus is given to the investigation of the influence of photonic structure of films on light emission from dye-doped CNC/HOBC composites, using luminescence spectroscopy measurements in function of the detection angle.

Finally, in the last chapter, the synthesis of organic inorganic hybrids monoliths based on silica and silk fibroin is described. The hybrids monoliths were morphologically characterized by SEM and structural characterized by Raman, and solid state RMN spectroscopies. Additionally, the chapter also describes the preparation of porous silica monoliths using the fibroin nanofibers as a biotemplate. The silica monoliths were morphologically characterized by SEM and their porous structure were characterized via nitrogen adsorption experiments. Moreover, the random laser action of silica monoliths was investigated.

1. INTRODUCTION

Commonly, natural materials provide a convincing template to reinterpretation and, in some cases, simplification of modern manufacturing, while rendering them sustainability and green. Biopolymers, produced and modified by living organisms are the pillars of self-assembly on structurally hierarchical micro and nanoscale systems, which occur naturally, such as chitin of butterfly wings, beetles exoskeletons, keratin in peacock feathers (PENNISI, 2013; WEAVER et al., 2012; YANG et al., 2013), and so forth. From the material science perspective, biopolymers can be a versatile source to design structured inorganic or inorganic/organic materials in the laboratory. The interest in the direct use and re-engineering of natural polymers as platforms for the development of technology materials has been growing in recent years. The challenge using these materials is to identify, among the options available, materials that present adequate properties to interface with current technology. In addition, such materials should be widely available and have competitive costs in the world market. Thus, in this thesis, there is an interest in the opportunities offered by bacterial cellulose produced through the *Gluconacetobacte*r *xylinus* bacteria and silk fibroin extracted from *Bombyx mori* silkworm cocoons biopolymers as platforms for technological applications.

1.1. Cellulose.

Cellulose is one of the most versatile polymers and most widely found in nature. Also, it has been used as a material by human civilizations for thousands of years. Currently, cellulose materials are used in a wide range of applications. Industrially, the pulp has been exploited as raw material to manufacture various products, including paper, cellophane film, explosives, textile and nutritive fibers.

Cellulose is produced by plants, trees, bacteria and some animals (tunicates) (KLEMM et al., 2005) via the condensate polymerization of glucose, which is a product of the photosynthesis process in plants and trees. Regardless of its source, cellulose can be characterized as a high molecular weight homopolymer of β-1,4-linked anhydro-D-glucose units, in which every unit is corkscrewed 180°, respecting its neighbors, and the repeated segment is frequently taken as a dimer of glucose, known as cellobiose (Figure 1). Each cellulose chain possesses a directional chemical asymmetry accounting the termini of its molecular axis: one end is a chemical reducing functionality, a hemiacetal unit, and the other

has a pendant hydroxyl group, the nominal nonreducing end. The degree of polymerization (DP) of cellulose chains varies according to its origin, though it is estimated the existence of approximately 10 000 glucose units in wood pulp and cotton and 15 000 in native cellulose (HABIBI, 2014).

One of the specific features of the cellulose is that each of the monomers carries three hydroxyl groups. The ability of these hydroxyl groups to form intra- and intermolecular hydrogen bonds (Figure 1) plays an important role in the formation of fibrils and semicrystalline packaging, which rules the physical properties of such highly cohesive materials.

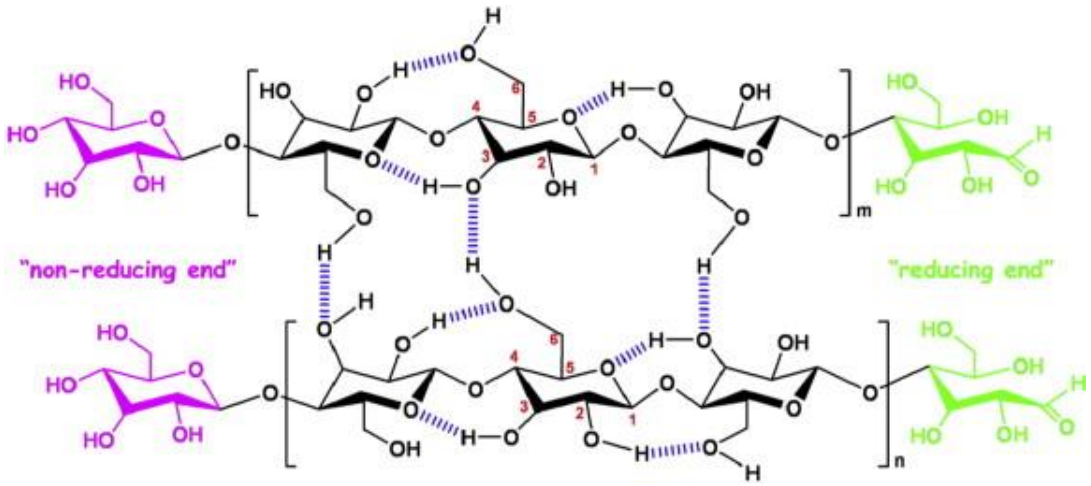


Figure 1. Chemical structure of cellulose. Inter and intramolecular hydrogen-bonding network (adapted from (LIN; DUFRESNE, 2014a)).

In nature, cellulose does not occur as an isolated individual molecule, but it is possible to find assemblies of individual cellulose chain-forming fibers (BROWN, 2004). This happens because cellulose is synthesized in form of individual molecules, which undergo spinning in a hierarchical order at the site of biosynthesis. In the plant cell wall, cellulose molecule chains connect with each other through hydrogen bonds and van der Waals forces, thus forming elementary fibrils, which are packed into larger microfibrils 5-50 nm in diameter and several micrometers in length, these are afterwards assembled into fibers in turns (MOON et al., 2011). Such microfibrils present highly ordered (crystalline) regions alternated with disordered (amorphous) regions. However, different sources of celluloses can exhibit different packing, which are managed by biosynthesis conditions (HABIBI; LUCIA, 2012).

In crystalline regions, the cellulose chains are organized and established by strong and complex hydrogen bonding networks. The hydrogen bonding network and molecular orientation of cellulose can vary widely, fact that can raise cellulose allomorphs or polymorphs,

depending on the respective source, method of extraction, or treatment. Six interconvertible polymorphs of cellulose, namely, I, II, III_I, III_{II}, IV_I and IV_{II}, have been identified.

Cellulose as it is found in nature is known as cellulose I. Cellulose I is still formed by two sub-allomorphs: cellulose Iα and cellulose Iβ (DEBZI; CHANZY, 1991). The proportions between the celulose Iα and celulose Iβ in any samples of native cellulose depend on their origin (Figure 2a). According to Klem et. al.(KLEMM et al., 2011) bacterial cellulose and algae contain higher quantity of unit cell Iα, while in cellulose taken from cotton, rami and wood the amount of unit cell Iβ is predominant.

In both structures, Iα and Iβ, cellulose chains adopt a parallel configuration, but they differ in their hydrogen-bonding patterns, which implies a difference in the crystalline structure (Figure 2b). In fact, the sub-allomorph Iα corresponds in one triclinic unit cell *P*1 (*a* = 6,717 Å, b = 5,962 Å, c = 10,400 Å, α = 118,08°, β = 114,80° e γ = 80,37°), which contains just one chain for unit cell, while Iβ exists in one monoclinic unit cell $P2_1$(a = 7,784 Å, b = 8,201 Å, c = 10,38 Å, α = 90°, e γ = 96,5°) with two cellulose chains.

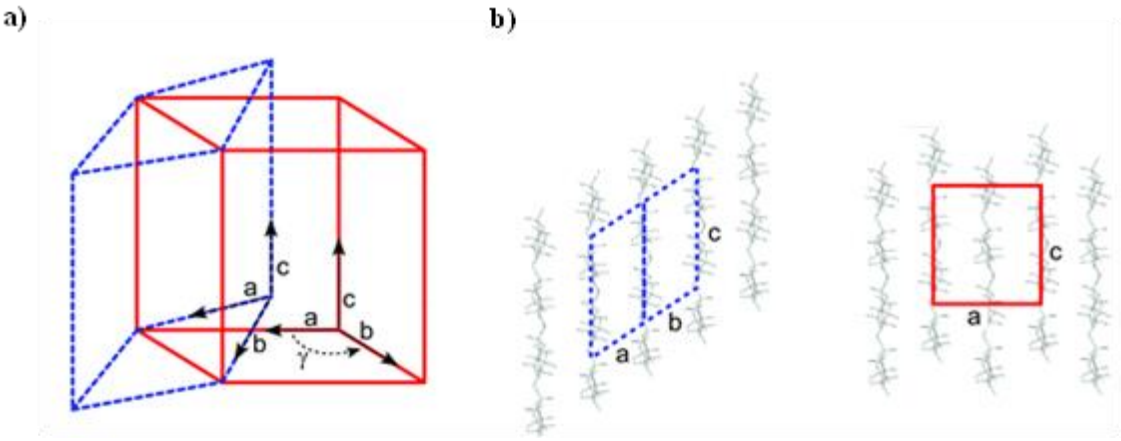


Figure 2. a) Schematic of the unit cells for cellulose Iα (triclinic, dashed line) and Iβ (monoclinic, solid line); b) Relative configuration of Iα with respect to Iβ unit cell. (Adapted from (MOON et al., 2011))

1.1.1. Nanocelluloses.

Due to its virtually unlimited availability, there has been considerable interest in developing renewable technologies based on cellulose. Due to the appearance and development of nanotechnology, cellulose attracts now more attention in the new form of ‘‘nanocellulose’’ to be used as novel and advanced material. Nanocellulose is described as a product or extract from native cellulose, composed by the nanoscaled structured material.

In a unique manner, these nanocelluloses combine important cellulose properties such as hydrophilicity, broad chemical-modification capacity, and the formation of versatile fiber morphologies with specific features of nanoscale materials, which are mainly caused by the very large surface area of these materials. On the basis of their dimensions, functions, and preparation methods, which depend mainly on the cellulosic source and on the processing conditions, different kinds of nanocelluloses can be prepared.

Using mechanical shearing, cellulose fibers can be disintegrated from cellulose fibers along their axis to their sub- structural units, resulting in micro/nanofibrillated cellulose (MFC/NFC), as can be seen on the Figure 3a and b, respectively. Furthermore, through mechanical, chemical or enzymatic processes, the amorphous regions of cellulose fibers can be dissociated transversely, leading to nanometric and rod-like fragments, without defects and higher crystallinity, referred as cellulose nanocrystal (CNC) (Figure 3c). The latter nanometric material is synthetized through microorganisms and it is known as bacterial cellulose (BC), Figure 3.

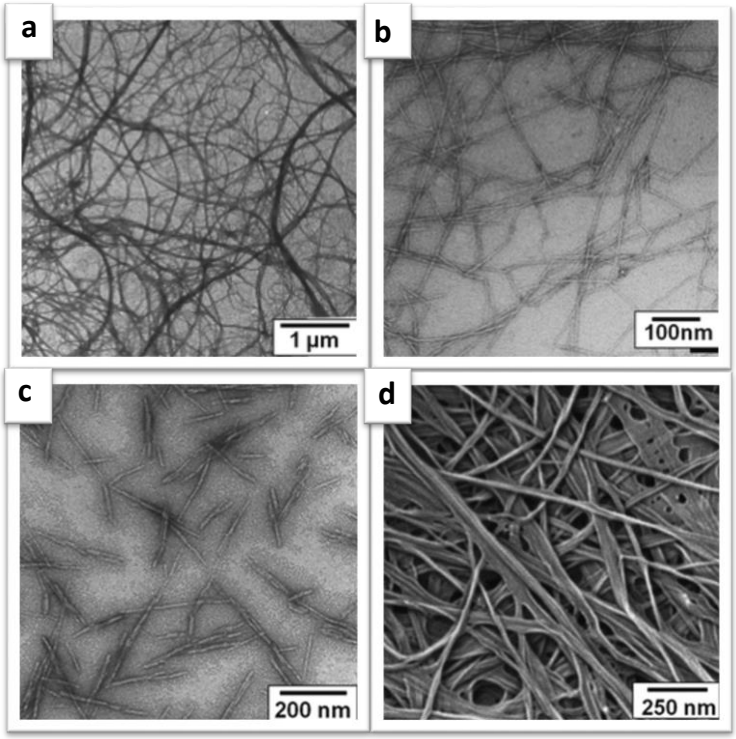


Figure 3. a) Transmission electron micrographs (TEM) of sugar beet CMF (adapted from ((DUFRESNE; CAVAILLE; VIGNON, 1997))); b) TEM hardwood CNF (adapted from ((SAITO et al., 2007))); c) Scanning electron micrographs (SEM) of wood CNC (adapted from ((HANLEY et al., 1997))); and BC ribbons (adapted from ((IFUKU et al., 2007))).

Contrary to the top-down production of CNC and CNF, the bottom-up biosynthesis of BC is a process of construction from a tiny unit (Å) to a small unit (nm), as shown in Figure 4. BC is typically synthesized by bacteria (such as *Acetobacter xylinum*) in a pure form, which requires no intensive processing to remove unwanted impurities or contaminants such as lignin, pectin and hemicellulose. During the BC biosynthesis, glucose chains are produced inside the bacterial body and extruded out through tiny pores present on the surface cell. Processes such as organization and crystallization of glucan chains through hydrogen bonds and Van der Waals forces, were arrayed in a hierarchy into ribbons. The resulting cellulosic network structure is in the pellicle form of randomly assembled ribbon shaped fibrils, being less than 100 nm wide, that are in turn composed by a bundle of much finer nanofibrils (2 to 4 nm in diameter). These bundles are relatively straight, continuous and dimensionally uniform.

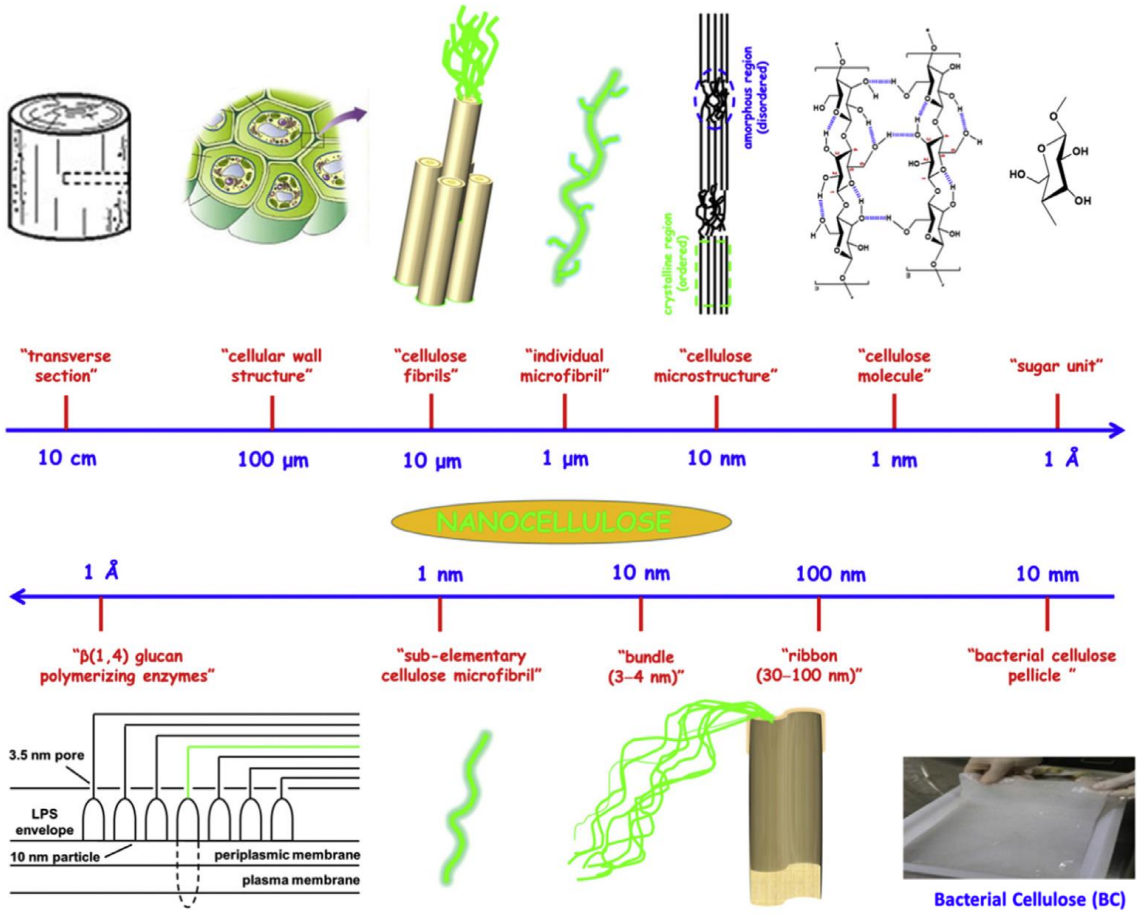


Figure 4. Hierarchical structure of cellulose; top image (from large unit to small unit): cellulose nanocrystals (CNC), micro/nanofibrillated cellulose (MFC and NFC); bottom image (from tiny unit to small unit), biosynthesis of bacterial cellulose (BC) (adapted from (LIN; DUFRESNE, 2014b)).

Moreover, BC also demonstrates some other unique physical properties, including high degree of polymerization (up to 8000), high crystallinity (70-80%) and high water content to 99%. Meanwhile, BC also exhibits good biocompatibility and nontoxicity. Due to the aforementioned characteristics of BC, it has been employed as a source to fabricate diverse materials, such as BC/inorganic solid, BC/ polymers, BC/nanoparticles, BC/nanostructured carbon composites and composites aerogels. (HU et al., 2014; SHAH et al., 2013; WU et al., 2016) They are widely used in biological and medical fields, environmental sciences, and optoelectronics (ABEER et al., 2014; FU; ZHANG; YANG, 2013; HU et al., 2014; HUANG et al., 2014). In addition, bacterial cellulose has been used as a source to prepare cellulose nanocrystals with higher aspect ratio without needing a purification pretreatment (ARAKI; KUGA, 2001; GRUNERT; WINTER, 2002; HIRAI et al., 2008).

1.1.2. Cellulose nanocrystals.

One of the recent strong trends, on an international scale, is to focus on the isolation of cellulose nanocrystals utilizing their enhanced properties to develop novel cellulose-based materials with diverse and advanced functionalities.

Cellulose nanocrystals are extracted from a raw cellulose sample following two main steps: the first is the purification and homogenization pretreatment of the source material to allow uniform reaction conditions, and the second is the separation of the purified cellulose material into its microfibrillar and/or nanocrystalline components. The purification and homogenization steps are adapted based on the cellulose source. For wood and plants, the most important step is the removal of the matrix materials hemicellulose and lignin. The second step, separation into microfibrillar or nanocrystalline components, can be performed by enzymatic hydrolysis, mechanical treatment or acid hydrolysis.

Although few examples of producing CNCs through processes involving enzymatic hydrolysis were reported (PIRANI; HASHAIKEH, 2013), the predominant method for isolating CNCs from cellulose fibers is based on acid hydrolysis, a technique that dates back to seminal studies by Ranby, (RÅNBY, 1951) with a number of more recent refinements. The amorphous regions of cellulose that act as structural defects are removed inducing a transverse cleavage of cellulose fibers into rodlike nanoparticles. Such transformation consists in disrupting the amorphous regions surrounding the microfibrils, as well as those embedded between them, while the crystalline segments are left intact. This cleavage is ascribed to the faster hydrolysis kinetics of amorphous domains compared to crystalline ones. When the CNCs

are prepared by hydrochloric acid hydrolysis, hydroxyl groups remain at the surface. The surface is consequently only weakly charged, and the colloidal stability is poor. (ARAKI et al., 1998). In contrast, when sulfuric acid is used as a hydrolyzing agent, it also chemically reacts with the surface hydroxyl groups of CNC to yield negatively charged (surface) sulfate groups that promote a perfect and uniform dispersion of the whiskers in water via electrostatic repulsions (Figure 5) (REVOL et al., 1992a).

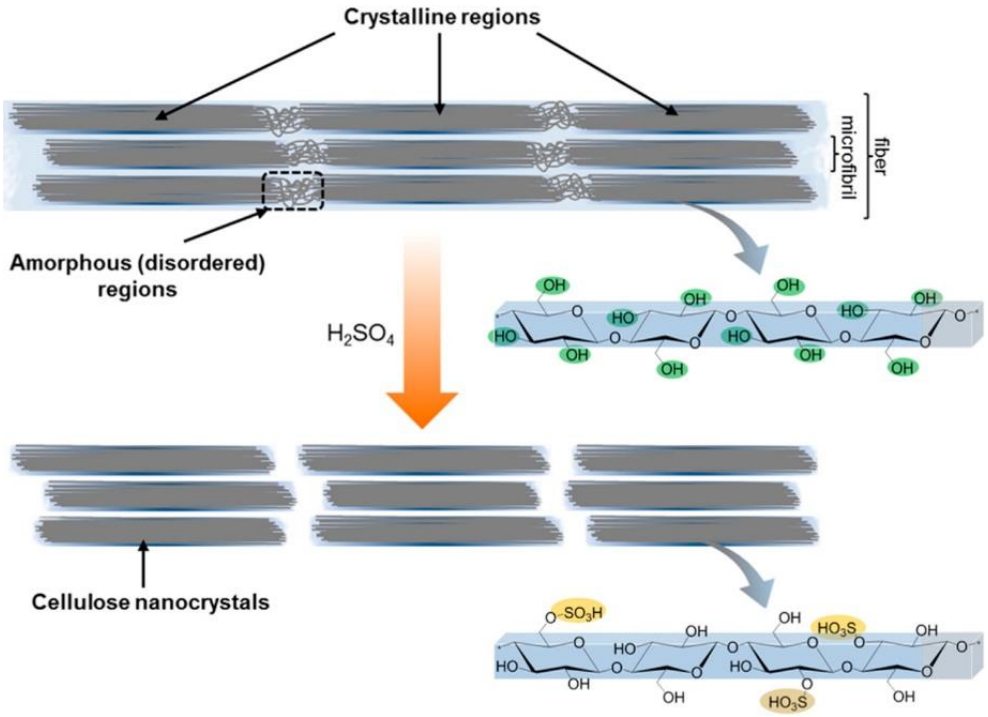


Figure 5. Schematics of idealized cellulose fibers showing one of the suggested configurations of the crystalline and amorphous regions, and cellulose nanocrystals after sulfuric acid hydrolysis of the disordered regions, exhibiting the characteristic sulfate half ester surface groups formed as a side reaction (adapted from (DOMINGUES; GOMES; REIS, 2014).

The most common cellulosic sources reported in the literature exploring the preparation of CNCs are listed in Table 1. The geometrical dimensions (width and length) of the CNCs are found varying with the cellulosic source material and their preparation conditions. However, typically, the width is only a few nanometers, whereas the length ranges from tenths of nanometers to several micrometers, as it can also be seen on Table 1.

Table 1. Examples of CNCs isolated from different sources.

Cellulose origin	Length (nm)	Width (nm)	Reference
Bacteria	100–1000	10–50	(ARAKI; KUGA, 2001; GRUNERT; WINTER, 2002; HIRAI et al., 2008)
Cotton	70–300	5–10	(DONG, X. M.; REVOL, J. F.; GRAY, 1998)
Soft wood	100–300	3–5	(ARAKI et al., 1998, 1999)
Ramie	50-250	5-10	(DE MATOS et al., 2007; DE MENEZES et al., 2009)
Sisal	100-500	3-6	(DE RODRIGUEZ; THIELEMANS; DUFRESNE, 2006; SIQUEIRA; BRAS; DUFRESNE, 2009)
MCC	35-270	3-48	(CAPADONA et al., 2009; ELAZZOUZI-HAFRAOUI et al., 2007)
Hard wood	140-150	4-5	(BECK-CANDANEDO; ROMAN; GRAY, 2005)
Tunicate	500–1000	10–30	(FAVIER; CHANZY; CAVAILLE, 1995)
Valonia	>1000	10-20	(BECK-CANDANEDO; ROMAN; GRAY,

1.1.3 Self-assembly and organization of cellulose nanocrystals.

A milestone in the development of science and technology of nanocellulose was discovered by Gray and co-workers (REVOL et al., 1992a). CNC suspensions, derived from natural cellulose sources via acid hydrolysis of cellulose, can form a stable chiral nematic liquid crystalline phase. The chiral nematic phase presents long-range CNC organization combined with a helical modulation. This phenomenon occurs due to self-assembly of the CNC in suspensions in order to adopt a configuration that minimizes the existing electrostatic interactions.

These chiral nematic orderings consist on stacked and aligned CNC planes along a vector (director), as shown in Figure 6a. The self-induced parallel alignment phenomenon of the CNC occurs above a certain critical concentration. The CNC critical concentration in

aqueous suspension depends on its charge density and rod aspect ratio (LAGERWALL et al., 2014), and it typically varies between 1% and 10% (w/w) (HABIBI; LUCIA; ROJAS, 2010). Indeed, CNC dispersion from different origins show chiral nematic orderings at different concentrations. The most notable difference occurs between plants derived versus bacterial CNCs. Bacterial CNC, with aspect ratio in the range between 50 and 100 show nematic orderings well below 1 wt% CNC (ARAKI; KUGA, 2001; HIRAI et al., 2008) while on CNCs derived from fresh wood, the critical concentration is found at ~2 wt%, reflecting the lower aspect ratios of these CNCs on ~20–50 (GEBAUER et al., 2011; SALAJKOVÁ; BERGLUND; ZHOU, 2012). The influence of the aspect ratio can also be recognized even when using a single CNC source. Utilizing CNC derived from bacterial cellulose, Hirai et al. confirmed a fractionation of longer CNC into the anisotropic phase and of shorter CNC into the isotropic fraction (HIRAI et al., 2008).

The self-assembly of CNC suspensions can be revealed by the appearance of ‘‘fingerprint’’ patterns obtained from suspensions, observed by polarized optical microscopy (Figure 6b). (REVOL et al., 1992a). The shortest distance between the lines on such “fingerprint” texture is half of the helical pitch (P/2), as it can be seen on Figure 6 c. The helical pitch (P) corresponds to the repeating distance for a full 360° turn on the chiral nematic ordering.

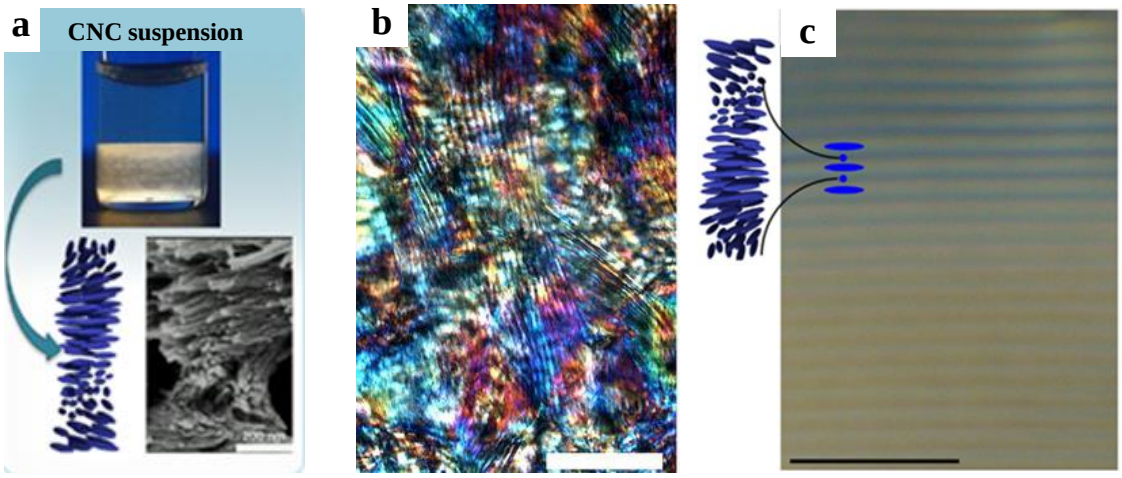


Figure 6. a) Shows the formation of a chiral nematic liquid crystal phase and its coexistence with an isotropic phase in a CNC suspension of 5wt% (upper image) (GRAY, 2012). The helical arrangement of CNC is illustrated schematically next to a scanning electron electron microscopy image of an actual CNC helix (adapted from (GRAY, 2012)). b) Optical microscope image (crossed polars) of the bulk CNC film (scale bar 40 μm (GRAY, 2012)). c) Characteristic regularly spaced lines in an aqueous suspension with 5 wt% CNC, observed in transmission (adapted from (LAGERWALL et al., 2014)).

The ability of CNC suspensions to form self-assembled helical structures is still present in solvent-free films after suspension drying. While in the fluid state, this helical modulation pitch is typically in the range of tens of micrometers, but upon drying, it frequently is reduced to submicrometer values, resulting in Bragg reflection of visible light from dried films, that is, the material acquires a photonic band gap (LAGERWALL et al., 2014) with a consequent iridescent color (Figure 7). Compared to photonic crystals formed via non-liquid crystalline self-assembly of spherical colloidal particles, the helical liquid crystalline self-assembly of rod-like CNC particles leads to a more complex internal structure, rendering the material chiral and adding sensitivity to circular polarization while, at the same time, it enhances its mechanical properties.

The reflected light wavelength (λ) from CNC films depends on the P of the chiral nematic order and also the incidence of the light angle (DE VRIES, 1951), as it can be readily calculated using a simple relation suggested by De Vries, in which

$$\lambda = nP \qquad \text{(I)}$$

In such, n is the material refractive index (~1.56 for CNC). Eq. (I) is valid when films or suspensions are observed along the cholesteric axis, but if they are obliquely viewed, then λ is reduced by a factor of cos θ; in which θ is the viewing angle from the cholesteric axis that is typically coincident with the normal to the surface.

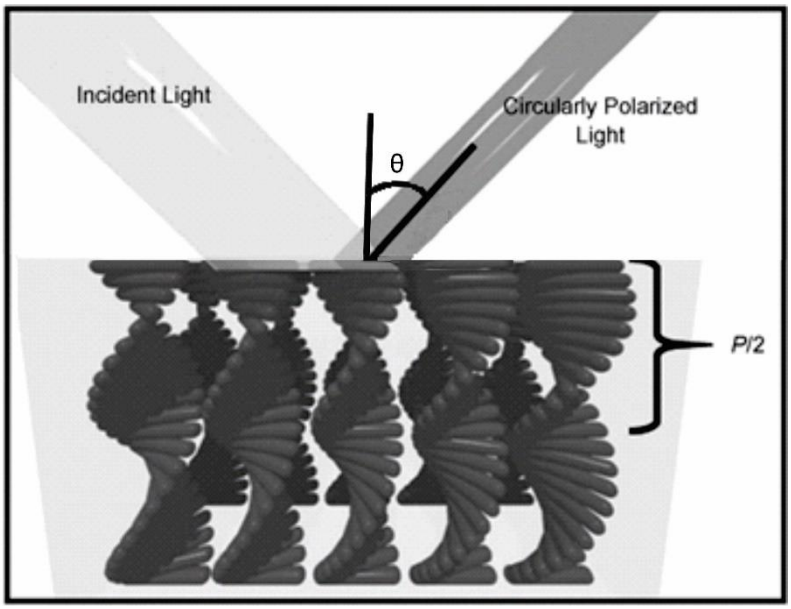


Figure 7. Selective reflection of circularly polarized light by a chiral nematic structure. The rods represent the average orientation of the director, which lies perpendicular to the films and rotates through the film (Adapted from (GIESE et al., 2015))

Recently, Vignolini and co-workers performed a quantitative optical characterization of iridescent CNC films (Figure 8a) correlated to their microstructure (STEINER; VIGNOLINI, 2014). The authors demonstrated that distinct color transitions between different domains of chiral nematic films can be correlated to different periodicities on the photonic structure (chiral nematic pitch, P), as can be seen on Figure 8b, c and d.

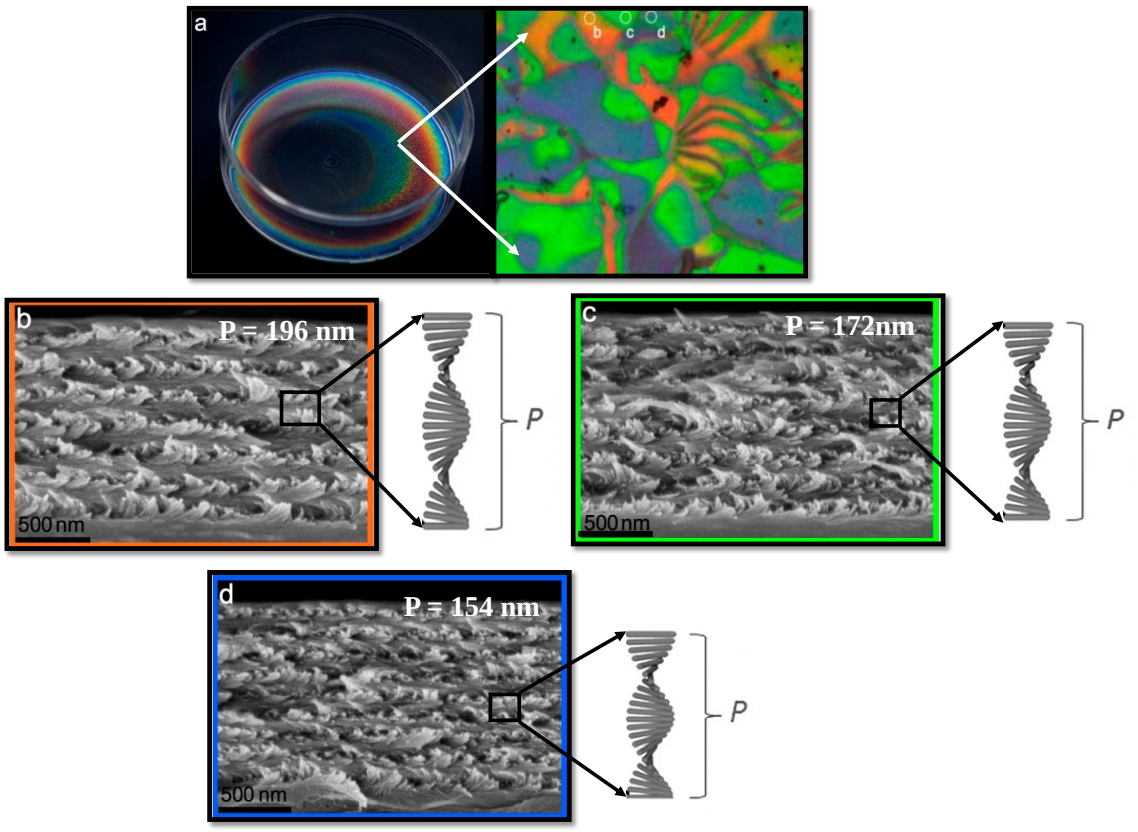


Figure 8. a) Dry chiral nematic CNC films in a polystyrene Petri dish. Polarization optical micrograph at the center of the film. Correlation of optical and electron microscopy of the different domains; b-d) Cross-sectional SEMs images correlated with the white circles show areas b, c and d. (Adapted from (STEINER; VIGNOLINI, 2014))

As a consequence of the surface sulfate esters on CNCs, the P of the chiral nematic liquid crystalline phase is highly sensitive concerning the quality of the CNC, the suspension concentration, the ionic strength of the solution and even the temperature (BECK et al., 2013). A variety of methods has been explored to influence the final helical pitch, and hence the color, of CNC films. Likewise, there is the addition of salt to the suspension (leading to a blue shift on its color), (PAN; HAMAD; STRAUS, 2010) the ultrasonication of the suspension prior to drying (leading to a red shift), (BECK; BOUCHARD; BERRY, 2011) and the variation on the drying temperature (higher temperature leads to a blue shift)(PAN; HAMAD; STRAUS, 2010).

The ability of CNC to form self-assembled helical structures films suggests a potential on CNCs to be utilized in novel materials with attractive photonic and mechanical properties, such as optical sensors (ZHANG et al., 2013b), decorative coatings (BECK et al., 2013), and security encryption in banknotes (KIRK; ANDREWS, 2012).

Another interesting source of functionality in this material is the ability to transfer chiral information molecules and nanoparticles encapsulated as guests into chiral nematic structures. Recently, chiroptical devices based on CNC films were reported. Some examples integrate noble metal nanoparticles and chiral nematic ordering of CNC films, such as silver nanowires, (CHU et al., 2015a) gold nanoparticles (QUEREJETA-FERNANDEZ et al., 2015) and gold nanorods (QUEREJETA-FERNÁNDEZ et al., 2014). These films show an optical response associated to the chiral assembly of nanoparticles, which leads to a strong plasmonic chiroptical activity. Metal NP assemblies within chiral nematic structure showed a circular dichroism (CD) signal assigned to the surface plasmon resonance (SPR) that arises from the helical organization on particles. Considering the importance of the SPR on metal NPs in biochemical sensing, these new chiral nematic NP composite materials open new directions on chemical sensing applications based on the CD response of chiral assemblies of NPs in chiral nematic hosts.

In 2015, Xu and co-workers reported a chiroptical device based on the incorporation of luminescent nanoparticles of $YVO_4:Eu^{3+}$ in CNC films (CHU et al., 2015). The nanoparticles could attach to the surface of twisted CNC, promoting the luminescence integration of rare-earth doped NPs and the chiral nematic ordering of films. Taken the advantages of this integration, the authors used the selective reflection of circularly polarized light property to achieve the modulation of the spontaneous emission through circularly polarized excitation of the samples.

Recently, chiroptical-dependent luminescent emission has also been reported by Xu team in CNC films containing AuNCs (QU et al., 2016). AuNCs are a special class of gold nanomaterials with dimensions smaller than 3nm. The spatial confinement of free electrons in AuNCs results in discrete and size-tunable electronic transitions, which leads to molecular-like properties such as luminescence (ZHENG; ZHANG; DICKSON, 2004). The authors demonstrated tuned fluorescence lifetime decay on AuNCs-CNCs, on the emission intensity by the stopband, and on the band edge-photoemission coupling effect of the films.

The examples mentioned above demonstrate the versatility of CNCs as a host for development of free-standing luminescent sensors. Furthermore, since 2010, MacLachlan's group has been demonstrating that the CNC self-assembly property can also be used as a template to develop new materials with chiral nematic ordering (KELLY et al., 2014). Thereby, they create a variety of inorganic or organic materials, which have been used as an alternative to CNC films in order to design novel optical devices (GIESE et al., 2015).

1.1.4. Cellulose nanocrystals as templates for the chemical synthesis of inorganic materials.

In the last years, cholesteric CNC suspensions have been used as templates to produce new kinds of materials. Examples of CNC-templated materials include porous TiO_2, (SHIN; EXARHOS, 2007) shape-controlled TiO_2 cubes (ZHOU; DING; LI, 2007). In addition, researchers have attempted to use the chiral nematic phase to template mesoporous solids. Mann and co-workers showed that CNC can be used to template birefringent silica, but no long-range helical ordering was observed and no porosity was measured (DUJARDIN; BLASEBY; MANN, 2003).

In 2010, Shopsowitz and co-workers discovered that alkoxysilane precursors, such as tetramethoxysilane (TMOS), are compatible with CNC self-assembly, since the isoelectric point of silica is near to the pH of such acidic CNC dispersions (SHOPSOWITZ et al., 2010). Furthermore, the alkoxysilane hydrolysis generates its corresponding alcohol, which does not disturb the evaporation-induced self-assembly of CNC. In addition, its slight acidity, and the high water ratio of CNC dispersions suppress of silica polymerization until the later stages of evaporation. Taken advances these features, the authors produced iridescent composite films by adding inorganic sol-gel precursors followed by drying the suspension under ambient conditions (Figure 9a). The iridescent composite films reflected colors can vary from the visible and into the near IR spectral region with increasing precursor content (Figure 9c). As the refractive index of CNC and silica are relatively similar, the shift in the reflected wavelength happens predominately due to an increase on the helical pitch.

Generally, the helical pitch of the CNC-silica composite before calcination is larger than visible light wavelengths, and the initial composite film, therefore, shows no color. However, after the cellulose has been removed, the remaining silica film frequently shows visible Bragg reflection and iridescent colors as a resulting characteristic (Figure 9 b-d). Scanning electron microscopy investigations in these cases revealed that the removal of CNC leads to a compression on the helical structure, meaning that the periodicity is small enough, thus the photonic bandgap falls within the visible range.

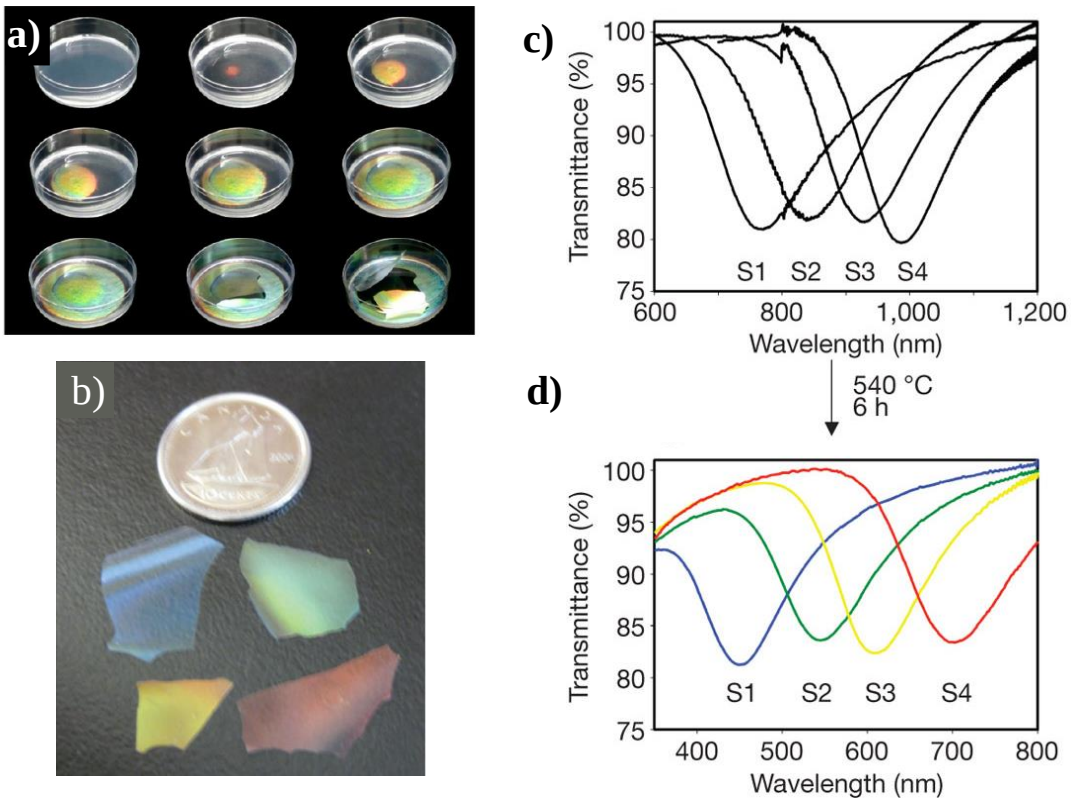


Figure 9. a) Evaporating and self-assembly of CNCs with silica sol-gel precursor to yield an iridescent composite, whose structural color depends on the silica loading. b) After removal of the CNCs through calcination or acid hydrolysis mesoporous sol-gel derived films are obtained that retain their intense structural colors. c) Transmittance spectra of the iridescent composite. d) Transmittance spectra of mesoporous silica films. (Adapted from (SHOPSOWITZ et al., 2010)).

Further, mesoporous silica films are attractive because they combine high surface area of materials to the long-range ordering of liquid crystals, specifically with the chiral nematic phase helical arrangement. According to MacLachlan's team approach, it is possible to endow other materials with photonic crystal properties, such as organosilica, (SHOPSOWITZ; HAMAD; MACLACHLAN, 2012) titania, (SHOPSOWITZ et al., 2012) carbon (SHOPSOWITZ; HAMAD; MACLACHLAN, 2011) and polymers (KHAN et al., 2013). The key ideas for this type of template approach and a comparison on ordinary drying of CNC suspensions are schematically summarized on Figure 10.

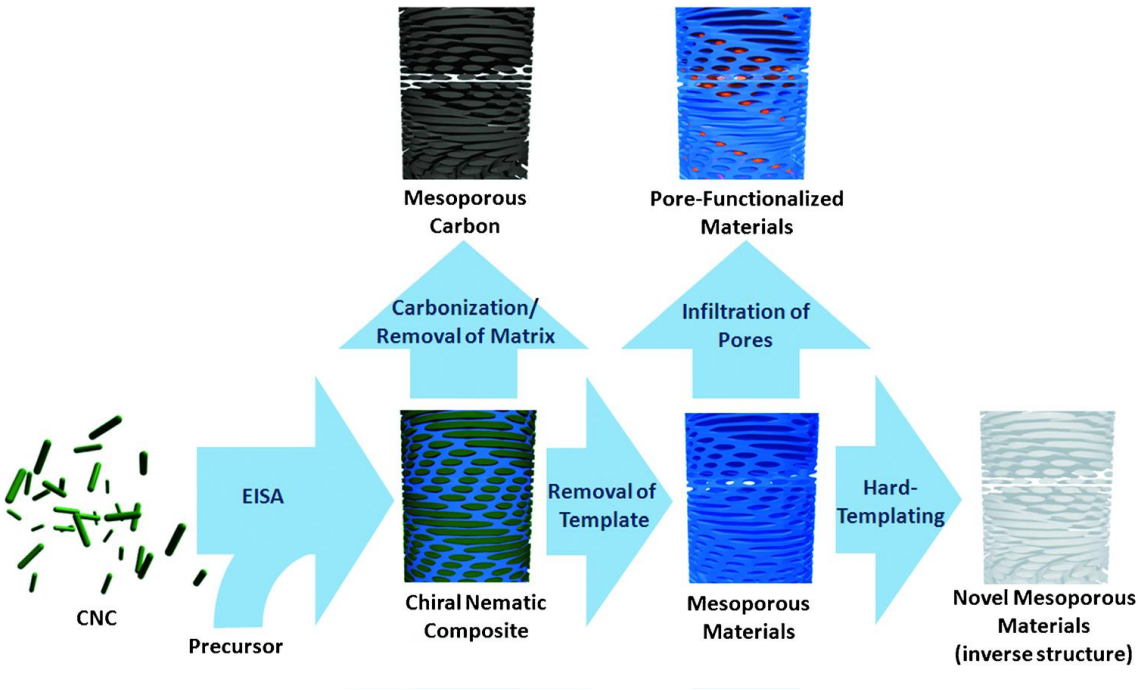


Figure 10. Synthetic route to new nanostructured materials with chiral nematic order. In the presence of a suitable precursor, CNCs form a composite material. Removal of the template leaves a mesoporous material which can be functionalized by infiltration of the pores or used as a hard template. Alternatively, carbonization followed by removal of silica yields chiral nematic mesoporous carbon (Adapted from (GIESE et al., 2015)) .

The high surface area and mesoporosity of these CNC templated sol-gel-derived materials facilitate their use as scaffolds for guest species, such as molecules, polymers, and nanoparticles, exhibiting novel optical properties coupled with chiral nematic organization. These hybrid materials have potential applications for catalysis, biosensing, and optoelectronic devices.

In 2013, Giese and co-workers embedded thermotropic liquid crystals (LCs), 4-Cyano-4′octylbiphenyl (8CB), as a responsive guest within the channels of a chiral nematic mesoporous silica, which could allow stimuli-induced changes on its refractive index, and thus, a dynamic modification of the composite optical properties (GIESE et al., 2013). The author demonstrated that selective reflection from the composite with chiral nematic organization can be reversibly switched by thermal cycling on the 8CB guest between its isotropic and liquid crystalline states, which was proven through solid state NMR experiments. The commutation on the optical properties of the chiral solid-state host by stimulus-induced transitions of the guest opens application possibilities for these novel materials on selective tunable optical filters or temperature sensors.

In the same year, Nguyen et al. reported the first LC-templated hybrid material by conjoining the chiral nematic mesoporous silica iridescence with the luminescence of CdS QDs (NGUYEN; HAMAD; MACLACHLAN, 2014). Such materials show both luminescence characteristics of the QDs and iridescence aspects of the chiral nematic mesoporous silica host. The authors suggest that such luminescent and mesoporous films could be used in optical sensing to trace the detection of explosives, once the CdS quantum dots undergo strong luminescence quenching when exposed to nitroaromatic compounds.

Hard template approach using nanocrystalline cellulose-templated silica was employed in order to design other examples of luminescent and iridescent chiral nematic mesoporous films. Just recently, Chu et al. reported the use of a hard-template method and nanocrystalline cellulose-templated silica to design new chiral nematic films based on europium-doped zirconia (ZrO_2/Eu^{3+}) (WANG; XU, 2014) and europium-doped yttrium oxide ($Y_2O_3:Eu^{3+}$) (CHU et al., 2014). The obtained films displayed luminescence characteristic of the Eu^{3+} combined with the photonic properties from the chiral nematic template. These films exhibited possibility of circularly polarized excitation, they also modulated spontaneous emission and the lifetime of luminescent Eu^{3+}, as showcased by CNC/ $YVO_4:Eu^{3+}$ composite films mentioned before (CHU et al., 2015b).

All of the studies described above have proven the suitability of chiral nematic mesoporous silica in the hard template of solid-state materials that combine the benefits of luminescence, photonic properties, and mesoporosity. Such films tend to crack during the last stages of evaporation into centimeter-sized pieces (Figure 9a), which displays a significant limitation to use these materials in applications that require large, homogeneous films. As observed in other mesoporous materials, this happens due to the generation of significant capillary pressure gradients during the evaporation process. In this context, there is a growing interest to develop composite materials based on CNC with higher mechanical properties than mesoporous films, and also on keeping the pure film optical properties (ABITBOL et al., 2016).

1.2. Silk fibroin.

Silk represents a unique family of biopolymers that consists on protein fibers, typically produced from different species of arthropods, such as spiders, scorpions, silkworms, mites and bees (JIN; KAPLAN, 2003). *Bombyx mori* (B. mori) silkworms are the main producer of silk

worldwide. At the end of larval stages, following a spinning process, silkworm generates silk fibers in the form of cocoons (Figure 11).

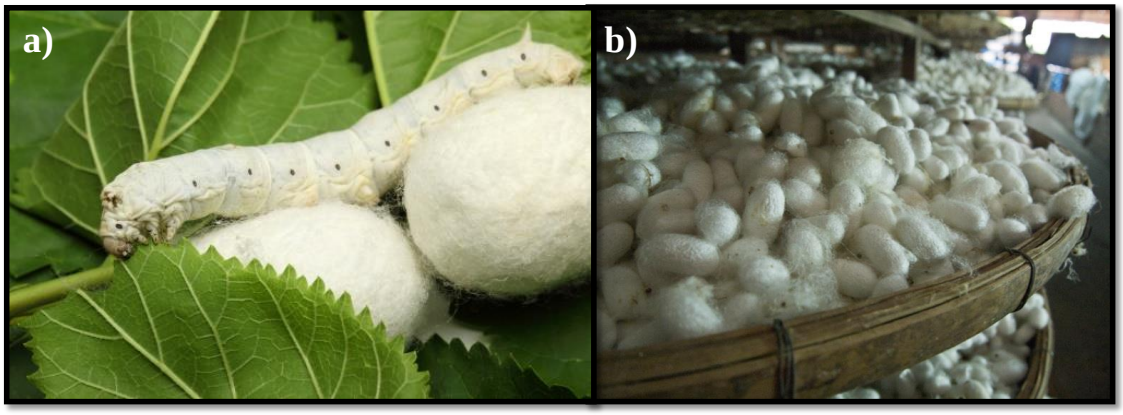


Figure 11. a) Bombyx mori (B. mori) silkworms together with two silk cocoons; b) Silk cocoons (Images from http://inhabitat.com/the-silk-pavilion-mit-researchers-to-3d-print-a-silkworm-inspired-structure/).

Structurally, *Bombyx mori* silkworm silk consists of two types of proteins: sericins and fibroin (KODAMA, 1926). The raw silk consists of two parallel fibroin fibers held together by a layer of sericin on their surfaces (Figure 12a). The fibroin filaments are made up of bundles of nanofibrils, which are oriented parallel to the axis of the fiber, and are thought to interact strongly with each other (Figure 12b). Glue-like sericins are glycoproteins amorphous that account for approximately 20−30 wt % of silkworm silk. Sericins are soluble in water due to the high presence of hydrophilic amino acids, with large sericin peptides soluble in hot water, while small peptides can be dissolved in cold water (ZHANG, 2002).

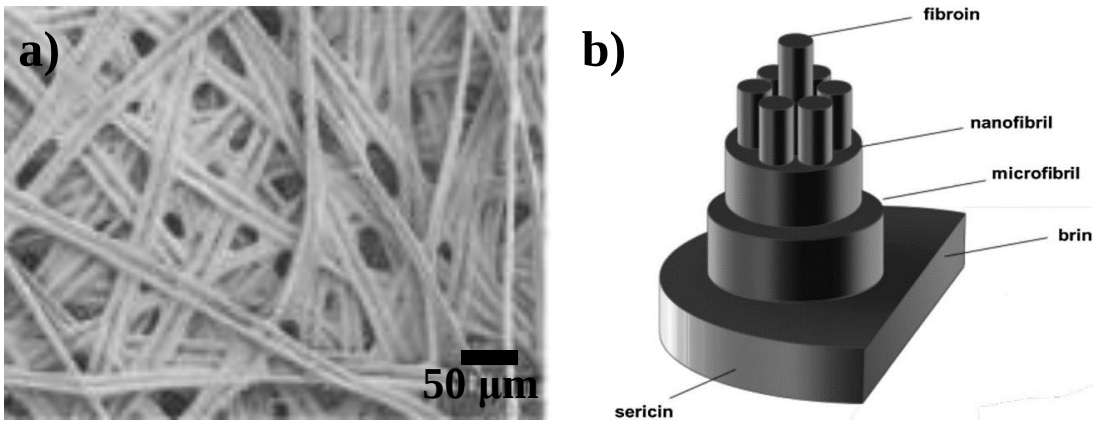


Figure 12. a) SEM images of the morphologies of silkworm cocoons from Bombyx mori;(Adapted from (ZHANG et al., 2013a)) b) Structure of Bombyx mori silk thread (Adapted from ((PEREIRA; SILVA; DE ZEA BERMUDEZ, 2015))).

1.2.1 Primary Structure of silk fibroin.

Silk fibroin (SF), the structural protein of silkworm silk fibers, is insoluble in many solvents including water and accounts for approximately 75 wt % of the total silkworm silk (KODAMA, 1926). SF consists of a light (L) polypeptide chain and a heavy (H) polypeptide chain linked together via a single disulfide bond at the C-terminus of the H-chain, forming a H–L complex (SHIMURA et al., 1976). Another component of silk fibroin is the glycoprotein P25 attached by noncovalent interactions to the covalently bonded heavy and light chain (TANAKA; INOUE; MIZUNO, 1999). Quantitatively, H-fibroin, L-fibroin, and P25 are present in the silk fibroin in a molar ratio of 6:6:1, respectively, suggesting that P25 is attached to a set of six (H-L fibroin) dimers [$(H\text{-}L)_6$.(P25)] (INOUE et al., 2000). The glycoprotein P25 has a molecular weight (Mw) of ~30 kDa, being secreted with H-fibroin, it is considered important to maintain the integrity of silk fibers; however, its role in the formation of silk fibroin is not clear.

Concerning the silk fibroin material, H-chains (MW ~ 350 kDa) are composed of more than 5000 amino acids, the majority of the protein consists of glycine (G) (~43 46%), alanine (A) (~25–30%) and serine (S) (~12%), whereas tyrosine (Y) (the larger amino acid with a polar side chain) occurs at ~5%. The next most abundant amino acid in the H-chain is valine (V) (~2%), and it is followed by aspartic acid (D), phenylalanine (F), glutamic acid (E), threonine

(T), isoleucine (I), leucine (L), proline (P), arginine (R), lysine (K) and histidine (H), present in much smaller percentages (less than 2% each) (KOH et al., 2015).

Organizationally, silk fibroin H-chain consists of 12 hydrophobic domains interspersed with 11 hydrophilic domains. The hydrophobic domains contain amino acids in a high and repetitive sequence of GAGAGS, GAGAGY, and GAGAGVGY, while the hydrophilic domains contain amino acids in non-repetitive sequence, which comprises mainly charged acidic amino acids, such as glutamic acid, aspartic acid, arginine and lysine. Furthermore, repetitive domains are capable of organizing themselves together into β-sheet crystallites via intramolecular or intermolecular forces including hydrogen bonds, van der Waals forces, which leads to the formation of highly ordered crystalline regions in silk fibroin. On the other hand, the non-repetitive domains form non-crystalline regions in silk fibroin (VOLLRATH; PORTER, 2009; ZHOU et al., 2001a).

In addition, silk fibroin heavy chains are very different from silk fibroin light chains, and consequently, the structural differences in both types of silk proteins affect the physical properties of their individual materials. Although the heavy chain character is dominant in terms of mass weight, the behavior of the total silk is significantly modified by the presence of the light chain component. The light chain (M_w ~ 25 kDa) has a more undifferentiated amino acid composition, which is formed by 262 amino acids containing A (14%), S (10%), and G (9%), and a N-acetylated terminal serine residue with non-repetitive sequence. The L-chain shows comparatively more hydrophilic properties, and is relatively elastic with little or no crystallinity (YAMAGUCHI et al., 1989).

1.2.2. Secondary structure of silk fibroin.

The primary structure of SF previously described can be considered as a simple and regular unit. Higher order structures of fibroin are somewhat complicated and have been a matter of controversy, which is probably also the key feature in silk research. Three different crystalline polymorphs are usually referred as secondary structures for fibroin: Silk I, Silk II and Silk III.

Firstly, Silk I corresponds to the conformation present in the middle gland in pre-spinning, is meta-stable and water-soluble, it has been described as lacking secondary structure, with a structure dominated by α -helix and random coil structures (ASAKURA et al., 2013).

Secondly, Silk II structure is antiparallel β-sheet type, in which the polypeptide chains are aligned and the adjacent chains are connected via hydrogen bonds. β-Sheet structures are

asymmetrical with one side occupied by hydrogen side chains from Gly and the other occupied by the methyl side chains from the Ala that populates the hydrophobic domains. The β-sheets are arranged so that the methyl groups and hydrogen groups of opposing sheets interact and form the intersheet stacking in the crystals. Strong hydrogen bonds and van der Waals forces generate a structure that is thermodynamically stable. The intersheets distances between two glycine faces or two alanine faces are 3.7 and 5.5˚ A, respectively. According to the pseudo unit, the β-sheet crystallite adopts an orthorhombic crystal lattice with unit cell dimensions of a = 9.20, b = 9.40, and c = 6.97, in which a is the direction along the stacking of β-sheets, b is the direction in a β-sheet perpendicular to the strand axis, and c is the direction along the strand axis (MARSH; COREY; PAULING, 1955).

Lastly, the Silk III is a threefold helical chain conformation and was identified for fibroin in an air–water interface (VALLUZZI et al., 1999).

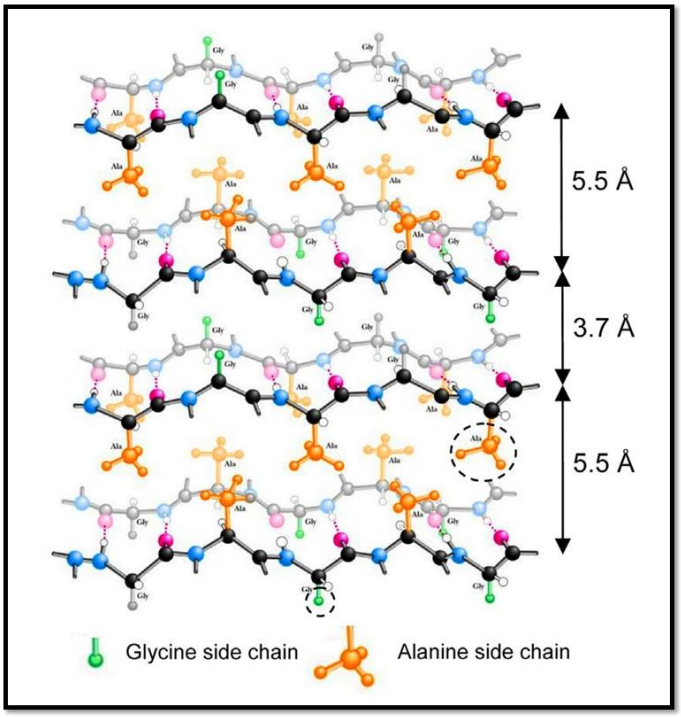


Figure 13. Illustration of antiparallel β-sheets, with the surface of one sheet projecting entirely methyl groups of alanine residues and the other surface of the same sheet projecting only hydrogen atoms of glycine residues. The intersheet distances alternate at5.5Å and 3.7Å respectively (Adapted from (KOH et al., 2015)).

The predominance of Silk II conformation within the fibroin structure imparts the protein-based materials with high mechanical strength and toughness. In terms of strength, silkworm silk is superior to commonly used polymeric degradable biomaterials, such as

collagen and poly (l-lactic acid) (PLA). The ultimate tensile strength of *B. mori* silk fibers is 740 MPa. In contrast, collagen has an ultimate tensile strength of 0.9-7.4 MPa and PLA 28-50 MPa (ALTMAN et al., 2003). In addition to its impressive mechanical properties, silk fibroin is also a biocompatible and biodegradable material. Therefore, silk fibroin is an excellent polymer candidate for biomedical applications.

Significantly, due to its excellent physical and biomedical properties, such as flexibility, mechanical strength, and most importantly, biocompatibility, silkworm silk has been used by the textile industry for thousands of years (OMENETTO; KAPLAN, 2008, 2010). In particular, the biocompatibility of silkworm silk has been demonstrated through its use in sutures for several millennia. Nowadays, this ancient material continues to play a significant role in our society. It is estimated that a hundred billion dollars are spent annually on silk-based products (PEREIRA; SILVA; DE ZEA BERMUDEZ, 2015). In the last years, silk has been studied as an attractive high-technology material platform, which offers new opportunities for photonics, optoelectronics and biomedical applications (TAO; KAPLAN; OMENETTO, 2012).

1.2.3. Extraction and processing of silk fibroin.

Preparation of fibroin-based materials starts by producing the SF solution from natural silk cocoons. In 2011, Rockwood et al. developed a completely water-based and organic solvent-free method of reverse engineering for SF extraction and purification from native fibers of *Bombyx mori* cocoons[46]. Such study was accomplished through a degumming process, which consists of boiling silk cocoons in a solution of 0.02M sodium carbonate. Upon degumming the raw silk to remove the sericin, the silk fibers can be dissolved in 9.3 M lithium bromide into an aqueous solution of silk fibroin protein, which is then purified, removing the salt by dialysis. Regenerated silk fibroin water-solution is a pure protein solution with high chemical and physical stability when stored at low temperature (~ 4°C) in order to slow down the gelation mechanisms (MATSUMOTO et al., 2006; WANG et al., 2005). The extracted silk fibroin is processed into one of the several formats, including hydrogels, ultrathin films, thick films, conformal coatings, 3D porous and solid matrices, so that fibers with diameter in nano and macroscale and many related material formats (KOH et al., 2015; LIMA et al., 2016; MARELLI et al., 2016; PEREIRA; SILVA; DE ZEA BERMUDEZ, 2015; TAO; KAPLAN; OMENETTO, 2012; WANG; CHEN; ZHANG, 2015).

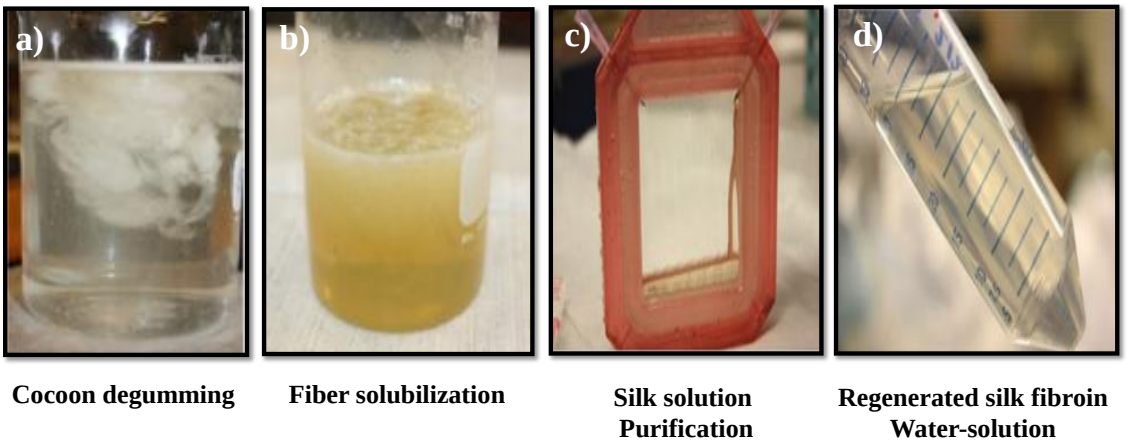


Figure 12. Main steps of extraction and purification processes of silk fibroin from cocoon: a) Degumming in alkaline solution for removing sericin from fibers of cocoon; b) Solubilization of silk fibroin fibers in a concentrated LiBr solution; c) Purification by dialysis in water of silk solution; d) Pure regenerated silk fibroin water solution.(Adapted from (PREDA et al., 2013))

Different approaches and methodologies are being used to produce silk-based materials with adjustable material forms aiming a wide variety of applications. They are mainly being developed for the biomedical field and in high-technology directions, such as tissue regeneration (ZHAO et al., 2009), photonics (KIM et al., 2012; TAO et al., 2015), electronics (KIM et al., 2010; WANG; HSIEH; HWANG, 2011), optical fibers, (APPLEGATE et al., 2015), and microfluidics (BETTINGER et al., 2007).

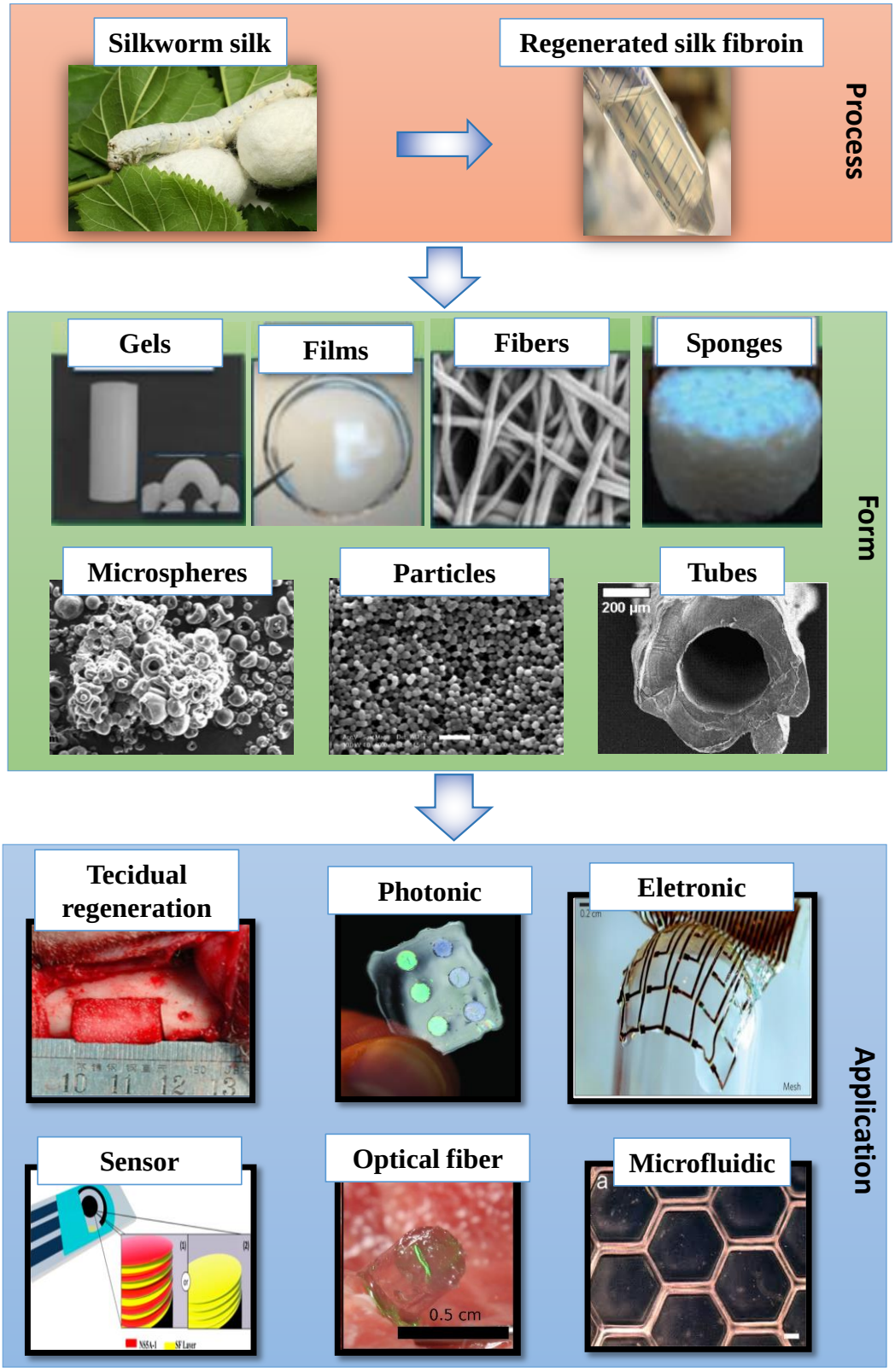


Figure 14. Generating new materials from silks. Native silkworm silk on the right illustration (Image from http://inhabitat.com/the-silk-pavilion-mit-researchers-to-3d-print-a-silkworm-inspired-structure/). Regenerated silk fibroin on the left illustration (Adapt from (PREDA et al., 2013) . The illustration above shows a range of materials can be generated from silks through processing into hydrogels, films fibers, sponges, microspheres, particles and tubes. The properties of these systems can be modified depending on the processing modes used and then generated into functional devices and technology platforms.

The poor mechanical properties of regenerated silk, in comparison to native silk fibers are attributed to the protein degumming and dissolution processes, which during some level of the hydrolysis chain inevitably occurs. However, the final processing step of the regenerated silk fibroin often happens to induce crystallinity. The meta-stable Silk I and a random coil structure can be converted into the most stable and crystalline Silk II through external disturbances, such as, fibroin concentration, processing temperature, solvent/salt treatment, water annealing treatment (HE; VALLUZZI; GIDO, 1999; HU et al., 2011; JIN et al., 2005; MATSUMOTO et al., 2006). The solvent treatment was done by immersion in an alcohol, such as methanol or ethanol. To improve β-sheet crystallinity on the fibroin films through alcohol immersion is simple and quick, but if the researcher wants to avoid the use of an alcohol, annealing water can be used.

Fibroin hydrogel is prepared through the sol-gel transition on fibroin aqueous solution. Silk fibroin sol-gel transition occurs through inter and intramolecular interactions, mainly forming hydrogen bonds and hydrophobic interactions among protein chains, which changes from amorphous to thermodynamically stable β-sheets. The sol-gel transition can be driven by exposure of silk solutions to shear forces, electric fields, pH near or below the isoelectric point (pI=3.8-3.9), polar solvents, heat and water removal (KIM et al., 2004; NAGARKAR et al., 2010). In Kaplan and co-workers studies about mechanisms of silk fibroin sol-gel transition, there is a correlation to the transition in the secondary gel structure with the extent measurement of gelation, considering time as function of changes in the temperature and the fibroin concentration. The authors demonstrated that the increase in the fibroin concentration and gel temperature accelerated the sol gel process and the precipitation of micrometers aggregated with insoluble and crystalline *β*-sheet conformation (KIM et al., 2004; MATSUMOTO et al., 2006). Silk hydrogels are found to be suitable for preparing scaffolds for load bearing tissue engineering and as drug delivery systems (CHAO et al., 2010; HOPKINS et al., 2013). These 3D polymer networks are physically durable to swell in aqueous solution without dissolving.

Fibroin can also be physically blended or chemically cross-linked with guest polymers for mechanical enhancement. Natural polymers and synthetic polymers can be used as guest polymers to enhance the mechanical properties of regenerated fibroin. Physical blending of fibroin with natural polymer, such as recombinant collagen, gives rise to sponges that have compressive stress ~33 times higher than pure fibroin sponges, along with enhanced biocompatibility (HU et al., 2008). Furthermore, blended fibroin-cellulose films have both enhanced strength and ductility. The improved mechanical properties were respectively attributed to the presence of intermolecular hydrogen bonding between cellulose and fibroin

(FREDDI et al., 1995). In another case, fibroin was first cross-linked with hydroxypropyl methyl cellulose (HPMC) to form an interconnected network of small and uniform fibroin structures, which served as crosslinking sites evenly distributed throughout the hydrogel (LUO; YANG; SHAO, 2016). Such impressive mechanical properties, in addition to their advantages in environmental stability, biocompatibility, controlled biodegradability, morphologic flexibility, and low density, makes these hydrogels and fibroin/polymer composites promising candidates to design a new generation of biomaterials (KUNDU et al., 2013; LIU; ZHANG, 2014; VEPARI; KAPLAN, 2007).

Furthermore, recently there has been much investment on the development of new systems concerning silk-based materials. Thus, it is necessary to mention the class of silk/silica hybrids. The high biocompatibility and the positive biological effects properties of the silica-based bioactive glasses have supplied successful solutions to soft tissue treatments during the last decades (ARCOS; VALLET-REGÍ, 2010). The combination of silica and silk leads to very promising and versatile materials with foreseen application in a variety of domains, including bone regeneration. Kaplan and coworkers reported osteoinductive and biodegradable hybrid biomaterials for bone regeneration prepared combining silk fibroin with silica particles (MIESZAWSKA et al., 2010). Silk/silica hybrid also was prepared by sol–gel crosslinking, and the silica particles were bounded to the fibroin, resulting in improved thermal properties on different scanning calorimetry patterns compared to SF (HOU; CHEN, 2010).

A simple alternative to create silk/silica composites was demonstrated through coating silk fibers of *N. Madagascariensis* spiders (HUANG et al., 2003) and cocoon fibers of *Bombyx mori* fibroin silkworms (XU et al., 2006) with silica precursors, such as tetraethylorthosilicate (TEOS). Subsequently, they were heated at 105 °C for several hours. Overall, in such studies, silk fibers were used as templates by selective removal through calcination at 600 °C, yielding a porous material in which the pore structure is determined by the silk-based material.

2. OBJECTIVES

Considering the unique opportunities offered by biopolymers, bacterial cellulose and silkworm silk, the main objective of this thesis is the preparation and characterization of multifunctional materials based on cellulose nanocrystals extracted from bacterial cellulose produced by bacteria Acetobacter xylinum, as well as regenerated silk fibroin stemmed from the cocoons of the silkworm (Bombyx mori). In this context, the PhD research activity can be summarized in the following objectives:

a) Preparation and characterization of free-standing CNC films coated with the low molecular weight nematic liquid crystal (LC), 4′-(hexyloxy)-4-biphenylcarbonitrile (HOBC), which integrates iridescence, conductive and thermal response.

b) Preparation and characterization of free-standing dye-doped CNC/silica composites, which integrates iridescence and luminesce properties.

c) Preparation and characterization of organic-inorganic hybrids based on silica and silk fibroin.

d) Preparation and characterization of hierarchical porous silica monoliths for random laser applications using silk fibroin as a biotemplate.

PART I. MULTIFUNCTIONAL MATERIALS BASED ON CELLULOSE NANOCRYSTALS.

3. Optical platform based on cellulose nanocrystals (CNC) – 4-(hexyloxy)-4-biphenylcarbonitrile (HOBC) bi-phase nematic liquid crystal films.

Novel multifunctional materials that integrates iridescence, conductive and thermal response were prepared from cellulose nanocrystals (CNC) and the low molecular weight nematic liquid crystal (NLC), 4′-(hexyloxy)-4-biphenylcarbonitrile (HOBC). Self-sustainable films exhibit thermal/electrical response typical of HOBC and the angular dependent reflection, typical of CNC films. Scanning electron microscopy (SEM) confirms the CNC film structure comprises multi-domain Bragg reflectors. The relationship between the morphology and thermoresponsivity in the micro/nanostructured materials was investigated by using transmission optical microscopy (TOM). Conductive response of the composite films was studied by Electrostatic force microscopy (EFM) measurement. The designed material possessed attractive final properties to the development of novel thermo- and electro-responsive devices and it can be a candidate for optical sensing, without the use of absorbing or emitting chromophores.

3.1. Introduction.

The optical response of liquid crystal (LC) materials is controlled by self-assembly in response to an external perturbation (electric, thermal, optical, or mechanical field forces) (CHOI et al., 2009). Chiral nematic liquid crystals display helical structure with remarkable photonic properties. Strong optical rotation of the light and selectively reflection are observed when the helical pitch of the chiral nematic LC is close to the wavelength of incident light (CHOI et al., 2009). Therefore, only circular polarized light with the same handedness as the chiral nematic cellulose, and with the corresponding color to the pitch, is reflected. Chiral nematic liquid crystals can be candidates for optical sensing because they can exhibit brilliant colors without the use of absorbing or emitting chromophores (COLES; PIVNENKO, 2005; KIKUCHI et al., 2002; OHZONO; YAMAMOTO; FUKUDA, 2014).

Cellulose nanocrystals are well known to form chiral nematic liquid crystal phases (REVOL et al., 1992b). Stable CNCs may be prepared through acid-catalysed hydrolysis of bulk cellulose (MARCHESSAULT; MOREHEAD; WALTER, 1959). In water, CNC suspensions organize into a helical structure that can be preserved upon air-drying, resulting in

iridescent films (REVOL; GODBOUT; GRAY, 1998). The band-gap position for the chiral nematic CNC film can be tuned from visible to the near-infrared light region by changing the preparation conditions, such as ultrasonic treatment and adding salts for example (BECK-CANDANEDO; ROMAN; GRAY, 2005; PAN; HAMAD; STRAUS, 2010). The self-organization ability of CNC has been employed to develop several applications such as optical sensors (CHU et al., 2014; SHOPSOWITZ et al., 2010; ZHANG et al., 2013b), chiroptical devices (CHU et al., 2015b), decorative coatings (BECK et al., 2013), and security encryption in banknotes (KIRK; ANDREWS, 2012).

In parallel, low molecular weight nematic liquid crystals (NLC) are organic macromolecules, that self-assembly depending on external stimuli such as electrical field, temperature and light (DOANE et al., 1986; DRZAIC, 1986). These materials have been extensively used combined with polymers to design electro- and thermo-sensitive material where the dispersed mesophase can be switched from opaque scattering state (OFF-state) to transparent state (ON-state) due to matching of the refractive index of the polymer and that of the oriented LC by applying an external electrical voltage or thermal gradient (CAMPBELL; TASINKEVYCH; SMALYUKH, 2014; GANESAN et al., 2010; GUTIERREZ et al., 2012; TERCJAK; GUTIERREZ, 2011; ZHOU et al., 2002). Also chiral nematic mesoporous silica have been combined with LCs to design thermal-optical devices (GIESE et al., 2013; MANNING et al., 2014).

We have designed new optical materials by preparing composite films from NLC and bacterial cellulose (BC) self-sustainable membranes (TERCJAK et al., 2016). Cellulose produced by *Gluconacetobacter xylinus* present superior physicochemical properties one compared to plant cellulose. In addition, it is obtained with high purity and crystallinity in a completely green process (QIU; NETRAVALI, 2014). BC membranes display peculiar and unique properties that allow the utilization of this green material in different applications from biomedicine to photonics (LEGNANI et al., 2008; PINTO et al., 2015; SHAH et al., 2013; SULAEVA et al., 2015). Emergent properties of the materials so prepared include conductive and thermal response, characteristic of the coated NLC, added to thermal stability and mechanical properties of the BC membrane. Therefore, the designed thermoresponsive materials displayed original tunable properties that would not be possible with the individual components (TERCJAK et al., 2016).

Taking all these described features into account, the design of a new optical sensing platform is proposed here, that is, composites prepared from NLC and CNC iridescent membranes.

Cellulose nanocrystals (CNC) were obtained from BC membranes that were prepared at our laboratory as described before (PINTO et al., 2015; TERCJAK et al., 2016). Acid hydrolysis of BC membranes lead to stable CNC suspensions. In the first step to obtain the new composites, iridescent CNC self-sustainable films around 40 μm thick were obtained by casting CNC suspensions on plastic substrates. In a second step CNC films were coated with the NCL 4′-(hexyloxy)-4-biphenylcarbonitrile (HOBC) by using the easy and inexpensive method proposed before (TERCJAK et al., 2016). This new material was obtained as self-sustainable iridescent films, with chiral nematic structure, that exhibit modulated optical properties, in response to thermal gradient or relatively small electrical voltage in addition to the liquid crystal properties of the CNC films. The relationship between the surface structure and thermo-responsive properties of investigated HOBC coated CNC film was investigated using transmission optical microscopy (TOM). Additionally, electrostatic force microscopy (EFM) measurement was employed to prove the effect of external stimuli, in this case applied voltage, on the HOBC liquid crystal coated CNC film.

3.2. Materials and methods.

3.2.1. Materials.

Sulfuric acid (95-98%) was purchased from Sigma-Aldrich. Water was purified (Millipore Milli-Q purification system). Low molecular weight nematic liquid crystal (LC), 4’-(hexyloxy)-4-biphenyl carbonitrile (HOBC), was supplied by Sigma-Aldrich, and used without further purification. The thermal behavior of HOBC liquid crystal was evaluated by DSC (Figure 15) and summarized in figure 16. HOBC displays crystalline-nematic transition at around 59 ºC and nematic-isotropic transition around 76 ºC.

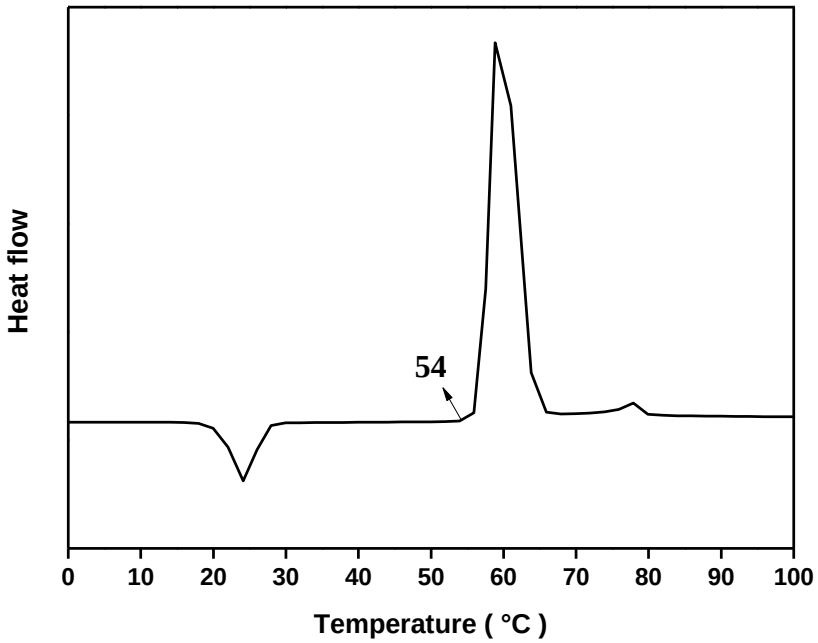


Figure 15. Differential Scanning Calorimetry (DSC) obtained for HOBC.

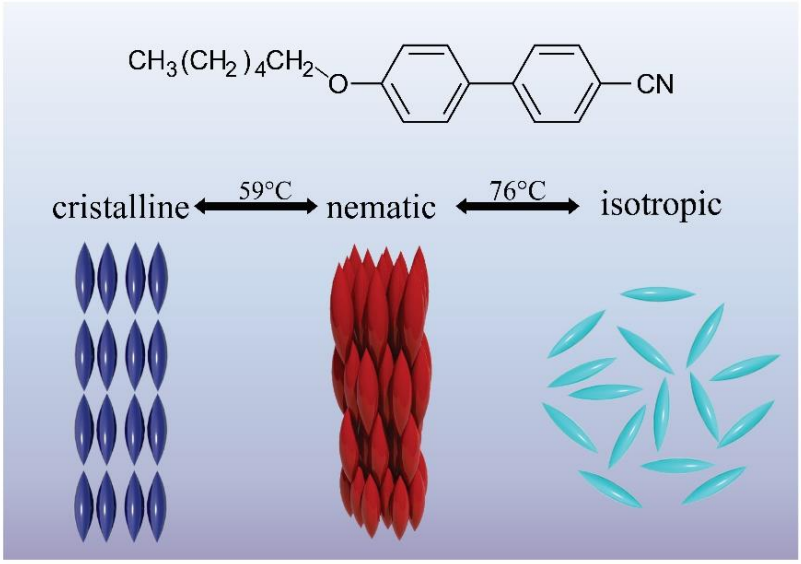


Figure 16. HOBC Structure, crystal-nematic transition (TC-N) and nematic-isotropic transition (TN-I) obtained by DSC.

Production of Bacterial cellulose inoculum: The cellulose producing strain used was *Gluconacetobacter xylinus* (ATCC 23760) supplied by André Tosello Foundation, Campinas-SP, Brazil. It was cultured in Hestrim-Schramm medium (HS medium) containing D-glucose

glycose, yeast extract, peptone, di-sodium hydrogen phosphate (Na_2HPO_4), citric acid, agar and purified water. Analytical grade chemicals were used as received. Before the bacterial strain inoculation, the strain culture medium was sterilized and then was cultivated during 1 day at 28 ºC in an air circulating oven as conditioning chamber.

Biosynthesis of bacterial cellulose: Bacterial cellulose (BC) culture medium was prepared according to the method previously reported [26,31]. 45 mL of culture medium and 5 mL of the inoculum were cultivated during 3 days in static conditions at 28 ºC in a 250 mL Erlenmeyer flask in an air circulating oven. After this time, jelly-like BC pellicle was harvested and purified to eliminate the culture medium (to remove the cells and other impurities). The purification protocol was realized following the pathway described before[32]. Finally, purified BC hydrated membrane was dried in order to obtain BC film.

3.2.2. Preparation of cellulose nanocrystals (CNC).

Dried BC films (5 g) were milled using an IKA® A11 basic analytical mill and sieved with a stainless steel sieve (mesh 35) to ensure uniform particle size and to increase the surface area. The milled BC was hydrolyzed in 88 mL of a 64 wt % sulfuric acid solution at 50 °C for 0.5 h under vigorous stirring. The suspension was then diluted (10x) with ultrapure cold water (resistivity 18.2 MΩ.cm at 25 °C) to stop the hydrolysis, and allowed to settle overnight. The clear top layer was decanted and the remaining cloudy layer was centrifuged at 6000 rpm for 10 min (Jouan C3i - CR3i multifunction centrifuge). The supernatant was decanted and the resulting thick white suspension was washed 3 times with ultrapure water. The thick white suspension was transferred to a dialysis cellulose membrane sleeve (12000-14000 molecular weight cut-off) and dialyzed against ultrapure water. The membrane sleeve containing the CNC were placed periodically in ultrapure water, and the procedure was continued until the pH of the water became constant (pH = 2.4) over a period of 1h. The suspension was diluted to the desired concentration (3.0 wt%) and dispersed using an ultrasound homogenizer (Sonics Vibra-Cell VC 505 500W 20 kHz) with a 6 mm diameter probe. Typically, 50 mL of a 3.0 wt % CNC suspension was placed in a 100 mL plastic tube and sonicated at 60% of the maximum power (300 W). Prolonged sonication (to an energy input over 2500 J/g of CNC) was performed in an ice bath, to prevent desulfation caused by the heating generated during the process.

3.2.3. Preparation of the composite film.

Considering potential applications of designed materials, we have proposed an easy painting method, which can also be applied over large-scale areas at ambient conditions relatively inexpensively (DUNDERDALE et al., 2014; TERCJAK et al., 2016). Thus, we fabricated CNC/HOBC films by the process illustrated in (Figure 17). The CNC film was used as support for the HOBC coating. CNC film surface were painted with HOBC solution (3 wt % in chloroform) in order to get NLC coated CNC film.

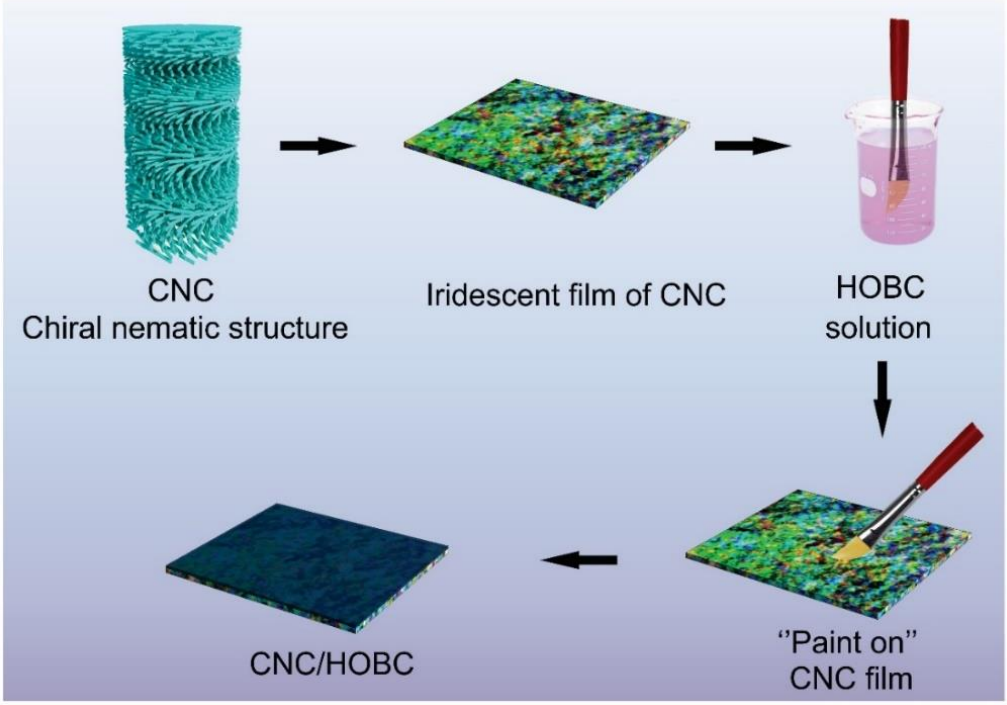


Figure 17. Schematic diagram of the preparation method of the CNC/HOBC.

3.2.4. Characterization of CNC and CNC/HOBC films.

Thermal characterization.

The thermal behavior of HOBC liquid crystal was analyzed on a Mettler Toledo DSC 822 differential scanning calorimeter equipped with a Sample Robot TSO 801 RO. Nitrogen was used as purge gas (10 ml min^{-1}). Temperature and enthalpy were calibrated by using an indium standard. Measurements were performed in sealed aluminum pans containing a sample

weight of around 7 mg. The thermal behavior of the HOBC liquid crystal was analyzed from 0 ºC to 150 ºC with scan rate 10 ºC min.

Morfological characterization

Morphological study of designed materials was performed using polarized optical microscopy (POM) and scanning electronic microscopy (SEM). The POM images were taken using an Olympus BX41 microscope, using the polarizers in a crossed arrangement. The SEM images were collected on a Hitachi SU-70 electron microscope. The samples were attached to aluminum stubs using double-sided carbon adhesive tape or carbon glue. The images were taken from the surface and the cross-section areas. All the samples were sputter-coated with carbon with an EMITECH K950X Turbo Evaporator using a single pulse, outgassing time of 30 s and evaporating time of 2 s.

Structural characterization

CNC and CNC/HOBC films were structurally characterized by ATR Fourier transform infrared spectroscopy carried out using a Nicolet Nexus Spectra equipped with a Golden Gate single reflection diamond ATR accessory. The ATR-FTIR spectra of CNC and CNC/HOBC films were taken with a 2 cm^{-1} resolution in a wavenumber range from 4000 to 400 cm^{-1}.

Optical characterization

Emission spectra were recorded at room temperature with a modular double grating excitation spectrofluorimeter with a TRIAX 320 emission monochromator (Fluorolog-3, Horiba Scientific) coupled to a R928 Hamamatsu photomultiplier, using a front face acquisition mode. The excitation source was a 450 W Xe arc lamp. UV-VIS spectroscopy was carried out using a Perkin-Elmer lambda 950 UV/Vis/NIR spectrophotometer and Spectralon integrating sphere (∅= 150 mm). The freestanding films surface was placed perpendicular to the incidence beam and the spectra were acquired as function of the angle ($20^\circ < \theta < 70^\circ$).

The effect of temperature on the properties of the investigated films was verified *in situ* by UV–Vis spectroscopy using a Cary 5000 UV-Vis spectrometer (Varian), in the range of energy from 1500 to 200 nm, coupled to an oven working in the temperature range from 20 to 80°C with the rate 1ºC/min.

Thermo-responsive properties

Thermo-responsive properties of CNC/HOBC film were studied by transmission optical microscopy (TOM) under cross-polarized light carried out using a Nikon Eclipse E600W microscope equipped with a hot stage Mettler FP 82 HT. Samples were exposed to a heating/cooling process from 30 ºC to 70 ºC at 2 ºC min^{-1} and the images were captured in both processes.

Conductive properties

AFM measurement was performed using a Dimension Icon scanning probe microscope equipped with Nanoscope V controller (Bruker). Tapping mode (TM) was employed in air using an integrated tip/cantilever (125 μm in length with ca. 300 kHz resonant frequency). Typical scan rates during recording were 0.9-1.1 line/s using a hybrid scan head with a maximum range of 100 × 100 μm. Electrostatic force microscopy (EFM) was used to study the conductive properties of liquid crystals coated CNC film. Measurements were performed using the same scanning probe microscopy (Nanoscope V, Dimension ICON from Bruker) operating in the Lift-Mode (lift height was ∼120−150 nm) in ambient conditions and equipped with a Pt/Ir coating tip with a resonance frequency around 75 kHz. The secondary imaging mode derived from tapping mode that measures electric field gradient distribution above the sample surface has been detected by applying a voltage to the cantilever tip. Locally charged LC phase domains on the samples surface were qualitatively mapped simultaneously with the height and phase AFM images. Different regions of the samples were scanned to ensure that both morphology and conductive properties of the investigated materials are the representative one.

3.3 Results and discussions

3.3.1- Morphological Characterization.

POM images of CNC film (Figure 18a) show pronounced iridescence under unpolarized room light. The first order Bragg reflection is observed (LAGERWALL et al., 2014). In selected regions of the sample, fingerprint lines, characteristic of chiral nematic regions viewed orthogonal to the chiral nematic axis, are in focus (Figure 18b). The images (Figure 18a and b)

display a mosaic of domains with different shapes and colors such as green, blue and orange due to anisotropy of CNC films. Pitch lengths and helicoid tilt axes are different in different regions, reflecting light with much wider bandwidth than single-pitch CNC films (STEINER; VIGNOLINI, 2014). Similarly, POM images of CNC/HOBC composite exhibit iridescence under unpolarized room light (Figure 18c) indicating that the chiral nematic phase was retained after LC coating (Figure 18b). However, the domains with different orientations are not visible. Spherulitic crystallization of HOBC covered surface of CNC film is observed instead (TERCJAK et al., 2008).

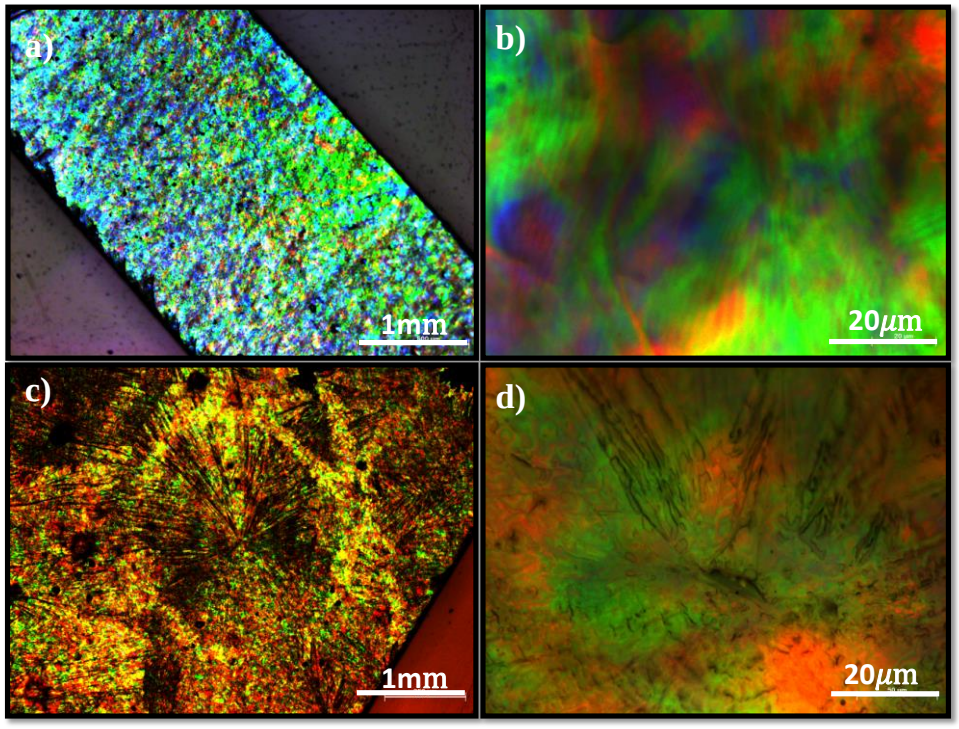


Figure 18. a and b) POM images of iridescent film of CNC showing a fingerprint texture characteristic of chiral nematic ordering; c and d) POM image of CNC/HOBC displays formation of spherulites of HOBC covering a larger area of the CNC surface.

Scanning electron microscopy provided further confirmation of the chiral nematic organization into the CNC films that was preserved after drying (Figure 19). The SEM image of the surface film (Figure 19a) shows aligned cellulose nanocrystals. The edge view of a cracked film (Figure 19b) shows the long-range layered structure with twisted spindle-like features rotated in a counter-clockwise direction, indicating the nanocrystals form a left-handed helicoids (GRAY, 2012). A representative SEM image of a fracture cross-section of the CNC film is shown in figure 19c. The thickness of the film is 40.8 μm. At higher magnification

(Figure 19d) one distinguishes the periodic structure formed by regularly spaced layers achieved due to self-assembly of the nanocrystallites, where each repeating band corresponds to a 180 ° rotation of the chiral nematic director (a half helical pitch) [10,34]. Deeper analysis of Figure 19d, allowed to conclude that the regularly spacing corresponds to a pitch value of 118± 12 nm.

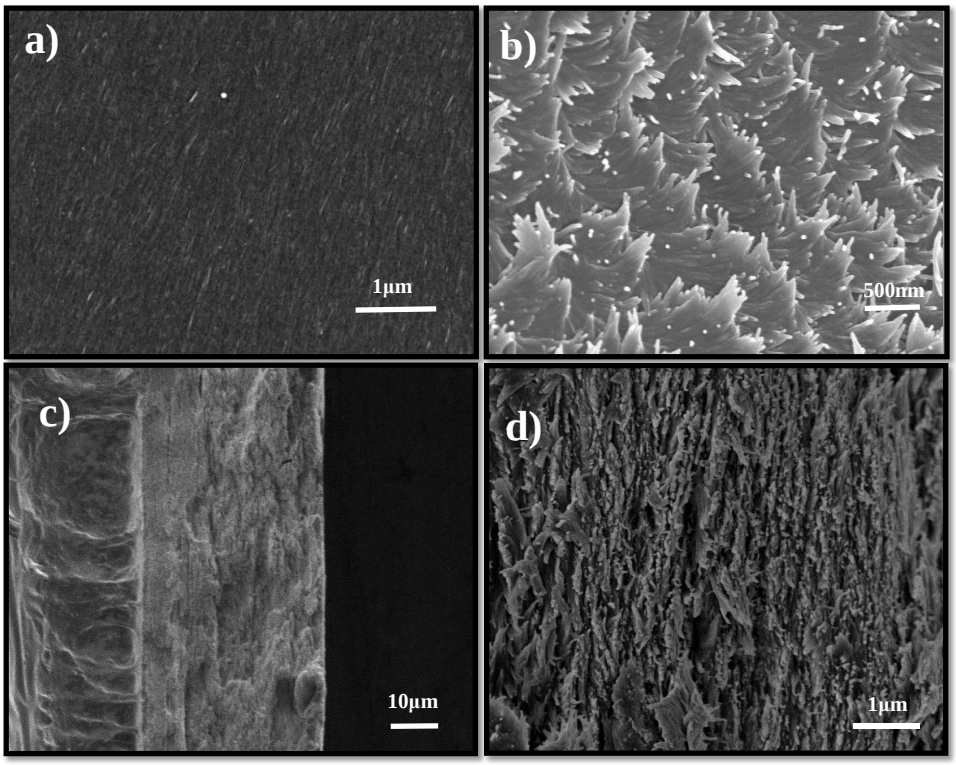


Figure 19. SEM images of CNC film: a) SEM image of film surface formed by aligned nanocrystals cellulose; b) Side view of a cracked film showing the layered structure of the nanocrystals and the rod-like morphology with the rods twisted in a left-handed orientation; c) Image of fracture surface across the CNC film; d) Higher magnification side view of fracture surface across the CNC film shows the stacked layers that result from the helical pitch of the chiral nematic phase.

SEM image of CNC/HOBC film (Figure 20a) shows the NLC coating on the cellulose nanocrystals of the CNC film. The cross-section micrographs are shown in Fig. 19b and d. Thickness was observed to increase from about 40.8 µm for initial CNC film to around 60.2 µm. The increasing thickness can be related not only to coating HOBC liquid crystals, but also to the swelling of the CNC film as result of penetration of part of the HOBC liquid crystals through the multilayered structure of cellulose nanocrystals of CNC film. Interesting enough, the edge micrograph of the cracked film (Figure 20b) and the higher magnification of cross-section show that the chiral nematic phase was retained in the CNC film after NLC coating.

Moreover, the higher magnification image (Figure 20d) exhibits the fingerprint lines throughout their entire thickness. The periodic structure observed in CNC film was preserved and regularly spacing corresponds to a pitch value of 118.14 ± 11.64 nm.

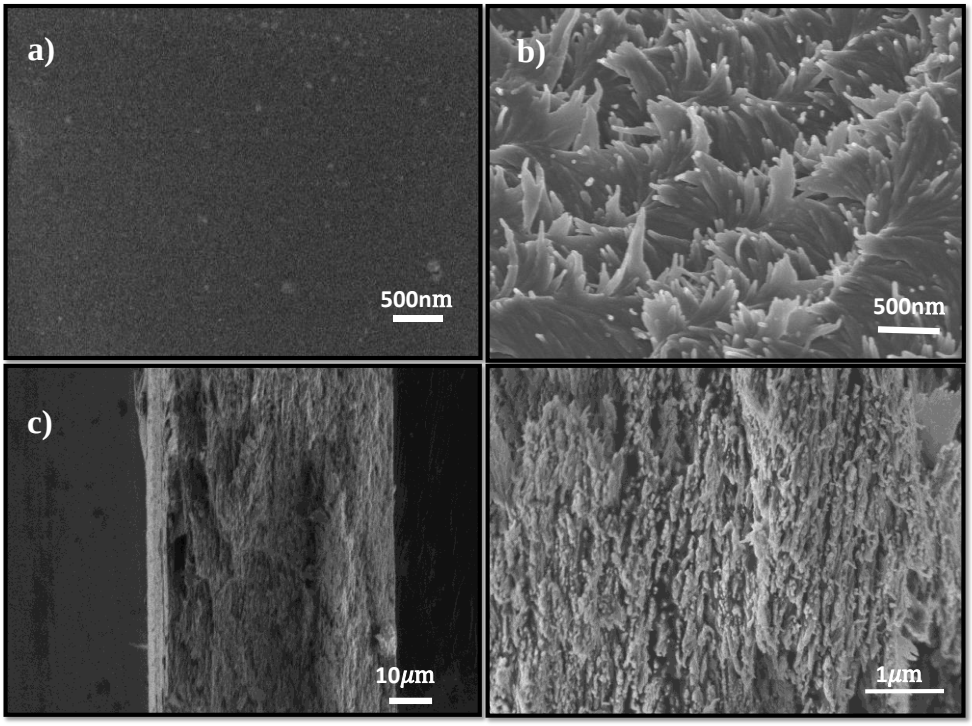


Figure 20. SEM images of CNC/ HOBC composite: a) Image of film surface of CNC covered by the liquid crystal HOBC; b) Side view of a cracked film shows the layered structure of the nanocrystals and the rod-like morphology with the rods twisting in a left-handed orientation; c) Image of cross section of fracture film (thickness 60.2 μm); d) The magnification of the side view of the fractured surface across film, shows the layered structure of the nanocrystals.

3.3.2- Structural Characterization.

Figure 21 shows ATR-FTIR spectra. The spectrum obtained for CNC film showed characteristics bands of cellulose at 3345 cm^{-1} (ν O−H of cellulose type I), 3240 cm^{-1} (hydrogen bond O−H), 2895 cm^{-1} (ν C-H of CH_2 groups), 2854 cm^{-1} (ν_{as} CH_2), 1650 cm^{-1} (bending motion of absorbed water, δ H−O−H), 1426 cm^{-1} (δ_s CH_2), 1365 cm^{-1} (δ C-H), 1160 cm^{-1} (ν_{as} C−O−C), and 1060 cm^{-1} (ν C−O) (BARUD et al., 2008; KONDO; SAWATARI, 1996; OH et al., 2005).

The spectrum obtained for HOBC displayed bands at 1098 cm^{-1} (ν C −O −C group of the ether bond), 1458 cm^{-1} (δ C −H), 1594 cm^{-1} (axial δ of C = C of the aromatic ring), 2355 and 2211cm^{-1} (axial δ of C ≡ N) and 2855 e 2915 cm^{-1} (ν C-H of CH_2 and CH_3 groups).

Spectra obtained for CNC/HOBC composites display bands observed for the two components of the composites. The decreasing relative intensity of the –OH stretching bands relates to the NCL coating on CNC film, as observed by SEM measurements (Figure 20a). Supporting this result the intensity of the ν C-H vibration of CH_2 and CH_3 groups was higher in the spectrum obtained for the composite film. Additional characteristic HOBC peaks are observed at 1458 cm^{-1} (δ C −H), 1594 cm^{-1} (axial δ of C = C of the aromatic ring) and 2211cm^{-1} (axial δ of C ≡ N).

No further new band, relative intensities change or band shift, that could be a signature of chemical interactions between the two counterparts, were observed.

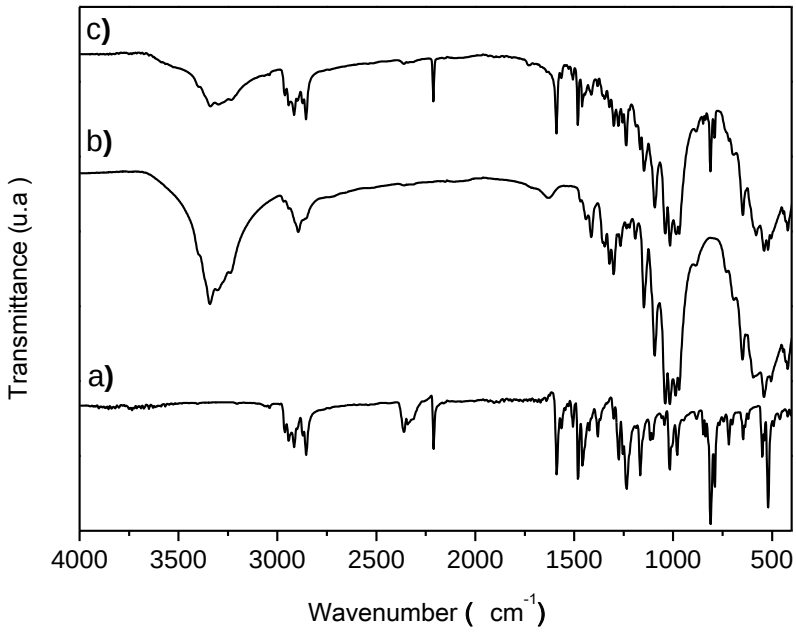


Figure 21. ATR-FTIR spectra: a) HOBC, b) CNC and c) CNC/HOBC.

Nematic HOBC liquid crystals show photoluminescence (PL) properties (TERCJAK et al., 2009). The PL spectra of pristine HOBC and CNC/HOBC composite are shown in Figure 22 The broad emission band observed for CNC/HOBC composite appears almost in the same range as the emission band of the pristine HOBC with the maximum intensity around 345 nm.

These results confirm the effective way of addition of low molecular weight HOBC liquid crystals coating CNC film, with preserved properties.

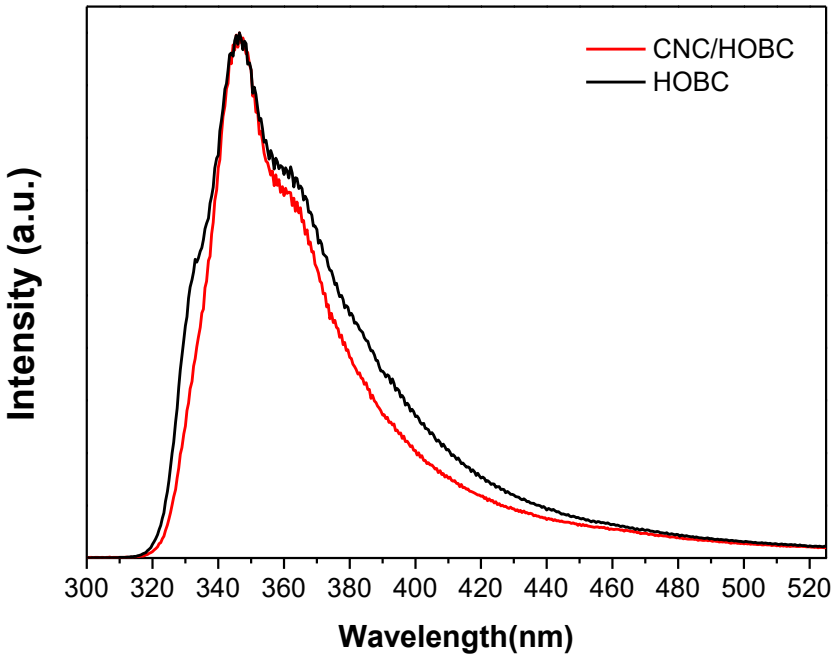


Figure 22. Emission spectra of neat HOBC and CNC/HOBC composite recorded at 298K, under excitation at 280nm.

3.3.3- Optical Characterization.

Figure 23 shows transmission spectra obtained at normal incident angle ($\theta = 0^{\circ}$). Bragg diffraction peaks are observed with a characteristic maximum wavelength (λ_0), in the visible part of the spectra at around 500 nm. Spectra obtained for CNC/HOBC composites show an additional absorption band of the liquid crystal at around 290nm, which refers to molecular electronic transition $\pi \rightarrow \pi^*$ of HOBC molecules.

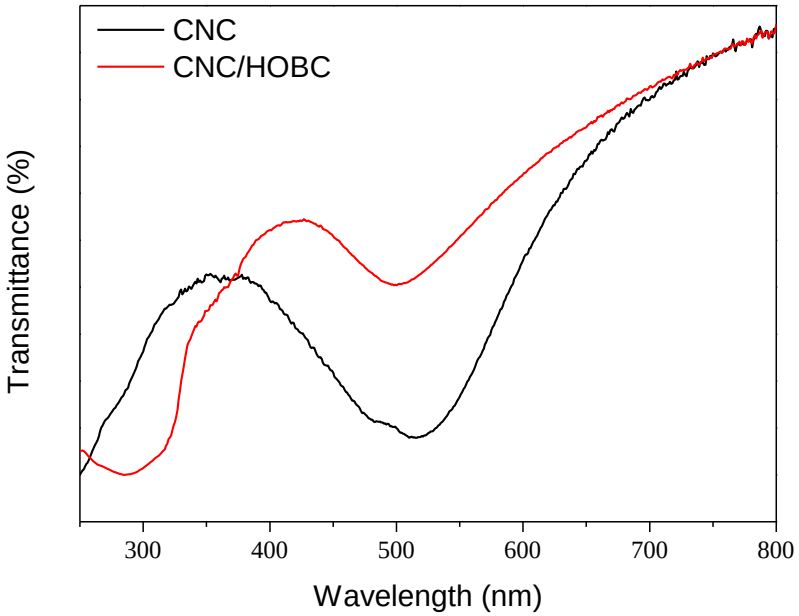


Figure 23. Transmission spectra of the films CNC and CNC/ HOBC

Figure 24a shows reflectance spectra obtained as function of the incident angle (15◦ < θ < 60◦). Bragg diffraction is confirmed by the variation of the peak position as function of incident angle (θ). The peak maximum wavelength (λ_0) obeys the Vries' relationship (Equation 1) where the reflection peak shifts to shorter wavelengths as the viewing angle increases relative to the normal of the film. These results suggest an advantage to employ these materials in optical sensing devices. The angular dependence lead to tunable colors that would be highly advantageous to design an optical sensor with wide detection angles.

$$\lambda_0 = n_{ave} P \cos \Theta \qquad \text{Eq. (1)}$$

(θ) is the incident angle between the surface normal and the incident ray, P is pitch of chiral nematic structure, and n_{ave} is the average refractive indice. Using de Vries equation and λ_0 the pitch of the chiral nematic structure P may be determined as shown in figure 24b. The pitch calculated is 118 ± 4 nm for CNC/HOBC, value comparable to that of pitch obtained from SEM measurements.

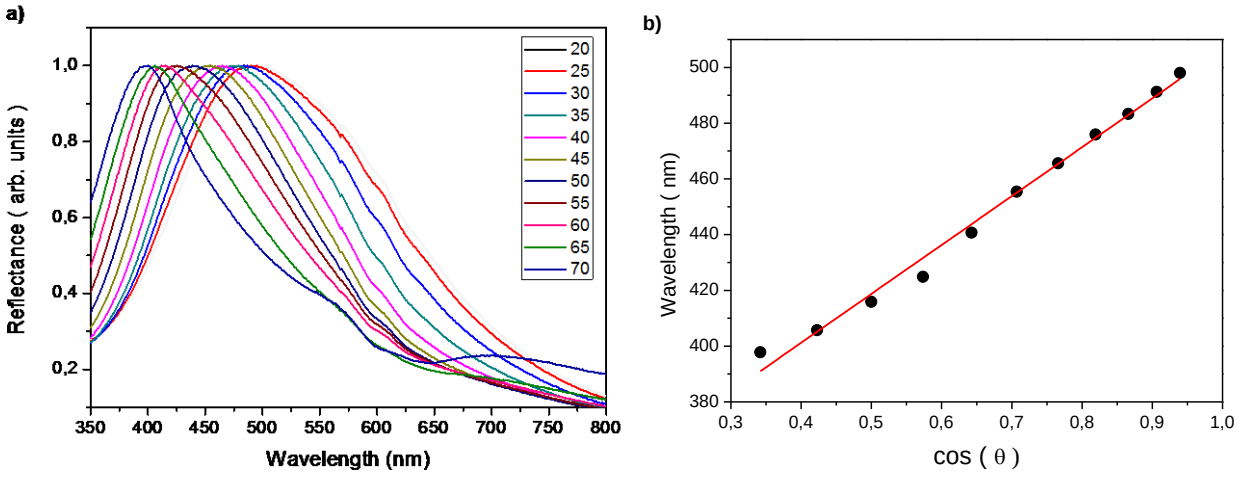


Figure 24. a) Specular reflectance of CNC/HOBC composite between 20 and 70 degree; b) Variation of the peak position of the reflectance spectra as function of the cos θ for CNC/HOBC.

Thermo-optical properties of CNC/HOBC composites were also studied by UV-VIS transmittance spectroscopy as function of the temperature. Figure 25a shows spectra obtained for pristine HOBC deposited on a quartz substrate. The opaque (OFF state) to transparent (ON state) transition is well known to be observed in the 56-60^{o} C range (TERCJAK et al., 2009, 2010; TERCJAK; GARCIA; MONDRAGON, 2008; TERCJAK; GUTIERREZ, 2011). Figure 25b also shows spectra obtained for the composites. The OFF-ON transition is well observed superposed to the band due to the pitch of the liquid crystalline CNC film. Therefore liquid crystalline properties from both NLC coating and CNC film substrate are well preserved in the new materials prepared. In previous work using BC membranes as substrates the NLC properties were also preserved in BC-NLC composites. Interesting enough here we present results where the substrate present LC behavior as well. These new materials present therefore angle dependent reflection and thermal dependent transmission allowing to propose new potential application in sensing.

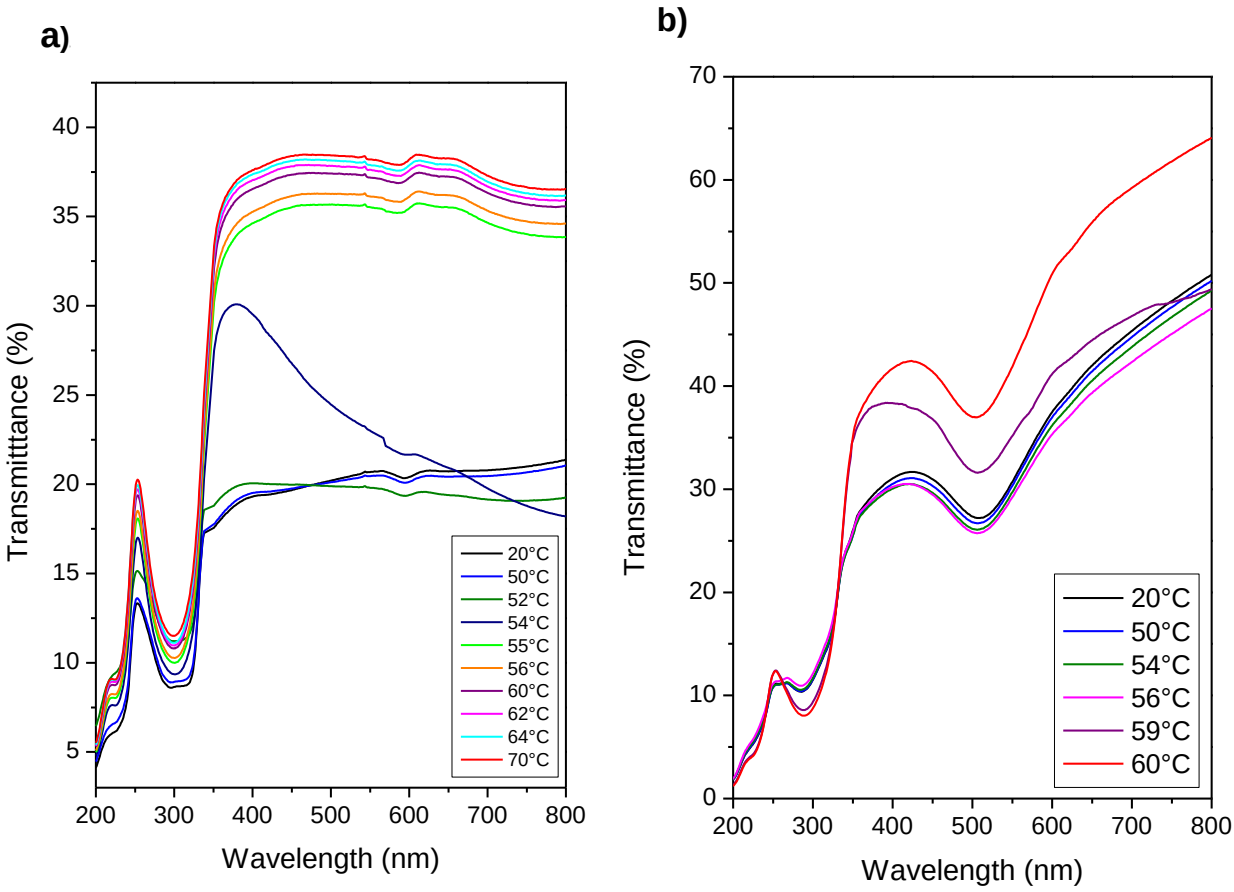


Figure 25. Transmission spectra as function of the temperature: a) HOBC; b) CNC/HOCB.

Thermo-responsive properties of CNC/HOBC composite were also investigated by transmission optical microscopy in heating/cooling processes under cross-polarized light using hot stage mode. Representative TOM micrographs taken during heating and cooling process are shown in figure 26. The melting transition of HOBC phase of CNC/HOBC composite took place at around 47 °C. Similarly, to the thermo-reversible behavior observed by UV-vis measurement, the range of switching between opaque and colorful state during cooling/heating cycle was narrower and switching took place almost in the same temperature in both cooling and heating processes, being at the temperature range 56-60 °C for heating process and 55-60 °C for the cooling process. Thermo-reversible behavior of CNC/HOBC composite confirmed that pristine HOBC transfer their properties to the investigated composite.

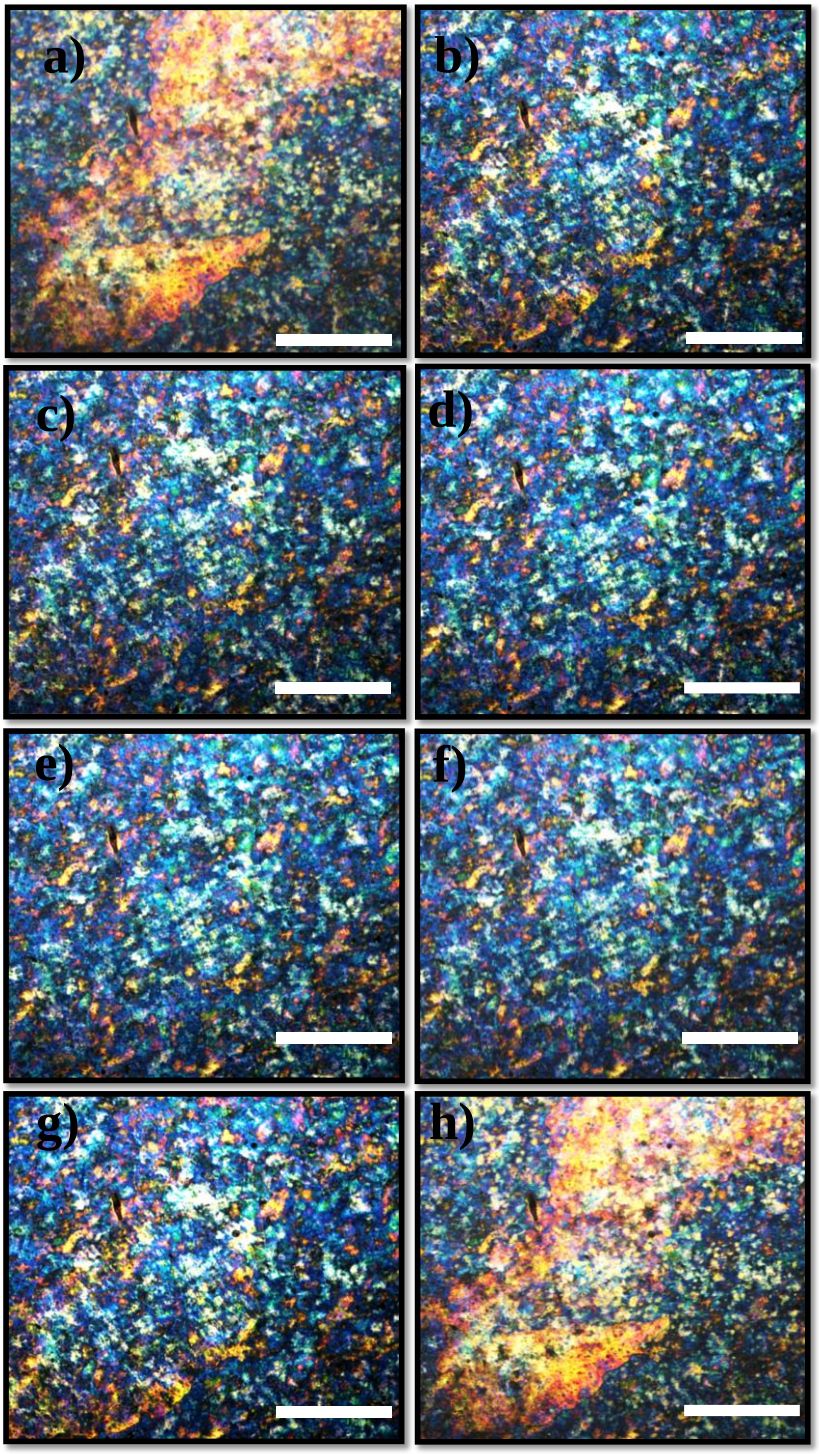


Figure 26. TOM micrographs of CNC/HOBC during heating taken at: (a) 30 ºC (b) 47 °C, (c) 56 °C, (d) 60 °C and during cooling at: (e) 60°C (f) 55°C (g) 45°C (h) 30°C. (scale bar, 200 μm).

TM-AFM height and phase images are shown in figure 27. Results obtained for the CNC film confirmed orientation of nanocrystals as already observed by SEM results. Moreover, using AFM one could easily distinguish individual nanocrystals composing the CNC film. The

regular size of homogeneously distributed nanocrystals was 25± 5 nm in diameter and 200 ± 20 nm in length (Figure 27b). Comparing results obtained for CNC and CNC/HOBC films, it observed liquid crystal coating on cellulose nanocrystals surface lead to smoother surface which confirmed the TM-AFM height images (40 nm for CNC film and 30 nm for HOBC coated CNC film). This behavior was verified with decrease of the average roughness (Ra), extracted from TM-AFM height images, from 5 nm to 4 nm for CNC and CNC/HOBC films, respectively.

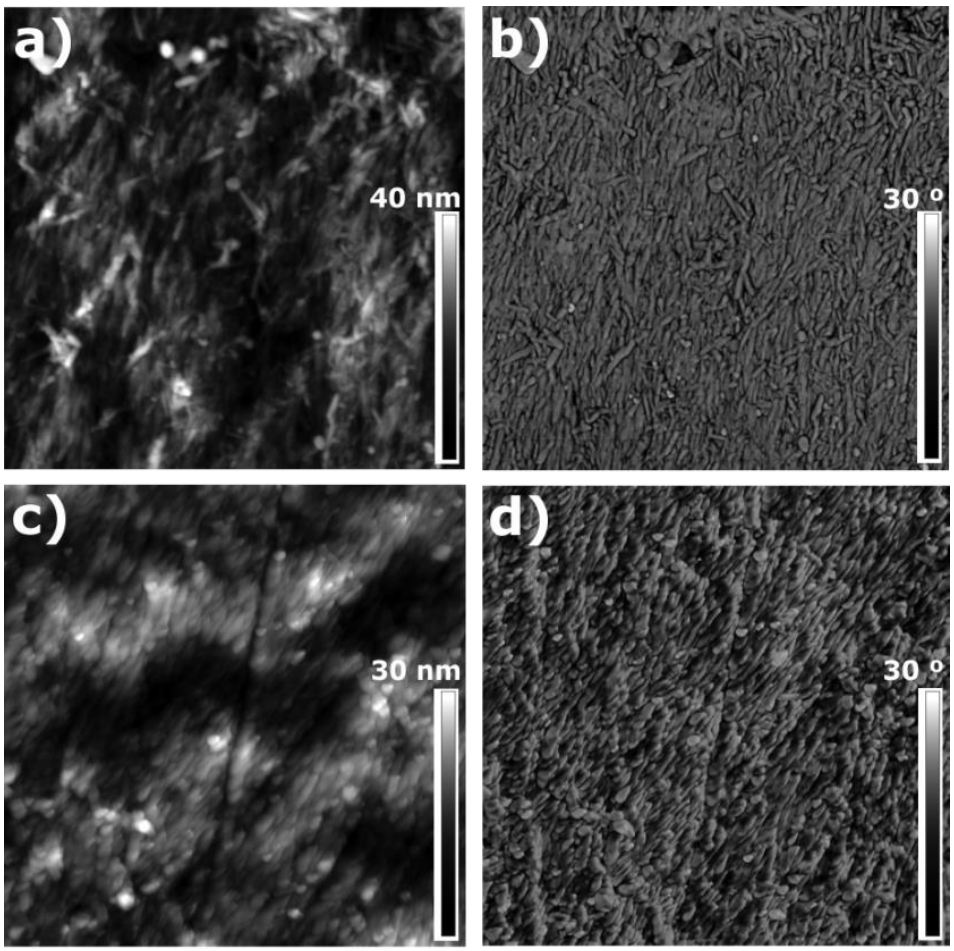


Figure 27. TM-AFM (3μm x 3μm) height (a) and phase (b) images of CNC and TM-AFM height (a) and phase (b) images of CNC/HOBC film.

Electrostatic force microscopy was employed to verify transfer of the conductive response of the HOBC liquid crystal to composites. Figure 28 shows AFM phase and EFM phase images, taken simultaneously, scanned applying 0, 6, -6 V. As expected, any charged domains were detected at the surface of HOBC coated CNC film when 0 V was applied to the

EFM-tip (Figure 28 b). On the contrary, as seen in the figure 28c and d, by applying 6 and -6 V to the EFM-tip allowed to distinguish charged domains confirming that HOBC coated CNC film respond on the applied voltage independently on the sign (positive or negative) of the voltage values. Applying both 6 and -6 V one can easily detect charged domains well distributed on the whole investigated surface mapped with low contrast level of the EFM phase image around 3°. Low contrast ensure weak response on the applied voltage corresponding to electrostatic force between the sample and EFM-tip. Here it should be pointed out that CNC film did not show any charged domains, when 6 and -6 V were applied to the EFM-tip indicating that HOBC liquid crystal transfer its ability to respond on the external stimuli (applied voltage) to the fabricated HOBC coated CNC film**.**

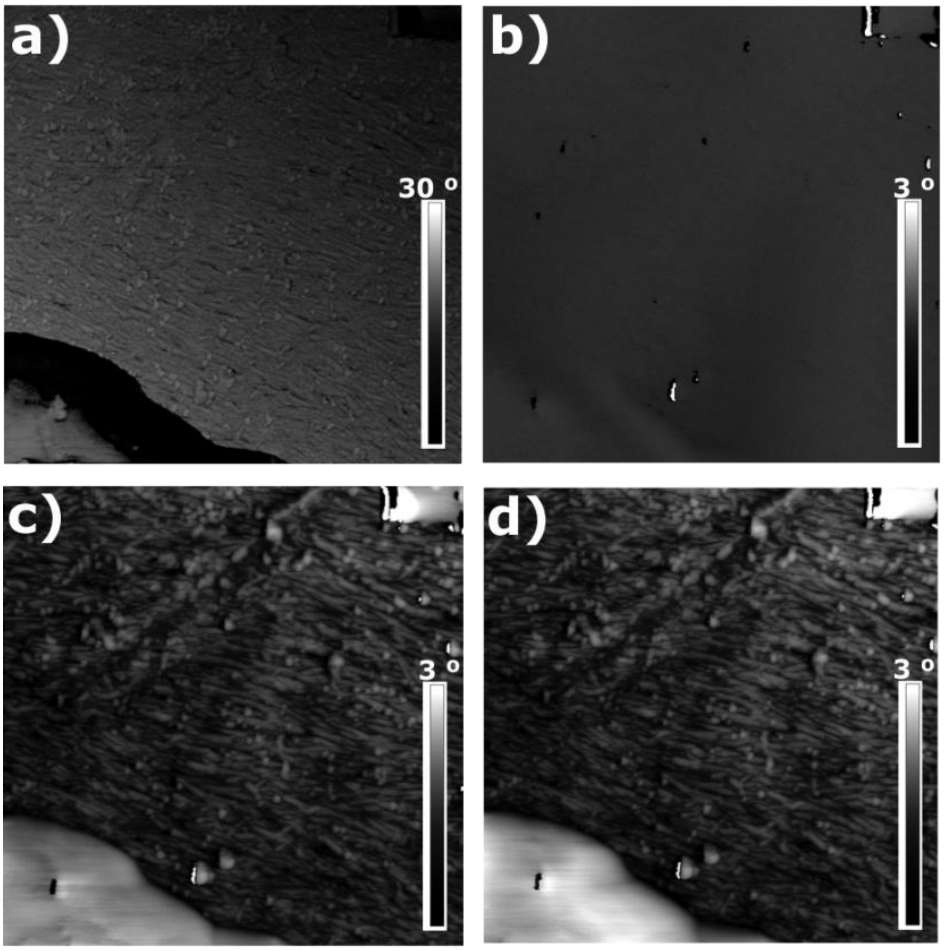


Figure 28. a) AFM phase image (3µm x 3µm) and EFM phase images (3µm x 3µm) of CNC/HOBC film obtained applying b) 0 V, c) 6 V and d) -6 V.

3.4. Conclusions

By using cellulose nanocrystals (CNC) films and 4′-(hexyloxy)-4-biphenylcarbonitrile (HOBC) novel bi-phase multifunctional nematic liquid crystal films were obtained. The new materials integrate iridescence, conductive and thermal response. The designed material was obtained as self-sustainable iridescent film with chiral nematic organization. The cross-section SEM images confirmed that HOBC liquid crystals not only covered surface of CNC films however part of it were presence also in between of multilayered structure of cellulose nanocrystals of CNC film. The thermo-optical property evaluated by UV-VIS transmittance spectroscopy as function of the temperature demonstrated that brush surfaces possess modulated optical properties as response to temperature. Additionally, EFM measurement confirmed conductive response brush surfaces to the voltage applied to the AFM tip. These new materials present therefore angle dependent reflection and thermal/electrical dependent transmission allowing to propose new sensing potential applications.

The composites presented attractive properties to the development in the field of thermo- and electro optical devices, such as smart windows, optical sensors and display devices.

4. Cellulose based photonic materials displaying modulated photoluminescence.

The simultaneous integration of iridescence and light emission in a photonic material is an attractive proposal for the design of novel optical devices. Here we describe the luminescent study of a new optical device that integrates light emission and iridescence through a liquid crystal self-assembly of rhodamine-doped cellulose nanocrystal-template silica approach. These materials were obtained as freestanding composite films with chiral nematic organization. The Scanning Electron Microscopy (SEM) confirms that the CNC film structure comprises multi-domain Bragg reflectors. The optical properties of these films can be tuned through changes in the silica/CNC relative content. Moreover, rhodamine 6G incorporation allows a complementary control of the optical properties. The photonic structure effects on the emission properties were investigated. Overall, such findings demonstrated that the photonic structure plays the role as an inner- filter, causing selective suppression of the light emitted with a detection angle variation. This behavior was found to be dependent on the bandgap position of each photonic structure in these materials.

4.1. Introduction

There is a growing interest on the self-ordering of chiral liquid crystals towards a wide variety of applications. Chiral nematic liquid crystals, which consist on mesogens organized into a long-range helical assembly, exhibit unique properties, such as the angle-dependent selective reflection of circularly polarized light. This reflection results in the observation of iridescence, occurring when the helical pitch is of the order of the wavelength of visible light (DE VRIES, 1951). For this reason, chiral nematic liquid crystals have been studied for their photonic properties and used for applications such as a tunable filters (DRIESEN et al., 2007; PENNINCK et al., 2012), polarizing mirrors (BROER; LUB; MOL, 1995), reflective displays (YANG et al., 1994) and lasers (KOPP et al., 1998).

In the last years, there has been significant interest on the study of cellulose nanocrystals (CNC), fibrils with nanometer dimensions that have high surface area and can behave as lyotropic liquid crystals (EICHHORN, 2011; HABIBI; LUCIA; ROJAS, 2010; KLEMM et al., 2011). Stable suspensions of CNC can be obtained through cellulosic hydrolysis, using sulfuric

acid from different sources of cellulose including plants (BECK-CANDANEDO; ROMAN; GRAY, 2005; HABIBI et al., 2008), bacteria (ROMAN; WINTER, 2004) and tunicates (FAVIER; CHANZY; CAVAILLE, 1995). In addition, above a certain critical value of CNC concentration in aqueous suspension, a chiral nematic ordering occurs. Interestingly, it can be preserved upon slow drying, thereby resulting in iridescent films (REVOL et al., 1992; REVOL; GODBOUT; GRAY, 1998). The self-organization ability of CNC has been particularly exploited in order to produce ordered materials. Under this study context, CNC samples have been employed as a template to control size, structure and organization of inorganic materials (HABIBI, 2014; KELLY et al., 2014; VAN OPDENBOSCH; ZOLLFRANK, 2014).

Chiral nematic liquid crystals CNC suspensions can be cast to produce freestanding inorganic films with chiral nematic structure (SHOPSOWITZ et al., 2010, 2012, 2014). MacLachlan and co-workers showed that the CNC chiral nematic phase can be used in order to prepare silica photonic crystals and organosilica films (SHOPSOWITZ et al., 2010). After the CNC removal, mesoporous solid structures were obtained with high surface area and long helical twist range on the chiral nematic CNC. Both helical pitch and porosity, in these materials, can be tailored by changing the concentration of silica-based sol–gel precursors, allowing tunable photonic structures. In addition, these materials were used to obtain the first luminescent iridescent demonstration integrated into freestanding chiral nematic mesoporous silica-encapsulated CdS quantum dots (QDs) films (NGUYEN; HAMAD; MACLACHLAN, 2014). The authors suggest that such luminescent and mesoporous films could be used in optical sensing to trace detection of explosives, once the CdS quantum dots undergo strong luminescence quenching when exposed to nitroaromatic compounds. However, these new functional materials, which combine luminescence and the chiral nematic order, also promise the development of new optical devices. Recently, the incorporation of rare earth compounds in chiral nematic structures lead to the possibility of circularly polarized excitation and modulating spontaneous emission as exhibited by ZrO_2:Eu^{3+}, Y_2O_3:Eu^{3+} , YVO_4:Eu^{3+} and AuNCs (CHU et al., 2014, 2015; QU et al., 2016; WANG; XU, 2014).

In this work, luminescent iridescent films were prepared by combining tetraethoxysilane (TEOS), a CNC suspension (obtained from bacterial cellulose) and an ethanolic solutions of a broad band emitter (Rhodamine 6G (Rh6G)). The materials were obtained as self-sustainable composite films with chiral nematic organization. Concerning optical properties of the films, these can be tuned through changes in the silica concentration. Herein, we report a study, considering the influence of the films photonic structure on the photoluminescence, regarding the selective reflection of light. Such findings demonstrate that, the simultaneous integration of

light emission and photonic structure, lead to an inner filter effect on these CNC films, causing selective suppression of the light emitted with a variation of the detection angle. This behavior was found to be dependent on the bandgap position of each photonic structure in these materials.

4.2. Materials and methods.

4.2.1-Preparation of bacterial cellulose membranes:

Production of bacterial cellulose inoculum: Firstly, *Gluconacetobacter xylinus* (ATCC 23760), a cellulose producing strain, was used. The André Tosello Foundation, Campinas-SP, Brazil, supplied it. It was cultured in Hestrim-Schramm medium (HS medium), containing D-glucose glycose, yeast extract, peptone, di-sodium hydrogen phosphate (Na_2HPO_4), citric acid, agar and purified water. Analytical grade chemicals were used as received. Before the bacterial strain inoculation, its culture medium was sterilized and then it was cultivated for one day, at 28 ºC inside an air-circulating oven as a conditioning chamber.

Biosynthesis of bacterial cellulose: The bacterial cellulose (BC) culture medium was prepared according to the method previously reported (BARUD et al., 2011; TERCJAK et al., 2015). During such process, 45 mL of culture medium and 5 mL of the inoculum (*Gluconacetobacter xylinus* ATCC 23760) were cultivated for three days in static conditions, at 28 ºC, in a 250 mL Erlenmeyer flask inside an air-circulating oven. Previously, jelly-like BC pellicle was harvested and purified to eliminate the culture medium (to remove cells and other impurities). The purification protocol was accomplished following the pathway published by Tercjak et al. (TERCJAK et al., 2015). Finally, the purified BC pellicle was dried in order to obtain BC film.

4.2.2-Preparation of cellulose nanocrystals (CNC):

5 g of dried bacterial cellulose (BC) membranes were milled using an IKA® A11 basic analytical mill and sieved with a stainless steel sieve (mesh 35). The milled BC was hydrolyzed in 88 mL of a sulfuric acid (Synth 98%) solution, at a 64 wt% concentration, at 50°C for 0.5 h under vigorous stirring. Then, the suspension was diluted (10x) in ultrapure cold water (resistivity 18.2 MΩ.cm at 25 ° C,) stopping the hydrolysis, and allowing it to settle overnight. The clear top layer was decanted and the remaining cloudy layer was centrifuged at 6000 rpm

for 10 min (Jouan C3i - CR3i multifunction centrifuge). The supernatant was decanted and the resulting thick white suspension was washed three times with ultrapure water. The thick white suspension was transferred to a dialysis cellulose membrane sleeve (12000-14000 molecular weight cut-off) and dialyzed in ultrapure water. The membrane sleeve, containing CNC, was placed periodically in ultrapure water, and the procedure was continuous until the water pH became constant (pH = 2.4), over a period of one hour. The suspension was diluted to the intended concentration of 3.0 wt%, and dispersed using an ultrasound homogenizer (Sonics Vibra-Cell VC 505 500W 20 kHz), and a 6 mm diameter probe. Further, 50 mL of a 3.0 wt % CNC suspension was placed in a 100 mL plastic tube and it was sonicated at 60% of maximum power (300 W). In addition, a prolonged sonication (to an energy input over 7500 J/g of CNC) was performed in an ice bath, to prevent desulfation caused by the heating generation during the process.

4.2.3-Preparation of nanocrystalline CNC-silica composite films.

Initially, Tetraethoxysilane (33μL, 66μL, 98μL, 131μL) TEOS, Sigma-Aldrish 98%), was added to a 3.0 wt% aqueous CNC suspension (4 mL, pH 2.4), and the resulting mixture was stirred at room temperature for three hours, aiming the formation of a homogeneous mixture. The solution was transferred to polystyrene Petri dishes (diameter of 45 mm), process which allowed its evaporation at room temperature until self-sustained films were formed, and also yielding CNC/silica composites with chiral nematic organization (Figure 29). Films with distinct relative amounts of TEOS/CNC were prepared, as it follows according to their weight percentage: 0% (CNC), 12.5wt% (CS1), 25.0wt% (CS2), 33.3% (CS3), and 50.0wt% (CS4).

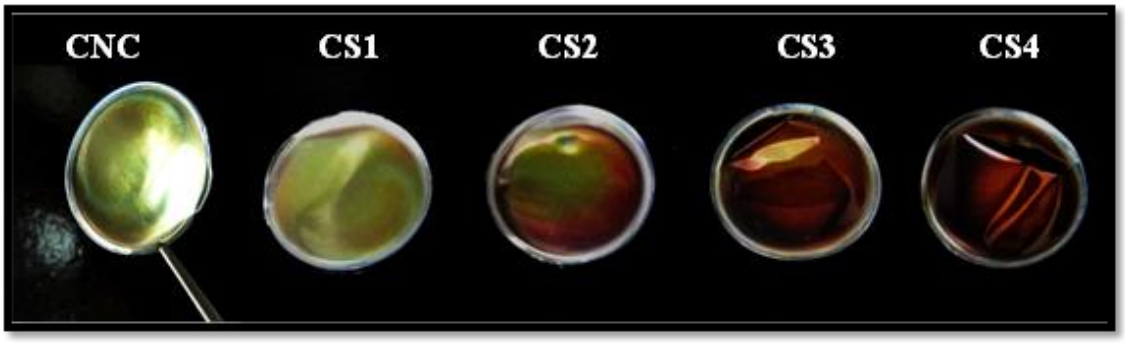


Figure 29. Photograph of CNC/silica composites films with different amount of silica. Viewing is normal to the film surface.

4.2.4- Preparation of nanocrystalline CNC-silica composite doped with broad band emitters (Rhodamine 6G (Rh6G)):

200 μL of 10^{-4} M ethanolic solution of Rhodamine 6G (Rh6G) (Sigma-Aldrich, 99%) were added to the homogeneous mixture containing CNC and TEOS. Mixtures were transferred to polystyrene Petri dishes (diameter 45 mm), allowing its evaporation at room temperature until self-sustained films were formed. The obtained composite films can be seen in the figure 30. Samples were designated CNC-Rh, CS1-Rh, CS2-Rh, CS3-Rh and CS4-Rh.

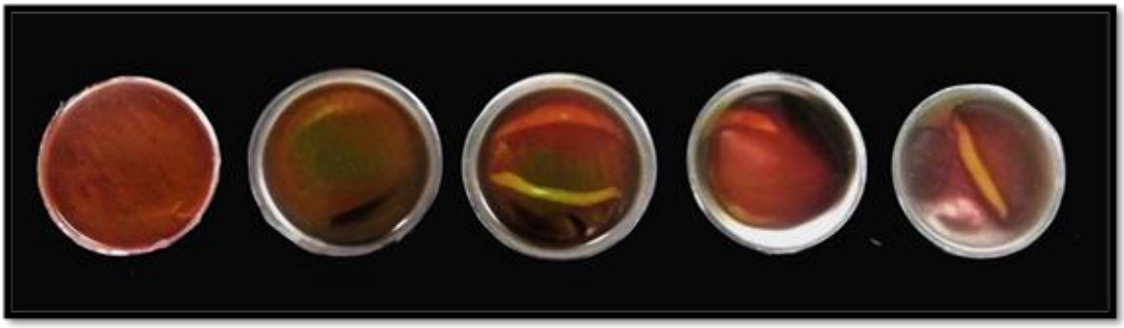


Figure 30. Photograph of CNC/silica doped with Rh6G composites films with different amount of silica. Viewing is normal to the film surface.

4.2.5. Characterization of CNC and composite films.

Thermogravimetric analysis (TGA) was performed using a Shimadzu TGA-50 system from 25 to 800 °C at a heating rate of 10 °C min^{-1}, under a static atmosphere of air.

Polarized optical microscopy images were obtained with an Olympus BX41 microscope, using crossed polarizers.

Scanning Electronic Microscopy (SEM) images were collected on a Hitachi SU-70 electron microscope. The samples were attached to aluminum stubs using double-sided carbon adhesive tape or carbon glue. Pictures were obtained from the surface and cross-section areas. All the samples were sputter-coated with carbon through an EMITECH K950X Turbo Evaporator, at a single pulse, on an outgassing time of 30 seconds and evaporating time of 2 seconds.

UV-VIS reflectance spectroscopy was carried out using a Perkin-Elmer lambda 950 UV/Vis/NIR spectrophotometer and a Spectralon integrating sphere (∅ = 150 mm). The

freestanding films surface was placed perpendicularly to the incident beam and the spectra were acquired as functions on the angle (15◦ < θ < 60◦), stepped by 5º as illustrated in (Figure 31).

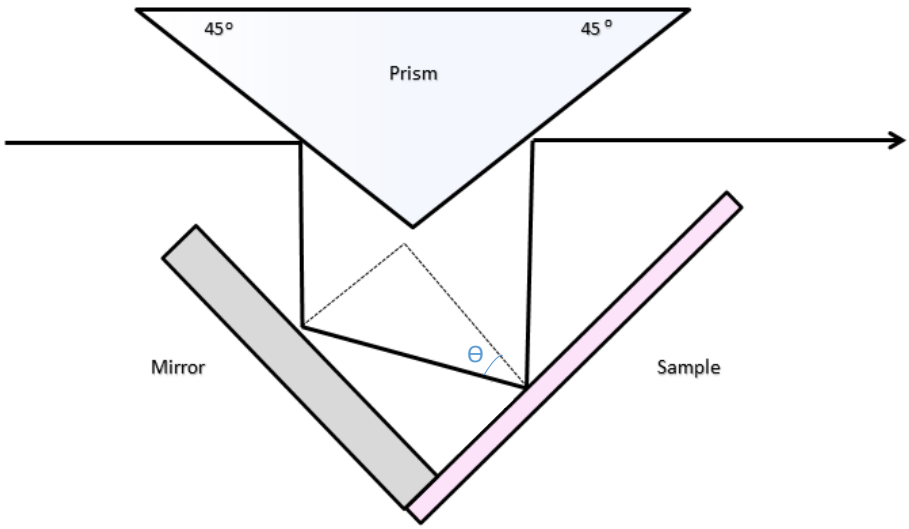


Figure 31. Specular reflectance scheme.

2.6. Photoluminescence.

Spectra were recorded at room temperature with a modular double grating excitation spectrofluorimeter through a TRIAX 320 emission monochromator (Fluorolog-3, Horiba Scientific), coupled to a R928 Hamamatsu photomultiplier, using the front face acquisition mode. To accomplish so, the excitation source was a 450 W Xe arc lamp.The emission spectra were corrected for detection and optical spectral response of the spectrofluorimeter and the excitation spectra were corrected for the spectral distribution of the lamp intensity using a photodiode reference detector. The room temperature time-resolved spectroscopy data was recorded by a Fluorolog time-correlated single photon, considering the (TCSPC) spectrofluorometer (Horiba Scientific) coupled to a TBX-04 photomultiplier tube module (950 V), 200 ns time-to-amplitude converter and 95 ns delay. Its excitation source was provided by a Horiba Jobin Yvon pulsed diode (NanoLED-330, peak at 321 nm, 1.2 ns pulse duration, 1 MHz repetition rate, and 150 ns synchronization delay). The quantum yield values on its emission were measured at room temperature using the C9920–02 system from the Hamamatsu with a 150W Xenon lamp coupled to a monochromator aiming wavelength discrimination, an integrating sphere as sample chamber, and a multi-channel analyzer for signal detection. Three

measurements were made for each sample, and the obtained average values were reported. The method has a precision of 10%.

The photoluminescence spectra as a function of the angle (- 90◦ < θ < 90◦) were recorded at room temperature through a modular experimental setup, as illustrated in figure 32. The modular experimental setup consists of an Ocean Optics HR2000+ES USB spectrometer; and a jacketed optical fiber (Ocean Optics) QP600-UV-Vis (core diameter of 600μm; total length of 1m) in order to collect the luminescence emission. As well as a 5mW diode laser at 405nm (CW mode, FWHM 4nm), aiming excitation of Rh6G molecules, in which the laser beam is directed to an angle of 45ºC regarding the detection plane, and the optical fiber tip is aligned perpendicularly to the sample surface. At last, there is a rotatory base with a goniometer, in which the sample holder is fixed at the center of the rotatory base and the fiber tip collects the emitted signal, allowing free rotation around it.

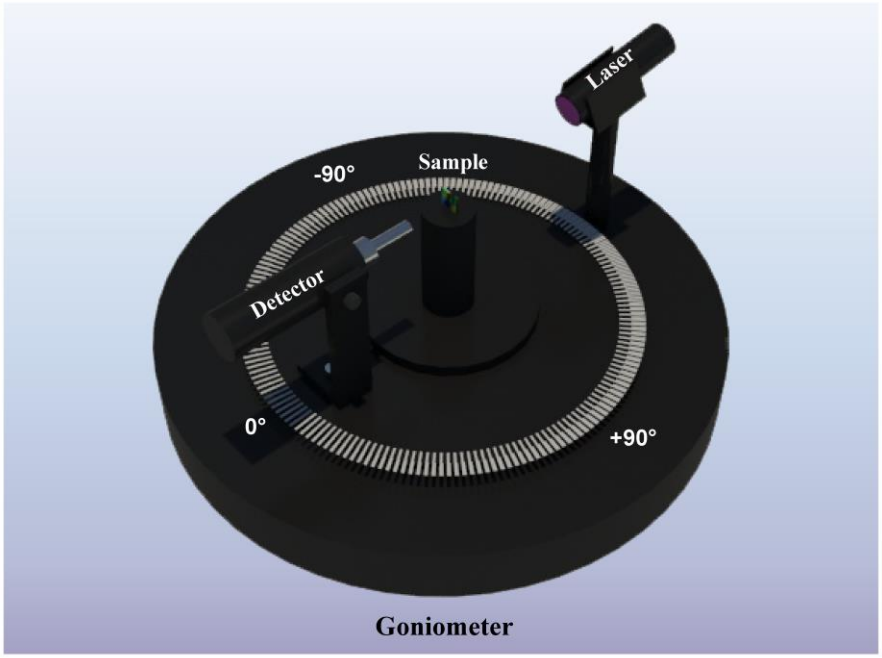


Figure 32. The modular experimental setup to measurements of photoluminescence spectra as function of the angle (-90° < θ < 90°).

4.2- Results and discussions

Composite materials were obtained with compositions (0%, 8.5%, 15.4%, 20.7% and 35.2% wt% of silica as obtained from thermal gravimetric analysis) (Figure 33). The chiral

nematic phase was retained in composites films after controlled drying. Films displayed strong iridescence under the unpolarized room light (Figure 34). Varying the silica/CNC proportion in the preparations allows a control on the optical properties of the composites. Polarized optical microscopy (POM) images of the composites show a red shift on their color with the increase in silica relative content, while the overall texture remained essentially unchanged. Fingerprint lines, characteristic of chiral nematic regions, were observed orthogonally to the chiral nematic axis. The shortest distance between lines equals P/2, where P is the chiral nematic pitch. Figure 34 shows that P/2 values range from 2 to 3 μm.

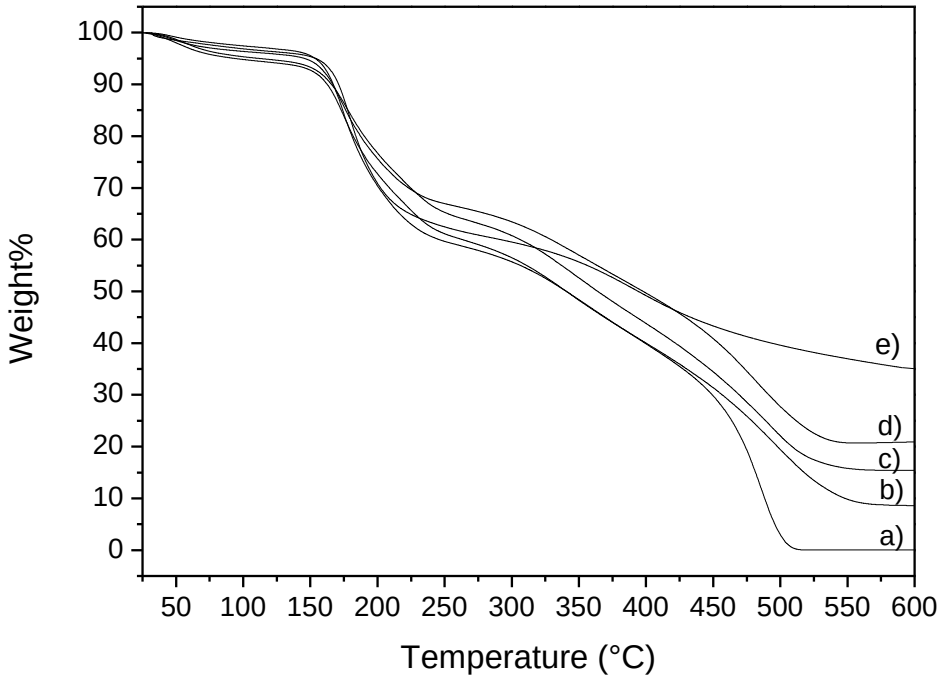


Figure 33. TG curves of composite films) CNC-Rh; b) CS1-Rh; c) CS2-Rh; d) CS3-CS4-Rh.

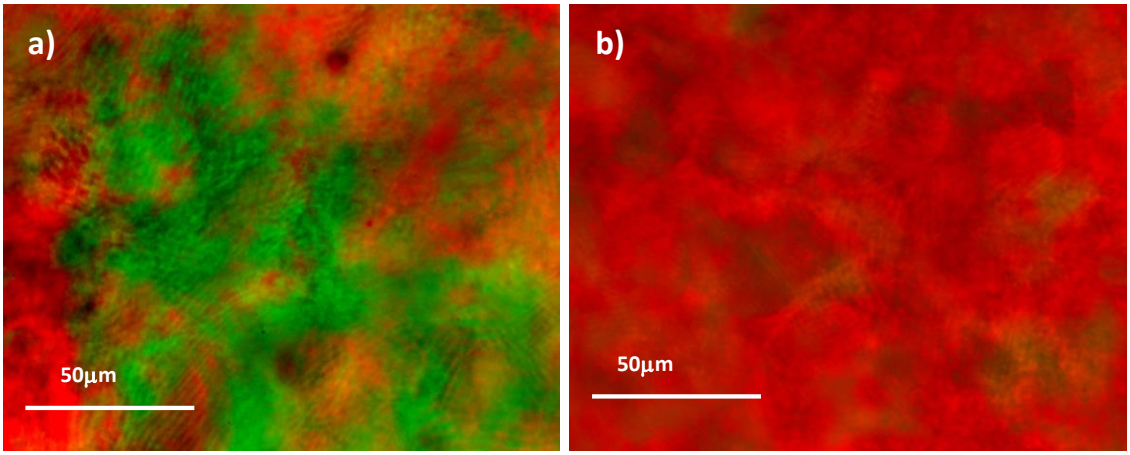


Figure 34. Polarized optical microscopy (POM) images with crossed polarizers: a) CS1-Rh and b) CS4-Rh.

Scanning Electron Microscopy (SEM) provided further confirmation about the chiral nematic organization preserved during silica and Rh6g incorporation. The oblique sectional view of the cracked film edge (Fig. 35b), shows a long-range layered structure with twisted spindle-like features rotated in a counter-clockwise direction, which indicates the nanocrystals form as left-handed helicoids. The interpretation of the fan-like texture observed by SEM on a fractured surface is thus aligned to a normal chiral nematic helicoidal arrangement (GRAY, 2012). The SEM image of a fractured cross-section of the film is presented in (Fig. 35c). The chiral nematic axis orientation is observed at the same position, but in this case perpendicularly to the film surface. Such image also reveals the regular spaced layers that are formed through the self-assembly of nanocrystallites. The periodic structure is present throughout their entire thickness, in which each repeating band corresponds to a 180° rotation of the chiral nematic director (a half helical pitch). The periodic fingerprint lines have been widely observed in chiral nematic liquid crystals (ARRIGHI et al., 2002). Recently, Andrews and co-workers demonstrated a proper correlation between the periodicity of the structure observed in SEM images on vertical sections and the value of half the pitch on cellulose nanocrystals films (ZHANG et al., 2013b).

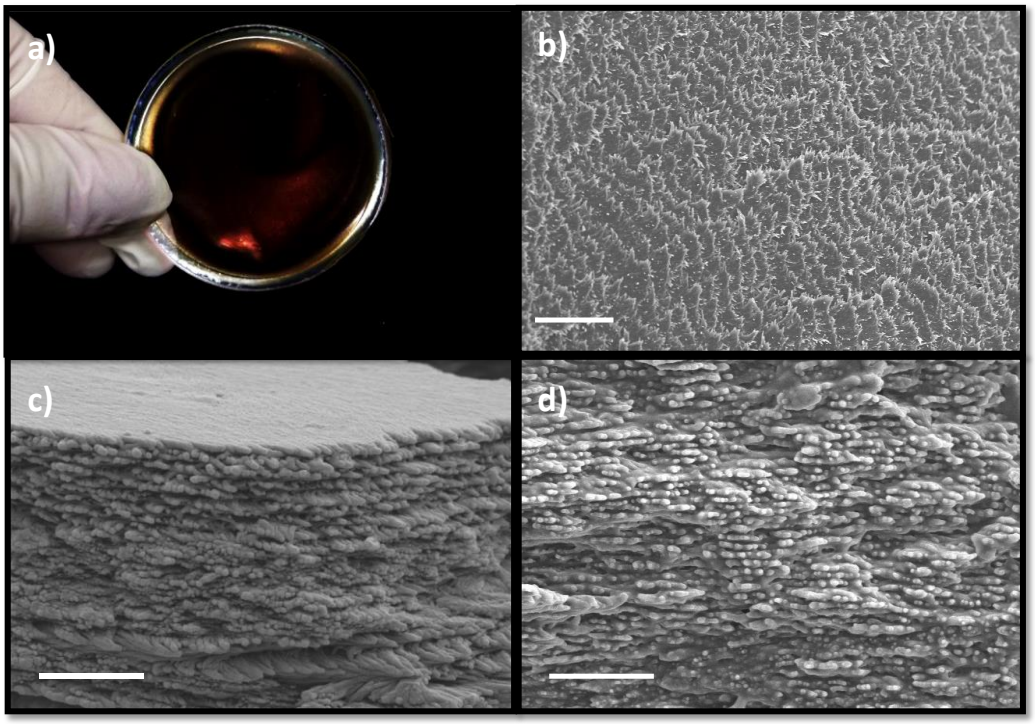


Figure 35. a) Photograph of composite CS4-Rh; b) oblique sectional view of a fracture surface across of composite CS4-Rh; c) and d) SEM images of its cross –section of CS4-Rh.

Optical characterization of films has been performed for transmittance and reflectance modes, as shown in figures 36 and 37. Transmission spectra were obtained at normal incident angle ($\theta = 0°$). Bragg diffraction peaks were observed in the visible part of the spectra between 550-700nm. Spectra obtained for dye-doped CNC/silica composites showed an additional absorption band at around 530nm, which refers to the absorption of Rh6G molecules (MARTNEZ et al., 2005). Concerning the CNC-Rh composite, the band due to the absorption of Rh6G molecules was observed at around 540nm. These results are consistent with the dimers fluorescent (J-type) formation, due to the aggregation of Rh6G molecules when encapsulated into solid composite films. Indeed, the adsorption spectrum on the aggregate shift to lower energies with the increase in dye concentration (LOFAJ; VALENT; BUJDAK, 2013). The addition of silica in the composites, reduced the aggregation of dye molecules.

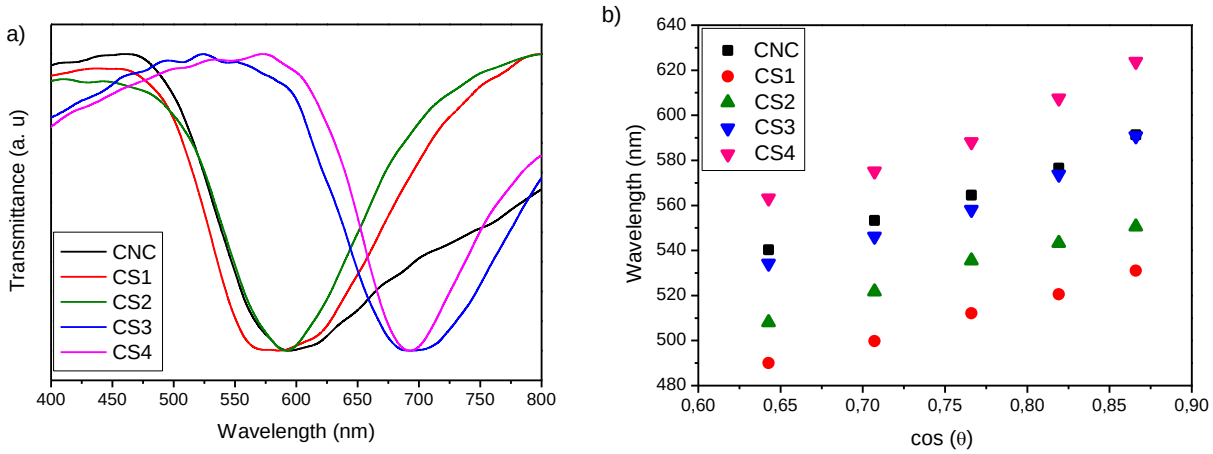


Figure 36. a) Transmission spectra of CNC, CS1, CS2, CS3 and CS4; b) Variation of the peak position of the reflectance spectra as function of the cos θ for CNC/silica composites.

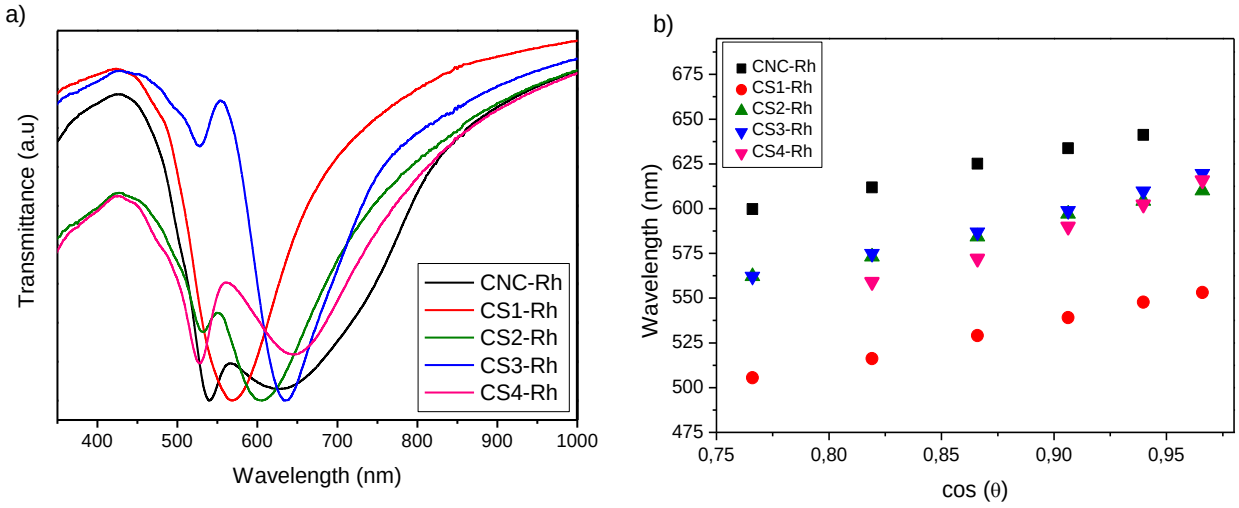


Figure 37. a) Transmission spectra of CNC, CS1-Rh, CS2-Rh, CS3-Rh and CS4-Rh; b) Variation of the peak position of the reflectance spectra as function of the cos θ for CNC/silica composites doped with Rh6G.

Reflectance spectra were obtained as a function of the incident angle ($15^\circ < \theta < 60^\circ$) (Figure 37). Figure 36b and figure 37b display the variation on the band position of the reflectance spectra as a function of the cos θ. The composite spectra show that there is Bragg diffraction presenting a characteristic maximum wavelength (λ_0), which obeys the Vries' equation (Equation 1). In such case, the reflection peak shifts to shorter wavelengths as the viewing angle increases relatively to normal on the film.

$$\lambda_0 = n_{ave} P \cos \Theta \qquad \text{Eq.1}$$

where, θ is the incident angle between the normal surface of the sample and the incident ray, P is the pitch of chiral nematic structure, and n_{ave} is the average refractive index.

The specular reflectance spectra of the CS4-Rh composite (Figure 38b), shows at 50° a valley centered at 528nm due to the re-absorption process, *i.e.* part of the reflected light is absorbed by the dye molecules. A similar behavior was observed for every sample containing Rh6G, even in luminescence measurements, as discussed in what follows.

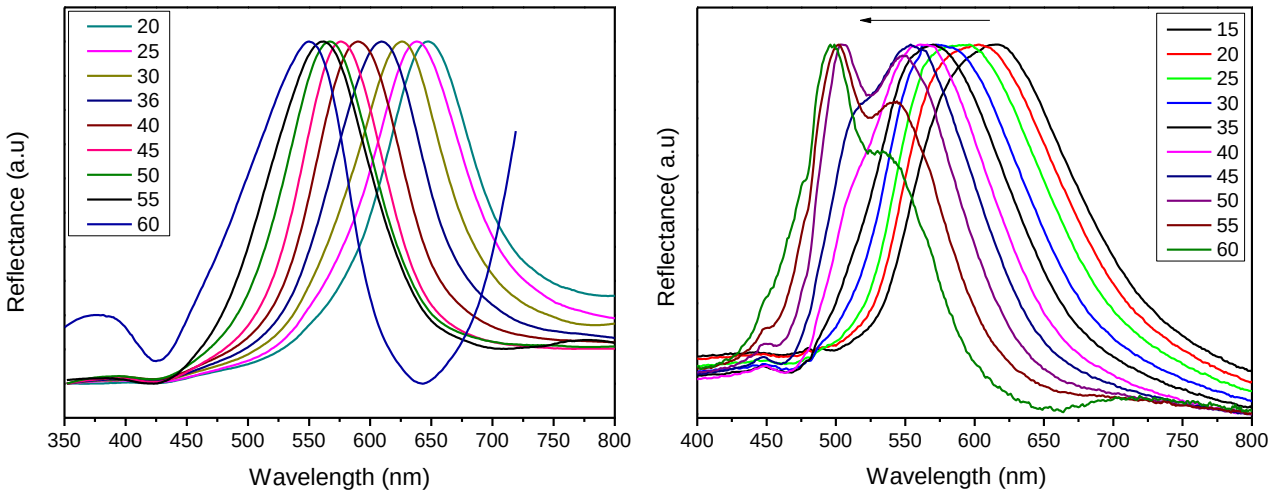


Figure 38. Figure S3. a) Specular reflectance of CS4 between 20 and 60 degree, b) Specular reflectance of CS4-Rh between 15 and 60 degree.

Using the Vries equation, λ_0 may be calculated by using the P value obtained from the chiral nematic structure. These values were calculated and determined from cross section SEM images of the composites as well (Table 2). P values depend on the relative amount of silica and at least two groups with similar values of P may be identified for lower and higher silica content (Figure 39). The P value obtained for CNC is larger than the values observed for samples with lower silica proportion. These results indicate that changes in P are caused by larger silica thickness at the nanocrystals walls, as well as through ionic interactions between negatively charged silica species and crystalline cellulose. This interpretation become clear in the transmittance spectra of CNC/silica composites, where the addition of silica caused band narrowing in the transmittance band (Fig. 36a), which demonstrates that the silica presence implies in the improvement of the chiral nematic organization. The same behavior was observed

on composites containing Rh6G, although the presence of Rh6g contributes to increase on P values compared to composites spectrum without dye. There is therefore a complementary control of optical properties of the composites.

Table 2. Variation of the helicoidal pitch of composites films.

Samples	**P – Specular reflectance (nm)**	**P/2– SEM (nm)**
CNC	143 ± 4	-
CS1	122 ± 6	-
CS2	119 ± 3	-
CS3	168 ± 5	-
CS4	190 ± 8	-
CNC-Rh	141 ±5	78 ± 1
CS1-Rg	138 ± 7	82 ± 2
CS2-Rh	140 ±5	81 ± 5
CS3-Rh	191 ±7	96 ± 7
CS4-Rh	240 ±10	116 ±3

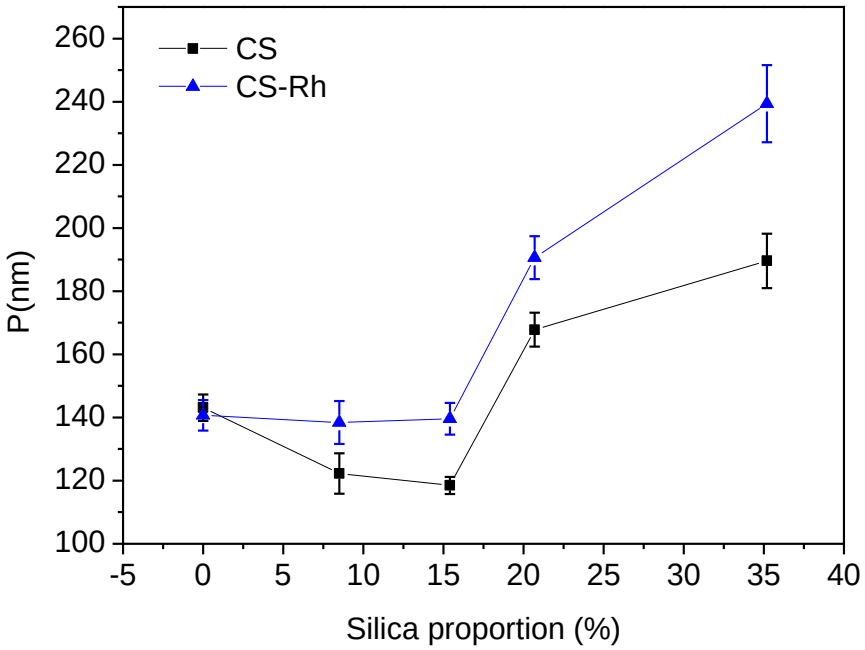


Figure 39. Variation of the P of chiral nematic structure of composites with different silica proportion.

According to the analysis performed on results presented in figure 35d, there is a regular spacing corresponding to the P/2 value of 116 ± 3nm for the CS4-Rh composite. This value is comparable to the one obtained for P, which can be calculated using the De Vries equation, that is 240 ±10 nm. However, the texture is rich in parallel lines, with a distance about 2-3 μm, suggesting the presence of P one order of magnitude larger than the Bragg reflection of visible light. Such intriguing superposed phenomena and apparent contradictions were discussed recently by Lagerwall and collaborators (LAGERWALL et al., 2014). They proposed an explanation to the observation discussed above, taking into account the possible non uniform drying at the surface and at the core. During drying process the CNC concentration increases rapidly at the surface as the water evaporates leading to the helix development on the film plane, with P in the range of order of microns. Nevertheless, in the core, the sample is still in a liquid crystalline state and the diffusion slows dramatically because the surface regime has been solidified. Hence, the increase in core concentration is much slower than at the surface. In the core, the CNC concentration could increase further, yielding a sufficiently short pitch to produce a photonic bandgap in the visible wavelength range, as it was observed in the composite films.

Photoluminescence properties of CNC/silica doped with Rh6G composites films were also investigated. The emission spectra of dye doped CNC/silica composites are reported in figure 40. When excitation is set at 348 nm, two emission bands can be observed: the first one peaked at about 430 nm due to the emission of cellulose nanocrystals (LI et al., 2009), confirmed through the spectrum emission of pure CNC excited at 345nm (Figure 41). The second band is characteristic of rhodamine 6G.

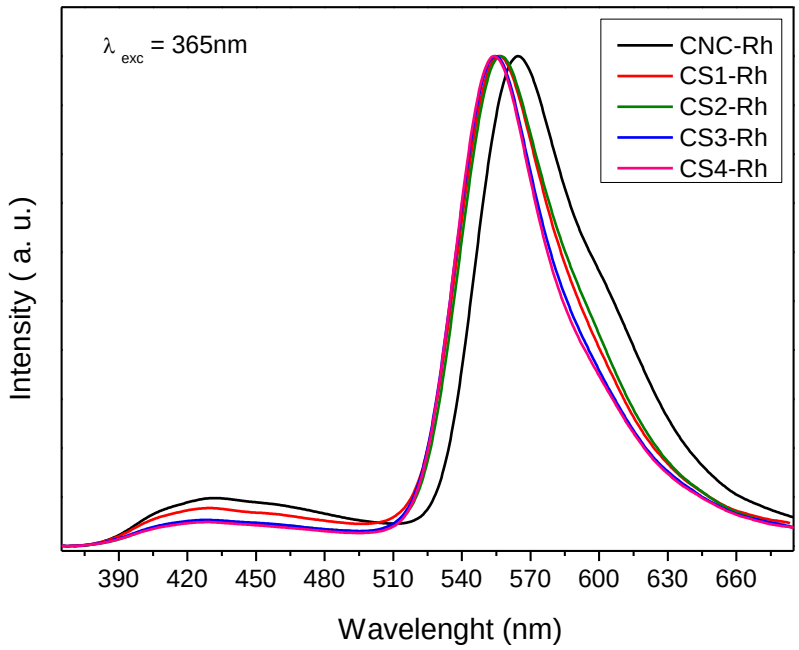


Figure 40. Emission spectra of composite CNC/silica doped with Rh6G in front face acquisition mode excited at 348nm.

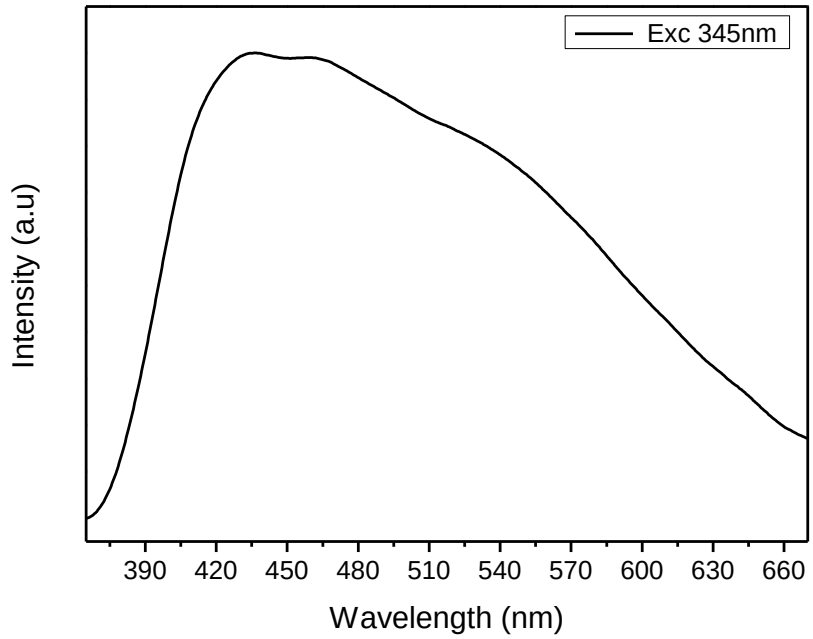


Figure 41. Emission spectra of CNC film in front face acquisition mode excited at 345nm.

The photoluminescence response was observed to be dependent on the relative dye content (ANEDDA et al., 2005, 2007; BUJDÁK, 2006; CARBONARO et al., 2009). Concerning low contents, R6G monomer properties could be observed, with an emission band centered at about 550 nm (ANEDDA et al., 2005, 2007; BUJDÁK, 2006; CARBONARO et al., 2009). The emission spectra of dye doped CNC/silica composites (Figure 40), display a band centered at about 556 nm, and a shoulder above 605 nm. Besides, the emission spectrum of samples not containing silica (CNC-Rh) showed a band centered at about 565 nm, and a shoulder above 610 nm. Bathochromic spectral shift related to the monomer can be attributed to formation of fluorescent dimers (J-type). Usually, at relatively high concentrations of Rh6G, fluorescent (J-type) and non-fluorescent (H-type) dimers are formed (BUJDÁK, 2006). In addition, the dye aggregation causes concentration quenching of dye luminescence (MARTNEZ et al., 2005). The J-type dimers emission is red shifted in relation to the monomer emission and the total emission spectra showed an overlap with emission spectra from two molecular species. These results can also be attributed to changes in the chemical properties on their surroundings and to the loading decrease of Rh6g, as silica was added to the composites, which was observed in the transmittance spectra.

Table 3 shows decay time and quantum yield values for CNC, CNC-Rh and CS-Rh samples. Concerning the emission attributed to cellulose nanocrystals, a decay time value of 6.83 ± 0.05 ns is observed. For the composite films, an increase is observed for decay time values with the addition of silica. This increase must be related to the silica emission contribution at the same wavelength range (BARUD et al., 2008). Concerning rhodamine emission, the values obtained are in agreement with the literature (ANEDDA et al., 2005). The decay time obtained for the composite with higher silica content (CS4-Rh), with emission monitored at 556 nm, is 4.23 ± 0.01 ns. The estimated quantum yield is 0.5. The values obtained for the sample not containing silica (CNC-Rh), emission monitored at 567 nm, are 3.74 ± 0.02 ns for the decay time and 0.15 for the quantum yield. As already mentioned the addition of silica implies in the reduction on the total amount of Rh6G molecules dimers, once part of the molecules migrates to SiO_2 phase, leading to a dilution effect.

Table 3. Decay time values (λ_{EXC}= 330nm): CNC (λ_{EM}= 480nm) (τ_1); Dye-doped CNC/silica composites, λ_{EM}= 400nm (τ_1) and λ_{EM}= 560 nm (τ_2). Quantum yield values: CNC-Rh, λ_{EXC}= 528nm and λ_{EM}= 567nm; Dye-doped CNC/silica composites, λ_{EXC}= 528nm and λ_{EM}= 556nm.

Sample	**τ_1 (ns)**	**τ_2 (ns)**	**ϕ**
CNC	6,83	-	-
CNC-Rh	7,62	3,74 ±	0,15 ± 0,1
CS1-Rh	9,47	3,88 ±	0,40 ± 0,1
CS2-Rh	10,81	4,21 ±	0,50 ± 0,1
CS3-Rh	12,76	4,44 ±	0,65 ± 0,1
CS4-Rh	12,03	4,23 ±	0,50 ± 0,1

Photoluminescence measurements were performed as function of the detection angle ($-90^o < \theta < 90^o$). Figure 42a-b shows emission spectra obtained of the sample CS4-Rh. The bandwidth was observed to decrease with a simultaneous red shift for the maximum wavelength (λ_0) in the angle range between 40° to 90° and -40° to 90°. Figure 42b shows the variation of λ_0 and the bandwidth with detecting angle (Figure 42c). These pronounced effects of the liquid crystal structure on emission characteristics indicated potential photonic applications for these new materials. Results obtained for a Rhodamine doped cellulose membrane are also shown in

order to make clear that the photonic effects are unique to the liquid crystalline samples (Figure 42d).

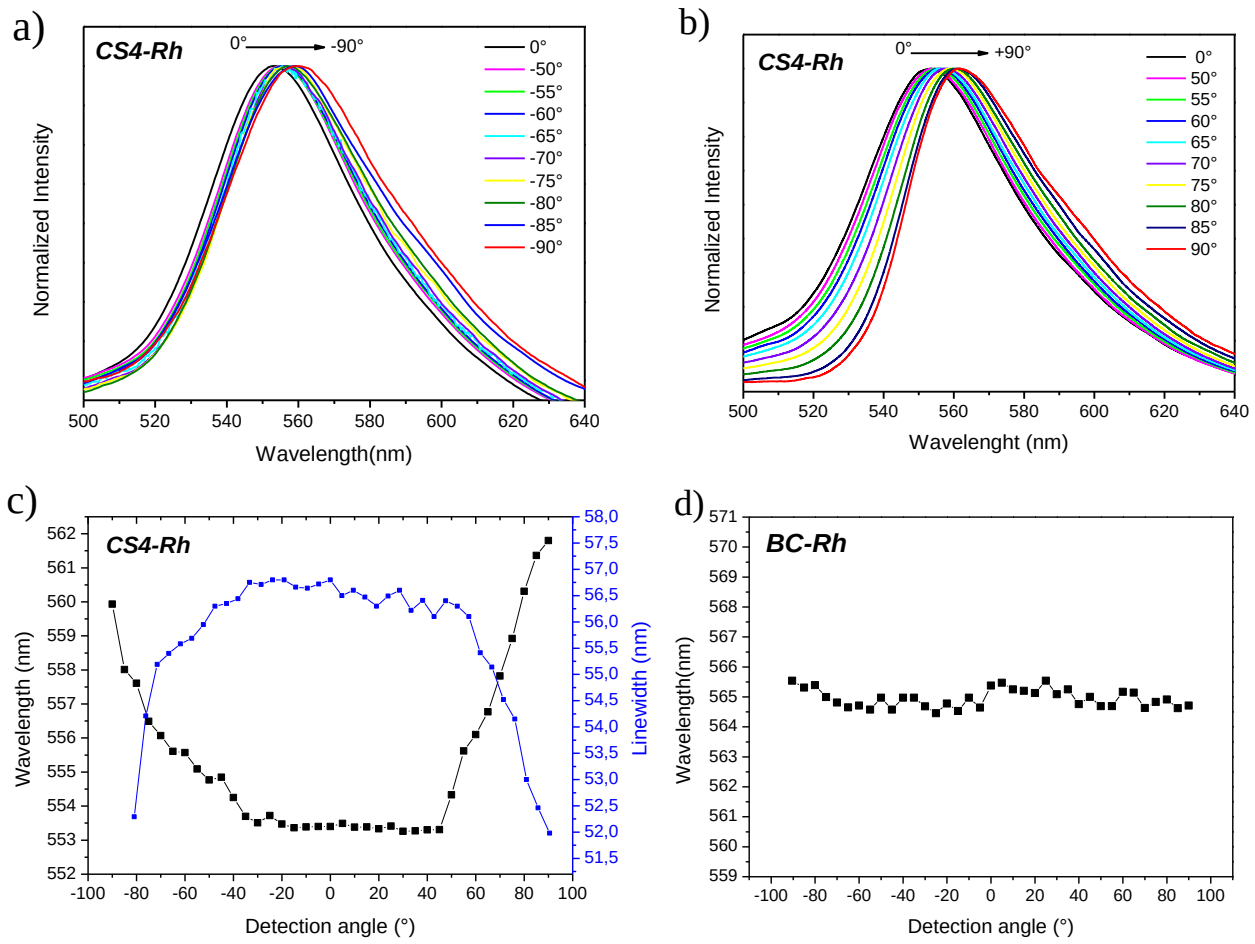


Figure 42. a) Emission spectra of CS4-Rh composite as function of the detection angle (0 ° to -90°), excited at 348nm; b) Emission spectra of CS4-Rh composite as function of the detection angle (0° to 90°), excited at 348nm; c) Variation of the λ_0 and linewidth of emission bands of composite CS4-Rh as function of the detection angle ($-90° < \theta < 90°$); d) Variation of the maximum wavelength (λ_0) of emission bands of composite BC-Rh as function of the detection angle ($-90° < \theta < 90°$).

Figures 43a and 43b show color coordinates diagrams. Shift of emission color observed at different detecting angles is a clear manifestation of the liquid crystal photonic properties of the host. Figure 44 shows the emission spectra obtained for the sample CS4-Rh is shown for detection angles of 20° and 90°. Reflectance spectra are also shown for incident angles of 20° and 50°. With increasing detecting angle a blue shift is observed for the emission band while a red shift if observed for reflection spectra.

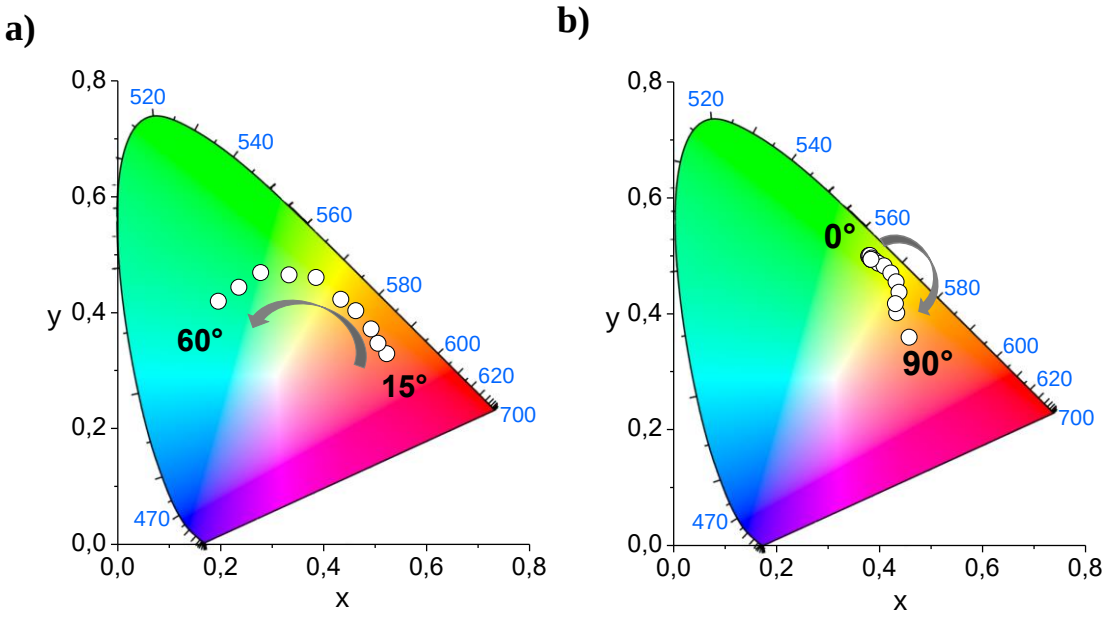


Figure 43. a) Color diagram of reflection of CS4-Rh composite film as function of the detection angle ($0^\circ < \theta < 60^\circ$); b) Color diagram of emission color of CS4-Rh composite film as function of the detection angle ($0^\circ < \theta < 90^\circ$), excited at 348nm

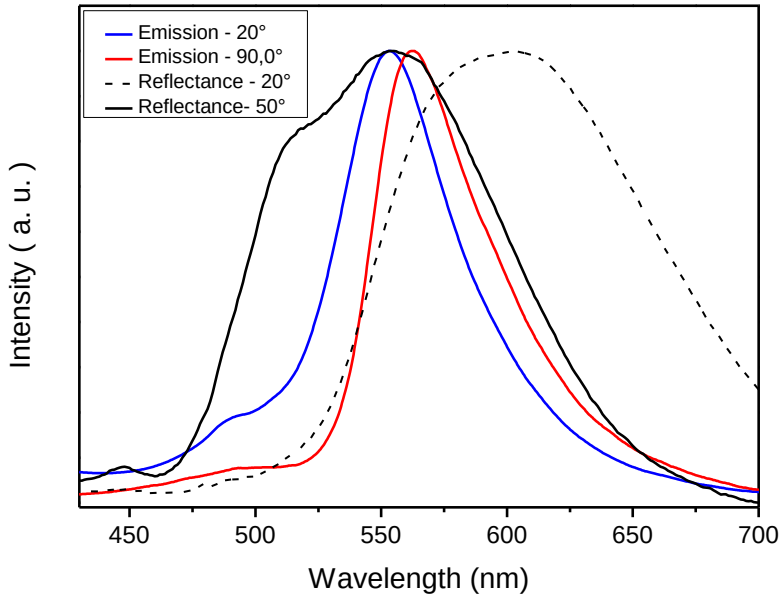


Figure 44. Emission spectra of CS4-Rh excited at 348 nm acquired at 20° and 90°. Reflectance spectra acquired at 20° and 50°.

Figure 43 and figure 44 show that in fact the observed emission spectra can be obtained from a convolution of rhodamine 6G emission and the stop band due to the liquid crystal structure which as is well known, changes with the detecting angle.

Figure 45 shows the results obtained for the other samples. The same effect of the liquid crystalline structure on the emission spectra is observed. Interesting enough, since P values change with the silica content, so does the photonic effect. That is, the angular range where the red shift on the emission band is observed changes from sample to sample. Therefore, the periodic structure with chiral nematic ordering leads to a selective suppression of a range of emitted wavelength. Additionally, this behavior is dependent on the material optical properties, which are influenced by the position of the bandgap on the photonic structure.

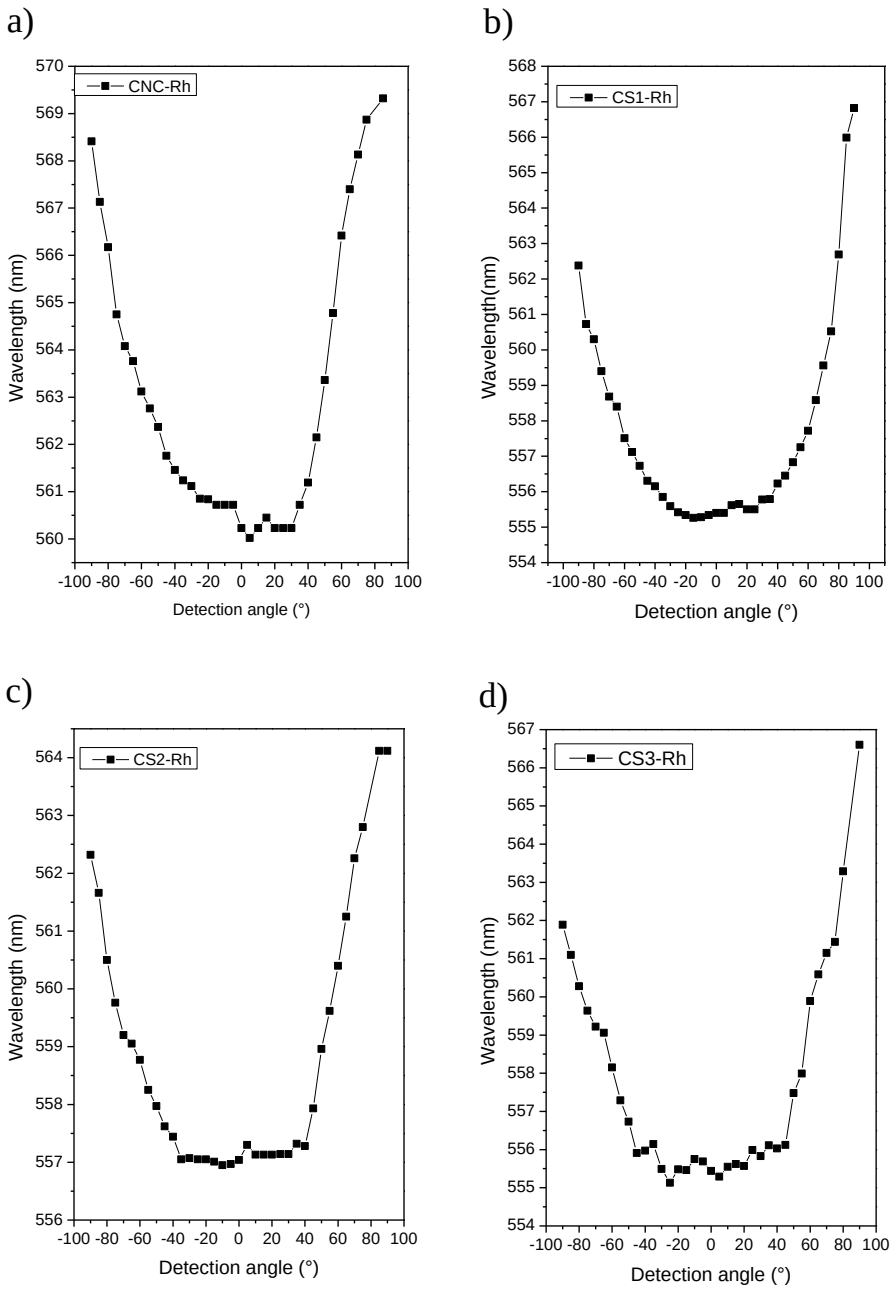


Figure 45. Variation of the maximum emission wavelength for composite films CNC/silica doped with Rh6G as function of the detection angle (-90° < θ < 90°) a) CNC-Rh; b) CS1-Rh; c) CS2-Rh; d) CS3-Rh.

4.4 Conclusions

We presented a new iridescent luminescent material with chiral nematic ordering that displays angle dependent photonic properties. Composite materials prepared with CNC and silica doped with either Rhodamine 6G were obtained in the form of free-standing films, iridescent, luminescent, and with chiral nematic structure. The composites demonstrated tunable optical properties through changes in silica concentration. The insertion of silica also implies the improvement in the quality of the material photoluminescence. Composite materials

also displayed the property of modulate emission according to the detecting angle. This effect suggests that the periodic structure with chiral nematic ordering of the film strongly affects the emission spectra. These functional materials demonstrated the benefit of the integration of luminescence and iridescence on self-sustainable film with chiral nematic structure. It suggests also a novel strategy to modulate the emission of luminescent species for applications in optical devices, such as, sensors, lasers or tunable filters.

PART II. MULTIFUNCTIONAL MATERIALS USING SILK FIBROIN AS A BIOTEMPLATE.

5. Silk fibroin as a biotemplate for hierarchical porous silica monoliths for random laser applications.

Bombyx mori silk fibroin offers unlimited opportunities for functionalization, processing, and biological integration. Taking advantage of the relationship between structure and processing of the silk fibroin, we describe in this work the design of structured organic inorganic hybrids based on silica and silk fibroin. In situ self-assembly of fibroin nanofibers along with hydrolysis and polycondensation of tetraethyl orthosilicate was employed. Structural characterization was performed by Raman and solid state NMR spectroscopies. Our findings demonstrated that fibroin precipitates with prevailing β-sheet conformation. The transition of amorphous to crystalline state was favored by the increase of the fibroin concentration in the samples. The samples were obtained as robust and biocompatible monoliths, which can be candidate to several applications, particularly in biomedical field. As a novel development of the present work, the fibroin nanofibers were used as pore biotemplates to create mechanically robust silica monoliths with a hierarchical macro–mesoporous network in an easy templating process. Surface areas of the final structures ranged from 704 to 1057 m^2g^{-1} and a maximum pore volume of 0.621 mL g^{-1} were achieved. The porous silica monoliths doped with rhodamine 6g exhibited typical random laser action, with minimum laser threshold of 9.7 μJ/pulse and a linewidth narrowing from 40 to 4 nm. In addition, by analysing the emission spectra it was shown two gain mechanisms coupled, which were the random lasing and the stimulated Raman scattering, allowing us to observe a Stokes line of the dye.

5.1. Introduction

In nature, biopolymers appear as controlling agents or as templates of inorganic precipitation and crystallization. Besides, they also may assemble structures that serve as confining spaces or scaffolds in which the formation of the inorganic component takes place (DARDER; ARANDA; RUIZ-HITZKY, 2007). From a materials science perspective, biopolymers can be a versatile source for the design of structured inorganic materials in the laboratory (GIESE et al., 2015; VAN OPDENBOSCH; ZOLLFRANK, 2014).

Silk proteins represent a unique family of biopolymers due to their structural and biological properties. Fibroin extracted from the cocoons of the silkworm (*Bombyx mori*) is mainly composed by 43% glycine (Gly), 30% alanine (Ala) and 12% of serine (Ser) (MORI;

TSUKADA, 2000; NELSON; COX, 2011). The structure of a silk fibroin molecule consists of two chains interconnected by S bond (TANAKA et al., 1999). The chain with higher molecular weight (~350kDa) is formed by repetitive domains Gly-Ala-Gly-Ala-Gly-Ser and polyelectrolytes such as glutamic acid and aspartic distributed at the end of the chains. Jointly with a large number of hydrophobic residues, this chain has hydroxyl residues (serine and tyrosine) that promote their affinity for water(HOSSAIN et al., 2003).

Silk fibroin may present an amorphous conformation (random coil, water soluble) or in increasing levels of crystalline conformation (β-sheet, water insoluble), which allows to modulate its stability in water (NUMATA; CEBE; KAPLAN, 2010). Stabilization can be further enhanced when the amorphous structure of silk is converted into the crystalline state (LIU; ZHANG, 2014) through external stimuli, such as fibroin concentration, treatments with organic solvents, temperature, pH value, ion strength or mechanical stress (KOH et al., 2015). All these features have led to the transformation of this commodity material, into a variety of new materials including, hydrogels, ultrathin films, thick films, conformal coatings, 3D porous or solid matrices, fibers with diameters spanning the nano- to the macroscale and many related morphologies (KOH et al., 2015; LIMA et al., 2016; PEREIRA; SILVA; DE ZEA BERMUDEZ, 2015; TAO; KAPLAN; OMENETTO, 2012; WANG; CHEN; ZHANG, 2015).

In parallel, hierarchical porous materials are of high interest for applications where optimizing mass transport is an issue, as sorption media, separation processes, heterogeneous catalysis, photocatalysis, filters, among others (COASNE, 2016; GALARNEAU et al., 2016; GUIOCHON, 2007; UNGER; SKUDAS; SCHULTE, 2008). In addition, these porous materials can also be used in order to optimize light diffusion and amplification, since light amplification through stimulated emission is possible in a random medium with a gain (WIERSMA, 2008).

The interplay between gain and scattering in disordered materials can sustain laser oscillations, named random lasers (RLs) (BALACHANDRAN; LAWANDY, 1994; LETOKHOV, 1967; MARKUSHEV; ZOLIN; BRISKINA, 1986). Several materials have been studied for RL emission (LUAN et al., 2015a; WIERSMA, 2008). For demonstration of functionality and optical effects, ethanol solutions of Rhodamines and TiO_2 nanoparticles are among the most studied, due to its simplicity and high gain provided by the dyes. One main drawback with liquid samples is the particles agglomeration, which implies in degradable RL (BRITO-SILVA et al., 2010), due to the precipitation of the scatterer particles. RLs are promising to be applied in image systems, thanks to the low spatial coherence which allows obtain speckle-free images (REDDING; CHOMA; CAO, 2012). Solid samples are desired

because they avoid precipitation of the particles, can be designed in several geometries, and decrease health and environmental hazards. In this context, structured inorganic or organic-inorganic hybrid (OIH) materials are promising for RL applications (GARCÍA-REVILLA et al., 2008, 2009).

In this work structured OIH materials based on silica and silk fibroin were designed. The new materials were obtained through *in situ* self-assembly of fibroin nanofibers along with hydrolysis and polycondensation of tetraethyl orthosilicate (TEOS). Fibroin was observed to precipitate with prevailing β-sheet conformation. The amorphous to crystalline state transition was favored by the increase the relative fibroin concentration. The samples were obtained as robust and biocompatible monoliths, which can be candidate to several applications, particularly in biomedical field (ARCOS; VALLET-REGÍ, 2010; HOU; CHEN, 2010; KISHIMOTO et al., 2013; MIESZAWSKA et al., 2011).

We have used these materials to prepare porous silica monoliths for random laser applications. In a traditional templating approach, mesoporous and macroporous silica monoliths were obtained by using fibroin nanofibers as sacrificial scaffolds which were selectively removed from the monoliths *via* thermal treatment of IOH. The porous silica monoliths doped with rhodamine 6g (Rh6G) exhibited typical RL characteristics such as emitted nonlinear intensity dependence with the excitation intensity, large spectral bandwidth narrowing with the increase of the excitation intensity and excitation threshold behavior. In addition, by analyzing the emission spectra, the concurrence of two gain coupled mechanisms was shown: the random lasing and the stimulated Raman scattering, allowing us to observe a Stokes line of the dye. Random Raman lasers have recently been resported in the literature (HOKR et al., 2014) and it has been observed in porous materials such as vesicular polymeric films (YASHCHUK, 2015), silica foams (BACHELARD et al., 2014a) and silica/titanate foams (GAIKWAD et al., 2015).

5.2. Materials and methods.

5.2.1- Extraction of silk fibroin

Fibroin solution was obtained from silk cocoons produced by *Bombyx mori* silkworms which were supplied by Bratac, Fiação de Seda S.A. (Bastos/SP, Brazil). The method was based on previous reports (ROCKWOOD et al., 2011). Five grams of silk cocoon pieces was washed

with 2L of 0.02M Na_2CO_3 solution at 100°C for 30 minutes and washed thoroughly with distilled water, in order to remove sericin (degumming). Degummed silk (fibroin fibers) was dissolved in 9.3 M LiBr in a proportion of 1:4 (w/v) of fibroin to LiBr and the solution heated at 60°C for dissolution for 4 hours. Each 25mL of the resulting solution was dialyzed against 2 liters of milli-Q water for 48 hours in order to remove salts. A 8.5% (w/V) aqueous fibroin solution free of impurities was obtained after the centrifugation (twice) of the dialyzed solution at 20,000rpm at 4ºC for 20min. The final solution is stored at 4º C before use.

5.2.2-Preparation of organic-inorganic hybrids monoliths based on silica and fibroin.

The steps of the sol–gel process exploited in the preparation of the samples are shown in Scheme1. The tetraethoxysilane (TEOS, Sigma-Aldrish 98%) based sol was prepared by mixing TEOS, 0.3 M aqueous HCl (Chloride acid Synth 98%) and EtOH (Ethanol, Synth 98%) in a 1:0.008:3.82 molar ratio. Then the silica/fibroin composites (SF) were prepared by combining the sol with a mix of 8,5wt% aqueous fibroin suspension and 1ml of 0,6M aqueous NH_4OH to achieve the desired proportion TEOS:fibroin (wt%): 1.00:0.00 (SF0), 0.985:0.015 (SF1), 0.97:0.03(SF2), 0.925:0.075 (SF3), 0.85:0.15 (SF4), respectively. The mixtures were aged for 15 days and afterward it was dried for 24h under ambient conditions forming whitish monoliths, which were heated in the oven at 40°C for 24h.

5.2.2-Preparation of porous silica monoliths.

The organic-inorganic hybrids monoliths based on silica and fibroin prepared in section 5.2.1 were thermally treated in an oven in order to prepare the correspondent porous silica monolith. The heating ramp used to calcinate the organic fraction is shown in Table 4. Silica monoliths so obtained were designated as S0, S1, S2, S3 and S4, and are related to their respective organic-inorganic hybrids monoliths SF0, SF1, SF2, SF3 and SF4.

Table 4. Heat ramp used to calcinate the fibroin fraction in the silica/fibroin hybrids monoliths. Heat temperature, heating rate and the time that the samples were kept in the matching temperature are presented.

Temperature (°C)	Rate (°C.min^{-1})	Time (h)
40	1	4
60	1	12
80	1	12
100	1	4
120	1	4
150	1	1
200	2	2
250	2	2
300	2	2
400	2	2
500	2	2
600	2	2
700	2	4

5.2.3-Preparation of porous monoliths of silica containing Rh6G.

Silica monoliths were immersed in 2 mL of an ethanol solutions 10^{-4} mol.L^{-1} of Rh6G and kept during 24 h at room temperature. Finally, the silica monoliths were removed from the dye solution and placed in an oven at 40 ºC, during 2 h, for evaporation of the ethanol.

5.2.4-Characterization of materials.

The morphology of the materials was evaluated by scanning electron microscopic (SEM) images obtained with a JSM-7500F field emission scanning electron microscope from JEOL. Samples were covered with a Platinum layer on copper supports.

Thermogravimetric (TG) curves of dried samples were obtained in a SDT Q600 equipment from TA Instruments. Samples were heated in open alumina crucible from 20 to 600^{o}C under oxygen atmosphere at flow rate of 100 mL min^{-1} and heating rate of 10 ^{o}C. min^{-1}.

Raman spectra of the samples were collected on a RFS 100 FT-Raman Bruker spectrometer equipped with a Ge detector using liquid nitrogen as the coolant and a Nd:YAG laser emitting at 1064 nm. The laser light power was varied from 30 to 150 mW. Back-scattering configuration was used. An average of 1024 scans was performed at a resolution of 4 cm-1 over a range from 3500 to 50 cm-1. The OPUS 6.0 (Bruker Optik, Ettlingen, Germany) software was used for Raman data acquisition. For all of the FT-Raman spectra obtained in this work, the samples did not undergo any previous preparation, and all spectra were obtained at least twice to be sure about position and intensity.

Solid state NMR of ^{9}Si{^{1}H} and ^{13}C{^{1}H} cross polarization and experiments were conducted using a Bruker Avance spectrometers at magnetic fields of 9.4 and 17.6 T, respectively. The ^{29}Si{^{1}H} CP-MAS spectra of SiO_2:fibroin composites was measured under spinning speed of 10kHz, using a CP contact time of 2.5 ms and relaxation delay of 5s. ^{13}C{^{1}H}CP-MAS spectra were measured under speed spinning at 10kHz, using a CP contact time of 1.0ms and relaxation delay of 5s. All spectra were acquired with TPPM proton decoupling during the data acquisition applying decoupling pulses. The ^{1}H experiments were acquired at magnetic fields of 17.6 T under speed spinning at 14kHz, using a spin echo sequence, with spinning sincronizated and saturation train of 56. The FSLG ^{13}C{^{1}H} CP HETCOR experiments were measured using two CP contact times 0.5 e 2.5ms. The experiments were carried out under spinning speed at 14kHz and recycle delay of 5s. Chemical shifts are reported relative to TMS referencing standard.

Surface area and porosimetry measurements were performed using the Micrometrics ASAP 2020.

The random laser action in the silica monoliths containing Rh6g was achieved using the second-harmonic of a Nd:YAG pulsed laser at 532 nm with a Q-switched pulse duration of 6ns as excitation source. A biconvex lens was used to focus the beam at the sample surface with a cross sectional area of 1.6x10^{-2} cm^{2}. The emitted light was analyzed using a monochromator equipped with a CCD camera.

5.3. Results and discussions

5.3.1. Characterization of organic-inorganic hybrid monoliths based on silica and fibroin.

Macroscopically homogeneous silica/fibroin hybrids monoliths showed transparent to milky appearance, depending on the fibroin content (Figure 46a). Under the experimental conditions the final fibroin content were (in weight) 3.9, 7.9, 10.2 and 15.8%, according to TGA analysis which is shown hereafter.

Figure 46b shows representative SEM micrograph of silica/fibroin hybrids containing 10.2wt.% fibroin (SF3). Fibroin nanofibers embedded in the structure of spherical silica nanoparticles are clearly observed. The micrograph of the surface of monolith shows fibroin nanofibers getting out of the bulk. SEM image of agglomerate in the surface of monolith (Figure 46c) reveal nanofibers fibroin with diameter of 20-30nm. The increase of fibroin concentration implies in higher precipitation and agglomeration of fibroin nanofibers, as seen in Figure S1 (Supporting information).

Image of fracture of the monolith (Figure 46d) shows nanofibers fibroin inside of the bulk of silica. These results suggest that hydrolysis and condensation of TEOS in the composites lead to the formation of fibroin nanofibers between the silica nanoparticles. These nanofibers cause scattering in the visible light range and lead to a gradually increase of optical density to opaque white color with the increasing fibroin concentration.

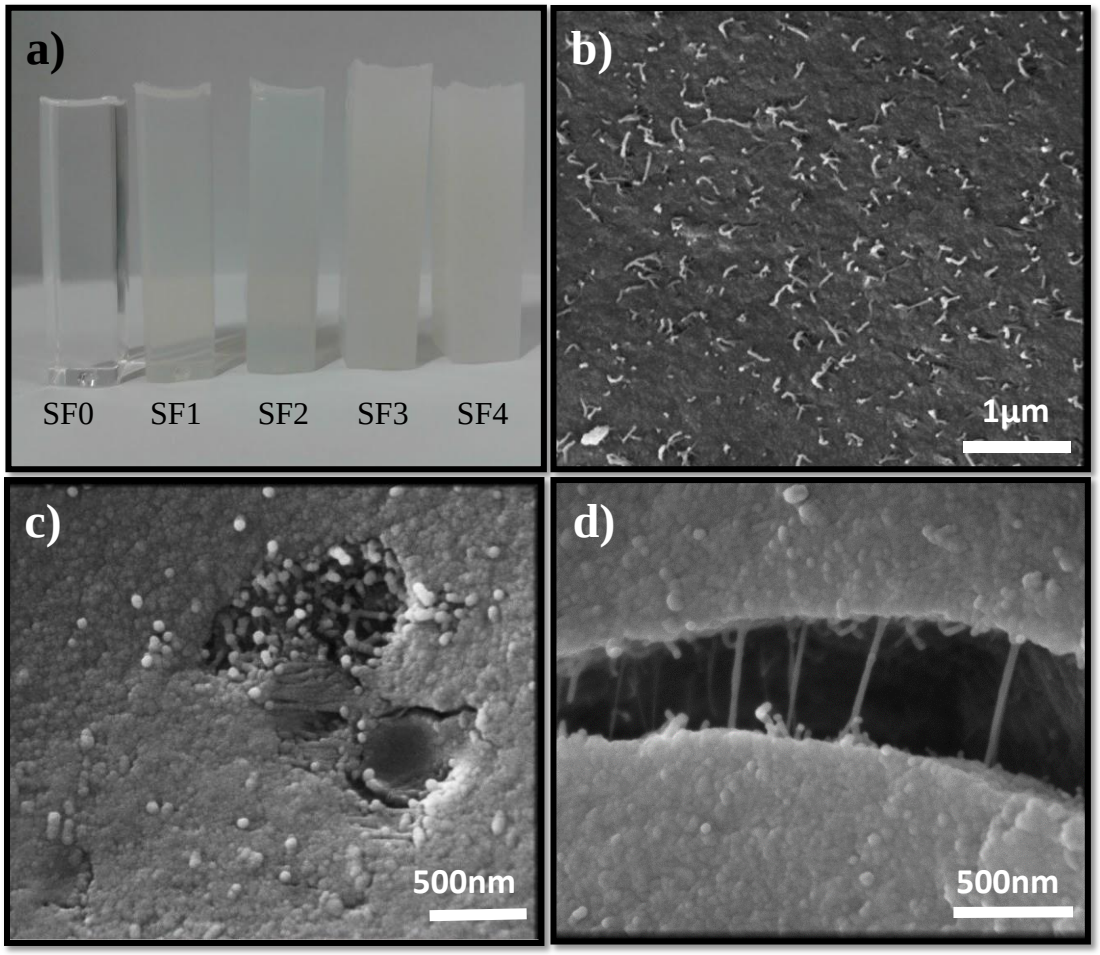


Figure 46. a) Photograph of silica/fibroin hybrids monoliths. b) SEM image of the surface of monolith SF3; c) SEM image of agglomerate of fibroin nanofibers on the surface of monolith SF3; d) Image of the fracture of the monolith SF3.

As already mentioned, fibroin can be present in different conformations, which in turn show significantly different properties. The materials presenting β-sheet conformation exhibits high crystallinity, has high breaking strength and stiffness (KAPLAN; MCGRATH, 2012). Silk fibers have outstanding mechanical properties and they are insoluble in organic solvents and water due to hydrophobic nature of the protein and the presence of a high content of β-sheet structure. Thus, the preparation of fibroin in silica/fibroin hybrids with this conformation is of great interest because of the high performance that it can provide. In order to investigate the conformation of fibroin nanofibers in the silica/fibroin hybrids a thermal a structural study were carried out using thermogravimetric analysis, Raman and solid state NMR spectroscopy.

TGA results on samples are shown in figure 47 and the main data corresponding to the analysis of the curves are listed in Table 5. Curves can be divided in three regions. The first, in the temperature range of 35 to 100°C, is attributed to the removal of physisorbed water. The

second one, in the range of 240 to 400°C, is associated with the fibroin degradation. Above 400°C mass loss can be assigned to the dehydroxylation of silica (PEREIRA et al., 2007).

Silk fibroin degradation occurring between 313 and 318°C, is characteristic of fibroin with prevailing β-sheet conformation (HU et al., 2011) (Table 5). Qualitatively, these characteristics could be related to the higher stability induced by crystallinity and orientated chain alignment of β-sheet conformation (JIN; KAPLAN, 2003). The results could indicate that fibroin assume prevailing β-sheet conformation during hydrolysis and condensation of TEOS in the samples. The same characteristics were observed by Motta et al. (MOTTA; FAMBRI; MIGLIARESI, 2002) after inducing the crystallization (β -sheet formation) of the fibroin films by treatment with ethanol.

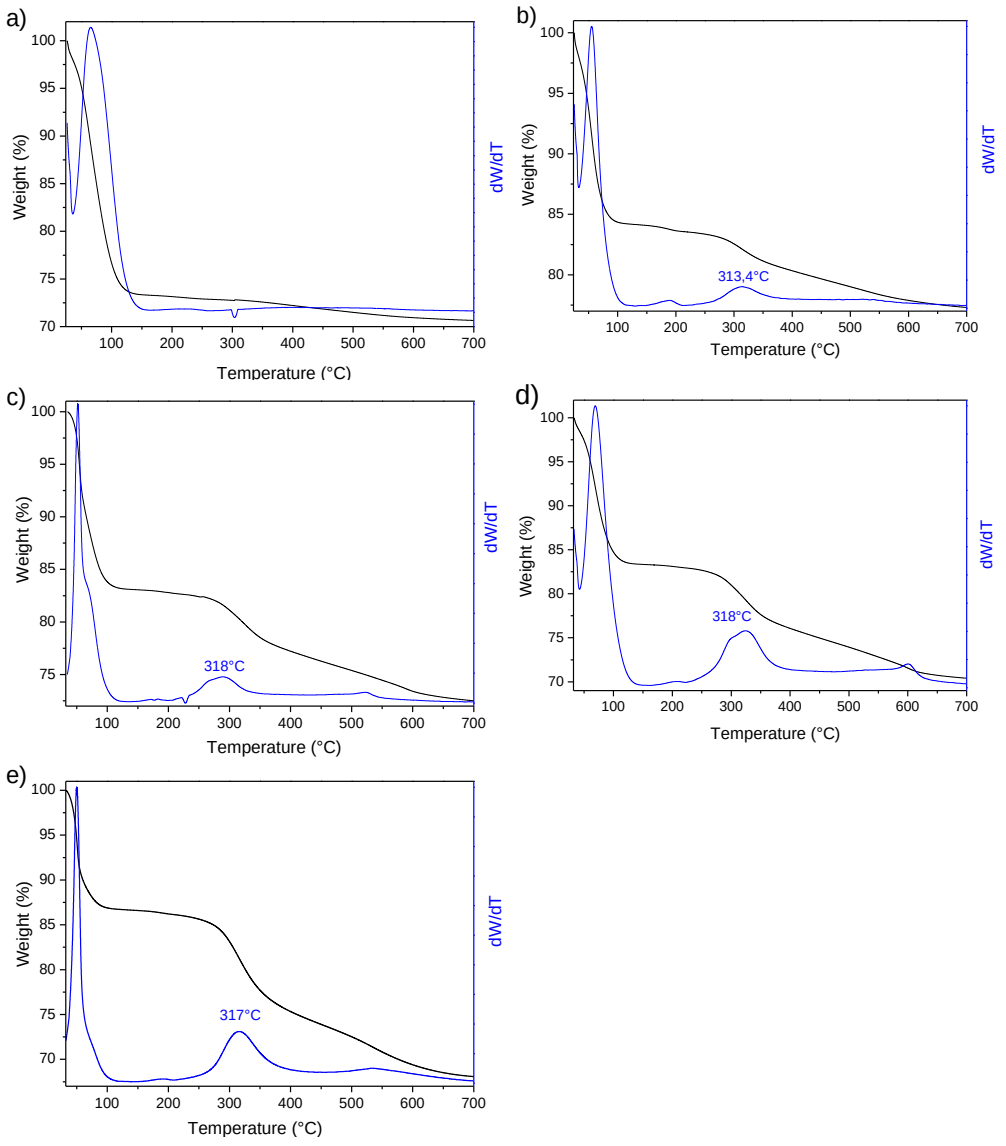


Figure 47. Thermogravimetric curves of silica/fibroin hybrid monoliths: a) SF0; b) SF1; c) SF2; d) SF3 and e) SF4.

Table 5. Samples composition and degradation temperature of fibroína (Tonset) determined by thermogravimetric curves.

Samples	Fibroin (%)	T_{onset} (°C)
SF0	0	-
SF1	3.9	313
SF2	7.9	318
SF3	10.2	318
SF4	15.8	317

Figure 48 shows Raman spectra of silica/fibroin hybrids. The Raman spectrum pattern recorded for all the samples is characteristic of silk fibroin with prevailing β-sheet conformation(MONTI et al., 2001). The amide I and amide III bands appear at 1666 cm^{-1} and 1233cm^{-1}, respectively. Another band appears at 1085cm^{-1}, which is also a sensitive band for β-sheet conformation. The relative intensity of those bands increases with the increasing fibroin relative content. These results corroborate with TGA results and suggest that the increasing of silk fibroin concentration in the composite induces β-sheet conformation. Similar results are reported by Matsumoto et al. (MATSUMOTO et al., 2006) studying silk fibroin sol-gel transition as a function of fibroin concentration. The authors associated the optical changes in fibroin gels to precipitation of micrometer size aggregates with insoluble and crystalline β-sheet conformation.

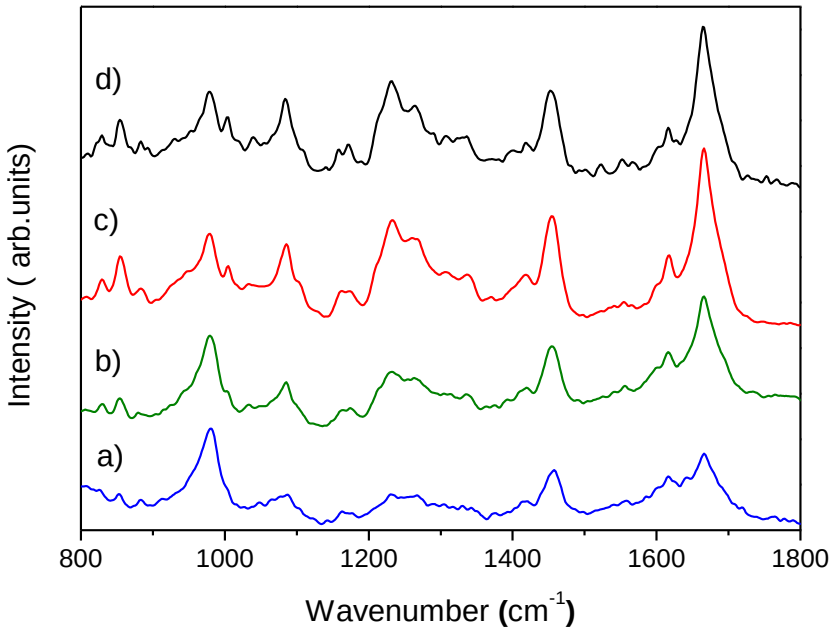


Figure 48. Raman spectra of silica/fibroin hybrid monoliths: a) SF1; b) SF2; c) SF3 and d) SF4.

Figure 49 shows ^{29}Si CP MAS spectra of silica/fibroin hybrids. Silica nanoparticles show three broad resonances lines convoluted with chemical shift in the range of -80 to -130ppm, that are assigned Q^2, Q^3 and Q^4 units (where Q^n correspond to SiO_4 tetrahedra in an amorphous network, where *n* represents the number of oxygen bond to another tetrahedron) (LIPPMAA et al., 1980). There is no significant change in the particles formed according to the silica/fibroin ratio.

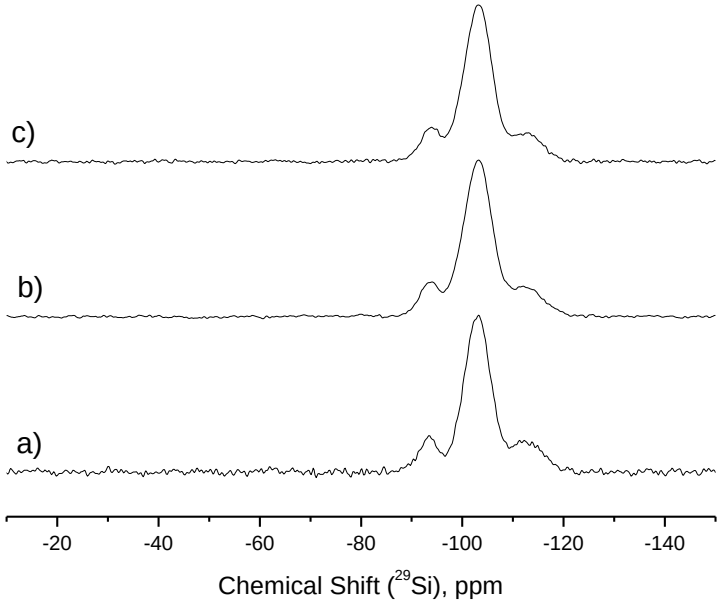


Figure 49. ^{29}Si{^{1}H} CP MAS spectra of silica/fibroin hybrid monoliths contained differents fibroin concentrations: a) SF1; b SF3 and d) SF4.

Several structural studies have been carried out using solid state NMR of fibroin and polypeptides (alanine, glycine)$_n$ allowing a better understanding of the conformational change (ASAKURA et al., 2002, 2005). In such studies the variation of the Cβ Ala chemical environment is directly related to the variation in the twist angle (φ, ψ, ω) of the peptide (ZHOU et al., 2001b).

Figure 50 shows ^{13}C CP-MAS NMR spectra of silica/fibroin hybrids. The spectra of show two resonance lines at 17.1ppm and 20.8ppm, related to Cβ of amino acid alanine (Ala) of fibroin in random coil and *β*-sheet conformations, respectively. The presence of the two conformations can also be evidenced from the change in the chemical shift of the Ala Cα at 49.4ppm and 50.5ppm attributed to *β*-sheet and random coil conformations, respectively (DANG et al., 2010). The ^{13}C CP-MAS NMR spectra also show the presence of the resonance line at 62.5ppm, assigned Cβ and Cγ serine in *β*-sheet conformation. The ^{13}C NMR data are in agreement with the residual signals observed from Gly and Ala in the β-sheet form (Ala-Gly)$_n$ (DANG et al., 2010; SAITÔ et al., 1984). In addition to the significant change in the local field observed Cβ alanine, the carbons of the carbonyl (C = O) also reflected of change in the conformation of secondary structure of fibroin. An overlay of four carbonyl resonance lines at 168, 169, 173 and 175 ppm are observed from the obtained samples, respectively. Furthermore,

by analyzing the relative intensity of the two resonance lines at 17.1ppm and 20.8ppm, related to C_β of alanine (Ala) amino acid, in random coil and *β*-sheet conformations, it is noteworthy that the relative proportion of the *β*-sheet forms significantly increases with the increasing of the fibroin ratio confirming what was previously observed in the Raman spectroscopy and TGA analysis results. Similar results were reported by a study of hydration of silk fibroin film in which the *β*-sheet conformation is predominant after 30 minutes of hydration (M. ISHIDA, T. ASAKURA, M. YOKOI, 1990), ie, confirming the transition from random coil to *β*-sheet conformation.

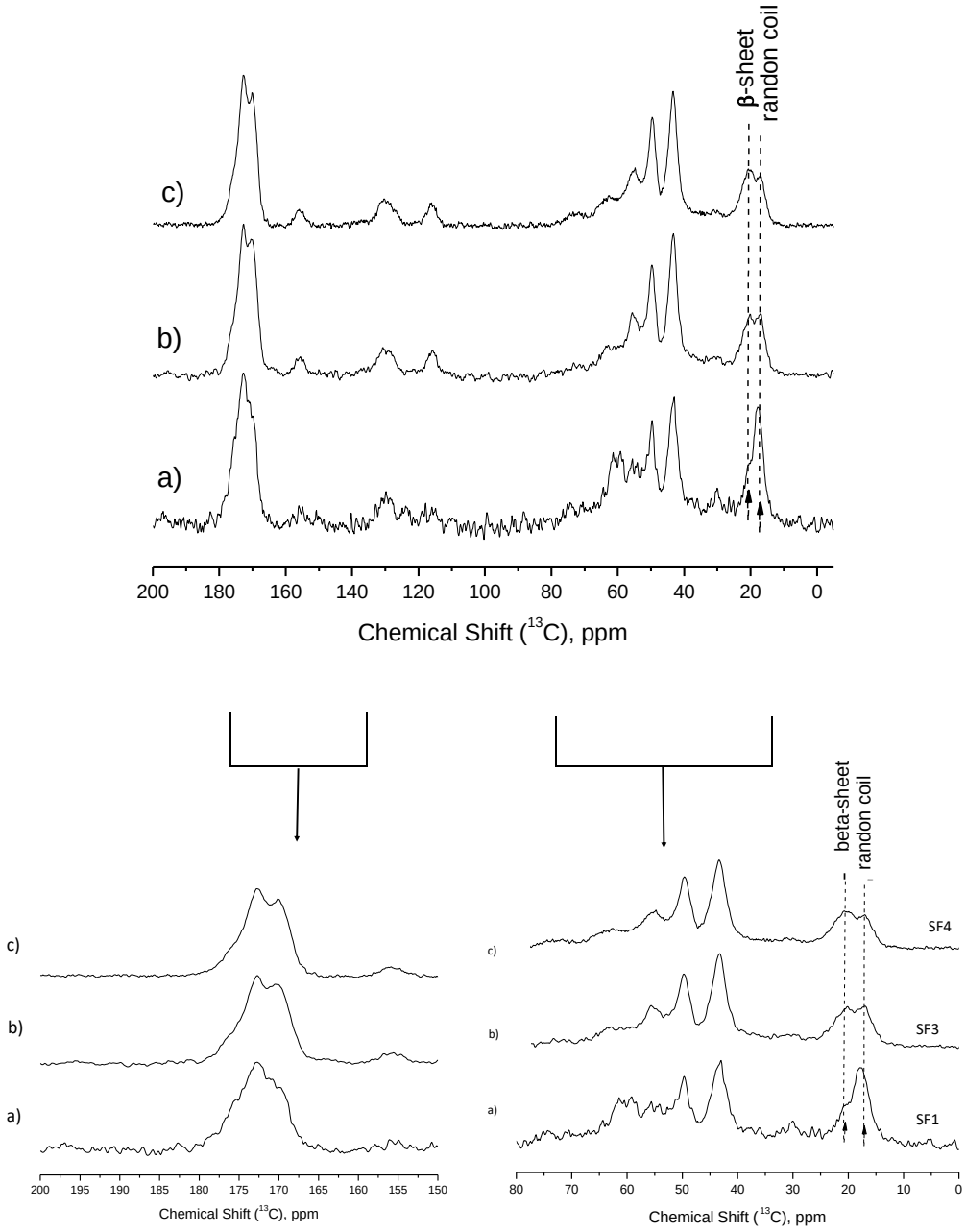


Figure 50. 13C{1H} CP-MAS spectra of silica/fibroin hybrid monoliths containing differents fibroin concentrations: a) SF1; b) SF3 and c) SF4.

Figure 51 shows ^{1}H spectrum obtained for silica/fibroin hybrid monoliths SF4. A broad resonance line is observed at 4.7ppm, characteristic of the SiOH-(H_2O) species. It is known that water on the surface of the SiO_2 particles exchange between the silanol groups (TRÉBOSC et al., 2005). As observed from TG data (Figure 47), the sample has approximately 18% of H_2O in weight, these molecules jump between the silanol groups with rates of 1-2kHz. Despite the high mobility the homonuclear dipolar interaction this leads to short T2 values, so the use of the spin echo experiment allowed the loss of frequency coherence of water, and then it was possible to obtain higher resolution spectra lines in the resonance, characteristics of hydrogen from fibroin.

In the same spectrum, resonance lines of the βH Ala in the two conformations, random coil and β-sheet, may be observed at 1.403 and 1.186 ppm, respectively. This observation corroborates the results observed in the ^{13}C CP-MAS NMR data. The resonance lines observed at 7.034 and 6.775 ppm can be attributed to the phenyl groups of tyrosine amino acids. The two resonance lines observed in the range of 8-9ppm can be attributed to the NH. This may be related to the NH of Ala and Gly amino acids which form the peptide bonds of the protein (M. ISHIDA, T. ASAKURA, M. YOKOI, 1990).

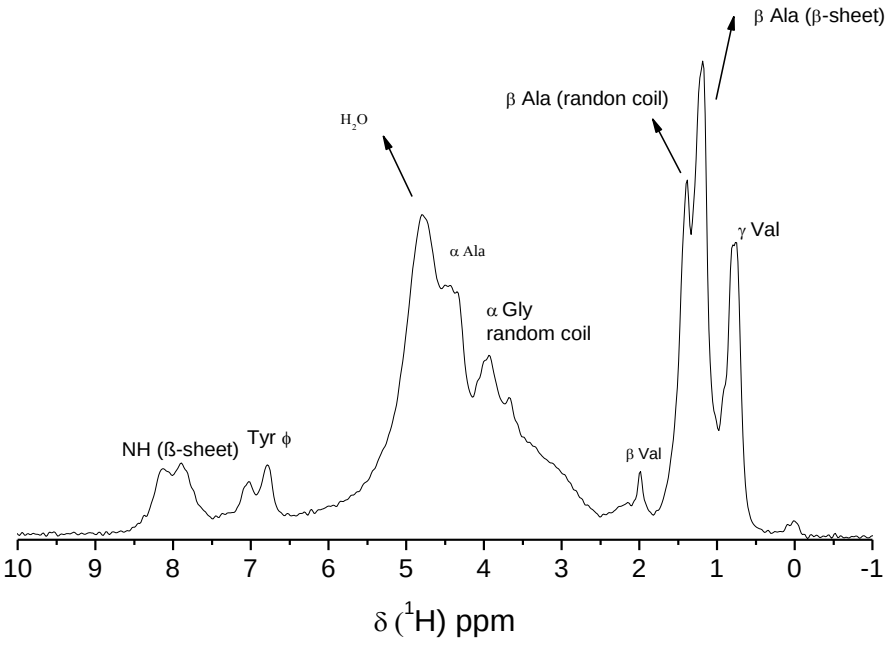


Figure 51. ^{1}H spin echo MAS spectrum of SF4 silica/fibroin hybrid monoliths.

The NMR study allows not only to investigate the structure, but to understand the organic/inorganic interface as well. $^{13}C\{^{1}H\}$ FSLG CP-HETCOR experiments were used to obtain spatial information from heteronuclear dipolar interaction and consequently understand the organic/inorganic interface of silica/fibroin composites. Figure 53 shows the correlation map ^{1}H-^{13}C in the 2D spectra obtained with two different contact times, 0.5 and 2.5ms respectively. The advantage of this experiment is to simultaneously obtain the chemical shift information of ^{13}C and ^{1}H and the correlation of carbon and hydrogen which involves only the dipolar coupling. In this experiment, the correlation signal is only observed if there is proximity C-H atom (<0.35nm), as the polarization is transferred from each type of carbon and hydrogen in the vicinity and in the absence of ^{1}H-^{1}H spin diffusion.

Figure 52 shows results for the experiment carried out with contact time of 0.5ms. Only hydrogens bonded directly to the hydrogen, with distances below 1.5Å (BROWN; SPIESS, 2001) are observed. The αCH_2 of Gly and the CH of Ala at 49.5 ppm and 43.5, as well as the βH of Ala at 1.3 and 1.4 ppm on the *β*-sheet and random coil conformations are observed in the spectra. The chemical environment of hydrogen bonded to βC of Ala amino acids is affected by the changes in the conformation of fibroin. The chemical shift values of hydrogen of CH_2 groups of Gly and CH of Ala are clearly resolved, at 4.3 and 5.2 ppm, respectively. The correlation of hydrogen bonded to βC of Ala with Cα (49.5 ppm) and with carbonyl groups (173 ppm) are also observed but with less intensity. An interesting observation is the presence of correlations of carbonyl which is not protonated. According to the literature, this correlation is observed due to the presence of serine and tyrosine peptides present in low concentration(WHITE; WANG, 2002). However in our mesostructured composite, the correlation with βH Ala were also observed. The correlations observed for carbonyl groups shows a chemical shift in the range of 4-5 ppm, the other correlations related to the hydrogen have a chemical shift in the range of 8-9.5ppm, from the dipolar coupling of carbonyl with

amino (NH) groups. It is possible to observe the dipolar coupling correlation between atoms in longer ranges when the experiment is carried out with contact time of 2.5ms. So, correlations between all hydrogen and all carbon atoms were observed.

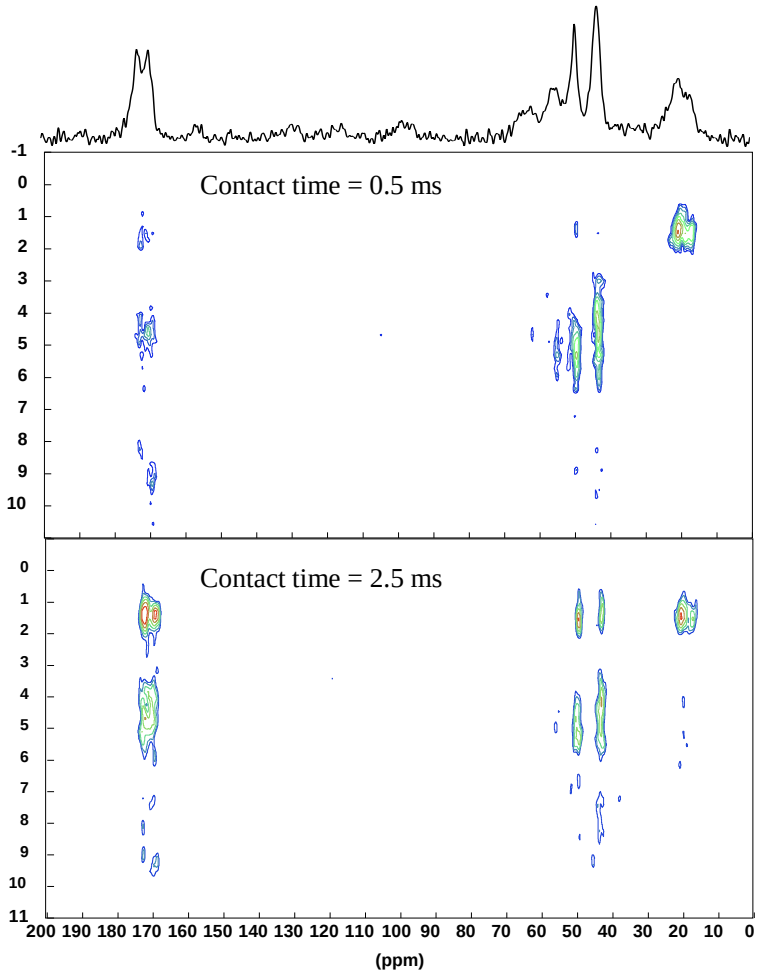


Figure 52. FSLG $^{13}C\{^{1}H\}$ CP HETCOR spectra of SF4 sample obtained with two contact times 0.5 e 2.5ms. (υr=14kHz, υ0=188.6MHz, t1=5s).

Recently, Luo et. al. (LUO; YANG; SHAO, 2016) reported a novel robust hydrogel with significant elasticity and mechanical performance formed by the strong interaction between silk fibroin and hydroxypropyl methyl cellulose (HPMC). The secondary structural transition of silk fibroin molecular chains from random coil to β-sheet is induced by hydrophobic interaction between HPMC and silk molecules forming small and uniform structures, which served as crosslinking sites evenly distributing throughout the hydrogel.

As previously stated, herein the 3D network silica gel hybrids are reinforced by the interpenetrated fibroin nanofibers, which can improve the robustness and the hardness of monoliths when compared with silica xerogel. An illustration of the self-assembly of the fibroin nanofibers inside the bulk of silica is shown in figure 53.

The silica/fibroin hybrid monoliths are obtained by hydrolysis and polycondensation of TEOS producing ethanol as a secondary product. Taken into account the results above we suggest that the ethanol gradually produced in the polymerization process induces the self-assembly of the fibroin nanofibers with prevailing β-sheet conformation. The growth of fibroin nanofibers starts in the initial stages of gelation, when the average cluster size is very small and continues during aging, when 3D silica gel network is reinforced through futher polymerization. Herein, the fibroin nanofibers inside the composite materials were used as organic spacers and selectively removed throught heat treatment, which allowed the formation of mesoporous and macroporous silica monoliths with high porosity as it will be shown hereafter.

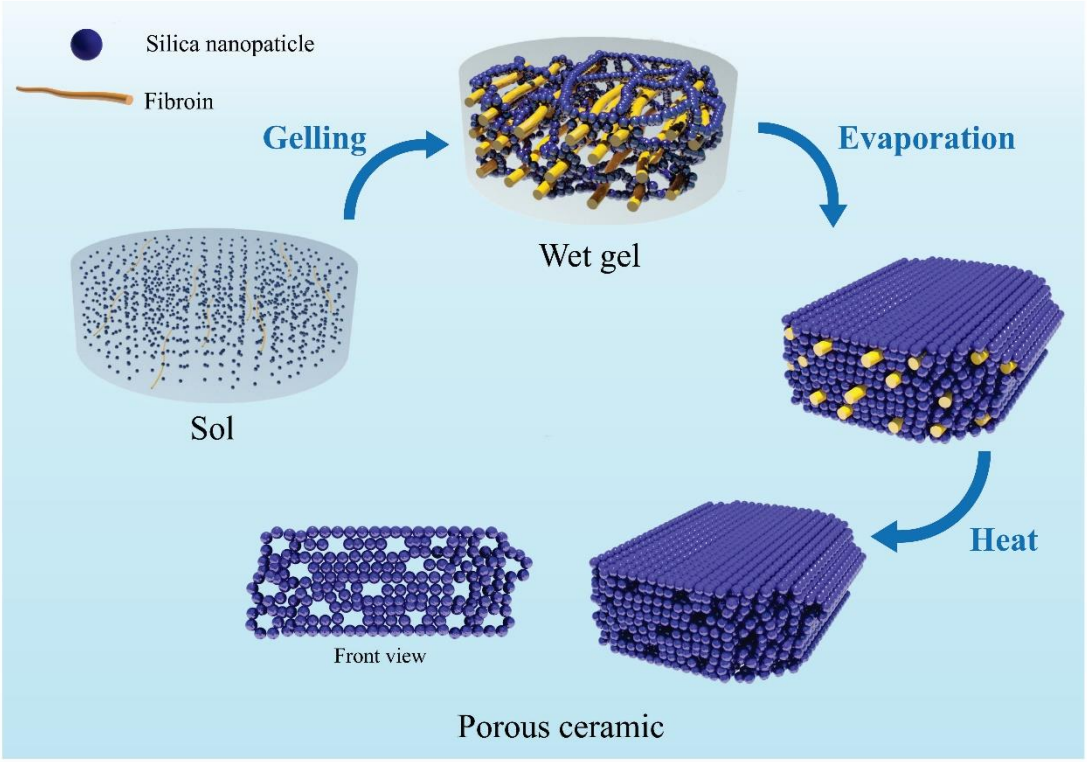


Figure 53. A schematic illustration of the self-assembly of fibroin nanofibers inside the bulk of silica composites materials and posterior calcination of fibroin nanofibers to form porous ceramic.

5.3.2. Characterization of porous silica monoliths

After heat treatment, all samples were obtained as robust monoliths with gradually optical density changes to opaque white color with increasing fibroin initial concentration (Figure 54a).

Figure 54 also shows representative SEM micrographs of porous silica monolith S3. Figure 54b shows pores dispersed in the whole of the silica monolith surface. SEM images of fracture monolith showed the presence of interstitial spaces between the particles (Figure 54c), whose structure looks channel-like pore with channel diameter of hundreds of nanometers (Figure 54d).

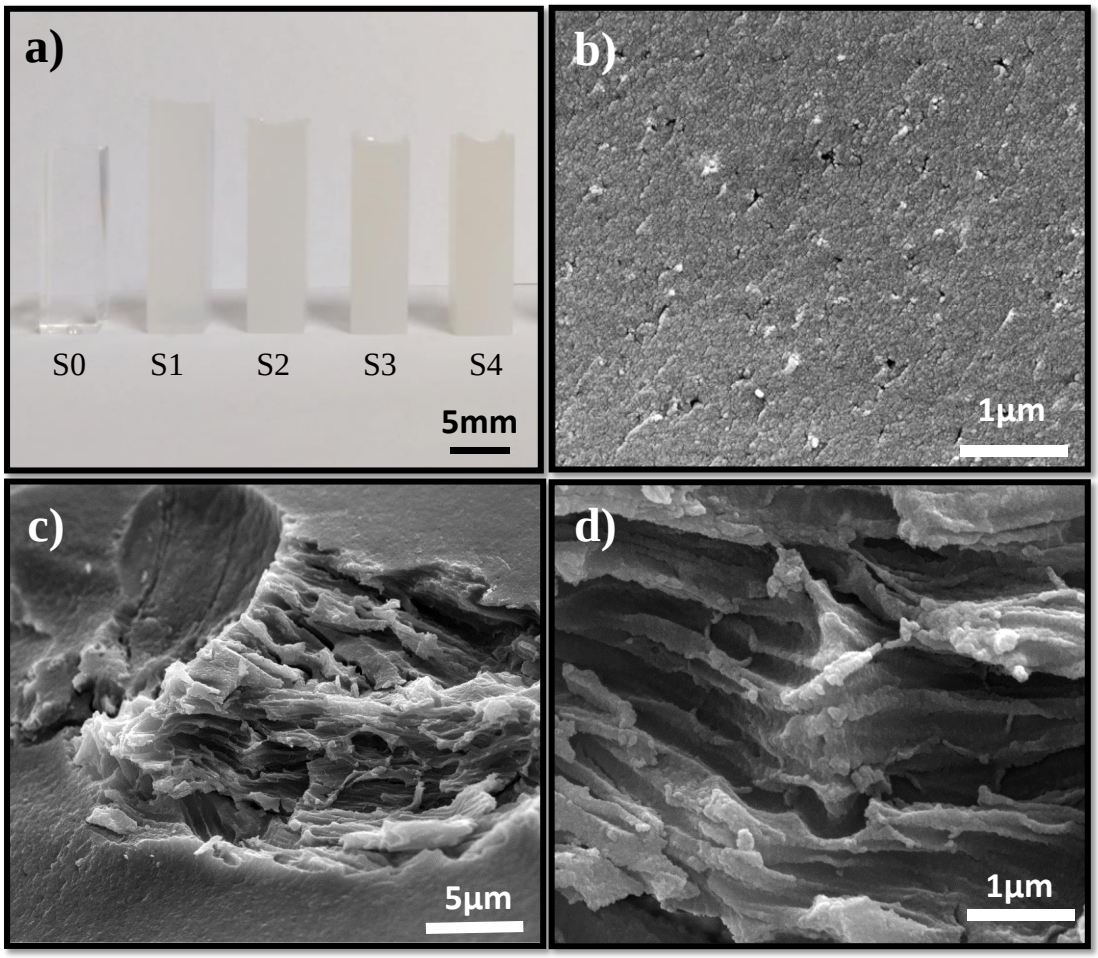


Figure 54. a) Photograph of silica monoliths; b) SEM image of the porous surface of monolith S3; c and d) Images of fracture of S3, showing porous with diameter of hundreds of nanometers inside the bulk of silica.

The porous structure of the silica monoliths was analyzed by nitrogen adsorption experiments. The nitrogen adsorption/desorption isotherms are reported in figure 55a. As the

fibroin concentration increases the hysteresis loop shifts toward higher pressure, characteristic of an increase of material porosity. All the samples presented a Type IV shape, characteristic of mesoporous, with a desorption loop due to the nitrogen condensation within mesoporous (LOWELL et al., 2004). Furthermore, texture information (e.g., pore size distribution, pore geometry, and connectivity) of a adsorbent can be obtained by analyzing the shape of the hysteresis loop (BATISTA et al., 2012; LOWELL et al., 2004; ROCHA et al., 2015; SMITH; LOBO, 2010). Thus, S0 sample presented a type H4 hysteresis, indicating a narrow slit pores. Concerning the other samples, type H2 hysteresis (three-dimensional connected network) (LOWELL et al., 2004) is observed. This H2 hysteresis is often associated to the disordered pores indicating that the distribution of pore size and shape is not well defined (LOWELL et al., 2004; PROUZET et al., 2009; SMITH; LOBO, 2010).

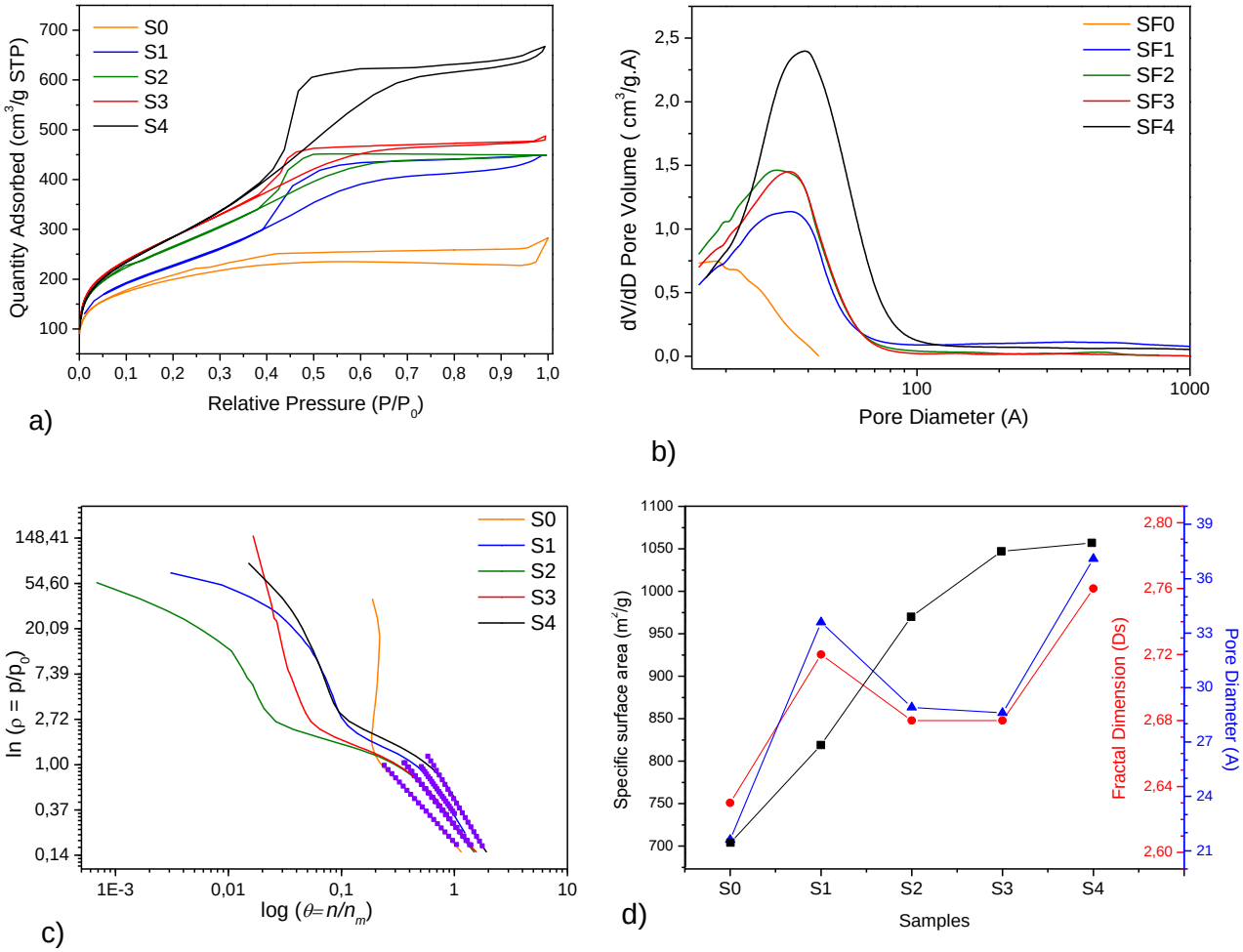


Figure 55. a) Nitrogen adsorption/desorption isotherms; b) Pore size distribution; c) plot of log(ln(ρ)) versus log(θ); d) Evolution of the specific surface area, pore diameter and surface fractal dimension of the samples.

Physico-chemical properties of various samples in the present study are given in Table 6. The results demonstrated that the addition of fibroin in the initial sol lead to an increase of surface area and pore volume with a clear dependence on the fibroin content. The increase of fibroin concentration in the samples SF2 and SF3 implies in formation of more fibroin nanofibers dispersed into the sample. Thus, after the calcination, the silica monoliths S2 and S3 presented a great amount of smaller pores. However, aggregation is observed for higher fibroin content (SF4), leading to larger pores in the silica monolith S4.

Table 6. Physico-chemical properties of calcinated samples.

Samples	S_{BET} (m^2/g)	V_p (cm^3/g)	D_p (Å)	Ds
S0	704	0.379	21.6	2.63
S1	819	0.496	33.6	2.72
S2	970	0.601	28.9	2.68
S3	1047	0.621	28.6	2.68
S4	1057	0.525	37.1	2.76

*D_p, S_{BET}, V_p and D_s stand for BET pore diameter, surface specific area, pore volume and surface fractal dimension, respectively.

The fractal nature of the silicate surface is seen as direct consequence of the fractal structure of the fibroin–silica interface. In this work, we used the Frenkel–Halsey–Hill (FHH) theory for adsorbent–adsorbate interactions in multilayer coverage (SMITH; LOBO, 2010). The fractal nature of the surface was studied by several works, which adopted the FHH theory to evaluate their materials (LIU et al., 2010; LOWELL et al., 2004; ROCHA et al., 2015). The thickness of the adsorbed film as given by the classic FHH equation provides the characteristic length scale for the fractal-FHH analysis:

$$\theta = [-\ln(\rho)/k]^{-1/s} \qquad (2)$$

where $\rho = p/p_0$, $\theta = n/n_{monolayer}$ and s and k are constants. Smith et al. (SMITH; LOBO, 2010) calculated the surface fractal dimension of the samples from the slope m of log-log plot of $\ln(\rho)$ versus θ. For the nitrogen adsorption, the values assumed were $s = 2.24$; $k = 2.27$ and the surface fractal dimension (Ds) were obtained from Eq. (3).

$$Ds = (1/m) + 3 \qquad (3)$$

Ds is a dimensionless number between 2 and 3: Ds = 2 describes a perfect smooth surface, 2 < Ds < 3 irregular surface and Ds = 3 would describe a theoretical volume in which all points would be assigned to the surface (SMITH; LOBO, 2010). Furthermore, important information about surface roughness can be obtained by the Ds interpretation (PROUZET et al., 2009).

Figure 55c is a log-log plot of θ versus ln(ρ) for the calcined samples. The addition of fibroin in the initial sol has promoted apparent differences in observed slopes. The S0 sample presented a slope of -2.73 ± 0.03 whereas the S1, S2, S3 and S4 samples presented values of -3.52 ± 0.10, -3.12 ±0.05, -3.12 ±0.05 and -4.10 ± 0.07, respectively. It was observed that the addition of 15.8 wt% fibroin caused an increase in the Ds value from 2.63 up to 2.76. However, this non-integer value implies that he surface exhibits self-similarity, with a slight increase in the surface roughness promoted by the fibroin added in the system before calcination. The evolutions of Ds values, pore diameter and specific surface area in function of fibroin concentration in the matching silica/fibroin hybrids monoliths are shown in figure 55d.

5.3.3. Characterization of the random laser action in the silica monoliths containing Rh6g.

To characterize the RL emission in our samples, porous silica monoliths doped with Rh6G were exposed to the excitation beam at 532 nm, as above-mentioned, and the emission spectra were recorded for different excitation pulse energies (EPEs). The porosity plays the role of the scatters and, as shown in figure 56, all samples showed the typical behavior of colloidal RL with nonresonant feedback (LUAN et al., 2015b), i.e., an increase in the slope efficiency when crossing the EPE threshold, and smooth narrowing of the bandwidth (see also fig. 56) . The EPE threshold and slope efficiency values are summarized in Table 3. One can see that the samples present low EPE threshold and larger slope efficiency being suitable for RL applications.

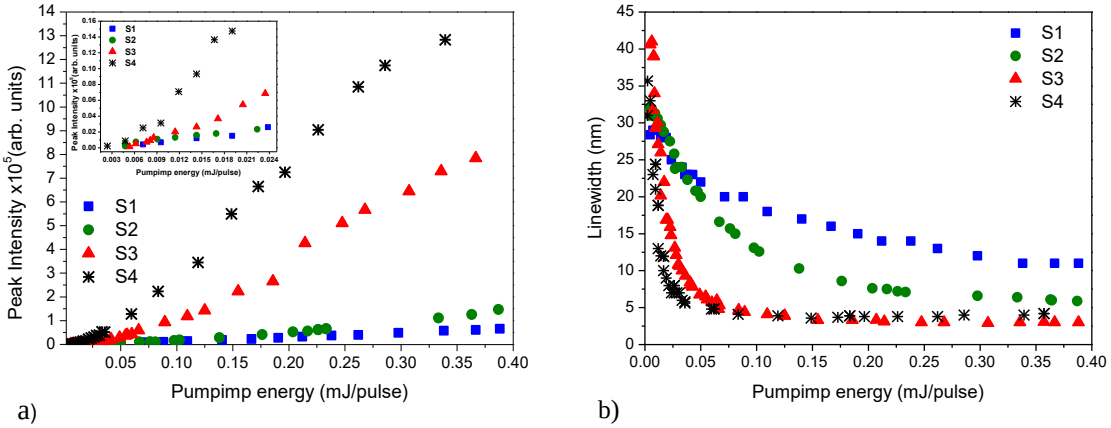


Figure 56. a) Peak intensity vs. pumping energy per pulse showing the nonlinear behavior of porous silica monoliths containing Rh6G; b) Full width half maximum (FWHM) linewidth vs. pumping energy per pulse. The minimum linewidth was ≈ 4 nm for pumping above the threshold.

Tabela 7. Values of energy thresholds and slope efficiency of silica monoliths.

Samples	Laser Threshold (mJ)	Slope efficiency (arb. units)
S1	0.1985	11
S2	0.0745	23
S3	0.0144	160
S4	0.0097	280

* The energy thresholds were determined considering the pumping energy per pulse corresponding to half of the maximum linewidth.

According to figure 57a and Table 7, the increasing of porosity of the samples implies in higher RL performance, the sample S4 presented larger slope efficiency and lower EPE threshold. Compared with the S1 sample, the EPE threshold of the S4 ones is about 20 times smaller and the slope efficiency 25 times larger.

The emission spectra for the S4 sample are shown in Figure 10, which shows typical behavior of RL with smooth and nonspiky emission characteristic of dye baser RL and sometimes indicated in the literature as due to nonresonant feedback. Increasing the EPE, the typical behavior of RL emission was observed, as described before, for EPE up to ~0.55 mJ, which is well above the determined threshold of 9.7×10^{-6}J (see table 3). Upon increasing the EPE beyond 0.55 mJ, where the spectral linewidth has already collapsed to its minimum value

of ~4nm, the spectra redshifts due to reabsorption/reemission processes, and some narrow spikes appeared superimposed on the RL spectra. These spikes are attributed to the interplay between the RL emission, the dye broadband emission and Stokes line of the dye, similar to the reports in Refs (YASHCHUK, 2015; YASHCHUK et al., 2014). The overall broadening for EPE beyond 0.55mJ arise due to these combined effects. However, it can be seen that narrow spikes, due to the stimulated Stokes emission, starts to appear with higher emission intensity beyond those EPE, which follows the Raman spectra of Rh6G shown in ref. 35. This is clearly shown in the inset of fig. 10, which displays the spectrum at $1.2x10^{-2}$J with its lines at 572nm, 573.8nm and 578,6nm corresponding to 1316 cm^{-1}, 1370cm^{-1}, 1514cm^{-1} Raman shift with respect to the excitation laser line can be attributed to aromatic C-C stretching vibrations of Rh6G molecules.

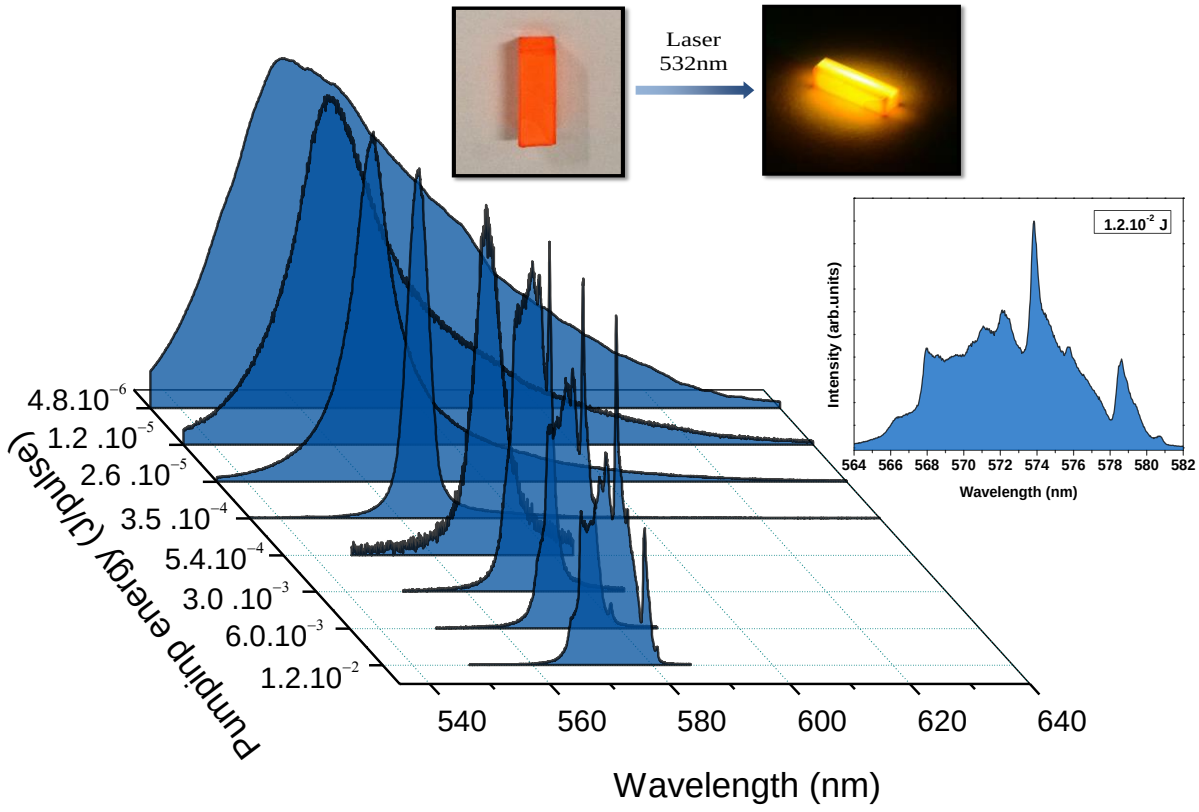


Figure 57. Spectral behavior of the S4 containing Rh6G as of pumping energy per pulse. Minimum linewitdh observed is about 0.5 nm. The inset shows the yellow emission colour of the sample S4 doped with Rh6G excitedwith irradiated with a laser ate 532nm.

5.3. Conclusions

Multifunctional organic inorganic hybrids were prepared based on silica and silk fibroin extracted from the cocoons of the silkworm (*Bombyx mori*). Robust and biocompatible monoliths were obtained with different contents of fibroin. The SEM images demonstrated *in situ* self assembly of fibroin nanofibers dispersed into the IOH monoliths. We suggest that the formation of fibroin nanofibers is induced by the ethanol formed during the hydrolysis and polycondensation of tetraethyl orthosilicate (TEOS). Raman and solid state NMR spectroscopies show that the prevailing protein conformation of the fibroin nanofibers is the β-sheet type. Futhermore, we demonstrated that the fibroin nanofibers can be used as biotemplates, acting as a sacrificial material to develop porous silica monoliths. When infiltrated with rhodamine dye the porous monoliths demonstrated efficient RL action with low threshold power excitation and linewidth narrowing. From the spectral behavior, it is inferred the RL operates in the diffusive regime in hierarchical macro–mesoporous network. This work opens the possibility of new applications of the RL phenomenon in specklefree laser imaging. In addition, when higher values of EPE are inserted, the emission spectra obtained has the stimulated emission and stimulated Raman scattering mechanisms coupled, suggesting that designed materials can also be promising for random Raman laser applications.

6. GENERAL CONCLUSION.

The main goal of this PhD research was to exploit the self-assembly properties of cellulose nanocrystals (CNC) extracted from bacterial cellulose produced by *Acetobacter xylinum* bacteria, as well as, regenerated silk fibroin (SF) stemmed from the cocoons of the silkworm (*Bombyx mori*) in order to prepare nanostructured materials for optical applications. In this context, different multifunctional materials were prepared.

Initially, a composite structure formed from two different liquid crystal forming materials, a low molecular weight 4′-(hexyloxy)-4-biphenylcarbonitrile (HOBC) and cellulose nanocrystals (CNC), was prepared. The HOBC was applied on a CNC film by simple painting. In this case, HOBC liquid crystal was used as a functional compound to promote new properties of the CNC films. The new material here proposed was obtained as a free-standing iridescent film, with chiral nematic structure. The films exhibited modulated optical properties, in response to thermal gradient or relatively small electrical voltage, in addition to liquid crystal properties of the CNC films. Further, the HOBC coating did not change the morphological and optical properties of the cellulose nanocrystal film. It is noteworthy that, for this record, cellulose nanocrystals iridescent films with thermochromic or conductive properties have not been reported in the literature yet. This work presented a new platform for utilization of CNC film, which opens the possibility of applications for this material in the field of thermo- and electro optical devices.

Moreover, still in the field of optical applications of CNC, the preparation of iridescent luminescent composite films by combining tetraethoxysilane (TEOS) to a CNC suspension and to ethanolic solutions of a broad band emitter (Rhodamine 6G (Rh6G)) was demonstrated. The composites were obtained as free-standing films with chiral nematic organization. The morphological and optical characterization demonstrated that the insertion of silica in the composites implies in the control of optical film properties, as well as in the improvement in the quality of the photoluminescence material. The cellulose based photonic materials also displayed modulated photoluminescence with detecting angle. This behavior suggests that the photonic structure with chiral nematic ordering has a strong effect in the emission spectra. In addition, it was demonstrated that this effect is tuned with the stop band position of composite films. Taken the advantages of the luminescence and chiral nematic ordering integration of the CNC films, some examples have been reported in the literature. However, in all of them, their focus was given to the modulating spontaneous emission through circularly polarized excitation of the samples. In this thesis, it is suggested a novel strategy to modulate the emission of

luminescent species exploring the inner filter effect of the periodic structure of films. Thus, it holds that this multifunctional material can be attractive to develop new optical devices with potential for various applications, such as, sensors, lasers or tunable filters.

Finally, multifunctional organic inorganic hybrids based on silica and silk fibroin were developed. Although there are several reports on the literature that present design silica/fibroin hybrids materials, this was the first time the preparation of robust monoliths containing until 15.8 wt% of fibroin was demonstrated. In addition, it was exhibited that these unique materials are formed by 3D network silica gel reinforced by the interpenetrated fibroin nanofibers with preferential crystalline β-sheet conformation, which can lead to an improve of the robustness and the hardness of monoliths when compared with silica xerogel. Likewise, considering the biocompatible property of these materials, the combination of silica and silk leads to very promising and versatile materials with foreseen application in a variety of domains, including bone regeneration. However, it was also possible to demonstrate that the fibroin nanofibers can be used as biotemplates, acting as a sacrificial material to develop porous silica monoliths. These porous monoliths demonstrated efficient RL action, operating in a diffusive regime in hierarchical macro–mesoporous network. In addition, when higher values of EPE are inserted, the emission spectra obtained present the stimulated emission and stimulated Raman scattering mechanisms coupled. These results suggest that designed materials can be promising for new applications of the RL phenomenon, such as specklefree laser imaging and random Raman laser.

EXTENDED ABSTRACT IN PORTUGUESE

Plataforma óptica baseada em um filme de nanocristais de celulose (NCC) revestido com cristal líquido nemático 4’-(hexiloxi)-4-bifenil carbonitrila (HOBC).

Parte experimental.

Preparação de filmes de nanocristais de celulose bacteriana (NCC).

Primeiramente, 5g de membranas de celulose bacteriana (CB) foram trituradas utilizando o triturador IKA A11 basic. Com intuito de assegurar um tamanho uniforme das partículas, a CB triturada foi peneirada em uma peneira granulométrica de aço inox com abertura de 0.5 mm. Posteriormente a CB foi hidrolisada utilizando 88 mL de uma solução aquosa de ácido sulfúrico (Synth 98 %) 64% m/v utilizando uma temperatura de 50°C sob agitação constante durante 30 minutos. A suspensão obtida foi então diluída com 880 mL de água ultrapura gelada para interromper a hidrólise. A suspensão resultante foi centrifugada a 6000 rpm durante 10 min (Jouan C3i - CR3i multifuncional centrífuga). O sobrenadante foi decantado e a suspensão resultante foi lavada três vezes com água ultrapura. A suspensão foi então dialisada em tubos de membrana de diálise de celulose (12000-14000 peso molecular) em água ultrapura até o pH da água tornar-se constante. A seguir, a suspensão foi diluída até à concentração de 3% m/v e dispersa por tratamento de ultrassom em um sonicador Sonics Vibra -Cell VC 505 500W 20 kHz com uma sonda de diâmetro de 6 mm utilizando 20% da potência máxima. Por fim, 8ml da suspensão resultante foi transferido para uma placa de petri de poliestireno com diâmetro de 45mm e após evaporação lenta em temperatura ambiente o filme iridescente de NCC obtido.

Preparação de um filme iridescente de NCC revestido com cristal líquido (CL) 4’-(hexiloxi)-4-bifenilcarbonitrila (HOBC).

O filme de NCC obtido foi revestido com o CL 4 '- (hexiloxi) -4-bifenilcarbonitrila (HOBC) (Sigma-Aldrich). O revestimento foi realizado através de um processo de pintura de um lado do filme de NCC com uma solução de HOBC (3% m/m em clorofórmio). Além disso, utilizando a mesma metodologia, um lado de substrato quartzo foi também revestido com HOBC.

Técnicas Empregadas na Caracterização dos Novos Materiais.

O revestimento foi confirmado por microscopia óptica de luz polarizada (MOLP), microscopia eletrônica de varredura (MEV) e microscopia de força atômica (AFM). Os materiais foram ainda caracterizados por espectroscopia vibracional na região do infravermelho (FTIR), espectroscopia eletrônica na região do ultravioleta-visível em modo de transmitância e refletância especular e através de medidas de luminescência. A relação entre a estrutura da superfície e as propriedades termocrômicas foram investigadas utilizando microscopia óptica de transmissão (MOT). A resposta condutora do filme foi comprovada através de medidas de microscopia de força eletrostática (MFE).

Resultados e discussões:

As imagens de MOLP do filme de NCC (Fig. 1) mostram iridescência do filme sob luz não polarizada, indicando que a ordenação nemática quiral da suspensão foi preservada após a secagem, formando uma estrutura periódica responsável pela reflexão de Bragg da luz visível. Algumas regiões apresentam texturas de impressão digital característica da ordenação nemática quiral dos NCC (Fig.1b). As imagens mostram ainda um mosaico de domínios com diferentes formas e cores, devido anisotropia do filme de NCC, onde os comprimentos de P e eixos de inclinação helicoidais são diferentes (GRAY, 2012). Semelhante ao observado para o filme de NCC, as imagens de MOLP do compósito NCC/HOBC (Fig. 1c e 1d) apresentaram iridescência sob exposição de luz não polarizada indicando que a fase nemática quiral da suspensão foi preservada após o revestimento com o cristal líquido. No entanto, a superfície do compósito não apresenta domínios com diferentes orientações sendo formada por um filme de cristais esferulíticos de HOBC (TERCJAK et al., 2008) comprovando o revestimento.

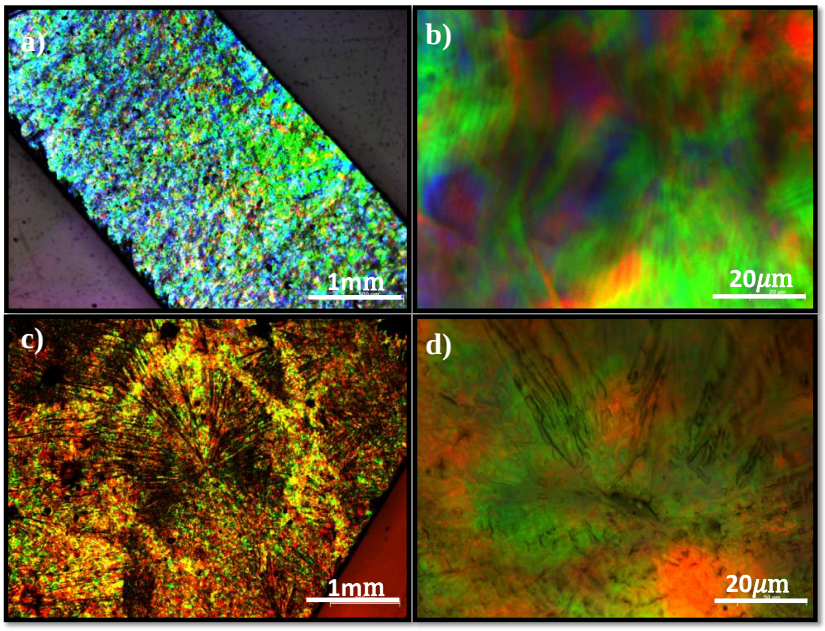


Figura 2. Imagens de MOLP: a e b) Filme iridescente de NCC; c e d) Imagens de MOLP NCC/HOBC.

Imagens de MEV confirmaram a preservação da organização nemática quiral da suspensão de NCC no filme obtido (Fig. 2). A imagem da superfície do filme (Fig. 2a) mostra os NCC alinhados paralelamente com defeitos na direção que surgem a partir de alterações na direção do eixo helicoidal da fase nemática quiral. Na imagem da borda da fratura do filme (Fig. 2b) observa-se uma estrutura em camadas, com organização de longo alcance e rotação no sentido anti-horário, referente a estrutura helicoidal formada pelos planos de NCC (GRAY, 2012). A imagens da secção transversal da fratura do filme podem ser observadas nas figuras 2c e 2d. Na imagem com maior ampliação (Fig. 2d), observar-se uma organização periódica formada por camadas regularmente espaçadas, onde cada período corresponde a uma rotação de 180° em relação ao eixo helicoidal da estrutura nemática quiral dos filmes (P/2). (STEINER; VIGNOLINI, 2014; ZHANG et al., 2013).

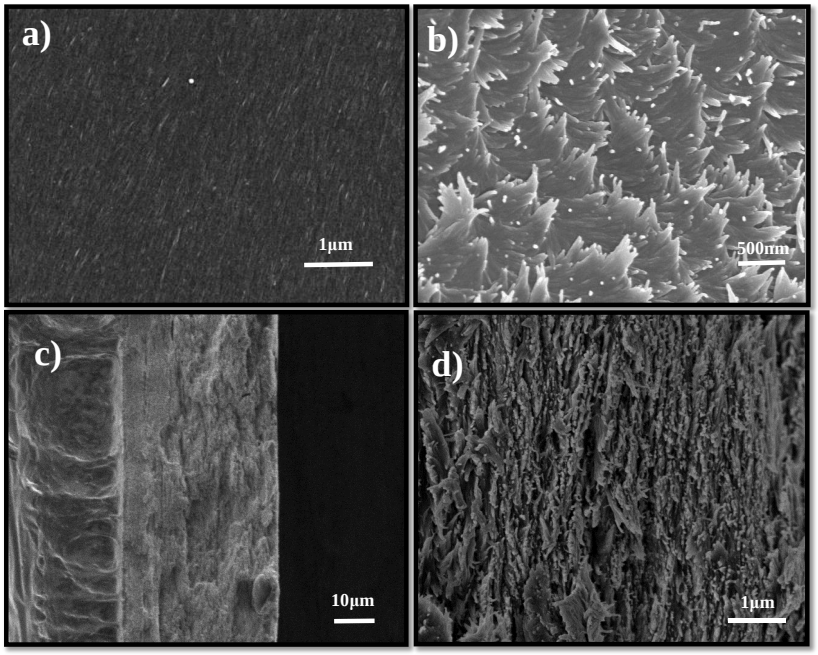


Figura 2. MEV do filme de NCC: a) Imagem da superfície do filme de NCC; b) Vista lateral da fratura do filme; c e d) Imagem da secção transversal da fratura ao longo do filme de NCC.

Imagens de MEV da superfície do filme compósito NCC/HOBC (figura 3a) confirmaram o revestimento da superfície filme de NCC pelo HOBC. A micrografia da borda do compósito (Fig.3b) revela que a estrutura nemática quiral formada pelos planos de NCC foi preservada após do revestimento do filme. As micrografias da secção transversal do filme (Fig. 3c e 3d) também confirmaram o revestimento do filme de NCC pelo HOBC. Observa-se na imagem da figura 3c que a espessura do filme NCC/HOBC aumenta em relação ao filme de NCC puro (de 40,8µm para 60,2 µm). Como não é possível observar uma diferença entre o revestimento de HOBC e o filme de NCC nas micrografias da secção transversal, o aumento da espessura pode ser explicado tanto pelo revestimento da superfície do filme de NCC pelo cristal líquido como também devido ao entumecimento do filme NCC causado pela penetração de parte do HOBC através das camadas de nanocristais de celulose.

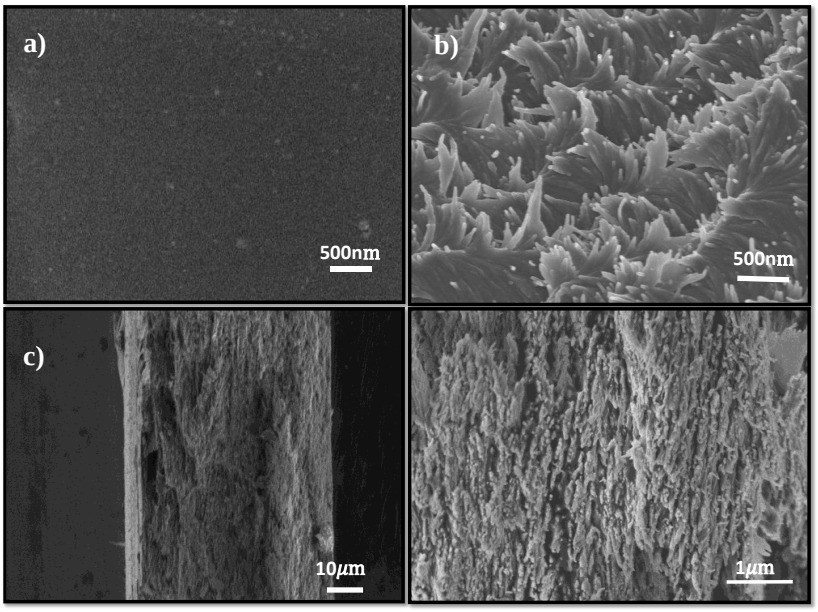


Figura 3. MEV do compósito NCC/HOBC: a) Imagem da superfície do filme; b) Imagem da fratura do filme; c e d) Imagem da secção transversal da fratura do filme.

O revestimento de HOBC no compósito NCC/HOBC foi ainda confirmado através de caracterizações por espectroscopia vibracional na região do infravermelho e luminescência.

As propriedades termocrômicas do HOBC e do compósito NCC/HOBC foram avaliadas por espectroscopia eletrônica na região do UV-VIS em função da temperatura (Fig. 4). Durante o processo de aquecimento, a superfície revestida do compósito muda de opaco para transparente entre 56 °C - 60 °C, semelhante ao comportamento típico de HOBC puro. Este comportamento é esperado uma vez que, como vem sendo descrito na literatura, este cristal líquido nemático pode alternar-se entre uma fase cristalina e nemática (opaco e transparente) através de estímulos externos, como temperatura, campo elétrico ou magnético (TERCJAK; GARCIA; MONDRAGON, 2008; TERCJAK; GUTIERREZ, 2011b; TERCJAK et al., 2009, 2010).

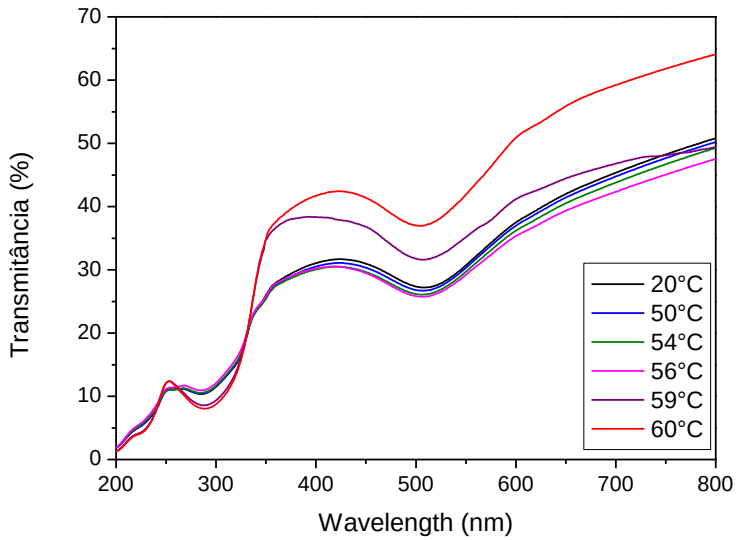


Figura 4. Espectros de transmitância em função da temperatura do compósito NCC/HOCB.

Propriedades termo-sensíveis do compósito NCC/HOBC foram ainda investigados por microscopia óptica transmissão (MOT) entre polarizadores cruzados. As imagens foram adquiridas tanto no processo de aquecimento quanto de resfriamento. As micrografias representativas de MOT durante o processo de aquecimento e resfriamento são apresentados na figura 5. A transição da fase do HOBC no compósito NCC/HOBC realizou-se em aproximadamente 47°C. Além disso, semelhante ao comportamento termo-reversível observado nos espectros de UV-vis em função da temperatura a faixa de transição entre o estado opaco e transparente do CL durante o ciclo de aquecimento/resfriamento é estreita e a transição ocorre na mesma temperatura em ambos processos, sendo a faixa de temperatura 56 a 60 °C para o processo de aquecimento e de 55 a 60°C durante o processo de resfriamento. O comportamento termo-reversível de compósito NCC/HOBC confirmou que o revestimento de HOBC transfere essa propriedade para o compósito investigado.

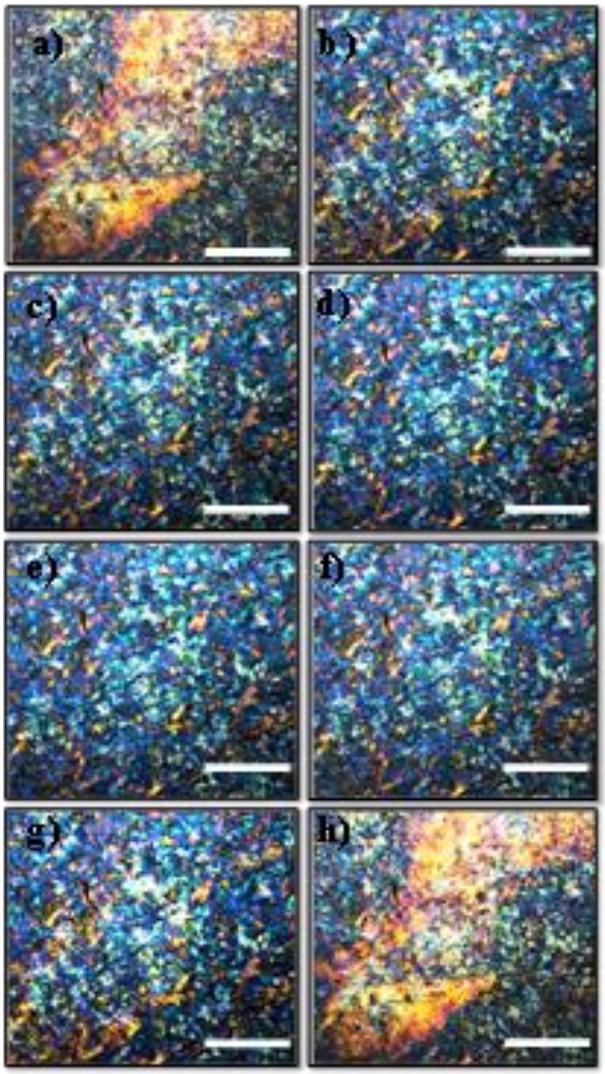


Figura 5. Micrografia de MOT de CNC / HOBC durante o aquecimento realizada em: (a) 30 ° C (b) 47°C, (c) 56 °C (d) 60°C. Durante o arrefecimento em: (e) 60°C (f) 55°C (g) 45°C (h) 30°C.

A microscopia de força eletrostática (EFM) foi utilizada para verificar a resposta condutora do filme compósito NCC/HOBC. A figura 6 apresenta, as imagens de fase de AFM (Fig. 6a) e de EFM aplicando uma voltagem de 0V, 6V, -6V (Fig. 6a-d). Como esperado, nenhum domínio de carga foi detectado na superfície do filme NCC revestido com HOBC quando a tensão de 0 V foi aplicada na ponta do EFM (Fig. 6b). Pelo contrário, como visto nas figuras 19c e d, a aplicação de 6 e -6 V da ponta do EFM permitiu a observação de domínios carregados confirmando que o HOBC na superfície do filme de NCC responde à tensão aplicada de forma independente do sinal (positivo ou negativo) dos valores de tensão. Aplicando ambos 6 e -6 V facilmente pode se detectar domínios carregados bem distribuídos em toda a superfície mapeada com baixo nível de contraste, em torno 30m na imagem de EFM de fase. O baixo

contraste demonstra a fraca resposta à tensão aplicada correspondente a força eletrostática entre a amostra e ponta do EFM. Aqui deve se salientar que as medidas realizadas com filme NCC, não apresentadas aqui, não mostraram quaisquer domínios carregados quando aplicadas as tensões de 6 e -6 V a ponta do EFM, indicando que o revestimento formado pelo cristal líquido HOBC transfere essa capacidade de responder aos estímulos externos (tensão aplicada) à superfície de filme NCC.

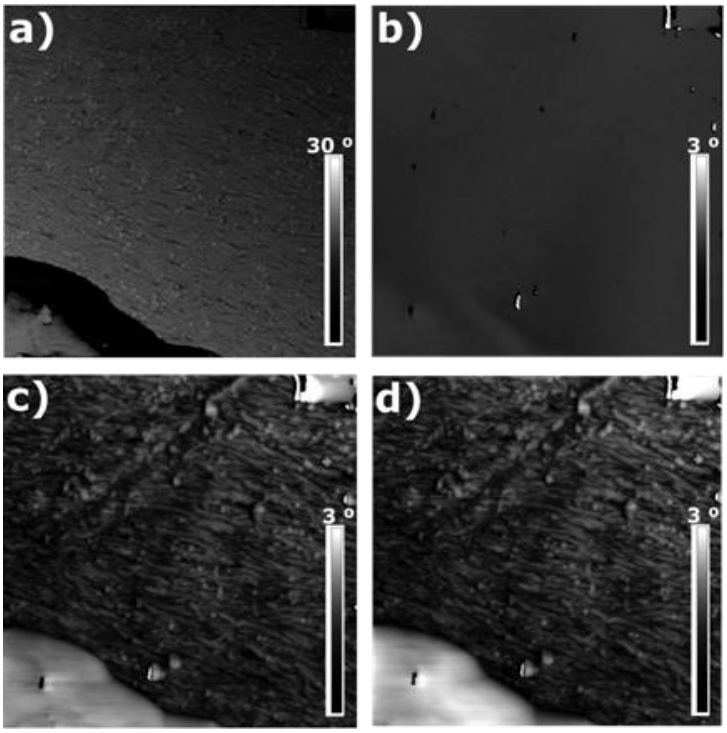


Figura 6. a) Imagens de fase de AFM (3µm x 3µm); Imagens de fase de EFM (3µm x 3µm) do filme NCC/HOBC aplicando-se voltagem de b) 0 V, c) 6 V e d) -6 V.

Conclusões:

Um novo material multifuncional que integra iridescência, resposta condutora e térmica foi preparado através do revestimento de um filme de NCC com o cristal líquido nemático 4'-(hexiloxi)-4-bifenil carbonitrila (HOBC). O material foi obtido como um filme iridescente e auto-suportados e com ordenação nemática quiral. As imagens de MEV confirmaram o revestimento da superfície do filme NCC com o cristal líquido HOBC. As propriedades termocrômicas do novo material foram avaliadas por espectroscopia eletrônica na região do UV-VIS em função da temperatura. O cristal líquido HOBC presente na superfície do filme apresentou resposta óptica em função da temperatura, alternando entre opaco e transparente.

Sendo assim, o revestimento de HOBC atuou como um filtro em relação a refletância seletiva do filme de NCC, resultando em um sensor térmico com propriedades ópticas moduladas em função da temperatura. Além disso, medidas de EFM confirmaram a resposta condutora da superfície revestida à tensão aplicada. Sendo assim, neste trabalho foi apresentada uma nova estratégia para a concepção de uma plataforma para a preparação de um sensor óptico baseado em um filme iridescente de nanocristais de celulose bacteriana que apresenta propriedades térmicas e condutoras e mantêm as propriedades morfológicas e ópticas do filme de NCC puro. O material obtido é promissor para o desenvolvimento de novos dispositivos ópticos, tais como janelas inteligentes e sensores ópticos.

Propriedades ópticas de filmes iridescentes/luminescentes baseados em nanocristais de celulose e corante Rh6G.

Parte experimental:

Preparação de filmes iridescentes/luminescentes baseados em NCC e silica dopados com Rh6G.

Preparação de nanocristais de celulose bacteriana (NCC).

Primeiramente, 5g de membranas de CB foram trituradas utilizando o triturador IKA A11 basic. Com intuito de assegurar um tamanho uniforme de partícula, a CB triturada foi peneirada em uma peneira granulométrica de aço inox com abertura de 0,5 mm. Posteriormente a CB foi hidrolisada utilizando 88 mL de uma solução aquosa 64 % m/v de ácido sulfúrico (Synth 98 %), temperatura em 50°C e sob agitação constante durante 30 minutos. A suspensão obtida foi então diluída com 880 mL de água ultrapura gelada para interromper a hidrólise. A suspensão resultante foi centrifugada a 6000 rpm durante 10 min (Jouan C3i - CR3i multifuncional centrífuga). O sobrenadante foi decantado e a suspensão branca espessa resultante foi lavada três vezes com água ultrapura. A suspensão foi então dialisada em tubos de membrana de diálise de celulose (12000-14000 peso molecular) em água ultrapura até o pH da água tornar-se constante. A seguir, a suspensão foi diluída até à concentração de 3% m/v e dispersa por tratamento de ultrassom em um sonicador Sonics Vibra -Cell VC 505 500W 20 kHz com uma sonda de diâmetro de 6 mm e 20% da potência máxima. Sonicação (energia de 7500 J / g NCC) de 50 ml da suspensão de NCC 3,0% m/v em um béquer de 100 mL.

Preparação de filmes compósitos baseados em NCC e sílica (NS):

Em 4ml uma suspensão aquosa de NCC 3,0% m/v (4 mL, pH 2,4) foi adicionado tetraetoxisilano (33μL, 66μL, 98μL, 131μL) (TEOS Sigma-Aldrich, 98%) sob agitação constante durante 3 horas. Em seguida, a suspensão foi transferida para placas de petri de poliestireno com diâmetro de 45 mm (Pleon). A secagem da suspensão foi realizada em condições ambiente. As amostras foram preparadas variando a quantidade de TEOS de acordo

com as seguintes proporções: 0% m/m (NCC), 12,5% m/m (NS1), 25,0% m/m (NS2), 33,3 % m/m (NS3), e 50,0% m/m (NS4).

Preparação de filmes compósitos NS dopados com Rodamina 6G (NS-Rh):

Em 4ml uma suspensão aquosa de NCC 3,0% m/v (4 mL, pH 2,4) foi adicionado tetraetoxisilano (33μL, 66μL, 98μL, 131μL) (TEOS Sigma-Aldrich, 98%) sob agitação constante durante 3 horas. Em seguida, 200 μL de rodamina 6G (Rh6G Sigma-Aldrich, 99%) 10^{-4}M foram inseridos à suspensão. A suspensão resultante foi então transferida para placas de petri de poliestireno (diâmetro de 45 mm). A secagem da suspensão foi realizada em condições ambiente. As amostras foram preparadas variando a quantidade de TEOS de acordo com as seguintes porcentagens: 0% m/m (NCC-Rh6g), 12,5% m/m (NS1-Rh6G), 25,0% m/m (NS2 - Rh6G), 33,3% m/m (NS3-Rh6G), e 50,0% m/m (NS4-Rh6G).

Preparação de filmes de celulose bacteriana e rodamina 6G (CB-Rh).

Membranas de celulose bacteriana hidratadas (4cm x 4cm x 0,3 cm) foram imersas em 25mL de uma solução etanólica de rodamina 6G 10^{-4} M e mantidas sob agitação (100 rpm) em uma mesa agitadora por 24 horas. Após esse período as membranas foram secas a temperatura ambiente.

Técnicas empregadas na caracterização dos novos materiais.

Os materiais foram obtidos como filmes auto-sustentáveis e caracterizados através das técnicas de microscopia óptica de luz polarizada (MOLP), microscopia eletrônica de varredura (MEV), microscopia eletrônica de transmissão (MET), espectroscopia eletrônica na região do ultravioleta-visível em modo de transmitância e refletância especular e luminescência. Foram também realizadas medidas de luminescência em função do ângulo de detecção ($0^\circ < \theta < 90^\circ$; $0^\circ < \theta < -90^\circ$)) utilizando uma configuração experimental modular, conforme demonstrado na fotografia da (Fig. 7). A configuração experimental modular consiste de um espectrômetro USB Ocean Optics HR2000 + ES , uma fibra óptica (Ocean Optics) QP600-UV Vis (diâmetro do núcleo de 600μm, comprimento total de 1m) para detectar a emissão de luz pela amostra; laser de diodo de 5mW de 405 nm (modo CW, 4nm FWHM) para a excitação de moléculas Rh6G (o feixe do laser é dirigida a um ângulo de 45 °C em relação ao plano de detecção, onde a ponta

da fibra óptica está alinhada perpendicularmente à amostra); uma base rotativa com um goniômetro (suporte da amostra é fixada na parte central da base rotativa e a ponta da fibra, a qual recolhe o sinal emitido, pode girar livremente em torno dele.)

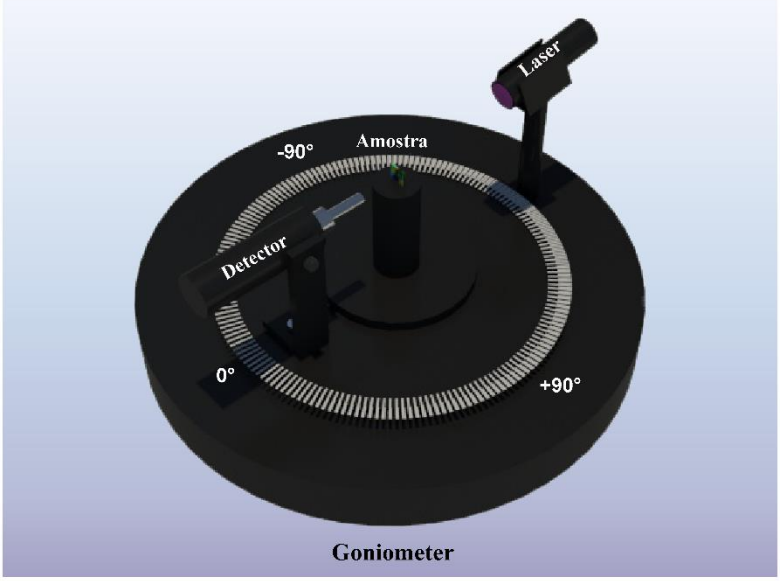


Figura 7. Configuração experimental das medidas de luminescência em função do ângulo de detecção ($0^\circ < \theta < 90^\circ; 0^\circ < \theta < -90^\circ$).

7.2.3. Resultados e discussões:

Os compósitos NS4 e NS4-Rh com diferentes concentrações de sílica foram preparados. A porcentagem de sílica presente nos filmes compósitos foi estimada através do resíduo das curvas TG realizadas em atmosfera oxidante. As amostras apresentaram 0%, 8.5%, 15.4%, 20.7% e 35.2% de resíduo.

A variação na proporção NCC/sílica nos filmes compósitos permitiu o controle das propriedades ópticas dos materiais compósitos. Imagens de microscopia óptica de luz polarizada (MOLP) dos compósitos NS-Rh (Fig. 8) mostraram o deslocamento da coloração para a vermelho com o aumento da proporção de sílica nos filmes, enquanto a textura característica da fase nemática quiral permaneceram inalteradas, com regiões que apresentam linhas semelhantes a impressões digitais.

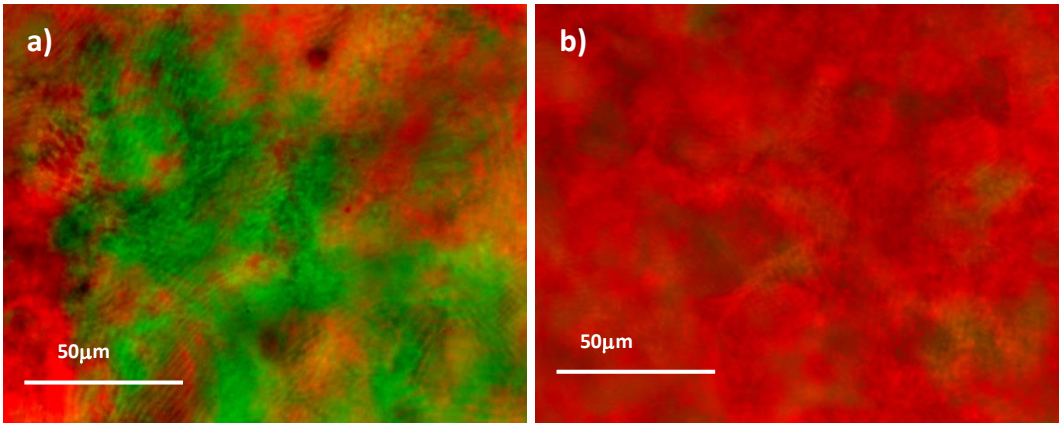


Figura 8. Imagens de MOLP dos compósitos: a) NS1-Rh e b) NS4-Rh.

A morfologia dos filmes compósitos NS-Rh foi avaliada através de medidas de microscopia eletrônica de varredura (MEV). As imagens de MEV podem ser observadas na figura 9.

As figuras 9a e 9b mostram imagens da borda do compósito NS4-Rh. Nestas imagens observa-se uma estrutura com organização de longo alcance formada por camadas rotacionadas no sentido anti-horário, esta estrutura é característica dos filmes de NCC sendo referente a planos de nanocristais de celulose com ordenação nemática quiral. A interpretação desta textura, semelhante a um leque, observada nas micrografias da fratura está, portanto, de acordo com a detecção da imagem na mesma direção do eixo diretor do arranjo a helicoidal dos filmes (GRAY, 2012).

A secção transversal de fratura do filme é mostrada nas figuras 9c e 9d. A orientação do eixo diretor do arranjo helicoidal é de novo observado com a posição, mas, neste caso, perpendicular à superfície do filme. As micrografias revelam as camadas regularmente espaçadas formadas pela automontagem dos nanocristais de celulose. A estrutura periódica está presente ao longo de toda a espessura do filme, e cada período corresponde a uma rotação de 180° entre planos da estrutura nemática quiral (P/2). Estas observações corroboram com os resultados obtidos através de MOLP dos filmes compósitos, confirmação que a organização nemática quiral dos mesmos foi preservada após a incorporação da sílica e Rh6g.

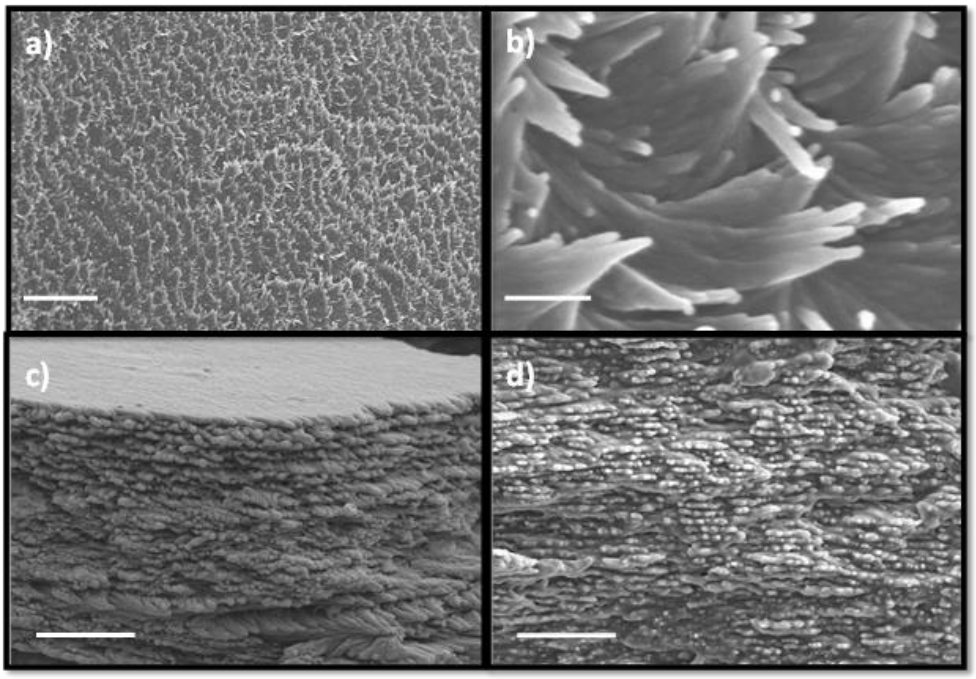


Figura 9. Imagens de MEV do compósito NS4-Rh: a) Imagem da fratura da superfície do filme mostrando a estrutura em camadas formada pelos nanocristais de celulose (barra de escala, 2.5μm; b) Imagem da fratura do filme mostrando a morfologia dos nanocristais de celulose semelhantes a nanofios e a torção dos mesmos à esquerda (barra de escala, 0.5μm); c e d) Secção transversal da fratura do filme (barra de escala, 2 μm e 2,5μm respectivamente).

Caracterização óptica dos compósitos NS e NS-Rh foi realizada nos modos de transmitância e refletância. Os espectros de refletância foram realizados em função do ângulo de incidência ($15^\circ < \theta < 60^\circ$) (Fig. 10). A figura 10 mostra os gráficos referentes a variação da posição do comprimento de onda máximo (λ_0) das bandas dos espectros refletância especular dos compósitos em função do cos θ. Os resultados são correspondentes a reflexão seletiva dos filmes devido a difração de Bragg. O comportamento dos espectros obedece a relação de De Vries (equação 1), onde λ_0 é deslocado para o azul com o aumento no ângulo de incidência em relação à normal do filme.

$$\lambda_0 = n_m P \cos \Theta \qquad (1)$$

Onde θ é o ângulo de incidência entre o raio incidente e normal a superfície, P é o passo de estrutura nemática quiral, (n_m) é o índice de refração médio.

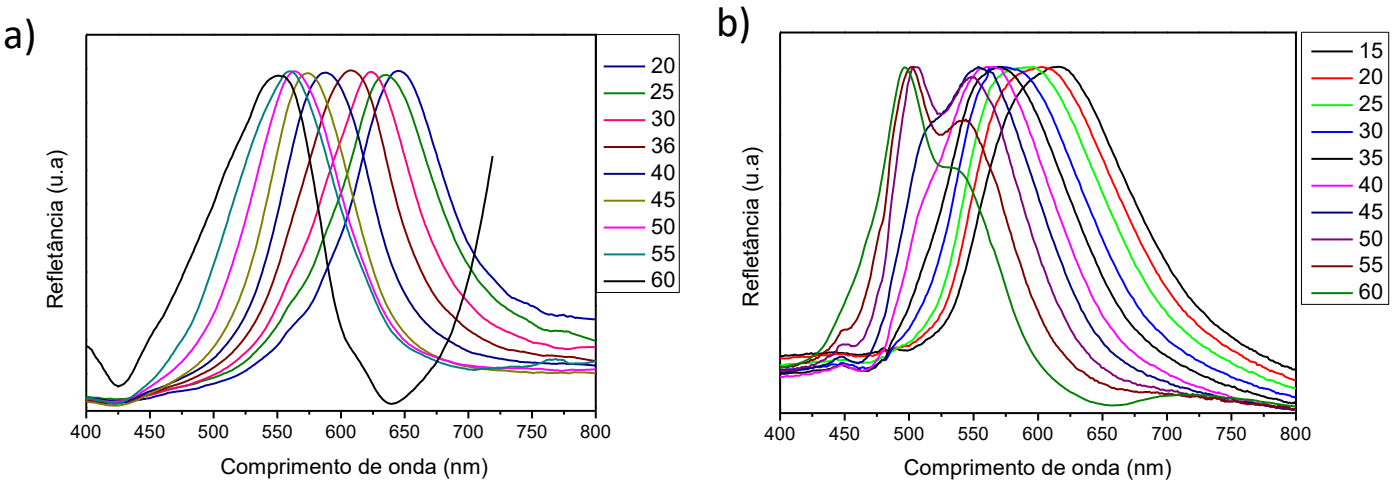


Figura 10. Espectros de refletância especular dos filmes compósitos: a) NS4 b) NS4-Rh.

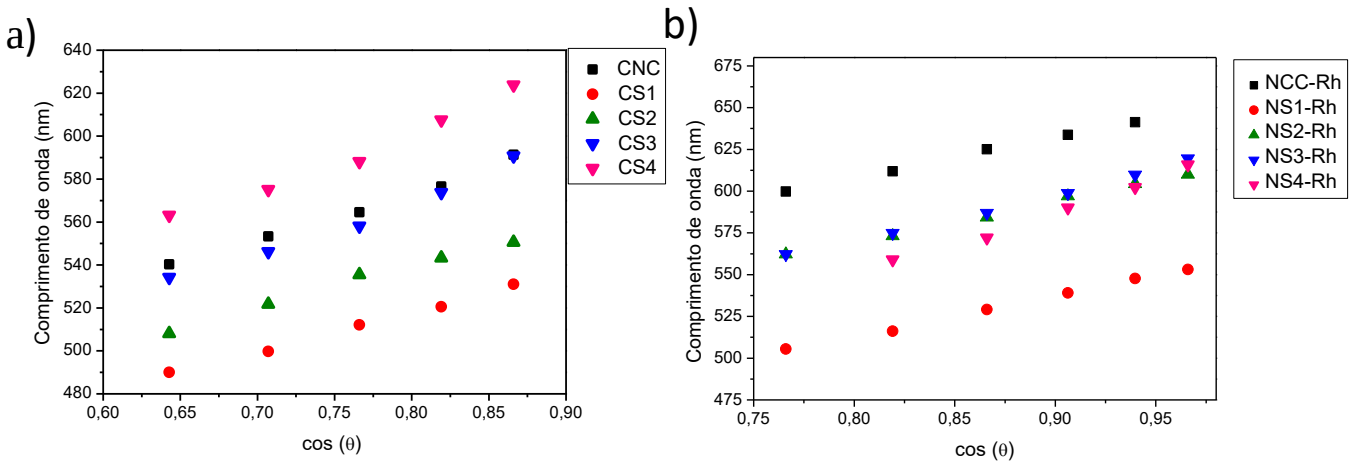


Figura 11. Variação do comprimento de onda máximo da banda de refletância em função do cos (Θ) para os compósitos: a) NS4 b) NS4-Rh.

Nos espectros de refletância especular da amostra NS4-Rh (Fig. 9b) observa-se ainda que a partir de 50°, os espectros de refletância apresentam um vale, centrado em 528nm, referente a banda de absorção do corante. Este comportamento foi observado em todos os compósitos NS-Rh e sugere que quando os filmes refletem na mesma região de absorção do corante ocorre um processo de retro absorção em que parte da luz refletida é absorvida pelas moléculas de Rh6G presente no filme. Um comportamento similar é observado quando a luz emitida pelo filme é detectada em diferentes ângulos, o qual será discutido mais à frente.

Usando a relação de De Vries, o P da estrutura nemático quiral pode ser determinado através do coeficiente angular dos gráficos da figura 11. A tabela 1 apresenta os valores de P que foram determinados para os diferentes compósitos. Observa-se que o aumento da porcentagem de sílica gera um aumento de P, porém o filme de NCC puro e dopado com Rh6G apresentam valores de P intermediários aos valores obtidos para as amostras com a maiores e menores proporção de sílica. Comportamento similar foi relatado por Shopsowitz e colaboradores (SHOPSOWITZ et al., 2010), demonstrando que o aumento na proporção de sílica nos compósitos gera um aumento do tamanho do P. Os autores propuseram que este comportamento é possivelmente causado pelo aumento da espessura de sílica na superfície dos nanocristais, bem como devido a interações eletrostáticas entre as espécies carregadas negativamente, sílica e celulose cristalina durante o processo de condensação. Estas sugestões são possíveis devido ao índice de refração da sílica e da celulose (1.46 e 1.54, respectivamente) serem muito próximos. O mesmo comportamento foi observado para os compósitos contendo Rh6G (NS-Rh) (Fig. 11b), a presença de Rh6g contribui para aumentar o P em comparação aos compósitos que não contém o corante, permitindo um controle complementar das propriedades ópticas destes materiais.

A periodicidade característica destes materiais têm sido amplamente observada em cristais líquidos nemáticos quirais (BECK-CANDANEDO; ROMAN; GRAY, 2005). Recentemente Andrews e colaboradores demonstraram uma boa correlação entre a periodicidade da estrutura observada em nas imagens de secção transversal de MEV e o valor de P/2 dos filmes dos filmes de NCC (ZHANG et al., 2013b).

A análise da figura 9d, mostra que os espaçamentos regulares correspondem a valor de P/2 igual a 115,0 ± 2, 6 nm para o compósito NS4-Rh. Este valor é comparável ao valor calculado usando a equação de De Vries (Tabela 1) em que P é 239,4 ± 12,2 nm para esta composição. Estes valores estão de acordo com a condição de Bragg em que P deve ser da ordem de algumas centenas de nanômetros.

Tabela 1. Determinação de P através de medidas de reflectância especular e MEV.

Amostra	**P – Reflectância Especular (nm)**	**P/2– MEV (nm)**
NCC	143 ± 4	-
NS1	122 ± 6	-
NS2	119 ± 3	-
NS3	168 ± 5	-
NS4	190 ± 8	-
NCC-Rh	141 ±5	78 ± 1
NS1-Rg	138 ± 7	82 ± 2
NS2-Rh	140 ±5	81 ± 5
NS3-Rh	191 ±7	96 ± 7
NS4-Rh	240 ±10	116 ±3

A luminescência dos compósitos dopados com Rh6G foram investigados. Os espectros de emissão de compósitos contendo diferentes concentrações de sílica são mostrados na figura 12. Quando a excitação é monitorada em 348 nm, duas bandas de emissão podem ser observadas: a primeira em 430 nm, devido a emissão de nanocristais celulose (LI et al., 2009); uma segunda banda observada é a banda de emissão característica da Rh6G.

Os espectros de emissão dos filmes compósitos, figura 12, apresentam uma banda de emissão em 556 nm e um ombro em 605 nm, e o espectro da amostra NCC-Rh que não contém sílica, apresenta uma banda em 567nm e um ombro acima de 610 nm, indicando da formação de dímeros fluorescentes (BUJDÁK, 2006). O desvio espectral batocrômico neste caso pode ser atribuído às alterações nas propriedades químicas do meio circundante e a diminuição da concentração de Rh6g com adição de sílica no compósito. A adição de sílica, portanto implica na diminuição da quantidade total de dímeros nas amostras.

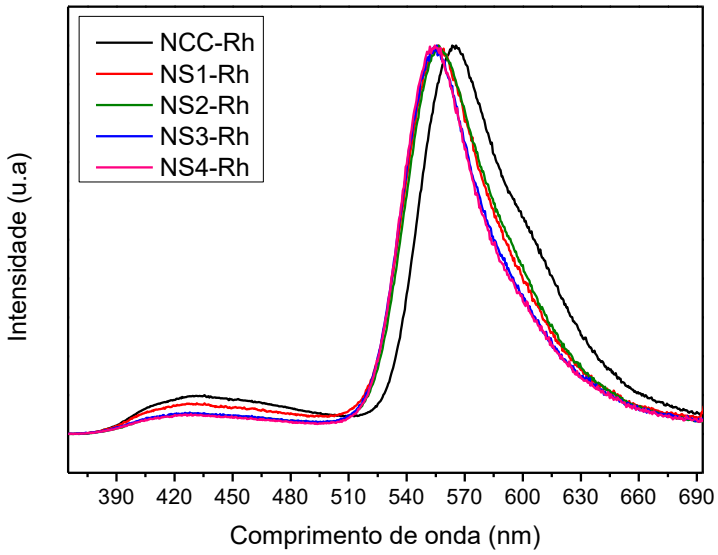


Figura 12. Espectros de emissão dos filmes compósitos NS- Rh, com excitação em 348nm.

Valores de rendimentos quânticos e tempos de vida de todas as amostras estão listadas na tabela 2. Para as moléculas Rh6G, os valores encontrados estão de acordo com o que vem sendo relatado na literatura (ANEDDA et al., 2005). O tempo de vida do compósito com maior concentração sílica (NS4-Rh), é 4.23 ± 0.01 ns e o rendimento quântico estimado é de 0.5, enquanto que para a amostra sem sílica (NCC-Rh), observamos a diminuição no tempo de vida, sendo este 3.74 ± 0.02 ns, enquanto o rendimento quântico diminui para 0.15. Os valores obtidos corroboram com a discussão anterior sobre os espectros de emissão dos filmes compósitos dopados com Rh6G, o quais indicam que a adição de sílica implica na diminuição da quantidade total de dímeros nas amostras e, portanto, em maiores valores de rendimento quântico e tempo de vida.

Tabela 2 – Valores de rendimentos quânticos e tempos de vida dos filmes: NCC-Rh com excitação monitorada em 528nm e emissão em 567nm; NS1-Rh, NS2-Rh, NS3-Rh e NS4-Rh com excitação monitorada em 528nm e emissão em 556nm.

Amostras	τ **(ns)**	ϕ
NCC-Rh	3,74 ± 0,018	0,15
NS1-Rh	3,88 ± 0,02	0,40
NS2Rh	4,21 ± 0,01	0,50
NS3Rh	4,44 ± 0,01	0,65
NS4Rh	4,23 ± 0,01	0,50

Com intuito de verificar a influência da estrutura fotônica destes materiais na luminescência dos filmes foram realizadas medidas de luminescência em função do ângulo de detecção ($0^\circ < \theta < 90^\circ$ e de $0^\circ < \theta < -90^\circ$). As figuras 13a e 13b apresenta os espectros de emissão da amostra NS4-Rh em função do ângulo de detecção. Analisando os espectros observa-se que ocorre um estreitamento da banda de emissão entre 45° a 90° e de -40° a -90° com simultâneo deslocamento do comprimento de onda máximo (λ_0) para o vermelho. Este comportamento pode ser melhor observado nos gráficos de λ_0 e largura a meia altura das bandas de emissão em função do ângulo de detecção (Fig. 13b). Analisando os gráficos da figura 13c observa-se que os deslocamentos de λ_0 ocorrem concomitante com as variações na largura a meia altura da banda emissão. Estes resultados, juntamente com os dados discutidos acima, sugerem que este comportamento ocorre devido a supressão de uma faixa de comprimentos de onda da luz emitida, quando a mesma é concomitante com a luz refletida.

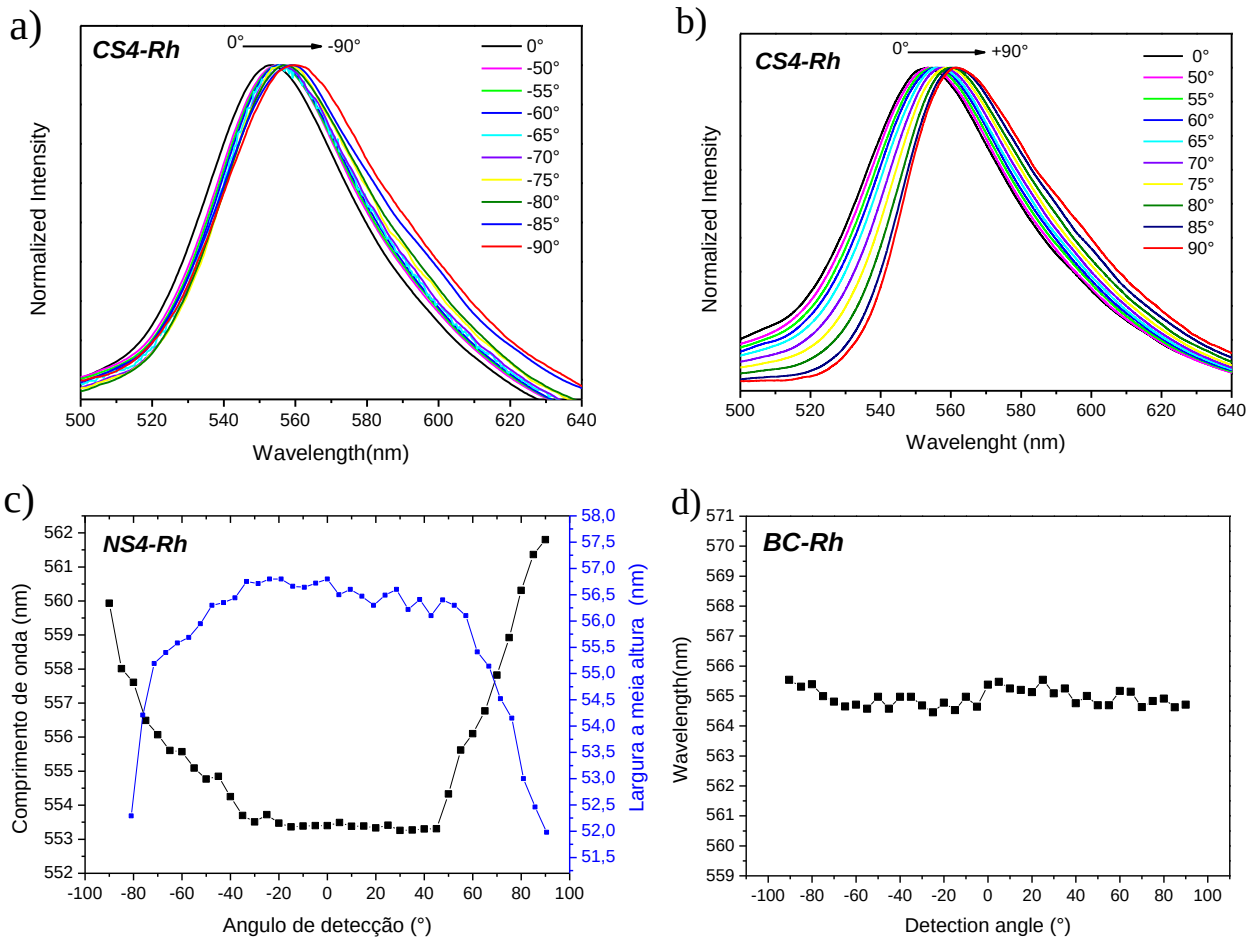


Figura 13. a) Espectros de emissão do filme compósito NS4-Rh em função do ângulo de detecção (0° a -90°), com excitação em 348nm; b) Espectros de emissão do filme compósito NS4-Rh em função do ângulo de detecção (0° a 90°), com excitação em 348nm; c) Variação do comprimento de onda máximo e da largura a meia altura dos espectros de emissão do compósito NS4-Rh em função do ângulo de detecção; d) Variação do comprimento de onda máximo dos espectros de emissão do compósito CB-Rh em função do ângulo de detecção.

Este comportamento pode ser melhor observado na figura 14 que apresenta uma comparação entre os espectros de emissão da amostra NS4-Rh detectados no ângulo de 20° e 90° e os espectros de refletância especular nos ângulos de 20° e 50°. Quando o ângulo de detecção aumenta de 20° para 90° o comprimento máximo da banda de emissão desloca-se para o vermelho, concomitantemente, o espectro de refletância desloca em direção ao azul à medida que o ângulo de incidência aumenta (de 20 a 50°).

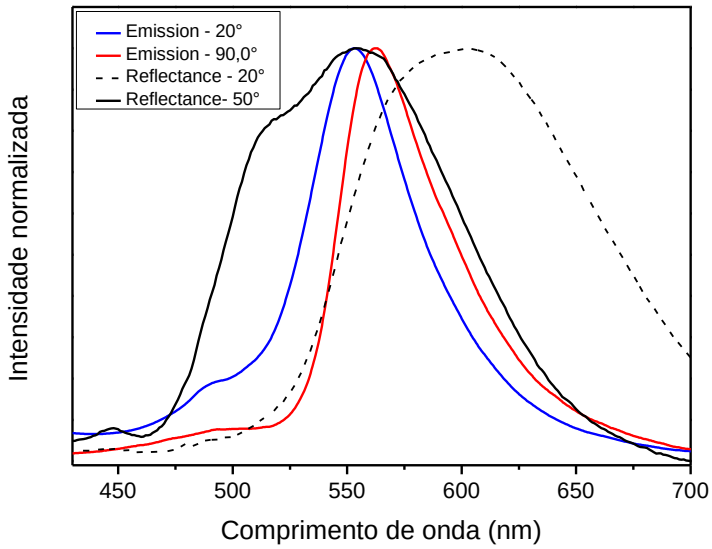


Figura 14. Comparação entre os espectros de emissão do filme compósito NS4-Rh detectados com ângulo de 20° e 90° e excitação em 348nm e os espectros de refletância especular nos ângulos de 20° e 50°.

Um comportamento similar ao discutido acima é também observado nas demais amostras, o qual é demonstrado nos gráficos da figura 15, que apresenta a variação de λ_0 dos espectros de emissão dos compósitos NS-Rh em função do ângulo de detecção. Observa-se que a variação em λ_0 no espectro ocorre em intervalos angulares diferentes, nas diferentes amostras.

Os resultados acima discutidos sugerem que a estrutura periódica com ordenação nemática quiral do filme atua como um filtro interno causando uma seletiva supressão de uma faixa de comprimentos de onda da luz emitida com variação do ângulo de detecção. Além disso, este comportamento depende das propriedades ópticas do material, sendo influenciado pela posição da banda proibida (do inglês “stop band”) da estrutura fotônica.

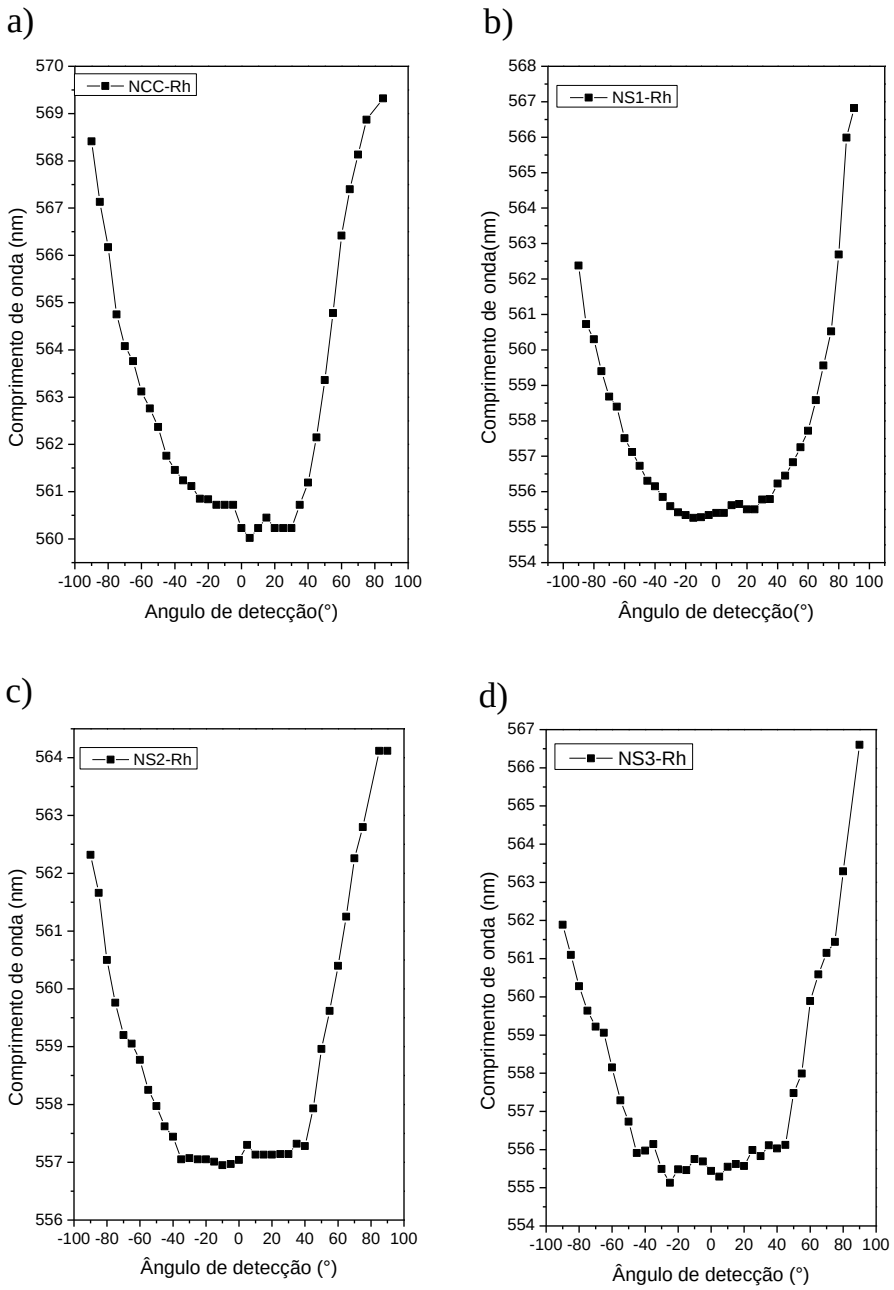


Figura 15. a) Variação do comprimento de onda máximo dos espectros de emissão dos compósitos NS-Rh em função do ângulo de detecção ($-90° < \theta < 90°$).

Conclusões

Novos materiais compósitos baseados em NCC e sílica dopados com Rh6G foram obtidos na forma de filmes auto-suportados, iridescentes, luminescentes e com ordenação nemática quiral. As propriedades ópticas dos filmes compósitos mostraram se sintonizáveis por meio alterações na concentração de sílica. Os filmes mostraram ainda a capacidade de modular a emissão de luz em função do ângulo de detecção. Este efeito sugere que estrutura periódica

com ordenação nemática quiral do filme atua como um filtro interno causando uma seletiva supressão da luz emitida pelo filme. Estes novos materiais funcionais demonstram o benefício da integração da luminescência e iridescência em um filme auto suportado com ordenação nemática quiral e sugerem uma nova via para modular a emissão de espécies luminescentes, sendo assim uma promessa para o desenvolvimento novos dispositivos ópticos com potencial para aplicações como, sensores, lasers ou filtros sintonizáveis.

7.3 Fibroína da seda como um biotemplate para a preparação de monolitos de sílica porosa hierárquicos para aplicações em lasers aleatórios.

7.3.1. Parte experimental:

Extração de fibroína de seda.

O método de extração de fibroína utilizado foi baseado em métodos anteriormente reportados na literatura (ROCKWOOD et al., 2011). Cinco gramas de casulo do bicho da seda foram inseridos em 2L de solução de Na_2CO_3 a 0,02 M a 100 °C durante 30 minutos, posteriormente foram lavados em 1L de água destilada por 20 min, este processo foi repetido 3 vezes de modo a remover a sericina restante nas fibras de fibroína. As fibras de fibroína foram então dissolvidas em uma solução de LiBr a 9.3M em uma proporção de 4 ml solução a cada 1 g de fibroína. A solução resultante foi dialisada por 48 h utilizando 2 litros de água ultrapura a cada 25 ml de solução, neste período foram realizadas quatro trocas de água, uma a cada 12 horas. Um de solução aquosa de fibroína 8,5% (m/v) foi obtida após a duas centrifugações da solução dialisada a 20,000rpm a 4ºC durante 20 minutos. A solução final foi armazenada a 4 °C antes da utilização.

Preparação de monolitos híbridos orgânico-inorgânicos (HOI) baseados em sílica e fibroína (SF).

O tetraetoxissilano (TEOS, Sigma-Aldrish 98%), solução aquosa de HCl 0,3 M (cloreto de ácido Synth 98%) foram misturados em uma proporção molar de 1: 0,008 respectivamente e mantidos sob agitação por 1 hora. Em seguida, híbridos orgânico-inorgânicos baseados em sílica e fibroína foram preparados através da inserção da mistura de uma solução aquosa de fibroína 8,5% m/v e 1 mL de uma solução aquosa de NH_4OH 0,6M. As amostras foram preparadas contendo as seguintes proporções em massa de sílica e fibroína: 1.00:0.00 (SF0), 0.985:0.015 (SF1), 0.97:0.03(SF2), 0.925:0.075 (SF3), 0.85:0.15 (SF4), respectivamente. As misturas foram envelhecidas durante 15 dias e depois tratadas em um forno a 40 °C durante 24 h.

Preparação de monólitos de sílica porosa.

Com intuito de preparar monolitos de sílica porosa, os monolitos obtidos foram tratados termicamente. A rampa de aquecimento utilizada para calcinar a fração orgânica das amostras pode ser observada na tabela 3. Os monolitos de sílica obtidos foram nomeados de S0, S1, S2, S3 e S4, correspondentes aos respectivos monolitos híbridos SF0, SF1, SF2 SF3 e SF4.

Tabela 3. Rampa de aquecimento utilizada para calcinar a fração de fibroína presente nos monolitos híbridos SF. Temperatura de aquecimento, taxa de aquecimento e o tempo que as amostras foram mantidas nas correspondentes temperaturas são apresentadas na tabela.

Temperatura (°C)	**Taxa de Aquecimento ($°C.min^{-1}$)**	**Tempo (h)**
40	1	4
60	1	12
80	1	12
100	1	4
120	1	4
150	1	1
200	2	2
250	2	2
300	2	2
400	2	2
500	2	2
600	2	2
700	2	4

Preparação das amostras de sílica porosa contendo Rodamina 6G.

Os monolitos de sílica obtidos foram inseridos em 1 mL de uma solução etanólica de Rodamina 6G (Rh6G) 10^{-4}M durante 24 horas e então secas por 2 horas em uma estufa a 40°C.

Técnicas Empregadas na Caracterização dos Novos Materiais.

Os materiais foram obtidos na forma de monolitos e caracterizados através das técnicas de microscopia eletrônica de varredura (MEV), análise termogravimétrica (TG), espectroscopia Raman e espectroscopia de ressonância magnética nuclear do estado sólido (RMN). Os monolitos porosos de sílica foram ainda caracterizados por medidas de porosimetria e área superficial e avaliados quanto a sua ação laser aleatório.

7.3.2 Resultados e discussões:

Caracterização dos híbridos orgânico – inorgânicos (HOI) baseados em sílica e fibroína (SF).

Os HOI baseados em sílica e fibroína foram obtidos na forma de monolitos rígidos apresentando coloração gradual de transparente para branco opaco com o aumento da concentração de fibroína (Fig. 15a). De acordo com análises termogravimétricas as quantidades finais de fibroína nos monolitos preparados foram de 3.9, 7.9, 10.2 e 15.8% (m/m).

Os monolitos obtidos foram caracterizados morfologicamente através de medidas de MEV. A figura 16 apresenta micrografias do monolito SF3. Nestas imagens observar-se claramente a precipitação de nanofibras de fibroína entre as nanopartículas esféricas de sílica. Em uma micrografia da superfície (Fig. 16b) é possível observar as nanofibras de fibroína saindo do monolito. Na figura 16c observa-se a imagem de um aglomerado na superfície do monolito formado por nanofibras de fibroína com diâmetro de 20-30 nm. A imagem de uma fratura do monolito (Fig. 16d) mostra ainda nanofibras de fibroína no interior do monolito. Estes resultados sugerem que no processo de preparação das amostras a hidrólise e a condensação de TEOS pode levar à formação de nanofibras de fibroína entre as nanopartículas de sílica. A precipitação das nanofibras de fibroína são responsáveis pela dispersão da luz visível, levando a um aumento gradual da densidade óptica das amostras com o aumento de concentração de fibroína.

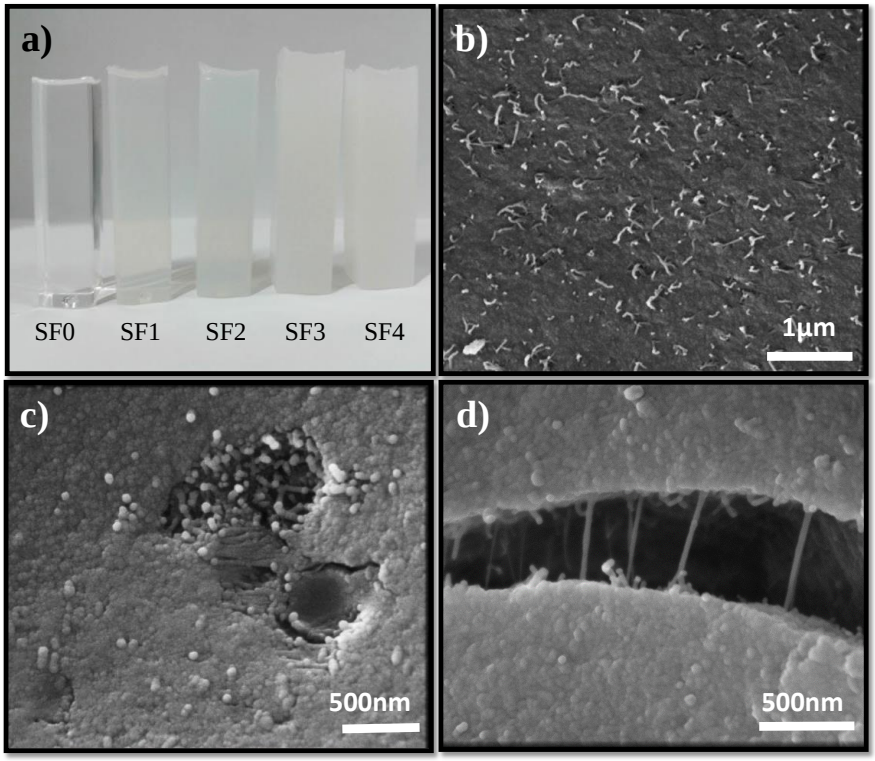


Figura 16. a) Fotografia dos monolitos HOI baseados em sílica e fibroína; b) Imagem de MEV da superfície do monolito SF3; c) Imagem de MEV de um aglomerado de nanofibras na superfície do monolito SF3; d) Imagem de uma fratura do monolito SF3.

A fibroína da seda pode apresentar diferentes conformações, que por sua vez apresentam diferenças significativas em suas propriedades. Os materiais que apresentam fibroína com preferencial conformação folha-β apresentam alta cristalinidade, resistência à ruptura e rigidez (KAPLAN; MCGRATH, 2012). Fibras de seda têm propriedades mecânicas excepcionais e são insolúveis em solventes orgânicos e água devido à natureza hidrofóbica da proteína e a presença de um alto teor de conformação folha-β. Assim, a preparação de HOI baseados em sílica e fibroína nos quais a fibroína apresente preferencialmente esta conformação é de grande interesse devido as características que a mesma pode proporcionar aos novos materiais.

A fim de investigar a conformação das nanofibras de fibroína presentes nos monolitos os mesmos foram caracterizados por espectroscopia Raman e espectroscopia de RMN de estado sólido. Os resultados indicaram a precipitação de nanofibras de fibroína nas amostras com preferencial conformação folha-β. Os resultados demonstraram ainda que o aumento da concentração de fibroína de seda nos monolitos induz a formação de fibroína com maior proporção de conformação folha-β.

Os monolitos híbridos baseados em sílica e fibroína foram obtidos via hidrólise e policondensação de TEOS produzindo etanol como um produto secundário. De acordo com os

resultados discutidos acima, sugere-se que o etanol produzido gradualmente no processo de polimerização induz a auto-montagem de cadeias de fibroína na forma de nanofibras com preferencial conformação folha-β. Sendo assim, o crescimento de nanofibras de fibroína inicia-se na fase de gelificação e continua durante o envelhecimento, quando uma rede de sílica tridimensional é formada. Em seguida, neste trabalho, as nanofibras de fibroína formadas dentro dos monolitos foram utilizadas como espaçadores orgânicos e removidas seletivamente através de tratamento térmico. Este processo permitiu a formação de monolitos porosos de sílica como demonstrado na ilustração abaixo (Figura 17).

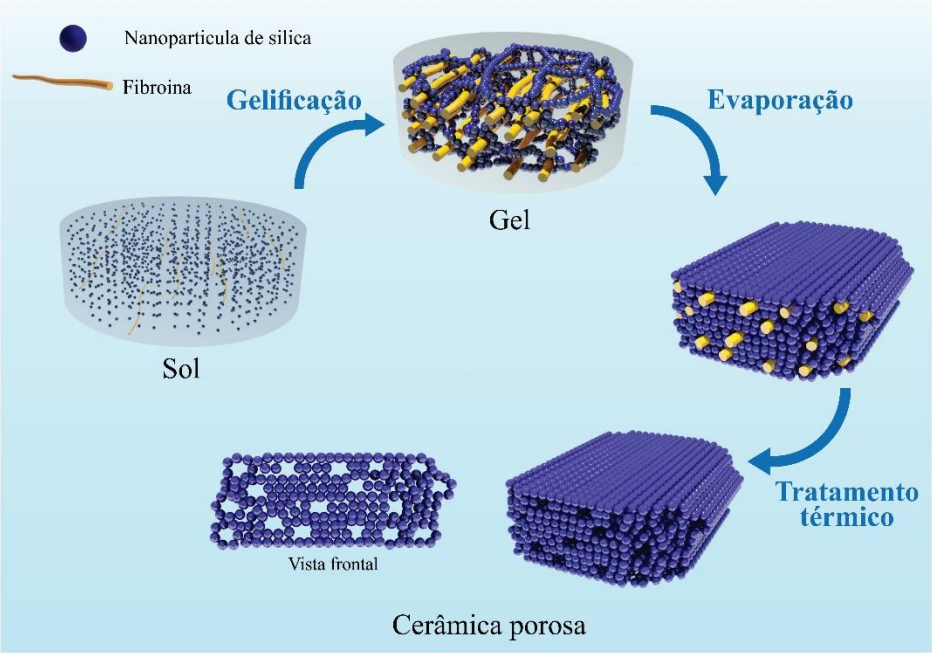


Figura 17. Uma ilustração esquemática da precipitação da nanofibras de fibroína entre as nanopartículas de sílica com posterior calcinação formando uma cerâmica porosa.

Após o tratamento térmico todas as amostras foram obtidas como monólitos rígidos e, como esperado, com mudança gradual de coloração de transparente para branco opaco com o aumento da concentração inicial de fibroína (Figura 18a).

A caracterização morfológica dos monolitos de sílica obtidos foi realizada através de medidas de MEV. A figura 18 apresenta as micrografias representativas do monolito poroso de sílica S3. Na figura 18b é possível observar a presença de poros dispersos em toda a superfície monólito. Imagens da fratura monólito podem ser observadas nas figuras 18c e 18d, onde observa-se claramente a presença de poros na forma de canais com diâmetros de centenas de nanômetros. A estrutura porosa dos monolitos de sílica foi também analisada por meio de medidas de adsorção de nitrogênio. Os resultados demonstraram que após a calcinação da

nanofibras de fibroína, poros hierárquicos foram formados, sendo estes da ordem de macroporos como observado nas imagens de MEV e da ordem de mesoporos como demonstrado pelos resultados da análise de adsorção de nitrogênio.

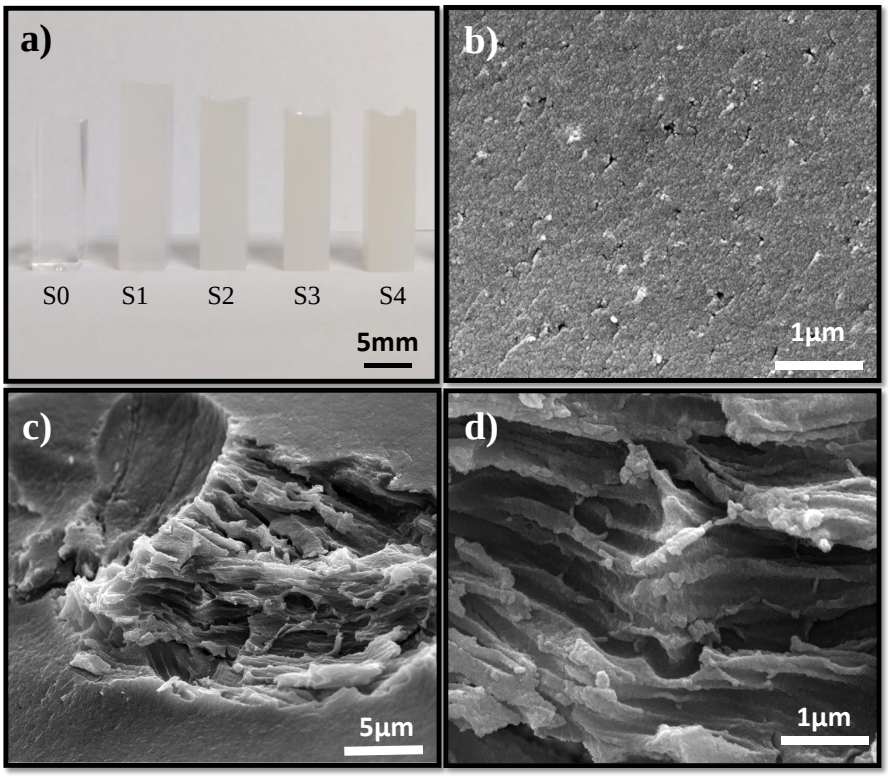


Figura 18. a) Fotografia dos monolitos de sílica; b) Imagem do MEV da superfície do monolito S3; c e d) Imagem de MEV de uma fratura do monolito S3.

Com intuito de caracterizar a ação laser aleatório (LA) das amostras preparadas, monolitos de sílica porosa dopados com Rh6G foram de expostos a excitação em 532 nm utilizando o segundo harmônico de um laser Nd:YAG pulsado, e espectros de emissão LA foram registrados após cada pulso de excitação em diferente energias. As figuras 19a e 19b mostram os gráficos de intensidade e de largura da banda de emissão em função da energia de excitação. Nestes gráficos é possível observar um aumento da eficiência de emissão após o limiar laser concomitante com um estreitamento da largura de banda. Os valores referentes ao limiar laser e eficiência de inclinação estão resumidos na Tabela 4. Observa-se que as amostras apresentam baixo limiar laser e alta eficiência de inclinação sendo assim adequados para aplicações em LA. Observa-se ainda que como esperado o aumento na porosidade das amostras implica em maior desempenho LA, sendo a amostra S4 a que apresentou maior eficiência de inclinação e menor limiar laser.

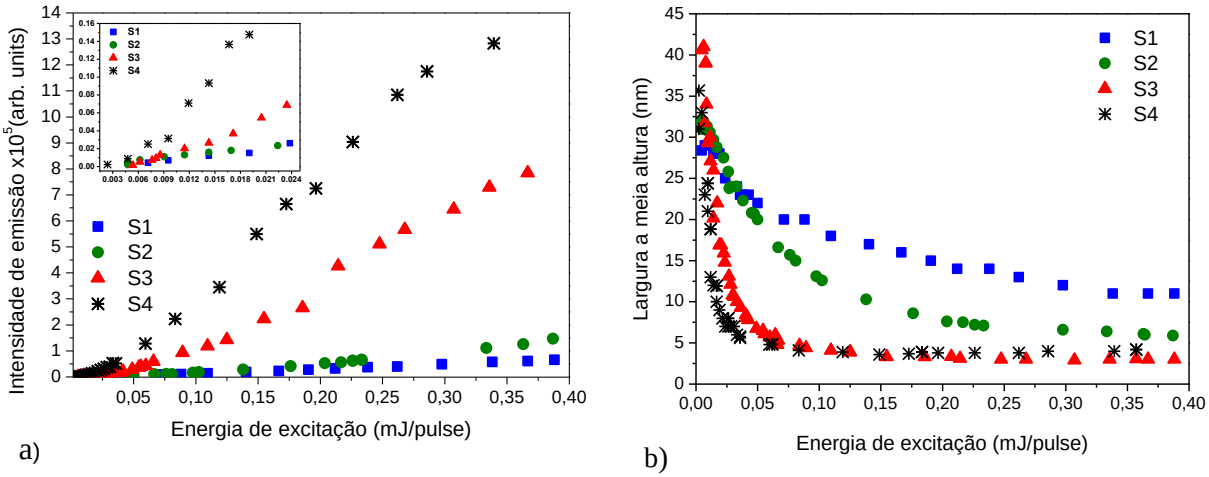


Figura 19. a) Intensidade da banda de emissão em função da energia de excitação; b) Largura a meia altura da banda de emissão em função da energia de excitação.

Tabela 4: Valores de limiar laser e eficiência de inclinação.

Amostras	Limiar laser (mJ)	Eficiência de inclinação (arb. units)
S1	0.1985	11
S2	0.0745	23
S3	0.0144	160
S4	0.0097	280

Os espectros de emissão em função da energia de excitação da amostra S4 podem ser observados na figura 20. Com o aumento da energia de excitação, observou-se um comportamento típico de emissão LA, tal como descrito antes. Entretanto com o aumento da energia de excitação acima de 0,55 mJ, ocorre o deslocamento do espectro de emissão para o vermelho devido a processos de reabsorção/reemissão concomitante com o aparecimento de algumas bandas estreitas. Estas bandas podem ser atribuídas a sobreposição entre a emissão LA e bandas Stokes do corante, similares a exemplos que vem sendo relatados na literatura (YASHCHUK, 2015; YASHCHUK et al., 2014). Esse comportamento ocorre devido ao efeito de espalhamento Raman estimulado, sendo correspondente aos espectros Raman da Rh6G (BACHELARD et al., 2014b).

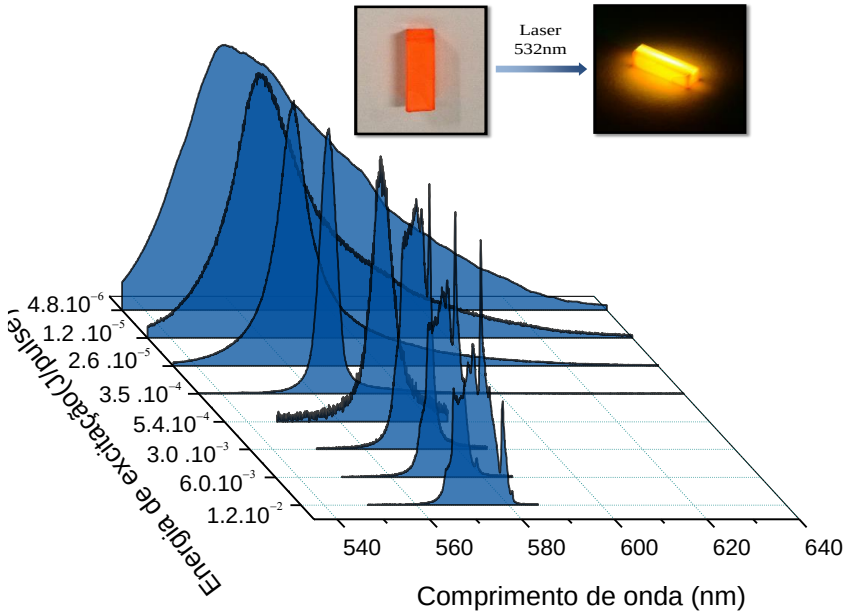


Figura 20. Espectros de emissão da amostra S4 dopada com Rh6G em função da energia de excitação. O esquema inserido acima mostra a coloração amarela da emissão da amostra S4 dopada com Rh6G, sob excitação em 532nm.

Conclusões

Híbridos inorgânicos orgânicos multifuncionais baseados em sílica e fibroína de seda extraída dos casulos de bicho da seda (*Bombyx mori*) foram preparados. Os materiais foram obtidos na forma de monolitos contendo diferentes concentrações de fibroína. As imagens de MEV demonstraram a auto-montagem *in situ* de nanofibras de fibroína dispersas nos HOI. Medidas de espectroscopia Raman e de RMN de estado sólido mostraram que as nanofibras de fibroína apresentam preferencial conformação folha-β. Nós sugerimos que a precipitação de nanofibras de fibroína é induzida pelo etanol formado durante a hidrólise e policondensação do tetraetoxisilano (TEOS) no processo de síntese do material. Estes resultados sugerem uma nova via para a utilização do processo sol gel e para o controle da precipitação de fibroína. Além disso, neste trabalho as nanofibras de fibroína foram utilizadas como um material de sacrifício para a produção de monolitos porosos de sílica para aplicações em lasers aleatórios. Além disso, quando inseridos valores elevados de energia de excitação, o espectro de emissão obtido apresenta o acoplamento do mecanismo de emissão estimulada com o de espalhamento Raman estimulado, sugerindo que os monolitos porosos de sílica preparados também podem ser promissores para aplicações de laser aleatório Raman.

REFERENCES

ABEER, M. M. et al. A review of bacterial cellulose-based drug delivery systems: their biochemistry, current approaches and future prospects. **Journal of Pharmacy and Pharmacology**, v. 66, n. 8, p. 1047-1061, 2014.

ABITBOL, T. et al. Nanocellulose, a tiny fiber with huge applications. **Current Opinion in Biotechnology**, v. 39, p. 76-88, 2016.

ALTMAN, G. H. et al. Silk-based biomaterials. **Biomaterials**, v. 24, n. 3, p. 401-416, 2003.

ANEDDA, A. et al. Rhodamine 6G-SiO_2 hybrids: a photoluminescence study. **Journal of Non-Crystalline Solids**, v. 351, n. 21/23, p. 1850-1854, 2005.

ANEDDA, A. et al. Formation of fluorescent aggregates in rhodamine 6G doped silica glasses. **Journal of Non-Crystalline Solids**, v. 353, n. 5/7, p. 481-485, 2007.

APPLEGATE, M. B. et al. Biocompatible silk step-index optical waveguides. **Biomedical Optics Express**, v. 6, n. 11, p. 4221-4227, 2015.

ARAKI, J.; KUGA, S. Effect of trace electrolyte on liquid crystal type of cellulose microcrystals. **Langmuir**, v. 17, n. 15, p. 4493-4496, 2001.

ARAKI, J. et al. Flow properties of microcrystalline cellulose suspension prepared by acid treatment of native cellulose. **Colloids and Surfaces A**: Physicochemical and Engineering Aspects, v. 142, n. 1, p. 75-82, 1998.

ARAKI, J. et al. Influence of surface charge on viscosity behavior of cellulose microcrystal suspension. **Journal of Wood Science**, v. 45, n. 3, p. 258-261, 1999.

ARCOS, D.; VALLET-REGÍ, M. Sol-gel silica-based biomaterials and bone tissue regeneration. **Acta Biomaterialia**, v. 6, n. 8, p. 2874-2888, 2010.

ARRIGHI, V. et al. Fine Structure and optical properties of cholesteric films prepared from cellulose 4-methylphenyl urethane/n-vinyl pyrrolidinone solutions. **Macromolecules**, v. 35, n. 19, p. 7354-7360, 2002.

ASAKURA, T. et al. Heterogeneous structure of silk fibers from *Bombyx mori* resolved by C-13 solid-state NMR spectroscopy. **Journal of the American Chemical Society**, v. 124, n. 30, p. 8794-8795, 2002.

ASAKURA, T. et al. Evidence from 13C solid-state NMR spectroscopy for a lamella structure in an alanine-glycine copolypeptide: a model for the crystalline domain of *Bombyx mori* silk fiber. **Protein Science**, v. 14, n. 10, p. 2654-2657, 2005.

ASAKURA, T. et al. Elucidating silk structure using solid-state NMR. **Soft Matter**, v. 9, n. 48, p. 11440-11450, 2013.

BACHELARD, N. et al. Disorder as a playground for the coexistence of optical nonlinear. **ACS Photonics**, v. 1, n. 11, p. 1206-1211, 2014.

BALACHANDRAN, R. M.; LAWANDY, N. M. Laser action in strongly scattering media. In: INTERNATIONAL QUANTUM ELECTRONICS CONFERENCE, 21st, 1994, Anaheins. **Proceedings**… Washington, DC: Optical Society of America, 1994, p. QFE1.

BARUD, H. S. et al. Bacterial cellulose-silica organic-inorganic hybrids. **Journal of Sol-Gel Science and Technology**, v. 46, n. 3, p. 363-367, 2008.

BARUD, H. S. et al. Antimicrobial bacterial cellulose-silver nanoparticles composite membranes. **Journal of Nanomaterials**, v. 2011, 2011. doi:101155120111721631.

BATISTA, J. N. M. et al. Controlling silicate meso-structures using sucupira oil as a new swelling agent. **Applied Surface Science**, v. 258, n. 12, p. 5111-5116, 2012.

BAUDOUIN, Q. et al. A cold-atom random laser. **Nature Physics**, v. 9, n. 6, p. 357-360, 2013.

BECK, S.; BOUCHARD, J.; BERRY, R. Controlling the reflection wavelength of iridescent solid films of nanocrystalline cellulose. **Biomacromolecules**, v. 12, n. 1, p. 167-172, 2011.

BECK, S. et al. Controlled production of patterns in iridescent solid films of cellulose nanocrystals. **Cellulose**, v. 20, n. 3, p. 1401-1411, 2013.

BECK-CANDANEDO, S.; ROMAN, M.; GRAY, D. G. Effect of reaction conditions on the properties and behavior of wood cellulose nanocrystal suspensions. **Biomacromolecules**, v. 6, n. 2, p. 1048-1054, 2005.

BETTINGER, C. J. et al. Silk fibroin microfluidic devices. **Advance Materials**, v. 19, n. 5, p. 2847-2850, 2007.

BRITO-SILVA, A. M. et al. Random laser action in dye solutions containing Stöber silica nanoparticles. **Journal of Applied Physics**, v. 108, n. 3, p. 33508/1- 33508/2, 2010.

BROER, D. J.; LUB, J.; MOL, G. N. Wide-band reflective polarizers from cholesteric polymer networks with a pitch gradient. **Nature**, v. 378, p. 467-469, 1995.

BROWN, R. M. Cellulose structure and biosynthesis: what is in store for the 21st century? **Journal of Polymer Science Part A**: Polymer Chemistry, v. 42, n. 3, p. 487-495, 2004.

BROWN, S. P.; SPIESS, H. W. Advanced solid-state NMR methods for the elucidation of structure and dynamics of molecular, macromolecuar and supramolecular systems. **Chemical Reviews**, v. 101, p. 4125-4155, 2001.

BUJDÁK, J. Effect of the layer charge of clay minerals on optical properties of organic dyes. A review. **Applied Clay Science**, v. 34, n. 1/4, p. 58-73, 2006.

CAMPBELL, M. G.; TASINKEVYCH, M.; SMALYUKH, I. I. Topological polymer dispersed liquid crystals with bulk nematic defect lines pinned to handlebody surfaces. **Physical Review Letters**, v. 112, n. 19, p. 19780/1-19780/5, 2014.

CAO, H. et al. Random laser action in semiconductor powder. **Physical Review Letters**, v. 82, n. 11, p. 2278-2281, 1999.

CAPADONA, J. R. et al. Polymer nanocomposites with nanowhiskers isolated from microcrystalline cellulose. **Biomacromolecules**, v. 10, n. 4, p. 712-716, 2009.

CARBONARO, C. M. et al. Light assisted dimer to monomer transformation in heavily doped rhodamine 6G-porous silica hybrids. **Journal of Physical Chemistry B**, v. 113, n. 15, p. 5111-5116, 2009.

CARREÑO, S. J. M. et al. Interplay between random laser performance and self-frequency conversions in Nd x Y 1.00−x $Al_3(BO_3)_4$ nanocrystals powders. **Optical Materials**, v. 54, p. 262-268, 2016.

CHAO, P. G. et al. Silk hydrogel for cartilage tissue engineering. **Journal of Biomedical Materials Research Part B**: Applied Biomaterials, v. 95, n. 1, p. 84-90, 2010.

CHOI, S. S. et al. Electrically tuneable liquid crystal photonic bandgaps. **Advanced Materials**, v. 21, n. 38/39, p. 3915-3918, 2009.

CHU, G. et al. Chiral nematic mesoporous films of Y_2O_3:Eu^{+3} with tunable optical properties and modulated photoluminescence. **Journal of Materials Chemistry C**, v. 2, p. 9189-9195, 2014.

CHU, G. et al. Chiral electronic transitions of YVO_4:Eu^{3+} nanoparticles in cellulose based photonic materials with circularly polarized excitation. **Journal of Materials Chemistry C**, v. 3, n. 14, p. 3384-3390, 2015a.

CHU, G. et al. Optically tunable chiral plasmonic guest-host cellulose films weaved with long-range ordered silver nanowires. **ACS Applied Materials and Interfaces**, v. 7, n. 22, p. 11863-11870, 2015b.

COASNE, B. Multiscale adsorption and transport in hierarchical porous materials. **New Journal of Chemistry**, v. 40, n. 5, p. 4078-4094, 2016.

COLES, H. J.; PIVNENKO, M. N. Liquid crystal 'blue phases' with a wide temperature range. **Nature**, v. 436, n. 7053, p. 997-1000, 2005.

DANG, Q. et al. Silk fibroin/montmorillonite nanocomposites: effect of pH on the conformational transition and clay dispersion. **Biomacromolecules**, v. 11, n. 7, p. 1796-1801, 2010.

DARDER, M.; ARANDA, P.; RUIZ-HITZKY, E. Bionanocomposites: a new concept of ecological, bioinspired, and functional hybrid materials. **Advanced Materials**, v. 19, n. 10, p. 1309-1319, 2007.

DE VRIES, H. Rotatory power and other optical properties of certain liquid crystals. **Acta Crystallographica**, v. 4, n. 3, p. 219-226, 1951.

DEBZI, H. M.; CHANZY, H. The Iα →Iβ transformation of highly crystalline cellulose by annealing in various mediums. **Macromolecules**, v. 24, n. 26, p. 6816-6822, 1991.

DOANE, J. W. et al. Field controlled light scattering from nematic microdroplets. **Applied Physics Letters**, v. 48, n. 4, p. 269-271, 1986.

DOMINGUES, R. M. A.; GOMES, M. E.; REIS, R. L. The potential of cellulose nanocrystals in tissue engineering strategies. **Biomacromolecules**, v. 15, n. 7, p. 2327-2346, 2014.

DONG, X. M.; REVOL, J.-F.; GRAY, D. G. Effect of microcrystallite preparation conditions on the formation of colloid crystals of cellulose. **Water**, v. 5, p. 19-32, 1998.

DRIESEN, K. et al. Near-infrared luminescence emitted by an electrically switched liquid crystal cell. **Journal of Luminescence**, v. 127, n. 2, p. 611-615, 2007.

DRZAIC, P. S. Polymer dispersed nematic liquid crystal for large area displays and light valves. **Journal of Applied Physics**, v. 60, n. 6, p. 2142-2148, 1986.

DUFRESNE, A.; CAVAILLE, J.-Y.; VIGNON, M. R. Mechanical behavior of sheets prepared from sugar beet cellulose microfibrils. **Journal of Applied Polymer Science**, v. 64, n. 6, p. 1185-1194, 1997.

DUJARDIN, E.; BLASEBY, M.; MANN, S. Synthesis of mesoporous silica by sol–gel mineralisation of cellulose nanorod nematic suspensions. **Journal of Materials Chemistry**, v. 13, n. 4, p. 696-699, 2003.

DUNDERDALE, G. J. et al. Large-scale and environmentally friendly synthesis of pH-responsive oil-repellent polymer brush surfaces under ambient conditions. **ACS Applied Materials and Interfaces**, v. 6, p. 11864-11868, 2014.

EICHHORN, S. J. Cellulose nanowhiskers: promising materials for advanced applications. **Soft Matter**, v. 7, n. 2, p. 303-315, 2011.

ELAZZOUZI-HAFRAOUI, S. et al. The shape and size distribution of crystalline nanoparticles prepared by acid hydrolysis of native cellulose. **Biomacromolecules**, v. 9, n. 1, p. 57-65, 2007.

FAVIER, V.; CHANZY, H.; CAVAILLE, J. Y. Polymer nanocomposites reinforced by cellulose whiskers. **Macromolecules**, v. 28, p. 6365-6367, 1995.

FREDDI, G. et al. Silk fibroin/cellulose blend films: preparation, structure, and physical properties. **Journal of Applied Polymer Science**, v. 56, n. 12, p. 1537-1545, 1995.

FU, L.; ZHANG, J.; YANG, G. Present status and applications of bacterial cellulose-based materials for skin tissue repair. **Carbohydrate Polymers**, v. 92, n. 2, p. 1432-1442, 2013.

GAGNÉ, M.; KASHYAP, R. Demonstration of a 3 mW threshold Er-doped random fiber laser based on a unique fiber Bragg grating. **Optics Express**, v. 17, n. 21, p. 19067-19074, 2009.

GAIKWAD, P. et al. Competition and coexistence of Raman and random lasing in silica/titania-based solid foams. **Advanced Optical Materials**, v. 3, n. 11, p. 1640-1651, 2015.

GALARNEAU, A. et al. Comptes rendus chimie hierarchical porous silica monoliths: a novel class of microreactors for process intensification in catalysis and adsorption. **Comptes Rendus Chimie**, v. 19, n. 1/2, p. 231-247, 2016.

GANESAN, L. M. et al. Piezo-optical and electro-optical behaviour of nematic liquid crystals dispersed in a ferroelectric copolymer matrix. **Journal of Physics D**: Applied Physics, v. 43, n. 1, p. 015401/1-015401/6, 2010.

GARCIA DE RODRIGUEZ, N. L. G.; THIELEMANS, W.; DUFRESNE, A. Sisal cellulose whiskers reinforced polyvinyl acetate nanocomposites. **Cellulose**, v. 13, n. 3, p. 261-270, 2006.

GARCÍA-REVILLA, S. et al. Ultrafast random laser emission in a dye-doped silica gel powder. **Optics Express**, v. 16, n. 16, p. 12251-12263, 2008.

GARCÍA-REVILLA, S. et al. 1Low threshold random lasing in dye-doped silica nano powders. **Optics Express**, v. 17, n. 15, p. 13202-13215, 2009.

GEBAUER, D. et al. A transparent hybrid of nanocrystalline cellulose and amorphous calcium carbonate nanoparticles. **Nanoscale**, v. 3, n. 9, p. 3563-3566, 2011.

GIESE, M. et al. Thermal switching of the reflection in chiral nematic mesoporous organosilica films infiltrated with liquid crystals. **ACS Applied Materials and Interfaces**, v. 5, p. 6854-6859, 2013.

GIESE, M. et al. Functional materials from cellulose-derived liquid-crystal templates. **Angewandte Chemie International Edition**, v. 54, n. 10, p. 2888-2910, 2015.

GRAY, D. G. SEM imaging of chiral nematic films cast from cellulose nanocrystal suspensions. **Cellulose**, v. 19, n. 5, p. 1599-1605, 2012.

GRUNERT, M.; WINTER, W. T. Nanocomposites of cellulose acetate butyrate reinforced with cellulose nanocrystals. **Journal of Polymers and the Environment**, v. 10, n. 1/2, p. 27-30, 2002.

GUIOCHON, G. Monolithic columns in high-performance liquid chromatography. **Journal of Chromatography A**, v. 1168, n. 1/2, p. 101-168, 2007.

GUTIERREZ, J. et al. Conductive properties of TiO_2 / bacterial cellulose hybrid fibres. **Journal of Colloid And Interface Science**, v. 377, n. 1, p. 88-93, 2012.

HABIBI, Y. Key advances in the chemical modification of nanocelluloses. **Chemical Society Reviews**, v. 43, n. 5, p. 1519-1542, 2014.

HABIBI, Y.; LUCIA, L. A. Nanocelluloses: emerging building blocks for renewable materials. In: _____. (Ed). **Polysaccharide building blocks**: sustainable approach to the development of renewable biomaterials. Hoboken: Wiley, 2012. Chap. 3 p. 105-125.

HABIBI, Y.; LUCIA, L. A.; ROJAS, O. J. Cellulose nanocrystals: chemistry, self-assembly, and applications. **Chemical Reviews**, v. 110, p. 3479-3500, 2010.

HABIBI, Y. et al. Bionanocomposites based on poly (ε -caprolactone) -grafted cellulose nanocrystals by ring-opening polymerization. **Journal of Materials Chemistry**, v. 18, n. 41, p. 5002-5010, 2008.

HANLEY, S. J. et al. Atomic force microscopy and transmission electron microscopy of cellulose from *Micrasterias denticulata*; evidence for a chiral helical microfibril twist. **Cellulose**, v. 4, n. 3, p. 209-220, 1997.

HE, S.-J.; VALLUZZI, R.; GIDO, S. P. Silk I structure in *Bombyx mori* silk foams. **International Journal of Biological Macromolecules**, v. 24, n. 2, p. 187-195, 1999.

HIRAI, A. et al. Phase separation behavior in aqueous suspensions of bacterial cellulose nanocrystals prepared by sulfuric acid treatment. **Langmuir**, v. 25, n. 1, p. 497-502, 2008.

HOKR, B. H. et al. Bright emission from a random Raman laser. **Nature Communications**, v. 5, 2014. doi:10.1038/ncomms5356.

HOPKINS, A. M. et al. Silk hydrogels as soft substrates for neural tissue engineering. **Advanced Functional Materials**, v. 23, n. 41, p. 5140-5149, 2013.

HOSSAIN, K. S. et al. Dilute-solution properties of regenerated silk fibroin. **The Journal of Physical Chemistry B**, v. 107, p. 8066-8073, 2003.

HOU, A.; CHEN, H. Preparation and characterization of silk/silica hybrid biomaterials by sol-gel crosslinking process. **Materials Science and Engineering B**: Solid-State Materials for Advanced Technology, v. 167, n. 2, p. 124-128, 2010.

HU, K. et al. Preparation of fibroin/recombinant human-like collagen scaffold to promote fibroblasts compatibility. **Journal of Biomedical Materials Research Part A**, v. 84, n. 2, p. 483-490, 2008.

HU, W. et al. Functionalized bacterial cellulose derivatives and nanocomposites. **Carbohydrate Polymers**, v. 101, p. 1043-1060, 2014.

HU, X. et al. Regulation of silk material structure by temperature-controlled water vapor annealing. **Biomacromolecules**, v. 12, n. 5, p. 1686-1696, 2011.

HUANG, L. et al. Single-strand spider silk templating for the formation of hierarchically ordered hollow mesoporous silica fibers. **Journal of Materials Chemistry**, v. 13, n. 4, p. 666-668, 2003.

HUANG, Y. et al. Recent advances in bacterial cellulose. **Cellulose**, v. 21, n. 1, p. 1-30, 2014.

IFUKU, S. et al. Surface modification of bacterial cellulose nanofibers for property enhancement of optically transparent composites: dependence on acetyl-group DS. **Biomacromolecules**, v. 8, n. 6, p. 1973-1978, 2007.

IGNESTI, E. et al. Experimental and theoretical investigation of statistical regimes in random laser emission. **Physical Review A**, v. 88, n. 3, p. 33820/1-33820/8, 2013.

INOUE, S. et al. Silk fibroin of *Bombyx mori* is secreted, assembling a high molecular mass elementary unit consisting of H-chain, L-chain, and P25, with a 6: 6: 1 molar ratio. **Journal of Biological Chemistry**, v. 275, n. 51, p. 40517-40528, 2000.

ISHIDA, M. et al. Solvent- and mechanical-treatment-induced conformational transition of silk fibroins studied by high. **Macromolecules**, v. 94, n. 37, p. 88-94, 1990.

JIMENEZ-VILLAR, E. et al. Novel core–shell (TiO_2@ silica) nanoparticles for scattering medium in a random laser: higher efficiency, lower laser threshold and lower photodegradation. **Nanoscale**, v. 5, n. 24, p. 12512-12517, 2013.

JIN, H.-J.; KAPLAN, D. L. Mechanism of silk processing in insects and spiders. **Nature**, v. 424, n. 6952, p. 1057-1061, 2003.

JIN, H.- J. et al. Water-stable silk films with reduced β-sheet content. **Advanced Functional Materials**, v. 15, n. 8, p. 1241-1247, 2005.

KAPLAN, D.et al. Silk. In: KAPLAN, D.; McGRATH, K. (Ed.). **Protein-based materials**. Boston: Birkhäuser, 2012. Chap. 4, p. 103-133.

KELLY, J. A. et al. The development of chiral nematic mesoporous materials. **Accounts of Chemical Research**, v. 47, n. 4, p. 1088-1096, 2014.

KHAN, M. K. et al. Flexible mesoporous photonic resins with tunable chiral nematic structures. **Angewandte Chemie International Edition**, v. 52, n. 34, p. 8921-8924, 2013.

KIKUCHI, H. et al. Polymer-stabilized liquid crystal blue phases. **Nature Materials**, v. 1, n. 1, p. 64-68, Sept. 2002.

KIM, D.-H. et al. Dissolvable films of silk fibroin for ultrathin conformal bio-integrated electronics. **Nature Materials**, v. 9, n. 6, p. 511-517, 2010.

KIM, S. et al. Silk inverse opals. **Nature Photonics**, v. 6, n. 12, p. 818-823, 2012.

KIM, U. J. et al. Structure and properties of silk hydrogels. **Biomacromolecules**, v. 5, n. 3, p. 786-792, 2004.

KIRK, A. G.; ANDREWS, M. P. Nanocrystalline cellulose for covert optical encryption. **Journal of Nanophotonics**, v. 6, n. 1, p. 63511-63516, 2012.

KISHIMOTO, Y. et al. Nanocomposite of silk fibroin nanofiber and montmorillonite: fabrication and morphology. **International journal of biological macromolecules**, v. 57, p. 124-128, 2013.

KLEMM, D. et al. Cellulose: fascinating biopolymer and sustainable raw material. **Angewandte Chemie International Edition**, v. 44, n. 22, p. 3358-3393, 2005.

KLEMM, D. et al. Nanocelluloses: a new family of nature-based materials. **Angewandte Chemie International Edition**, v. 50, n. 24, p. 5438-5466, 2011.

KODAMA, K. The preparation and physico-chemical properties of sericin. **Biochemical Journal**, v. 20, n. 6, p. 1208-1222, 1926.

KOH, L. D. et al. Structures, mechanical properties and applications of silk fibroin materials. **Progress in Polymer Science**, v. 46, p. 86-110, 2015.

KONDO, T.; SAWATARI, C. A fourier transform infra-red spectroscopic analysis of the character of hydrogen bonds in amorphous cellulose. **Polymer**, v. 37, n. 3, p. 393-399, 1996.

KOPP, V. I. et al. Low-threshold lasing at the edge of a photonic stop band in cholesteric liquid crystals. **Optics Letters**, v. 23, n. 21, p. 1707-1709, 1998.

KUNDU, B. et al. Silk fibroin biomaterials for tissue regenerations. **Advanced Drug Delivery Reviews**, v. 65, n. 4, p. 457-470, 2013.

LAGERWALL, J. P. F. et al. Cellulose nanocrystal-based materials: from liquid crystal self-assembly and glass formation to multifunctional thin films. **NPG Asia Materials**, v. 6, n. 1, 2014. doi:10.1038/am.2013.69.

LEGNANI, C. et al. Bacterial cellulose membrane as flexible substrate for organic light emitting devices. **Thin Solid Films**, v. 517, n. 3, p. 1016-1020, 2008.

LETOKHOV, V. S. Stimulated emission of an ensemble of scattering particles with negative absorption. **ZhETF Pisma Redaktsiiu**, v. 5, p. 212-215, 1967.

LI, X. et al. In situ synthesis of CdS nanoparticles on bacterial cellulose nanofibers. **Carbohydrate Polymers**, v. 76, n. 4, p. 509-512, 2009.

LIMA, L. R. et al. Silk fibroin-antigenic peptides-YVO_4:Eu^{3+} nanostructured thin films as sensors for hepatitis C. **Journal of Luminescence**, v. 170, p. 375-379, 2016.

LIN, N.; DUFRESNE, A. Nanocellulose in biomedicine: current status and future prospect. **European Polymer Journal**, v. 59, p. 302-325, 2014.

LIPPMAA, E. et al. Structural studies of silicates by solid-state high-resolution 29Si NMR. **Journal of the American Chemical Society**, v. 102, n. 15, p. 4889-4893, 1980.

LIU, L. et al. Mesoporous hybrid from anionic polyhedral oligomeric silsesquioxanes (POSS) and cationic surfactant by hydrothermal approach. **Microporous and Mesoporous Materials**, v. 132, p. 567-571, 2010.

LIU, X.; ZHANG, K. Silk fiber - molecular formation mechanism, structure-property relationship and advanced applications. In: LESIER, C. (Ed.). **Oligomerization of chemical and biological compounds**. Rijeka: Intech, 2014. Chap. 3, p. 69-102.

LOFAJ, M.; VALENT, I.; BUJDAK, J. Mechanism of rhodamine 6G molecular aggregation in montmorillonite colloid. **Open Chemistry**, v. 11, n. 10, p. 1606-1619, 2013.

LOWELL, S. et al. **Characterization of porous solids and powders**: surface area, pore size and density. Dordrecht: Springer, 2004.

LUAN, F. et al. Lasing in nanocomposite random media. **Nano Today**, v. 10, n. 2, p. 168-192, 2015.

LUO, K.; YANG, Y.; SHAO, Z. Physically crosslinked biocompatible silk-fibroin-based hydrogels with high mechanical performance. **Advanced Functional Materials**, p. 872-880, 2015.

MANNING, A. P. et al. NMR of guest-host systems: 8CB in chiral nematic porous glasses. **Magnetic Resonance in Chemistry**, v. 52, n. 10, p. 532-539, 2014.

MARCHESSAULT, R. H.; MOREHEAD, F. F.; WALTER, N. M. Liquid crystal systems from fibrillar polysaccharides. **Nature**, v. 184, n. 4686, p. 632-633, 1959.

MARELLI, B. et al. Silk fibroin as edible coating for perishable food preservation. **Scientific Reports**, v. 6, 2016. doi:10.1038/srep25263.

MARKUSHEV, V. M.; ZOLIN, V. F.; BRISKINA, C. M. Luminescence and stimulated emission of neodymium in sodium lanthanum molybdate powders. **Quantum Electronics**, v. 16, n. 2, p. 281-283, 1986.

MARSH, R. E.; COREY, R. B.; PAULING, L. An investigation of the structure of silk fibroin. **Biochimica et Biophysica Acta**, v. 16, p. 1-34, 1955.

MARTÍNEZ, V. M. et al. Characterization of rhodamine 6G aggregates intercalated in solid thin films of laponite clay . 1 . Absorption spectroscopy characterization of rhodamine 6G aggregates intercalated in solid thin films of laponite. **Journal Physical Chemistry B**, v. 109, p. 7443-7450, 2005.

MATOS, C. J. S. de et al. Random fiber laser. **Physical Review Letters**, v. 99, n. 15, p. 153903/1-153903/4, 2007.

MATSUMOTO, A. et al. Mechanisms of silk fibroin sol-gel transitions. **Journal of Physical Chemistry B**, v. 110, n. 43, p. 21630-21638, 2006.

MENEZES, A. J. de et al. Extrusion and characterization of functionalized cellulose whiskers reinforced polyethylene nanocomposites. **Polymer**, v. 50, n. 19, p. 4552-4563, 2009.

MIESZAWSKA, A. J. et al. Osteoinductive silk–silica composite biomaterials for bone regeneration. **Biomaterials**, v. 31, n. 34, p. 8902-8910, 2010.

MONTI, P. et al. Raman spectroscopic characterization of *Bombyx mori* silk fibroin: Raman spectrum of silk I. **Journal of Raman Spectroscopy**, v. 32, p. 103-107, 2001.

MOON, R. J. et al. Cellulose nanomaterials review: structure, properties and nanocomposites. **Chemical Society Reviews**, v. 40, n. 7, p. 3941-3994, 2011.

MORI, H.; TSUKADA, M. New silk protein: modification of silk protein by gene engineering for production of biomaterials. **Reviews in Molecular Biotechnology**, v. 74, n. 2, p. 95-103, 2000.

MOTTA, A.; FAMBRI, L.; MIGLIARESI, C. Regenerated silk fibroin films: thermal and dynamic mechanical analysis. **Spectrum**, v. 203, p. 1658-1665, 2002.

MOURA, A. L. et al. Multi-wavelength emission through self-induced second-order wave-mixing processes from a Nd^{3+} doped crystalline powder random laser. **Scientific Reports**, v. 5, 2015. doi:10.1038/srep13816.

NAGARKAR, S. et al. Structure and gelation mechanism of silk hydrogels. **Physical Chemistry Chemical Physics**, v. 12, n. 15, p. 3834-3844, 2010.

NELSON, D. L.; COX, M. M. **Princípios de bioquímica de Lehninger**. Porto Alegre: Artmed, v. 6, 2011.

NGUYEN, T.; HAMAD, W. Y.; MacLACHLAN, M. J. CdS quantum dots encapsulated in chiral nematic mesoporous silica : New iridescent and luminescent Materials. **Advanced Functional Materials**, v. 24, p. 777-783, 2014.

NOGINOV, M. A. Other types of solid-state random lasers. In: _____. **Solid-state random lasers**. New York: Springer, 2005. Chap. 9, p. 198-221. (Springer series in optical sciences, v. 105).

NUMATA, K.; CEBE, P.; KAPLAN, D. L. Mechanism of enzymatic degradation of beta-sheet crystals. **Biomaterials**, v. 31, n. 10, p. 2926-2933, 2010.

OH, S. Y. et al. Crystalline structure analysis of cellulose treated with sodium hydroxide and carbon dioxide by means of X-ray diffraction and FTIR spectroscopy. **Carbohydrate Research**, v. 340, n. 15, p. 2376-2391, 2005.

OHZONO, T.; YAMAMOTO, T.; FUKUDA, J. A liquid crystalline chirality balance for vapours. **Nature Communications**, v. 5, 2014. doi:10.1038/ncomms4735.

OMENETTO, F. G.; KAPLAN, D. L. A new route for silk. **Nature Photonics**, v. 2, n. 11, p. 641-643, 2008.

OMENETTO, F. G.; KAPLAN, D. L. New opportunities for an ancient material. **Science**, v. 329, n. 5991, p. 528-531, 2010.

PAN, J.; HAMAD, W.; STRAUS, S. K. Parameters affecting the chiral nematic phase of nanocrystalline cellulose films. **Macromolecules**, v. 43, n. 8, p. 3851-3858, 2010.

PENNINCK, L. et al. Light emission from dye-doped cholesteric liquid crystals at oblique angles: simulation and experiment. **Physical Review E**: Statistical, Nonlinear, and Soft Matter Physics, v. 85, n. 4, pt. 1, p. 041702/1-041702/7, 2012.

PENNISI, E. Diverse crystals account for beetle sheen. **Science**, v. 341, n. 6142, p. 120, 2013.

PEREIRA, C. et al. Copper acetylacetonate anchored onto amine-functionalised clays. **Journal of Colloid and Interface Science**, v. 316, n. 2, p. 570-579, 2007.

PEREIRA, R. F. P.; SILVA, M. M.; DE ZEA BERMUDEZ, V. *Bombyx mori* silk fibers: an outstanding family of materials. **Macromolecular Materials and Engineering**, v. 300, n. 12, p. 1171-1198, 2015.

PING, Y. et al. Structured color humidity indicator from reversible pitch tuning in self-assembled nanocrystalline cellulose films. **Sensors & Actuators B**: Chemical, v. 176, p. 692-697, 2013.

PINTO, E. R. P. et al. Transparent composites prepared from bacterial cellulose and castor oil based polyurethane as substrates for flexible OLEDs. **Journal of Materials Chemistry C**, v. 3, n. 44, p. 11581-11588, 2015.

PIRANI, S.; HASHAIKEH, R. Nanocrystalline cellulose extraction process and utilization of the byproduct for biofuels production. **Carbohydrate Polymers**, v. 93, n. 1, p. 357-363, 2013.

PREDA, R. C. et al. Bioengineered silk proteins to control cell and tissue functions. In: GERRARD, J. A. (Ed.). **Protein nanotechnology**: protocols, instrumentation, and applications. 2nd ed. New York: Humana Press, 2013. p. 19-41. (Methods in molecular biology, v. 996).

PROUZET, E. et al. Roughness of mesoporous silica surfaces deduced from adsorption measurements. **Microporous and Mesoporous Materials**, v. 119, p. 9-17, 2009.

QIU, K.; NETRAVALI, A. N. A Review of fabrication and applications of bacterial cellulose based nanocomposites. **Polymer Reviews**, v. 54, n. 4, p. 598-626, 2014.

QU, D. et al. Chiral fluorescent films of gold nanoclusters and photonic cellulose with modulated fluorescence emission. **Journal Material Chemistry C**, v. 4, n. 9, p. 1764-1768, 2016.

QUEREJETA-FERNÁNDEZ, A. et al. Chiral plasmonic films formed by gold nanorods and cellulose nanocrystals. **Journal of the American Chemical Society**, v. 136, p. 4788-4793, 2014.

QUEREJETA-FERNANDEZ, A. et al. Circular dichroism of chiral nematic films of cellulose nanocrystals loaded with plasmonic nanoparticles. **ACS Nano**, v. 9, n. 10, p. 10377-10385, 2015.

RÅNBY, B. G. Fibrous macromolecular systems. Cellulose and muscle. The colloidal properties of cellulose micelles. **Discussions of the Faraday Society**, v. 11, p. 158-164, 1951.
REDDING, B.; CHOMA, M. A.; CAO, H. Speckle-free laser imaging using random laser illumination. **Nature Photonics**, v. 6, n. 6, p. 355-359, 2012.

REVOL, J. et al. Helicoidal self-ordering of cellulose microfibrils in aqueous suspension. **International Journal of Biological Macromolecules**, v. 14, p. 170-172, 1992.

REVOL, J.-F.; GODBOUT, L.; GRAY, D. G. Solid self-assembled films of cellulose with chiral nematic order and optically variable properties. **Journal of Pulp and Paper Science**, v. 24, n. 5, p. 146-149, 1998.

ROCHA, L. A. et al. Luminescence properties of Eu-complex formations into ordered mesoporous silica particles obtained by the spray pyrolysis process. **Nanotechnology**, v. 26, n. 33, p. 335604/1-335604/11, 2015.

ROMAN, M.; WINTER, W. T. Effect of sulfate groups from sulfuric acid hydrolysis on the thermal degradation behavior of bacterial cellulose. **Biomacromolecules**, v. 5, p. 1671-1677, 2004.

SAITÔ, H. et al. High-resolution 13C NMR study of silk fibroin in the solid state by the cross-polarization-magic angle spinning method. Conformational characterization of silk I and silk II type forms of *Bombyx mori* fibroin by the conformation-dependent 13C chemical shif. **Macromolecules**, v. 17, n. 35, p. 1405-1412, 1984.

SAITO, T. et al. Cellulose nanofibers prepared by TEMPO-mediated oxidation of native cellulose. **Biomacromolecules**, v. 8, n. 8, p. 2485-2491, 2007.

SALAJKOVÁ, M.; BERGLUND, L. A.; ZHOU, Q. Hydrophobic cellulose nanocrystals modified with quaternary ammonium salts. **Journal of Materials Chemistry**, v. 22, n. 37, p. 19798-19805, 2012.

SANTOS, M. V. dos et al. Random laser action from flexible biocellulose-based device. **Journal of Applied Physics**, v. 115, n. 8, p. 083108/1-083108/5, 2014.

SHAH, N. et al. Overview of bacterial cellulose composites: a multipurpose advanced material. **Carbohydrate Polymers**, v. 98, n. 2, p. 1585-1598, 2013.

SHIMURA, K. et al. Studies on silk fibroin of *Bombyx mori.* I. Fractionation of fibroin prepared from the posterior silk gland. **Journal of biochemistry**, v. 80, n. 4, p. 693-702, 1976.

SHIN, Y.; EXARHOS, G. J. Template synthesis of porous titania using cellulose nanocrystals. **Materials Letters**, v. 61, n. 11, p. 2594-2597, 2007.

SHOPSOWITZ, K. E.; HAMAD, W. Y.; MacLACHLAN, M. J. Chiral nematic mesoporous carbon derived from nanocrystalline cellulose. **Angewandte Chemie International Edition**, v. 50, n. 46, p. 10991-10995, 2011.

SHOPSOWITZ, K. E.; HAMAD, W. Y.; MacLACHLAN, M. J. Flexible and iridescent chiral nematic mesoporous organosilica films. **Journal of the American Chemical Society**, v. 134, n. 2, p. 867-870, 2012.

SHOPSOWITZ, K. E. et al. Free-standing mesoporous silica films with tunable chiral nematic structures. **Nature**, v. 468, n. 7322, p. 422-425, 2010.

SHOPSOWITZ, K. E. et al. Hard templating of nanocrystalline titanium dioxide with chiral nematic ordering. **Angewandte Chemie International Edition**, v. 51, n. 28, p. 6886-6890, 2012.

SHOPSOWITZ, K. E. et al. Biopolymer templated glass with a twist: controlling the chirality, porosity, and photonic properties of silica with cellulose nanocrystals. **Advanced Functional Materials**, v. 24, n. 3, p. 327-338, 2014.

SILVA, R. R. da et al. Silk fibroin biopolymer films as efficient hosts for DFB laser operation. **Journal of Materials Chemistry C**, v. 1, n. 43, p. 7181-7190, 2013.

SIQUEIRA, G.; BRAS, J.; DUFRESNE, A. Cellulose whiskers versus microfibrils: influence of the nature of the nanoparticle and its surface functionalization on the thermal and mechanical properties of nanocomposites. **Biomacromolecules**, v. 10, p. 425-432, 2009.

SMITH, M. A.; LOBO, R. F. A fractal description of pore structure in block-copolymer templated mesoporous silicates. **Microporous and Mesoporous Materials**, v. 131, p. 204-209, 2010.

STEINER, U.; VIGNOLINI, S. Digital color in cellulose nanocrystal films. **ACS Applied Materials and Interfaces**, v. 6, n. 15, p. 12302-12306, 2014.

SULAEVA, I. et al. Bacterial cellulose as a material for wound treatment: properties and modifications. A review. **Biotechnology Advances**, v. 33, n. 8, p. 1547-1571, 2015.

SZNITKO, L.; MYSLIWIEC, J.; MINIEWICZ, A. The role of polymers in random lasing. **Journal of Polymer Science, Part B**: Polymer Physics, v. 53, n. 14, p. 951-974, 2015.

TANAKA, K.; INOUE, S.; MIZUNO, S. Hydrophobic interaction of P25, containing Asn-linked oligosaccharide chains, with the HL complex of silk fibroin produced by *Bombyx mori*. **Insect Biochemistry and Molecular Biology**, v. 29, n. 3, p. 269-276, 1999.

TANAKA, K. et al. Determination of the site of disulfide de linkage between heavy and light chains of silk fibroin produced by *Bombyx mori*. **Science**, v. 1432, p. 92-103, 1999.

TAO, H.; KAPLAN, D. L.; OMENETTO, F. G. Silk materials - a road to sustainable high technology. **Advanced Materials**, v. 24, p. 2824-2837, 2012.

TAO, H. et al. Inkjet Printing of regenerated silk fibroin: from printable forms to printable functions. **Advanced Materials**, v. 27, n. 29, p. 4273-4279, 2015.

TERCJAK, A.; GUTIERREZ, J. Conductive properties of photoluminescent Au/Ps-b-PEO inorganic/organic hybrids containing nematic liquid crystals. **The Journal of Physical Chemistry C**, v. 115, n. 5, p. 1643-1648, 2011.

TERCJAK, A.; GARCIA, I.; MONDRAGON, I. Liquid crystal alignment in electro-responsive nanostructured thermosetting materials based on block copolymer dispersed liquid crystal. **Nanotechnology**, v. 19, n. 27, p. 275701/1- 275701/5, 2008.

TERCJAK, A. et al. Polymer dispersed liquid crystals based on poly(styrene-b-ethylene oxide), poly(bisphenol a carbonate) or poly(methylphenylsiloxane), and 4′-(hexyloxy)-4-biphenyl-carbonitrile: analysis of phase diagrams and morphologies generated. **Journal of Applied Polymer Science**, v. 108, n. 2, p. 1116-1125, 2008.

TERCJAK, A. et al. Thermoresponsive inorganic/organic hybrids based on conductive TiO_2 nanoparticles embedded in poly (styrene-b-ethylene oxide) block copolymer dispersed liquid crystals. **Acta Materialia**, v. 57, n. 15, p. 4624-4631, 2009.

TERCJAK, A. et al. Conductive properties of switchable photoluminescence thermosetting systems based on liquid crystals. **Langmuir**, v. 26, n. 6, p. 4296-302, 2010.

TERCJAK, A. et al. Nano- and macroscale structural and mechanical properties of in situ synthesized bacterial cellulose/PEO-\nb\n-PPO-\nb\n-PEO biocomposites. **ACS Applied Materials & Interfaces**, v. 7, n. 7, p. 4142-4150, 2015.

TERCJAK, A. et al. Switchable photoluminescence liquid crystal coated bacterial cellulose films with conductive response. **Carbohydrate Polymers**, v. 143, p. 188-197, 2016.

TRÉBOSC, J. et al. Solid-state NMR study of MCM-41-type mesoporous silica nanoparticles. **Journal of the American Chemical Society**, v. 127, n. 9, p. 3057-3068, 2005.

UNGER, K. K.; SKUDAS, R.; SCHULTE, M. M. Particle packed columns and monolithic columns in high-performance liquid chromatography-comparison and critical appraisal. **Journal of Chromatography A**, v. 1184, n. 1/2, p. 393-415, 2008.

VALLUZZI, R. et al. Orientation of silk III at the air-water interface. **International Journal of Biological Macromolecules**, v. 24, n. 2, p. 237-242, 1999.

VAN OPDENBOSCH, B. D.; ZOLLFRANK, C. Cellulose-based biotemplated silica. **Advanced Engineering Materials**, v. 16, n. 6, p. 699-712, 2014.

VAVELIUK, P.; SILVA, A. M. de B.; OLIVEIRA, P. C. de. Model for bichromatic laser emission from a laser dye with nanoparticle scatterers. **Physical Review A**, v. 68, n. 1, p. 13805/1-13805/9, 2003.

VEPARI, C.; KAPLAN, D. L. Silk as a biomaterial. **Progress in Polymer Science**, v. 32, n. 8/9, p. 991-1007, 2007.

VOLLRATH, F.; PORTER, D. Silks as ancient models for modern polymers. **Polymer**, v. 50, n. 24, p. 5623-5632, 2009.

WANG, C.; HSIEH, C.; HWANG, J. Flexible organic thin-film transistors with silk fibroin as the gate dielectric. **Advanced Materials**, v. 23, n. 14, p. 1630-1634, 2011.

WANG, H. et al. A study on the flow stability of regenerated silk fibroin aqueous solution. **International Journal of Biological Macromolecules**, v. 36, n. 1, p. 66-70, 2005.

WANG, H. Y.; CHEN, Y. Y.; ZHANG, Y. Q. Processing and characterization of powdered silk micro- and nanofibers by ultrasonication. **Materials Science and Engineering C**, v. 48, p. 444-452, 2015.

WANG, Y.; XU, Y. Chiral nematic mesoporous films of ZrO_2:Eu^{3+}: new luminescent materials. **Dalton Transactions**, v. 43, n. 41, p. 15321-15327, 2014.

WEAVER, J. C. et al. The stomatopod dactyl club: a formidable damage-tolerant biological hammer. **Science**, v. 336, n. 6086, p. 1275-1280, 2012.

WHITE, J. L.; WANG, X. Structural investigations of solid proteins at natural abundance using. **Macromolecules**, v. 35, p. 2633-2639, 2002.

WU, Z. et al. Bacterial cellulose: a robust platform for design of three dimensional carbon-based functional nanomaterials. **Accounts of Chemival Research**, v. 49, n. 1, p. 96-105, 2015.

XU, Q. et al. Novel and simple synthesis of hollow porous silica fibers with hierarchical structure using silk as template. **Materials Science and Engineering**: B, v. 127, n. 2, p. 212-217, 2006.

YAMAGUCHI, K. et al. Primary structure of the silk fibroin light chain determined by cDNA sequencing and peptide analysis. **Journal of Molecular Biology**, v. 210, n. 1, p. 127-139, 1989.

YANG, D. et al. Control of reflectivity and bistability in displays using cholesteric liquid-crystals. **Journal of Applied Physics**, v. 76, n. 2, p. 1331-1333, 1994.

YANG, W. et al. Natural flexible dermal armor. **Advanced Materials**, v. 25, n. 1, p. 31-48, 2013.

YASHCHUK, V. P. Coupled effect of stimulated Raman scattering and random lasing of dyes in multiple scattering medium. **Laser Physics**, v. 25, n. 7, p. 75702/1-75702/6, 2015.

YASHCHUK, V. P. et al. Stimulated Raman scattering of laser dye mixtures dissolved in multiple scattering media. **Quantum Electronics**, v. 44, n. 10, p. 921, 2014.

ZHANG, J. et al. Silkworm cocoon as natural material and structure for thermal insulation. **Materials and Design**, v. 49, p. 842-849, 2013.

ZHANG, Y. P. et al. Structured color humidity indicator from reversible pitch tuning in self-assembled nanocrystalline cellulose films. **Sensors and Actuators, B:** Chemical, v. 176, p. 692-697, 2013.

ZHANG, Y.-Q. Applications of natural silk protein sericin in biomaterials. **Biotechnology Advances**, v. 20, n. 2, p. 91-100, 2002.

ZHAO, J. et al. Apatite-coated silk fibroin scaffolds to healing mandibular border defects in canines. **Bone**, v. 45, n. 3, p. 517-527, 2009.

ZHENG, J.; ZHANG, C.; DICKSON, R. M. Highly fluorescent, water-soluble, size-tunable gold quantum dots. **Physical Review Letters**, v. 93, n. 7, p. 77402/1-77402/2, 2004.

ZHOU, C. et al. Silk fibroin: structural implications of a remarkable amino acid sequence. **Proteins**: Structure, Function, and Bioinformatics, v. 44, n. 2, p. 119-122, 2001.

ZHOU, J. et al. Control of the anchoring behavior of polymer-dispersed liquid crystals: effect of branching in the side chains of polyacrylates. **Journal of the American Chemical Society**, v. 124, p. 9980-9981, 2002.

ZHOU, P. et.al. Structure of *Bombyx mori* silk fibroin based on the DFT chemical shift calculation. **The Journal of Physical Chemistry B**, v. 105, n.50, p. 12469-12476, 2015.

ZHOU, Y.; DING, E.-Y.; LI, W.-D. Synthesis of TiO_2 nanocubes induced by cellulose nanocrystal (CNC) at low temperature. **Materials Letters**, v. 61, n. 28, p. 5050-5052, 2007.